Resolvent-based Estimation and Control of Aerodynamic Flows

by

Junoh Jung

A dissertation submitted in partial fulfillment
of the requirements for the degree of
Doctor of Philosophy
(Mechanical Engineering)
in the University of Michigan
2024

Doctoral Committee:

Professor Aaron Towne, Chair
Professor Solomon Adera
Professor Jesse Capecelatro
Professor Eric Johnsen

Junoh Jung
junohj@umich.edu
ORCID iD: 0000-0003-0962-3127

ACKNOWLEDGEMENTS

This doctoral dissertation would not have been possible without the support and help of many people. First and foremost, the most valuable and significant achievement during my PhD journey was meeting my wife. Juna, without your support, I would not have been able to complete this dissertation. Your unwavering emotional support gave me the strength to persevere and finish my PhD.

I am also deeply grateful to my parents and brother, who have always provided me with immense encouragement. Your material and emotional support have been invaluable to me. Thank you so much.

My sincere gratitude goes to my advisor, Aaron Towne. Aaron, your immense patience and support have been crucial to my growth. I am deeply thankful for the countless hours you spent meeting with me weekly, providing guidance and assistance. You not only shaped my academic journey but also provided the opportunity that led to meeting my wife by inviting me to the U.S. and allowing time for the internship. I am forever grateful for your profound impact on both my personal and professional life.

I would also like to express my appreciation to my defense committee, Prof. Jesse Capecelatro, Prof. Solomon Adera, and Prof. Eric Johnsen. Your input and support have been academically enriching, and I am thankful for your guidance in shaping this dissertation.

I would also like to thank Prof. Martini Eduardo and Prof. Cavalieri Andre, who worked with me despite my shortcomings. Your guidance helped me adapt and find my footing at the start of my PhD journey.

Special thanks to Dr.Thomas Peterka and Dr. David Lenz from Argonne National Laboratory for their significant interest and support during my internship and beyond. You provided me with valuable perspectives on computer science and academia and instilled confidence in me. The experiences I had during that summer at Argonne will never be forgotten.

I am also grateful to my lab colleagues. Rutvij Bhagwat, without your help, my research would have taken much longer. Thank you for your assistance. Peter Frame, I truly enjoyed chatting with you about research and our lives as we sat next to each other in our lab. Ali Farghadan, it has been a pleasure to work with you as a coauthor on your excellent research. I would also like to thank Min Zhu, James Paulson, Yuhao Zhou, Zhicheng Kai, Dheeraj Pulipaka, and Henry Tukel.

Finally, I extend my heartfelt thanks to the Ann Arbor Hope Church and the people I have met there.

TABLE OF CONTENTS

LIST OF FIGURES

LIST OF TABLES

ABSTRACT

Aerodynamic flows are prevalent across numerous engineering fields and play a crucial role in addressing critical societal challenges. In particular, chaotic fluctuations in wake flows can significantly degrade the performance of aerodynamic systems and generate noise. For example, wake flows are closely linked to upstream separated flow, which can reduce the efficiency of aircraft and cars. Additionally, wake perturbations contribute to noise generation in wind turbines and can negatively impact the performance of downstream turbines. Therefore, reducing wake perturbations is essential for enhancing efficiency and delivering broader societal benefits. However, predicting and controlling such flows is challenging due to their nonlinear behavior, significant computational demands, and our incomplete understanding of the underlying physics.

To address these challenges, we employ resolvent-based approaches to estimate and mitigate flow perturbations. Our estimators and controllers are derived using both operator-based and data-driven approaches. The operator-based approach, which relies on the linearized Navier-Stokes operator, offers low computational costs without requiring *a priori* model reduction and incorporates time-colored statistics of the nonlinear terms from the Navier-Stokes equations, interpreted as forcing on the linear dynamics, to partially capture the impact of nonlinearity. The data-driven approach, which uses training data from nonlinear simulations, avoids the need to construct linearized Navier-Stokes operators. This allows for the construction of kernels even for globally unstable flows and naturally incorporates the colored statistics of the nonlinear terms. For both approaches, the Wiener-Hopf formalism is employed to ensure optimal causality in the estimator and controller, enhancing real-time estimation and control performance.

As a first case, we apply these resolvent-based tools to the flow over a backward-facing step at $Re = 500$ using an implementation within the incompressible flow solver, NEK5000. By imposing random external forcing upstream, we generate unsteadiness at the downstream target and then achieve effective estimation and control of downstream fluctuations in both the linear and nonlinear

regimes. Next, we develop a new implementation of the resolvent-based estimation and control tools within the compressible flow solver CharLES for high-performance computing environments. With this implementation, we apply the resolvent-based tools to both laminar and turbulent flows over a NACA 0012 airfoil at Reynolds numbers of 5,000 and 23,000, respectively. For the laminar case, we introduce random upstream perturbations to disrupt the periodic vortex shedding, leading to chaotic fluctuations, which are then successfully predicted and suppressed by the resolvent-based estimator and controller. For the turbulent case, the resolvent-based estimator accurately captures the wake fluctuations present in the spanwise-averaged, spanwise-Fourier-transformed, and the mid-span-plane flows using a small number of shear-stress sensors on the surface of the airfoil.

CHAPTER 1

Introduction

1.1 Motivation and Background

Aerodynamic flows are crucial across various fields for several reasons. In the aerospace industry, aerodynamics plays a significant role in the design and performance of aircraft. Controlling aerodynamic flows in desired directions enhances fuel efficiency, safety, and sustainability by optimizing aerodynamic coefficients such as lift and drag, while also ensuring the structural integrity of flying vehicles [Anderson, 2010]. For example, the turbulent wake behind an aircraft can lead to flight control issues, as illustrated in figure 1.1(a). In the automotive industry, the wake flow behind a vehicle, as shown in figure 1.1(b), impacts drag, which in turn affects fuel efficiency. For aerodynamicists, understanding and managing these undesired flows is essential. Aerodynamic flow research is also vital in the wind energy sector, particularly in the design and optimization of wind turbines. By optimizing blade design, turbine placement, and considering the interactions between multiple turbines, as shown in figure 1.1(c) (e.g., within a wind farm), the efficiency of energy capture can be improved, and costs reduced. These advancements contribute to more sustainable energy solutions [Manwell et al., 2002, Barthelmie et al., 2010a, Barthelmie and Pryor, 2013a]. Moreover, a solid understanding of aerodynamic principles can help address environmental challenges. For example, effectively managing wake perturbations can reduce aerodynamic noise, thereby enhancing environmental compliance and reducing noise pollution [Wagner et al., 1996, Agrawal et al., 2015]. Thus, research in aerodynamic flows drives innovation, efficiency, and sustainability across multiple sectors. By advancing our understanding of air interactions with surfaces and structures, we can develop new technologies and improve existing ones, ultimately

FIGURE 1.1: Turbulent wakes: (*a*) behind an aircraft (credit: Ryoh Ishihara), (*b*) behind a car (source: NASA), and (*c*) behind a wind turbine in a wind farm (owned by Vattenfall, photo by Christian Steiness).

benefiting society as a whole.

Flow estimation is useful for many purposes. Practically, it enables the approximation of flow states at locations that cannot be directly measured or computed due to constraints posed by a limited set of achievable measurements. This is particularly advantageous in extreme environments, such as the high temperatures or pressures encountered in high-speed aircraft or submarines, where experimental equipment can be prohibitively expensive [Jiang et al., 2020]. Avoiding direct measurements in these conditions can yield substantial benefits. Fundamentally, accurate flow state estimation plays a crucial role in enhancing control performance, particularly in closed-loop systems. The effectiveness of control inputs often depends on the precision with which the flow dynamics are predicted by the estimator. For instance, in Linear Quadratic Gaussian (LQG) control [Kalman, 1964], the accuracy of the estimator directly influences the overall performance of the system by improving the prediction of the flow state and enabling more precise control actions. Recent studies have demonstrated that advances in machine learning techniques have further enhanced the ability to accurately estimate and predict flow states, leading to more effective control strategies in fluid dynamics [Koumoutsakos and Mezic, 2006, Duriez et al., 2017, Rabault et al., 2019]. These developments emphasize the critical role of robust estimation methods in achieving high-performance control. Thus, enhancing the accuracy of flow state estimation is essential for advancing control methodologies in fluid mechanics.

In previous studies on flow control for aerodynamic flows, particularly in backward-facing step and airfoil flows, the methods have primarily relied on passive control [Chun and Sung, 1996,

Strykowski and Sreenivasan, 1990, Oruç, 2012] or open-loop control [Meliga et al., 2010, Ma et al., 2011, Yeh and Taira, 2019]. While these methods can sometimes achieve high control performance, they are often inefficient due to the high energy input required, or impractical when structural modifications are needed for changing flow conditions. Closed-loop control has become increasingly attractive in fluid mechanics, but estimating and controlling unsteady, chaotic flows remains a significant challenge, particularly when considering energy efficiency.

Most flow control studies for airfoils focus on controlling flow separation to mitigate the influence of adverse pressure gradients, as suppressing separation can enhance aerodynamic performance [Gad-el Hak and Bushnell, 1991]. However, controlling the perturbations over an airfoil is a compelling area of study that remains largely unexplored and is important for several reasons. First, the perturbations over an airfoil are closely linked to the separation bubble, which contributes to increased drag [Alam et al., 2010, Chang et al., 2022]. Accurately estimating and controlling the perturbations over an airfoil can help identify and reduce drag sources, thereby improving overall aerodynamic efficiency. Second, in many flight control scenarios, such as during maneuvers at high angles of attack, landing, or takeoff, the chaotic motion of unsteady fluctuations over the airfoil can degrade aerodynamic performance. Additionally, unpredictable flight conditions, often influenced by changing weather, can lead to unexpected variations in control setups. In such cases, flow estimation and control of the perturbations become highly valuable. Third, wake perturbations are a major contributor to aerodynamic noise, which is a concern for rotorcraft, including drones and wind turbines [Wagner et al., 1996, Agrawal et al., 2015], and is also related to jet noise. Estimating and reducing aerodynamic noise is essential for improving environmental conditions and enhancing the quality of life in society. Thus, accurate estimation and cost-effective, high-performance closed-loop control of complex flows are critical in many engineering fields. This thesis presents a novel approach for the estimation and control of aerodynamic flows, aiming to improve the prediction and manipulation of these complex flows.

1.2 Physical Description of Aerodynamic Flows

We introduce three types of aerodynamic flows that will be addressed in this thesis: backward-facing step flow, and laminar and turbulent flows over an airfoil. Before delving into the research,

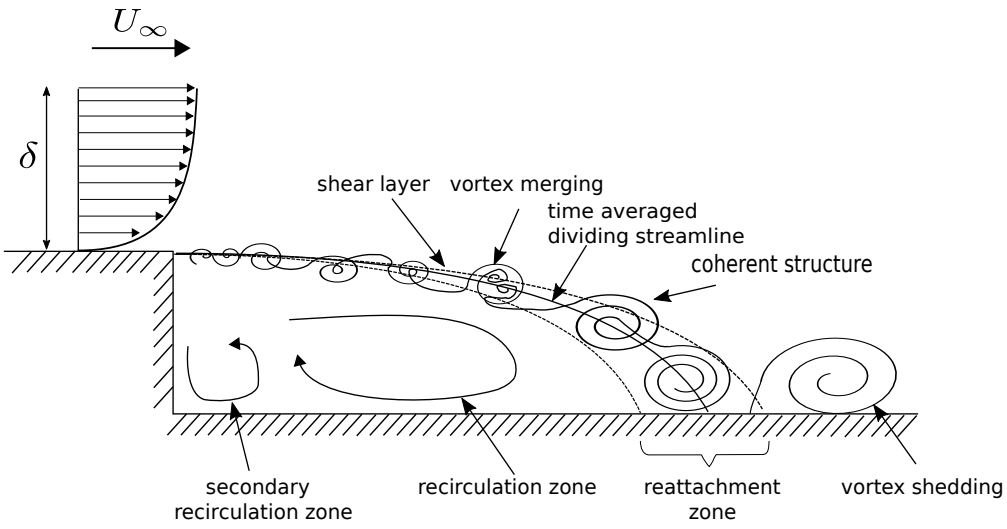

FIGURE 1.2: Diagram of backward-facing step flow, illustrating key flow characteristics.

we will first explore the general physics of these flows.

1.2.1 Backward-Facing Step Flow

The backward-facing step (BFS) is one of the common geometries studied in fluid mechanics. When the fluid suddenly drops off from a surface, it causes a sudden imbalance in the flow, leading to various fluid phenomena. These phenomena can impact the aerodynamic performance and structural design of applications that include this geometry. Depending on the Reynolds number based on the step length, the characteristics of the flow can vary. We briefly examine the fundamental characteristics of backward-facing step (BFS) flow, as illustrated in figure 1.2. The key regions of interest in BFS flow include the flow separation with recirculation, reattachment zone, and the shear layer, as these areas are crucial to the instabilities that occur downstream of the step. When the fluid flows over the step and encounters a sudden drop, it separates from the surface at the step edge, creating a recirculation zone behind the step. Eventually, the separated flow reattaches to the surface further downstream, at a point known as the reattachment point (or zone). The reattachment length, defined as the distance between the step and the reattachment point, depends on the Reynolds number. A shear layer develops over the recirculation zone due to the difference in velocity between the fast-moving flow above and the slower-moving flow within the recirculation zone. This shear layer generates vorticity and instability, especially in turbulent

flows.

Armaly et al. [1983] experimentally and theoretically examined the backward-facing step flows depending on different Reynolds numbers. For laminar BFS flow, the Reynolds number based on the step length can range below 1200. The transitional ($1200 < Re < 6600$) and turbulent ($Re > 6600$) regimes of the flow are observed. However, the critical Reynolds number indicating the transition to turbulent flow can vary depending on the specific system or geometry, for example, in the internal flow, laminar flow usually occurs at Reynolds numbers below 2300. At $Re = 500$, the secondary recirculation zone and vortex are not observed.

The BFS flow, despite its simple geometry, presents complex flow characteristics, making it an ideal test case for investigating boundary conditions and novel theoretical approaches in computational fluid dynamics (CFD). Specifically, the BFS flow at $Re = 500$, which is a transitional and globally stable flow, serves as a valuable benchmark for assessing new methodologies, as demonstrated in previous work [Hervé et al., 2012]. In this thesis, we employ the BFS flow at $Re = 500$ to illustrate our methods.

1.2.2 Airfoils

An airfoil is a streamlined structure designed to generate lift, usually used for aerodynamic applications in many engineering fields. Common examples of airfoils include wings, blades of propellers, wind turbines, race cars, and helicopter rotor blades. When similar designs are used with water as a medium, they are referred to as hydrofoils.

When an airfoil is placed in a stream of air at an appropriate speed, the airflow over the upper and lower surfaces of the airfoil experiences changes in velocity. According to Bernoulli's principle, this velocity difference creates a pressure differential between the two surfaces, resulting in an upward force. Let's briefly explore the nomenclature related to airfoils.

- **Suction surface (upper surface):** the surface that typically experiences higher velocity and lower static pressure.
- **Pressure surface (lower surface):** the surface that experiences higher static pressure relative to the suction surface. The difference in pressure between these two surfaces generates the

lift force.

- **Leading Edge:** the point at the front of the airfoil with the maximum curvature (minimum radius).

- **Trailing Edge:** the point on the airfoil furthest from the leading edge. The angle formed between the upper and lower surfaces at this point is called the trailing edge angle.

- **Chord Line:** the straight line connecting the leading and trailing edges. The length of this line is referred to as the chord length, or simply the chord.

- **Angle of attack:** the angle between the chord line of an airfoil and the direction of the oncoming airflow (relative wind).

$$\alpha = \theta - \gamma \tag{1.1}$$

  where α is the angle of attack, θ is the angle between the chord line of the airfoil and the horizontal reference line, and γ is the angle between the direction of the oncoming airflow (relative wind) and the horizontal reference line.

- **Camber:** the asymmetry between the two surfaces of an airfoil, where the upper surface of a wing (or the leading surface of a propeller blade) is typically more convex (positively cambered), contributes to its aerodynamic properties. An airfoil without camber is referred to as a symmetric airfoil.

- **Thickness:** the distance between the suction surface and the pressure surface of the airfoil, measured perpendicular to the chord line, is typically expressed as a percentage of the chord length. The maximum thickness refers to the greatest distance between these two surfaces, also measured perpendicular to the chord line.

- **Span:** the length of the wing in the direction perpendicular to the direction of freestream velocity.

- **Mid-span plane:** the plane that is located halfway between the two wingtips, running along the span of the wing.

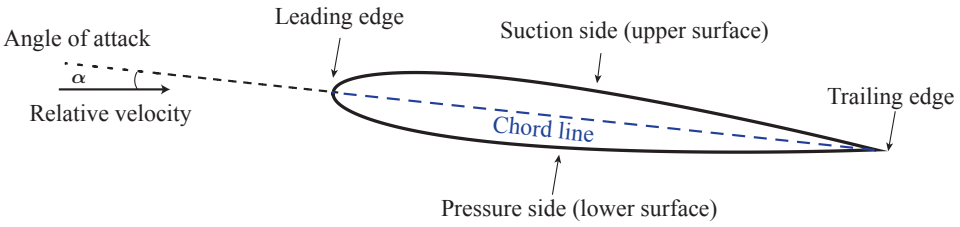

FIGURE 1.3: Two-dimensional NACA 0012 airfoil with associated nomenclature.

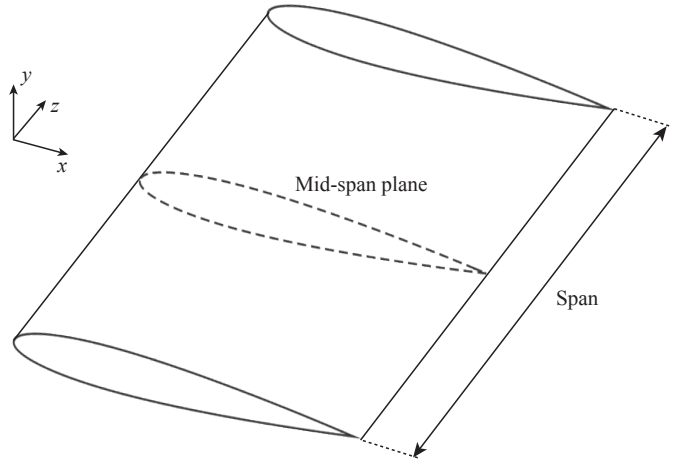

FIGURE 1.4: Diagram of the three-dimensional (spanwise-periodic) NACA 0012 airfoil.

Another important parameter for an airfoil is the NACA 4-digit series to describe the shape of the airfoil, developed by the National Advisory Committee for Aeronautics (NACA) [Allen, 2017]. Each airfoil in this series is defined by four digits, where each digit conveys specific information about the airfoil's geometry. The first digit represents the maximum camber as a percentage of the chord length. The second digit indicates the position of the maximum camber along the chord from the leading edge, expressed in tenths of the chord. The third and fourth digits denote the maximum thickness as a percentage of the chord length. For example, in the NACA 0012 airfoil, the first two digits are "00," indicating that this airfoil has no camber. The mean line is flat, meaning the airfoil is symmetric about the chord line. The last two digits are "12," indicating that the maximum thickness of the airfoil is 12% of the chord length. Therefore, the NACA 0012 airfoil is a symmetric airfoil with no camber and a maximum thickness of 12% of the chord length. The geometry of NACA airfoils can be described using mathematical equations. For example, the NACA 0012 airfoil is

defined by the equation [Jacobs et al., 1933]

$$y = \pm \frac{0.12\left(0.2969\sqrt{x} - 0.1260x - 0.3516x^2 + 0.2843x^3 - 0.1015x^4\right)}{2},$$

where x and y represent the streamwise and cross-streamwise directions, respectively. The positive sign (+) indicates the suction surface, while the negative sign (-) denotes the pressure surface.

In fluid mechanics research, NACA airfoils are commonly studied due to their well-documented aerodynamic properties in both experimental and numerical investigations. Notable examples include the NACA 0012, NACA 0015, NACA 0018, NACA 2412, and NACA 4412 airfoils. In this thesis, we use the NACA 0012 airfoil to demonstrate our approaches, as it has extensive data available for validation [Yeh and Taira, 2019, Kojima et al., 2020, Yeh et al., 2020, Marquet et al., 2022, Towne et al., 2023].

The flow characteristics over an airfoil are influenced by the Reynolds number, angle of attack, and the airfoil's shape. Similar to the backward-facing step flow, a shear layer develops over the surface of airfoils, and the wake behind them is of significant interest to researchers. For instance, for the NACA 0012 airfoil at an angle of attack of $\alpha = 0°$, the flow remains laminar at Reynolds numbers below 1×10^5 [Yousefi and Razeghi, 2018]. However, when the angle of attack increases to 6°, the transition from laminar to turbulent flow occurs at Reynolds numbers below 1×10^5 [Yeh and Taira, 2019]. For a different airfoil, such as the SD7003, the flow at an angle of attack of $\alpha = 4°$ remains laminar at Reynolds numbers below 20,000. Beyond this threshold, turbulent wakes with laminar separation bubbles are observed, and at even higher Reynolds numbers, the flow becomes fully turbulent [Ducoin et al., 2016]. In this thesis, we examine the laminar and turbulent flows of the NACA 0012 airfoil at a Reynolds number of 5,000 and an angle of attack of 6.5°, as described by Marquet et al. [2022], and at a Reynolds number of 23,000 and an angle of attack of 6°, as detailed by Yeh and Taira [2019].

We are interested in the aerodynamic forces exerted on airfoils by the surrounding air as it moves past them. These forces, resulting from the interaction between the air and the surface of the airfoil, are crucial in determining the behavior and performance of objects in flight, such as aircraft and automobiles. To quantify these forces, pressure coefficients, as well as drag and lift coefficients, are commonly used. These metrics enable the validation of the flow by comparison with the reference

data. The pressure coefficient and aerodynamic forces are defined as follows:

$$C_p = \frac{p - p_\infty}{\frac{1}{2}\rho_\infty U_\infty^2}, \quad C_D = \frac{F_D}{\frac{1}{2}\rho_\infty U_\infty^2 A}, \quad \text{and} \quad C_L = \frac{F_L}{\frac{1}{2}\rho_\infty U_\infty^2 A}, \tag{1.2}$$

where p is the pressure, p_∞ is the freestream pressure, F_D is the drag force, F_L is the lift force, A is the reference area of the airfoil surface, and ρ_∞ is the density of the freestream air.

1.3 Navier-Stokes Equations

By assuming continuum flow, the governing equations are the Navier-Stokes equations. This thesis primarily focuses on the compressible Navier-Stokes equations, but also considers the incompressible Navier-Stokes equations. Throughout this work, these equations are formulated in Cartesian coordinates and expressed using Einstein notation [Einstein, 1916]. The incompressible Navier-Stokes equations are given by

$$\frac{\partial u_i}{\partial x_i} = 0, \tag{1.3a}$$

$$\frac{\partial u_i}{\partial t} + \frac{\partial u_i u_j}{\partial x_j} + \frac{1}{\rho}\frac{\partial p}{\partial x_i} - \frac{\mu}{\rho}\frac{\partial^2 u_i}{\partial x_j \partial x_j} = 0, \tag{1.3b}$$

where u_i are the velocity components, ρ is the fluid density, μ is the dynamic viscosity, and p is the pressure. The compressible Navier-Stokes equations are expressed as

$$\frac{\partial \rho}{\partial t} + \frac{\partial (\rho u_i)}{\partial x_i} = 0, \tag{1.4a}$$

$$\frac{\partial (\rho u_i)}{\partial t} + \frac{\partial (\rho u_i u_j)}{\partial x_j} + \frac{\partial p}{\partial x_i} - \frac{\partial \tau_{ij}}{\partial x_j} = 0, \tag{1.4b}$$

$$\frac{\partial (\rho E)}{\partial t} + \frac{\partial \left[(\rho E + p) u_j\right]}{\partial x_j} - \frac{\partial (\tau_{ij} u_i)}{\partial x_j} - \frac{\partial}{\partial x_j}\left(\kappa \frac{\partial T}{\partial x_j}\right) = 0, \tag{1.4c}$$

where the viscous stress tensor τ_{ij} is defined as

$$\tau_{ij} = \mu\left(\frac{\partial u_i}{\partial x_j} + \frac{\partial u_j}{\partial x_i} - \frac{2}{3}\frac{\partial u_k}{\partial x_k}\delta_{ij}\right), \tag{1.5}$$

and the total energy per unit mass E is given by

$$E = e + \frac{1}{2}u_i u_i, \tag{1.6}$$

with T as the fluid temperature and κ as the thermal conductivity. The equation of state for an ideal gas is

$$p = \frac{\rho T}{\gamma}, \tag{1.7}$$

where γ is the specific heat ratio and T is the thermodynamic temperature.

1.4 Linearized Navier-Stokes Equations

In this thesis, the modeling of the estimator and controller is based on a linear system. To accurately represent the underlying physics of the dynamical system, we consider the linearized Navier-Stokes equations. We begin with the incompressible Navier-Stokes equations, expressed as

$$\frac{\partial \boldsymbol{q}}{\partial t} = \mathcal{F}(\boldsymbol{q}), \tag{1.8}$$

where $\boldsymbol{q}$ is a state vector of flow variables $[u_x, u_y, u_z, p]^T$, and $\mathcal{F}$ represents the nonlinear Navier-Stokes operator. The equations are linearized using a Reynolds decomposition, giving

$$\frac{\partial \boldsymbol{q'}}{\partial t} - \boldsymbol{A}\boldsymbol{q'} = \boldsymbol{f}(\bar{\boldsymbol{q}}, \boldsymbol{q'}), \tag{1.9}$$

where $\bar{\boldsymbol{q}}$ and $\boldsymbol{q'}$ represent the mean and perturbation state vectors of the flow variables, respectively. $\boldsymbol{A} = \frac{\partial \mathcal{F}(\bar{\boldsymbol{q}})}{\partial \boldsymbol{q}}$ is the linearized Navier-Stokes operator, and $\boldsymbol{f}$ consists the remaining nonlinear terms, including an external forcing.

The linearized Navier-Stokes equations can be explicitly expressed as

$$\underbrace{\nabla \cdot \boldsymbol{u}'}_{\text{Continuity eqn. part of the linearized Naver-Stokes Operator } \boldsymbol{A}} = 0, \tag{1.10a}$$

$$\frac{\partial \boldsymbol{u}'}{\partial t} = \underbrace{-(\bar{\boldsymbol{u}} \cdot \nabla \boldsymbol{u}' + \boldsymbol{u} \cdot \nabla \bar{\boldsymbol{u}} + \nabla p - \frac{1}{Re}\nabla^2 \boldsymbol{U}')}_{\text{Momentum eqn. part of the linearized Naver-Stokes Operator } \boldsymbol{A}} \underbrace{- \left((\bar{\boldsymbol{u}} \cdot \nabla \bar{\boldsymbol{u}} + \nabla p - \frac{1}{Re}\nabla^2 \bar{\boldsymbol{u}}) - (\boldsymbol{u}' \cdot \nabla \boldsymbol{u}') \right)}_{\text{nonlinear terms } \boldsymbol{f}}. \tag{1.10b}$$

If the linearization is around a steady solution of the Navier-Stokes equations, the terms involving $\bar{u}$ in the nonlinear terms are zero. However, when the linearization is around the mean flow, these terms do not vanish. The linearized Navier-Stokes operator can be also written in the matrix form as

$$\boldsymbol{A}(\bar{\boldsymbol{q}}) = \begin{bmatrix} -\frac{\partial u_x}{\partial x} - \bar{\boldsymbol{u}} \cdot \nabla + \frac{1}{Re}\nabla^2 & -\frac{\partial \bar{u}_y}{\partial y} & -\frac{\partial \bar{u}_x}{\partial z} & -\frac{\partial}{\partial x} \\ -\frac{\partial \bar{u}_y}{\partial y} & -\frac{\partial \boldsymbol{u}_y}{\partial y} - \bar{\boldsymbol{u}} \cdot \nabla + \frac{1}{Re}\nabla^2 & -\frac{\partial \bar{u}_y}{\partial z} & -\frac{\partial}{\partial y} \\ -\frac{\partial \bar{u}_z}{\partial x} & -\frac{\partial \bar{u}_y}{\partial y} & -\frac{\partial \boldsymbol{u}_z}{\partial y} - \bar{\boldsymbol{u}} \cdot \nabla + \frac{1}{Re}\nabla^2 & -\frac{\partial}{\partial z} \\ \frac{\partial}{\partial x} & \frac{\partial}{\partial y} & \frac{\partial}{\partial z} & 0 \end{bmatrix} \tag{1.11}$$

$$\boldsymbol{q}' = \begin{bmatrix} u_x' \\ u_y' \\ u_z' \\ p' \end{bmatrix} \tag{1.12}$$

For compressible Navier-Stokes equations, the state vector is conservative variables $[\rho, \rho u_x, \rho u_y, \rho u_z, \rho E]^T$, and the linearization is performed based on the solution of the conservative variables. For convenience, we omit $(\cdot)'$ for perturbation from this point on.

We consider the linear time-invariant system for estimation and control

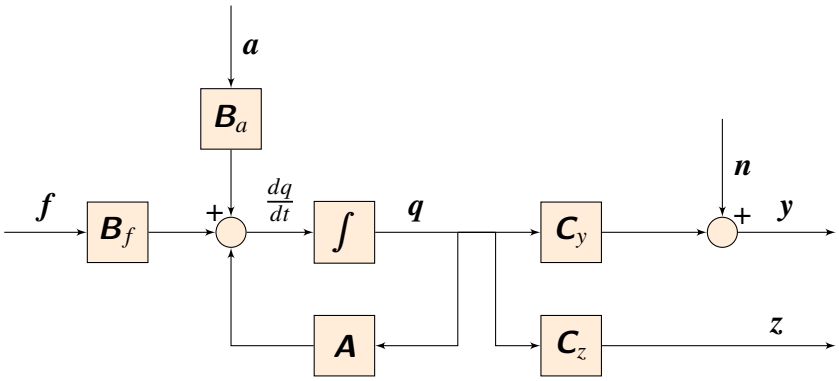

FIGURE 1.5: Plant: linear system.

$$\frac{d\boldsymbol{q}}{dt}(t) = \boldsymbol{A}\boldsymbol{q}(t) + \boldsymbol{B}_f\boldsymbol{f}(t) + \boldsymbol{B}_a\boldsymbol{a}(t), \tag{1.13a}$$

$$\boldsymbol{y}(t) = \boldsymbol{C}_y\boldsymbol{q}(t) + \boldsymbol{n}(t), \tag{1.13b}$$

$$\boldsymbol{z}(t) = \boldsymbol{C}_z\boldsymbol{q}(t), \tag{1.13c}$$

where $\boldsymbol{q} \in \mathbb{C}^n$ is the full state of flow, and $\boldsymbol{f} \in \mathbb{C}^{n_f}$ represents the external forcing $\boldsymbol{f}_{ext}$ and the nonlinear terms of the Navier-Stokes equations $\boldsymbol{f}_{nl}$. $\boldsymbol{y} \in \mathbb{C}^{n_y}$ and $\boldsymbol{z} \in \mathbb{C}^{n_z}$ indicate the sensor and target measurements taken from the full state $\boldsymbol{q}$, respectively. The system matrix $\boldsymbol{A} \in \mathbb{C}^{\mathrm{n}\times\mathrm{n}}$ is the linearized compressible Navier-Stokes operator. The forcing matrix $\boldsymbol{B}_f \in \mathbb{C}^{n\times n_f}$ contains information of the location for the vector $\boldsymbol{f}$. The actuation matrix $\boldsymbol{B}_a \in \mathbb{C}^{\mathrm{n}\times\mathrm{n_a}}$ exhibits the spatial information of the actuators with the number n_a on the airfoil surface. The measurement matrix $\boldsymbol{C}_y \in \mathbb{C}^{\mathrm{n}\times\mathrm{n_y}}$ and the target matrix $\boldsymbol{C}_z \in \mathbb{C}^{\mathrm{n}\times\mathrm{n_z}}$ show that the number of the sensor n_y and the target n_z and their locations. The sensor noise $\boldsymbol{n} \in \mathbb{R}^{\mathrm{n_y}}$ and the actuation signal $\boldsymbol{a} \in \mathbb{R}^{\mathrm{n_a}}$ indicate the measurement error and the output of the controller. The block diagram for the linear system is shown in figure 1.5.

1.5 Background of Flow Estimation and Control Methods

Flow estimation is to predict or infer the flow state based on available data, which may be incomplete, noisy, or delayed. The purpose of estimation is to reconstruct or approximate the full flow field or specific quantities of interest, such as pressure, velocity, or vorticity, from limited measurements. Flow control is to manipulate a flow field to achieve a desired outcome, such as reducing drag,

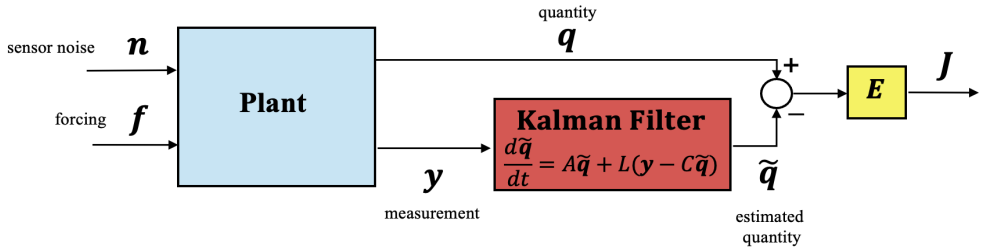

FIGURE 1.6: Block diagram of Kalman filter.

suppressing turbulence, enhancing lift, or stabilizing a flow. The aim of control is to modify the fluid flow behavior in a beneficial way, often through the use of actuators that apply forces, heat, or other influences to the fluid.

1.5.1 Kalman Filter

The Kalman filter [Kalman, 1964] is a typical real-time estimation method widely used in fluid mechanics [Simon, 2006, Furrer and Bengtsson, 2007, Kurtulus et al., 2007, Rafiee et al., 2009, Bordas et al., 2018, Illingworth et al., 2018, Gomez et al., 2019, Navaneeth and Chakravarthy, 2019, Hah et al., 2019]. The cost function of Kalman filter is designed to minimize the error between the actual quantity and the estimated quantity, as illustrated in figure 1.6. The linear time-invariant system is considered for estimation in (1.13), where $\boldsymbol{B}_a$ is set to zero. $\boldsymbol{f} \in \mathbb{C}^{n_f}$ in Kalman filter typically represents the external disturbance, which means that the nonlinear terms $\boldsymbol{f}$ are assumed to be white noise in time, which is also the same for the sensor noise $\boldsymbol{n}$,

$$\mathbb{E}\{\boldsymbol{f}^\dagger \boldsymbol{f}\} = \boldsymbol{F}\delta(t - t') \Rightarrow \hat{\boldsymbol{F}}(\omega) = \boldsymbol{F}, \tag{1.14a}$$

$$\mathbb{E}\{\boldsymbol{n}^\dagger \boldsymbol{n}\} = \boldsymbol{N}\delta(t - t') \Rightarrow \hat{\boldsymbol{N}}(\omega) = \boldsymbol{N}, \tag{1.14b}$$

where $\mathbb{E}\{\cdot\}$ denotes expectation, $\{\cdot\}^\dagger$ indicates the adjoint operator using a suitable inner product, and $\hat{\{\cdot\}}$ represents the frequency domain. When assuming the nonlinear terms are white noise, the Kalman filter is unable to account for the nonlinearity of the flow. The optimal estimate is determined by minimizing the cost function

$$\boldsymbol{J}(t) = \lim_{t\to\infty} \mathbb{E}\{(\boldsymbol{e}(t))^\dagger (\boldsymbol{e}(t))\}, \tag{1.15}$$

where the error $\boldsymbol{e}(t)$ is defined as $\boldsymbol{e} = \tilde{\boldsymbol{q}}(t) - \boldsymbol{q}(t)$, and $\tilde{\boldsymbol{q}}(t)$ represents the estimated values. The Kalman gain $\boldsymbol{L}$ is computed as $\boldsymbol{L} = \boldsymbol{Y}\boldsymbol{C}_y^{\dagger}\boldsymbol{N}^{-1}$, where $\boldsymbol{Y}(t)$ is the solution of the Riccati equation,

$$\boldsymbol{A}\boldsymbol{Y} + \boldsymbol{Y}\boldsymbol{A}^{\dagger} - \boldsymbol{Y}\boldsymbol{C}^{\dagger}\boldsymbol{N}^{-1}\boldsymbol{C}\boldsymbol{Y} + \boldsymbol{F} = 0. \tag{1.16}$$

Solving the Riccati equation has a computational cost of $O(n^3)$, where n is the number of full states (system size times the number of states). In fluid mechanics, especially for large systems such as turbulent flows, this cost is extremely high, making it infeasible to solve these equations directly. Alternative approaches, such as using reduced-order models, have been proposed to address this issue [Rowley, 2005, Rafiee et al., 2009, Colburn et al., 2011, Meldi and Poux, 2017]. The optimal estimates are computed by the system

$$\frac{d\tilde{\boldsymbol{q}}}{dt}(t) = \boldsymbol{A}\tilde{\boldsymbol{q}}(t) + \boldsymbol{L}(\boldsymbol{C}_y\tilde{\boldsymbol{q}}(t) + \boldsymbol{y}(t)). \tag{1.17}$$

1.5.2 Linear–Quadratic–Gaussian (LQG) control

Linear Quadratic Gaussian (LQG) control is an optimal control strategy that combines the Linear Quadratic Regulator (LQR), which is a popular strategy for state feedback control, with the Kalman filter for state estimation. By incorporating the actuation signal $\boldsymbol{a}(t) = -\boldsymbol{K}\tilde{\boldsymbol{q}}(t)$ into estimation system (Kalman filter), the LQG control system can be represented as in (1.13). The cost function,

$$\boldsymbol{J}(t) = \mathbb{E}\left\{\int_0^t (\boldsymbol{q}(t)^*\boldsymbol{Q}\boldsymbol{q}(t) + \boldsymbol{a}(t)^*\boldsymbol{P}\boldsymbol{a}(t))\, dt\right\}, \tag{1.18}$$

is minimized under the constraint on $\boldsymbol{a}(t)$, where the actuation cost matrix $\boldsymbol{P}$ is positive definite, penalizing the control input, and the weight matrix $\boldsymbol{Q}$ is positive semi-definite, penalizing deviations from the desired state. $\{\cdot\}^*$ indicates the conjugate transpose. The LQR gain ($\boldsymbol{K}$) is obtained with

$$\boldsymbol{K}(t) = -\boldsymbol{P}^{-1}\boldsymbol{B}_a^*\boldsymbol{X}(t), \tag{1.19}$$

where $\boldsymbol{X}(t)$ is the solution of the Riccati equation,

$$\boldsymbol{A}^*\boldsymbol{X} + \boldsymbol{X}\boldsymbol{A} - \boldsymbol{X}\boldsymbol{B}_a\boldsymbol{P}^{-1}\boldsymbol{B}_a^*\boldsymbol{X} + \boldsymbol{Q} = 0. \tag{1.20}$$

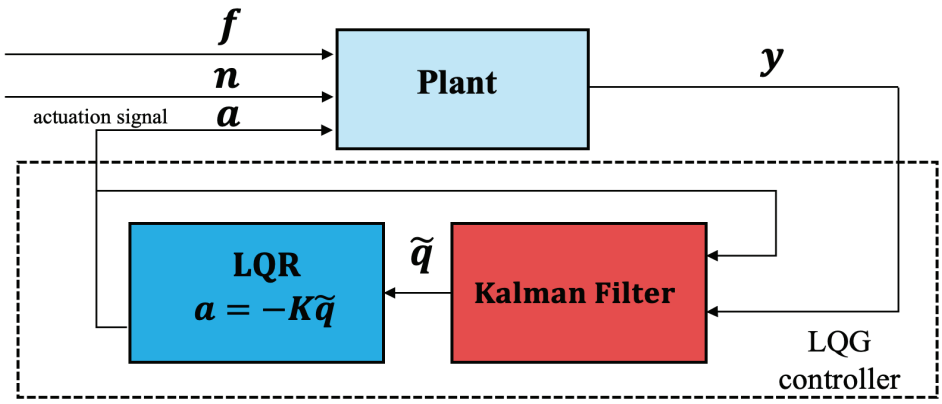

FIGURE 1.7: Block diagram of LQG control.

Similar to solving algebraic Riccati equations for the Kalman filter, solving (1.20) is also a high computational cost of $O(n^3)$, especially for large systems. Numerous studies have utilized LQG control in fluid mechanics, demonstrating its effectiveness in various applications [Or and Speyer, 2006, Sasaki et al., 2018a, Wang et al., 2022].

1.5.3 Wiener-Hopf Method

The Wiener-Hopf method [Noble, 1958] is a mathematical technique extensively used in applied mathematics. It enables the decomposition of arbitrary functions into components corresponding to the upper and lower halves of the complex plane. This thesis leverages the Wiener-Hopf method to impose causality on estimation and control kernels, following methodologies outlined by [Daniele and Lombardi, 2007, Martinelli, 2009, Martini et al., 2022]. Initially, we present the Wiener-Hopf problems from a theoretical standpoint, followed by numerical approaches in §3.

First, we define the Fourier transform as

$$\hat{f}(\omega) = \int_{-\infty}^{+\infty} f(t) e^{-i\omega t}\, dt, \tag{1.21}$$

where $\hat{f}(\omega)$ represents an arbitrary function in the frequency domain. This function can be decomposed into $\hat{f}_+(\omega)$ and $\hat{f}_-(\omega)$, which are analytic functions in the lower and upper complex

half-planes, respectively. These can also be analyzed in the time domain as:

$$\hat{\boldsymbol{f}}_{+}(\omega) = \int_{0}^{+\infty} \boldsymbol{f}(t) e^{-i\omega t}\, dt, \tag{1.22}$$

$$\hat{\boldsymbol{f}}_{-}(\omega) = \int_{-\infty}^{0} \boldsymbol{f}(t) e^{-i\omega t}\, dt, \tag{1.23}$$

where the (+) subscript indicates that the function contains values only in the positive time domain, while the (−) subscript denotes that the function contains values only in the negative time domain. Thus, the subscript (+) and (−) impose causality and non-causality on the function, respectively.

Now, we consider the two Wiener-Hopf problems [Martini et al., 2022] related to this thesis's work

$$\hat{\boldsymbol{H}}(\omega)\hat{\boldsymbol{\Gamma}}_{+}(\omega) = \hat{\boldsymbol{\Lambda}}_{-}(\omega) + \hat{\boldsymbol{G}}(\omega), \tag{1.24}$$

$$\hat{\boldsymbol{K}}(\omega)\hat{\boldsymbol{\Gamma}}_{+}(\omega)\hat{\boldsymbol{H}}(\omega) = \hat{\boldsymbol{\Gamma}}_{-}(\omega) + \hat{\boldsymbol{L}}(\omega)\hat{\boldsymbol{G}}(\omega), \tag{1.25}$$

where $\omega = i2\pi f$ with frequency f, and $\hat{\boldsymbol{H}}$, $\hat{\boldsymbol{G}}$, $\hat{\boldsymbol{K}}$, $\hat{\boldsymbol{L}}$ are known matrices (or functions), while $\hat{\boldsymbol{\Gamma}}_{+}(\omega)$ and $\hat{\boldsymbol{\Lambda}}_{-}(\omega)$ are the unknown matrices (or functions). The objective of the Wiener-Hopf problem is to determine $\hat{\boldsymbol{\Gamma}}_{+}(\omega)$ and $\hat{\boldsymbol{\Lambda}}_{-}(\omega)$.

This problem features two key aspects. Firstly, if $\hat{\boldsymbol{G}}(\omega)$ is a continuous Lipschitz function, the problem ensures a unique solution [Smirnov, 1964]. Secondly, to maintain non-singularity, the resulting inverse functions must be non-zero, implying the presence of sensor noise and a positive definite weight matrix (actuation signal) for effective flow estimation and control. This will be discussed in detail later.

To solve the two Wiener-Hopf problems, we employ two types of factorizations. The additive factorization decomposes the matrix into two ± components, separated only through the addition process

$$\hat{\boldsymbol{\Gamma}}(\omega) = (\hat{\boldsymbol{\Gamma}}(\omega))_{-} + (\hat{\boldsymbol{\Gamma}}(\omega))_{+}, \tag{1.26}$$

using the parenthesis $(\cdot)_{\pm}$. The multiplicative factorization, which is not commutative, is performed as

$$\hat{\boldsymbol{\Gamma}}(\omega) = \hat{\boldsymbol{\Gamma}}(\omega)_{-}\hat{\boldsymbol{\Gamma}}(\omega)_{+}. \tag{1.27}$$

where the subscripts (±) are used without parentheses. The solutions of the first Wiener-Hopf problems in (1.24) is given by

$$\hat{\boldsymbol{\Gamma}}_+(\omega) = \left(\hat{\boldsymbol{G}}(\omega)\hat{\boldsymbol{H}}_-^{-1}(\omega)\right)_+ \hat{\boldsymbol{H}}_+^{-1}(\omega), \tag{1.28}$$

where $\hat{\boldsymbol{H}}_-$ is obtained from the reverse multiplicative factorization. For (1.25), the solutions is

$$\hat{\boldsymbol{\Gamma}}_+(\omega) = \hat{\boldsymbol{K}}_+^{-1}(\omega)\left(\hat{\boldsymbol{K}}_-^{-1}(\omega)\boldsymbol{L}(\omega)\boldsymbol{G}(\omega)\boldsymbol{G}_-^{-1}(\omega)\right)_+ \hat{\boldsymbol{H}}_+^{-1}(\omega). \tag{1.29}$$

1.5.4 Resolvent Analysis for Flow Estimation and Control

Resolvent analysis, also known as input-output analysis, is a powerful methodology that utilizes a resolvent operator to investigate flow physics. It is based on a linear mapping between forcing (input) and response (output) modes, and it assesses the associated energetic gains in the frequency domain. For the linear system described by (1.13), the resolvent operator $\boldsymbol{R}$ is defined in the frequency domain as the inverse of the operator:

$$\boldsymbol{R} = (-i\omega\boldsymbol{I} - \boldsymbol{A})^{-1}, \tag{1.30}$$

where i is the imaginary unit, ω is the frequency, and $\boldsymbol{I}$ is the identity matrix.

Previous studies [Jovanović and Bamieh, 2005, Sharma et al., 2006, Sipp et al., 2010] have demonstrated that the Navier–Stokes equations can be treated as a linear system in the frequency domain to develop efficient flow control mechanisms. McKeon and Sharma [2010] extended resolvent analysis for turbulent flows, highlighting the nonlinear terms that act as forcing in linear dynamics. This has led to increased interest in resolvent analysis. Towne et al. [2018] shows that resolvent modes and spectral proper orthogonal decomposition modes are identical when resolvent expansion coefficients are uncorrelated, and that the leading resolvent mode provides a useful approximation of coherent structures observed in turbulent jet flow. However, for high-dimensional problems, resolvent analysis poses significant challenges, particularly in constructing resolvent operators. This process requires the inverse action of the linearized Navier-Stokes operator and singular value decomposition (SVD) of the resolvent operator. To address these difficulties, Ribeiro

et al. [2020] introduced randomized SVD. Martini et al. [2020] used a time-stepping approach to solve linear equations in the time domain, which eliminates the need to reduce the system and compute the inverse of large matrices. Farghadan et al. [2023, 2024] extended the capacity range of resolvent analysis by incorporating randomized SVD and the time-stepping approach and successfully applying the method to three-dimensional problems.

Resolvent analysis has actively been leveraged for the interpretation of airfoils at different Reynolds numbers and angles of attack. Thomareis and Papadakis [2018] performed resolvent analysis at $Re_{L_c} = 50,000$ and angle of attack 5° to study the physics of separated and attached flow over the airfoil. Symon et al. [2019] investigated two angles of attack, 0° and 10°, of a NACA 0018 airfoil and showed that these two cases behave as an oscillator and amplifier [Huerre and Monkewitz, 1990], respectively. Kojima et al. [2020] identified the origin of the two-dimensional transonic buffet over a NACA 0012 airfoil at $Re_{L_c} = 2,000$, $Ma_\infty = 0.85$ and $\alpha = 3°$ using resolvent analysis. Marquet et al. [2022] also conducted resolvent analysis over a NACA 0012 $Re_{L_c} = 5,000$, $Ma_\infty = 0.3$ between $\alpha = 6.5°$ and $\alpha = 9°$, with an incompressible Navier-Stokes linear operator using the mean flow obtained from the numerical simulation and experimental results.

Resolvent operator is closely related to building linear estimation and control kernels due to its foundation on the linear relationship between the forcing (input) and response (output) modes. That is, flow estimation and control that leverage the linear-based kernels to influence flow behavior can be effective using a resolvent-based approach. By identifying the optimal response mode to the optimal forcing mode, resolvent analysis helps in designing the desired estimator and controller. Yeh and Taira [2019] used resovlent analysis over a spanwise-periodic NACA 0012 airfoil at $Re_{L_c} = 23,000$, $Ma_\infty = 0.3$ and angle of attack 6° and 9° to design control input parameters for separation control. Recently, resolvent-based approaches were introduced to estimate space-time statistics and reconstruct time-series states using limited and non-causal measurements [Towne et al., 2020, Martini et al., 2020]. Amaral et al. [2021] used forcing statistics obtained from DNS to estimate turbulent channel flows. Liu et al. [2021] utilized resolvent analysis to create a physics-based, open-loop unsteady control strategy aimed at reducing pressure fluctuations in turbulent flow over a rectangular cavity. Lin et al. [2023] designed an open-loop flow controller for a plunging circular cylinder using resolvent analysis and further extended its application to closed-loop control for the same scenario [Lin and Tsai, 2024].

1.6 Objectives and Structure

The primary objective of this thesis is to develop and implement resolvent-based estimation and control tools within compressible flow solvers [Jung et al., 2023, Jung and Towne, 2024b, Towne et al., 2024, Jung et al., 2024, Jung and Towne, 2024a], extending their application to compressible and complex large-scale problems beyond simple cases in an incompressible flow solver [Martini et al., 2022]. This implementation is designed to enable efficient simulation using parallel computing. To do this, we first demonstrate the effectiveness of the estimator and controller of backward-facing step flow within an incompressible flow solver. Then, we extend the approach to more complex aerodynamic cases (laminar and turbulent flows around airfoils) and justify the results along with physical analysis.

The main contributions of this thesis are as follows:

1. Application of resolvent-based estimation and control tools to backward-facing step flow in an incompressible flow solver (Nek5000) [Martini et al., 2022].

2. New implementation (software development) of resolvent-based estimation and control tools within a compressible flow solver (CharLES) for high-performance computing.

3. Application of resolvent-based estimation and control tools to laminar airfoil flow [Jung et al., 2023, 2024].

4. Application of resolvent-based estimation tools to turbulent wake flow [Jung and Towne, 2024a,b].

The thesis is structured into seven chapters to comprehensively cover these contributions. Following the introduction, Chapter 2 introduces the concepts of resolvent-based estimation and control. Chapter 3 details the numerical approaches and solvers used to implement these methodologies. In Chapter 4, the application of backward-facing step flow is discussed, showcasing the results of estimation and control. Chapter 5 presents the resolvent-based estimation and control of a laminar airfoil wake, while Chapter 6 focuses on the estimation of a turbulent wake. Finally, Chapter 7 summarizes the thesis and outlines opportunities for future work.

CHAPTER 2

Resolvent-based Estimation and Control

The goal of the method is to estimate and mitigate wake fluctuations downstream of the aerodynamic bodies leveraging a resolvent-based approach [Towne et al., 2020, Martini et al., 2020, 2022]. This method is powerful for several reasons. First, unlike traditional estimation and control techniques such as the Kalman filter [Kalman, 1964] and LQG control, the resolvent-based approach can incorporate time-dependent statistics of the nonlinear terms from the Navier-Stokes equations. These terms are treated as forcing on the linear dynamics, allowing for the consideration of complex nonlinear behaviors, which enhances accuracy and control performance in chaotic and complex systems. Second, this approach enables the construction of estimation and control kernels with low computational costs, without the need for *a priori* model reduction. Third, by employing the Wiener-Hopf formalism [Noble, 1958], we ensure optimal causality in the estimator and controller, significantly improving real-time estimation and control performance. Finally, the resolvent-based estimator and controller can account for the coherent structures within the flow, resulting in more accurate estimation and higher control performance.

2.1 System Set-up

Following the work by Martini et al. [2022], we split the system (1.13) into two parts,

$$\frac{d\boldsymbol{q}_f}{dt}(t) = \boldsymbol{A}\boldsymbol{q}_f(t) + \boldsymbol{B}_f\boldsymbol{f}(t), \tag{2.1a}$$

$$\boldsymbol{y}_f(t) = \boldsymbol{C}_y\boldsymbol{q}_f(t) + \boldsymbol{n}(t), \tag{2.1b}$$

$$\boldsymbol{z}_f(t) = \boldsymbol{C}_z\boldsymbol{q}_f(t), \tag{2.1c}$$

$$\frac{d\boldsymbol{q}_a}{dt}(t) = \boldsymbol{A}\boldsymbol{q}_a(t) + \boldsymbol{B}_a\boldsymbol{a}(t), \tag{2.2a}$$

$$\boldsymbol{y}_a(t) = \boldsymbol{C}_y\boldsymbol{q}_a(t), \tag{2.2b}$$

$$\boldsymbol{z}_a(t) = \boldsymbol{C}_z\boldsymbol{q}_a(t), \tag{2.2c}$$

$$\boldsymbol{q} = \boldsymbol{q}_f + \boldsymbol{q}_a, \qquad \boldsymbol{y} = \boldsymbol{y}_f + \boldsymbol{y}_a, \quad \text{and} \quad \boldsymbol{z} = \boldsymbol{z}_f + \boldsymbol{z}_a, \tag{2.3}$$

where the subscript f in (2.1) represents the forcing system which contains the forcing of the linear system and the sensor noise, while the subscript a in (2.2) indicates the actuation system that includes the actuation signal for control. By applying the Fourier transform to (2.1) and (2.2) and using the resolvent operator defined in (1.30), we derive modified resolvent operators for the resolvent-based kernels used in estimation and control,

$$\hat{\boldsymbol{y}}_f = \boldsymbol{R}_{yf}\hat{\boldsymbol{f}} + \hat{\boldsymbol{n}}, \tag{2.4a}$$

$$\hat{\boldsymbol{z}}_f = \boldsymbol{R}_{zf}\hat{\boldsymbol{f}}, \tag{2.4b}$$

$$\hat{\boldsymbol{y}}_a = \boldsymbol{R}_{ya}\hat{\boldsymbol{a}}, \tag{2.4c}$$

$$\hat{\boldsymbol{z}}_a = \boldsymbol{R}_{za}\hat{\boldsymbol{a}}, \tag{2.4d}$$

with $\boldsymbol{R}_{yf} = \boldsymbol{C}_y\boldsymbol{R}\boldsymbol{B}_f$, $\boldsymbol{R}_{zf} = \boldsymbol{C}_z\boldsymbol{R}\boldsymbol{B}_f$, $\boldsymbol{R}_{ya} = \boldsymbol{C}_y\boldsymbol{R}\boldsymbol{B}_a$, and $\boldsymbol{R}_{za} = \boldsymbol{C}_z\boldsymbol{R}\boldsymbol{B}_a$.

2.2 Resolvent-based Estimation

We define three resolvent-based kernels for estimation: non-causal, truncated non-causal, and causal kernels. First, we start with a non-causal estimator using a convolution function, written as

$$\tilde{\boldsymbol{z}}_{nc}(t) = \int_{-\infty}^{\infty} \boldsymbol{T}_{nc}(t-\tau)\,\boldsymbol{y}(\tau)d\tau, \tag{2.5}$$

where $\boldsymbol{T}_{nc} \in \mathbb{C}^{n_z \times n_y}$ is a non-causal estimation kernel between the sensor measurement and the estimated target state with regard to the perturbation. To solve the estimation problem, a cost

function is defined as the time-integrated expected value of the error between readings at a target and estimates given by

$$\boldsymbol{J}_{nc}(t) = \int_{-\infty}^{\infty} \mathbb{E}\{\boldsymbol{e}(t)^{\dagger}\boldsymbol{e}(t)\}\, dt, \tag{2.6}$$

where the estimation error is defined as $\boldsymbol{e}(t) = \tilde{\boldsymbol{z}}(t) - \boldsymbol{z}(t)$, and $\{\cdot\}^{\dagger}$ denotes the adjoint operator using a suitable inner product. The operator $\mathbb{E}\{\cdot\}$ indicates an expectation. The cost function J_{nc} is minimized by setting its derivative with respect to T_{nc} to zero, yielding a non-causal estimation kernel [Martini et al., 2020],

$$\hat{\boldsymbol{T}}_{nc}(\omega) = \boldsymbol{R}_{zf}\hat{\boldsymbol{F}}\boldsymbol{R}_{yf}^{\dagger}(\boldsymbol{R}_{yf}\hat{\boldsymbol{F}}\boldsymbol{R}_{yf}^{\dagger} + \hat{\boldsymbol{N}})^{-1}, \tag{2.7}$$

where $\hat{\boldsymbol{F}} = \mathbb{E}\{\hat{\boldsymbol{f}}\hat{\boldsymbol{f}}^{\dagger}\}$ and $\hat{\boldsymbol{N}} = \mathbb{E}\{\hat{\boldsymbol{n}}\hat{\boldsymbol{n}}^{\dagger}\}$ represent the forcing CSD matrix and the sensor noise CSD matrix, respectively.

Second, for real-time estimation, the estimator's input consists of sensor measurements available only from the current and past times. Consequently, the non-causal kernel is truncated at the current time by setting the non-causal part, which is associated with unavailable future measurements, to zero. The truncated non-causal kernel is defined as

$$\boldsymbol{T}_{tnc}(\tau) = \begin{cases} \boldsymbol{T}_{nc}(\tau), & \tau \geq 0, \\ 0, & \tau < 0. \end{cases} \tag{2.8}$$

The truncated non-causal estimates are computed as

$$\tilde{\boldsymbol{z}}_{tnc}(t) = \int_{-\infty}^{0} \boldsymbol{T}_{tnc}(t-\tau)\, \boldsymbol{y}(\tau) d\tau. \tag{2.9}$$

Lastly, by enforcing causality through the Wiener-Hopf formalism in cost functions, we derive optimal causal estimation kernels under the constraint of causality. This approach ensures that the integration of the convolution evaluates only the causal part. A causal estimator

$$\tilde{\boldsymbol{z}}_{c}(t) = \int_{-\infty}^{0} \boldsymbol{T}_{c}(t-\tau)\, \boldsymbol{y}(\tau) d\tau, \tag{2.10}$$

is defined in terms of the causal estimation kernel $\boldsymbol{T}_c \in \mathbb{C}^{n_z \times n_y}$. To enforce causality, we modify

the cost function (2.6) to read

$$\boldsymbol{J}_c(t) = \int_{-\infty}^{\infty} \mathbb{E}\{e(t)^\dagger e(t)\} + (\boldsymbol{\Lambda}_-(t)\,\boldsymbol{T}_c(t) + \boldsymbol{\Lambda}_-^\dagger(t)\,\boldsymbol{T}_c^\dagger(t))\; dt, \tag{2.11}$$

where $\boldsymbol{\Lambda}$ is a Lagrange multiplier that is used for a constraint of the causal kernel to be zero for the non-causal part ($\tau < 0$). The subscript (+) and (−) represent the non-causal ($\tau < 0$) and causal ($\tau > 0$) parts of any matrix or function to be zero by achieving a Winer-Hopf factorization. Similar to the derivation of (2.7), we minimize the causal cost function in (2.11) by setting its derivative with respect to T_c to zero. We encounter the Wiener-Hopf problem (1.24). By substituting $\boldsymbol{R}_{zf}\hat{\boldsymbol{F}}\boldsymbol{R}_{yf}^\dagger$ and $\boldsymbol{R}_{yf}\hat{\boldsymbol{F}}\boldsymbol{R}_{yf}^\dagger + \hat{\boldsymbol{N}}$ into $\hat{\boldsymbol{G}}$ and $\hat{\boldsymbol{H}}$, respectively, in (1.28), the causal estimation kernel [Martini et al., 2022] is obtained as

$$\hat{\boldsymbol{T}}_c(\omega) \;=\; \left(\boldsymbol{R}_{zf}\hat{\boldsymbol{F}}\boldsymbol{R}_{yf}^\dagger(\boldsymbol{R}_{yf}\hat{\boldsymbol{F}}\boldsymbol{R}_{yf}^\dagger + \hat{\boldsymbol{N}})_-^{-1}\right)_+ \left(\boldsymbol{R}_{yf}\hat{\boldsymbol{F}}\boldsymbol{R}_{yf}^\dagger + \hat{\boldsymbol{N}}\right)_+^{-1}. \tag{2.12}$$

2.3 Resolvent-based Control

Similar to estimation, we also consider three types of control kernels (non-causal, truncated non-causal, and causal). The non-causal control kernel $\boldsymbol{\Gamma}_{nc}$, also referred to as control law in many studies, is convoluted to compute the actuation signal $\boldsymbol{a}(t)$ as

$$\boldsymbol{a}(t) = \int_{-\infty}^{\infty} \boldsymbol{\Gamma}_{nc}(t-\tau)\; \boldsymbol{y}_f(\tau) d\tau. \tag{2.13}$$

To derive the control kernel in terms of the modified resolvent operators, we minimize the cost function by setting its derivative with respect to Γ_{nc} to zero to optimize the quantity $z(t)$ under the constraint on the actuation signal,

$$\boldsymbol{J}_{nc,con}(t) = \int_{-\infty}^{\infty} \mathbb{E}\{\boldsymbol{z}(t)^*\boldsymbol{Q}\boldsymbol{z}(t) + \boldsymbol{a}(t)^*\boldsymbol{P}\boldsymbol{a}(t)\}\; dt, \tag{2.14}$$

where $\boldsymbol{Q}$ is the weight matrix that penalizes the states for the undesired values, while $\boldsymbol{P}$ is a positive-semi-definite weight matrix that penalizes actuation effort. $\{\cdot\}^*$ indicates the conjugate

transpose. Minimizing this cost function yields the control kernel [Martini et al., 2022]

$$\hat{\boldsymbol{\Gamma}}_{nc}(\omega) \quad = \quad (\boldsymbol{R}_{za}^{\dagger}\boldsymbol{R}_{za} + \hat{\boldsymbol{P}})^{-1}(-\boldsymbol{R}_{za}^{\dagger})\boldsymbol{R}_{zf}\hat{\boldsymbol{F}}\boldsymbol{R}_{yf}^{\dagger}(\boldsymbol{R}_{yf}\hat{\boldsymbol{F}}\boldsymbol{R}_{yf}^{\dagger} + \hat{\boldsymbol{N}})^{-1}. \tag{2.15}$$

The truncated non-causal control kernels is defined as

$$\boldsymbol{\Gamma}_{tnc}(\tau) = \begin{cases} \boldsymbol{\Gamma}_{nc}(\tau), & \tau \geq 0, \\ 0, & \tau < 0. \end{cases} \tag{2.16}$$

The actuation signal from the truncated non-causal control kernel is computed as

$$\boldsymbol{a}_{tnc}(t) = \int_{-\infty}^{0} \boldsymbol{\Gamma}_{tnc}(t-\tau)\, \boldsymbol{y}_f(\tau) d\tau, \tag{2.17}$$

which is not optimal for real-time control. By enforcing the causality to the cost function (2.14), in an analogous way to the estimation cost function (2.6), we derive the causal cost function

$$\boldsymbol{J}_{nc,con}(t) = \int_{-\infty}^{\infty} \mathbb{E}\{\boldsymbol{z}(t)^{*}\boldsymbol{Q}\boldsymbol{z}(t) + \boldsymbol{a}(t)^{*}\boldsymbol{P}\boldsymbol{a}(t) + (\boldsymbol{\Lambda}_{-}(t)\boldsymbol{\Gamma}_{c}(t) + \boldsymbol{\Lambda}_{-}^{\dagger}(t)\boldsymbol{\Gamma}_{c}^{\dagger}(t))\} dt, \tag{2.18}$$

which is optimal under the constraint on the causality. By minimizing the cost function (2.18), we encounter the Wiener-Hopf problem (1.25). By substituting $\boldsymbol{R}_{za}^{\dagger}\boldsymbol{R}_{za} + \hat{\boldsymbol{P}}$ and $-\boldsymbol{R}_{za}^{\dagger}$ into $\hat{\boldsymbol{K}}$ and $\hat{\boldsymbol{L}}$, respectively, in (1.29), we derive the causal resolvent-based control kernel $\boldsymbol{\Gamma}_c$,

$$\begin{aligned} \hat{\boldsymbol{\Gamma}}_{c}(\omega) \quad = \quad & (\boldsymbol{R}_{za}^{\dagger}\boldsymbol{R}_{za} + \hat{\boldsymbol{P}})_{+}^{-1}\Big((\boldsymbol{R}_{za}^{\dagger}\boldsymbol{R}_{za} + \hat{\boldsymbol{P}})_{-}^{-1}(-\boldsymbol{R}_{za}^{\dagger})\boldsymbol{R}_{zf}\hat{\boldsymbol{F}}\boldsymbol{R}_{yf}^{\dagger} \\ & (\boldsymbol{R}_{yf}\hat{\boldsymbol{F}}\boldsymbol{R}_{yf}^{\dagger} + \hat{\boldsymbol{N}})_{-}^{-1}\Big)_{+}(\boldsymbol{R}_{yf}\hat{\boldsymbol{F}}\boldsymbol{R}_{yf}^{\dagger} + \hat{\boldsymbol{N}})_{+}^{-1}. \end{aligned} \tag{2.19}$$

Considering the full linear system (1.13) combined with the split system (2.1) and (2.2), the resolvent-based kernel for closed-loop control is given by

$$\hat{\boldsymbol{\Gamma}}_{cl} \quad = \quad (\boldsymbol{I} + \hat{\boldsymbol{\Gamma}}\boldsymbol{R}_{ya})^{-1}\hat{\boldsymbol{\Gamma}}, \tag{2.20}$$

where $\hat{\boldsymbol{\Gamma}}$ is replaced by $\hat{\boldsymbol{\Gamma}}_c$ for the causal resolvent-based control kernel, and by $\hat{\boldsymbol{\Gamma}}_{tnc}$ for the truncated non-causal resolvent-based control kernel.

2.4 Computing Estimation and Control Kernels

In this section, we present two approaches to compute resolvent-based estimation and control kernels. First, we describe an operator-based approach [Martini et al., 2022]. The linearized Navier-Stokes operator, derived using a compressible flow solver, is both highly accurate and reliable. This approach allows for the efficient implementation of linear simulations without the need for inverting the operator or performing prior model reduction, making it particularly efficient for large-scale problems. Second, we explain a data-driven approach [Martini et al., 2022] that does not require the construction of the linearized Navier-Stokes operator. Instead, this method utilizes training data from DNS/LES or experiments to build cross-spectral densities, which are then used to compute the components of the estimation and control kernels. Previous works obtained these kernels empirically from experiments [Audiffred et al., 2023, 2024]. We numerically obtain the estimation and control kernels, as needed, using the operator-based approach for both clean and noisy freestream conditions in nonlinear systems.

2.4.1 Operator-based approach

The resolvent operator $\boldsymbol{R}$ is defined in terms of an inverse, which is computationally expensive to calculate. For an airfoil grid, directly computing the resolvent operator is not wise. To address this, we employ a time-stepping approach that avoids the inverse operation and instead constructs the low-rank matrices by solving linear equations in time [Martini et al., 2020, 2022, Farghadan et al., 2023], required for computing the estimation and control kernels. This operator-based method involves a single-stage run of the direct linear equations and two-stage runs of both the adjoint and direct linear equations. In this study, we use the single-stage run to derive the components of the control kernels ($\boldsymbol{R}_{za}$ and $\boldsymbol{R}_{ya}$). More importantly, the two-stage run is used to obtain the components of the estimation and control kernels ($\boldsymbol{R}_{zf}\hat{\boldsymbol{F}}\boldsymbol{R}_{yf}^{\dagger}$ and $\boldsymbol{R}_{yf}\hat{\boldsymbol{F}}\boldsymbol{R}_{yf}^{\dagger}$), which are necessary for computing (2.7), (2.12), (2.15), and (2.19). For the two-stage run, we apply the high-rank $\boldsymbol{B}_f$ and the low-rank $\boldsymbol{C}_y$ as well as the low- and high-rank $\boldsymbol{C}_z$.

2.4.1.1 Single-stage run

The direct equation for the actuation system (2.2) is given by:

$$\frac{d\boldsymbol{q}_{a,k}}{dt}(t) = \boldsymbol{A}\boldsymbol{q}_{a,k}(t) + \boldsymbol{B}_{a,k}\delta(t), \tag{2.21a}$$

$$\boldsymbol{y}_{a,k}(t) = \boldsymbol{C}_y\boldsymbol{q}_{a,k}(t), \tag{2.21b}$$

$$\boldsymbol{z}_{a,k}(t) = \boldsymbol{C}_z\boldsymbol{q}_{a,k}(t), \tag{2.21c}$$

where $\boldsymbol{y}_{a,k} \in \mathbb{C}^{n_y}$ is the sensor measurement of the direct solution in k-th actuator, and $\boldsymbol{z}_{a,k} \in \mathbb{C}^{n_z}$ is the target measurement of the direct solution in k-th sensor. By collecting the vectors of the k-th actuator and then Fourier-transforming, we obtain

$$\hat{\boldsymbol{Y}}_a = \begin{bmatrix} \hat{\boldsymbol{y}}_{a,1} & \hat{\boldsymbol{y}}_{a,2} & \dots & \hat{\boldsymbol{y}}_{a,n_a} \end{bmatrix} = \boldsymbol{R}_{ya}, \tag{2.22a}$$

$$\hat{\boldsymbol{Z}}_a = \begin{bmatrix} \hat{\boldsymbol{z}}_{a,1} & \hat{\boldsymbol{z}}_{a,2} & \dots & \hat{\boldsymbol{z}}_{a,n_a} \end{bmatrix} = \boldsymbol{R}_{za}, \tag{2.22b}$$

with $\hat{\boldsymbol{Y}}_a \in \mathbb{C}^{n_y \times n_a}$ and $\hat{\boldsymbol{Z}}_a \in \mathbb{C}^{n_z \times n_a}$. That is, Fourier- transforming of the $y_{a,i}$ solutions of the direct runs, for example, gives the columns of the product on the right-hand side of (2.22a).

2.4.1.2 Two-stage run

The procedure for the two-stage run begins with solving the adjoint system

$$-\frac{d\boldsymbol{q}_i}{dt}(t) = \boldsymbol{A}^\dagger\boldsymbol{q}_i(t) + \boldsymbol{C}_{y,i}^\dagger\delta(t), \tag{2.23a}$$

$$\boldsymbol{s}_i(t) = \boldsymbol{B}_f^\dagger\boldsymbol{q}_i(t), \tag{2.23b}$$

where $\boldsymbol{A}^\dagger$ is the adjoint linearized Navier-Stokes operator, $\delta(t)$ is the Dirac delta function used for impulse forcing at the initial step, and the subscript i indicates the sensor defined by the i-th row of the measurement matrix $\boldsymbol{C}_y$. The output of the adjoint run $\boldsymbol{s}_i$ is used as a forcing in a direct run. In

the second stage, a direct equation for the estimation system 2.1 is given by

$$\frac{d\boldsymbol{q}_i}{dt}(t) = \boldsymbol{A}\boldsymbol{q}_i(t) + \boldsymbol{B}_f\boldsymbol{s}_i(t), \tag{2.24a}$$

$$\boldsymbol{y}_i(t) = \boldsymbol{C}_y\boldsymbol{q}_i(t) + \boldsymbol{n}_i(t), \tag{2.24b}$$

$$z_i(t) = \boldsymbol{C}_z\boldsymbol{q}_i(t), \tag{2.24c}$$

where $\boldsymbol{y}_i \in \mathbb{C}^{n_y}$ is a vector measured from all the sensors in the direct solution forced by i-th sensor, and $\boldsymbol{z}_i \in \mathbb{C}^{n_z}$ is a vector measured at all the targets in the direct solution forced by i-th sensor. Similar to the single-stage run, by collecting the vectors of the i-th sensor and then Fourier-transforming, we obtain

$$\hat{\boldsymbol{Y}}_f = \begin{bmatrix} \hat{y}_1 & \hat{y}_2 & \dots & \hat{y}_{n_y} \end{bmatrix} = \boldsymbol{R}_{yf}\hat{\boldsymbol{F}}\boldsymbol{R}_{yf}^{\dagger}, \tag{2.25a}$$

$$\hat{\boldsymbol{Z}}_f = \begin{bmatrix} \hat{z}_1 & \hat{z}_2 & \dots & \hat{z}_{n_y} \end{bmatrix} = \boldsymbol{R}_{zf}\hat{\boldsymbol{F}}\boldsymbol{R}_{yf}^{\dagger}, \tag{2.25b}$$

with $\hat{\boldsymbol{Y}}_f \in \mathbb{C}^{n_y \times n_y}$ and $\hat{\boldsymbol{Z}}_f \in \mathbb{C}^{n_z \times n_y}$. The cost of this approach depends linearly on the problem dimension, avoiding the need to reduce the system via a priori model reduction and the associated loss of accuracy of the estimator.

As a result, the non-causal and causal estimation kernels in (2.7) and (2.12) are computed using (2.25) obtained from the operator-based (O) approach, given by

$$\hat{\boldsymbol{T}}_{nc,O}(\omega) = \hat{\boldsymbol{Z}}_f(\hat{\boldsymbol{Y}}_f + \hat{\boldsymbol{N}})^{-1}, \tag{2.26a}$$

$$\hat{\boldsymbol{T}}_{c,O}(\omega) = (\hat{\boldsymbol{Z}}_f(\hat{\boldsymbol{Y}}_f + \hat{\boldsymbol{N}})_-^{-1})_+(\hat{\boldsymbol{Y}}_f + \hat{\boldsymbol{N}})_+^{-1}. \tag{2.26b}$$

The non-causal and causal control kernels in (2.15) and (2.19) can be computed with the results of the operator-based approach (2.22) and (2.25), given by

$$\hat{\boldsymbol{\Gamma}}_{nc,O}(\omega) = (\hat{\boldsymbol{Z}}_a^{\dagger}\hat{\boldsymbol{Z}}_a + \hat{\boldsymbol{P}})^{-1}(-\hat{\boldsymbol{Z}}_a^{\dagger})\hat{\boldsymbol{Z}}_f(\hat{\boldsymbol{Y}}_f + \hat{\boldsymbol{N}})^{-1} \tag{2.27a}$$

$$\hat{\boldsymbol{\Gamma}}_{c,O}(\omega) = (\hat{\boldsymbol{Z}}_a^{\dagger}\hat{\boldsymbol{Z}}_a + \hat{\boldsymbol{P}})_+^{-1}\left((\hat{\boldsymbol{Z}}_a^{\dagger}\hat{\boldsymbol{Z}}_a + \hat{\boldsymbol{P}})_-^{-1}(-\hat{\boldsymbol{Z}}_a^{\dagger})\hat{\boldsymbol{Z}}_f(\hat{\boldsymbol{Y}}_f + \hat{\boldsymbol{N}})_-^{-1}\right)_+(\hat{\boldsymbol{Y}}_f + \hat{\boldsymbol{N}})_+^{-1}. \tag{2.27b}$$

Note that we compute the modified resolvent operators ($\boldsymbol{R}_{yf}$,$\boldsymbol{R}_{zf}$,$\boldsymbol{R}_{ya}$, and $\boldsymbol{R}_{za}$) without any reduction of the system, so there is no approximation for obtaining the resolvent operators.

2.4.2 Data-driven approach

When the linearized Navier-Stokes operator is not available, a data-driven approach [Martini et al., 2022] can be employed to build cross-spectral densities (CSD) equivalent to modified resolvent operators. This approach also circumvents the need for adjoint solvers, facilitating the construction of estimation and control kernels from the operator-based approach. Additionally, when the CSD is computed from the dataset of a nonlinear system, it can automatically include $\hat{\boldsymbol{F}}$ in the kernels. This can statistically account for the nonlinearity of the flow, thereby improving the estimation and control performance for the nonlinear system.

Instantaneous snapshots are collected from DNS/LES or experiments, and these datasets are used to compute the CSD. The empirical CSDs are associated with the resolvent operators [Towne et al., 2018, 2020], allowing us to use these CSDs for building resolvent-based kernels.

The nonlinear terms in the Navier-Stokes equations act as a forcing of the resolvent operator [McKeon and Sharma, 2010], and their influence is crucial in complex dynamic systems [Amaral et al., 2021]. To explicitly address the nonlinear terms, we split the forcing vector in (2.1) $\boldsymbol{f}$ into two components: the external forcing $\boldsymbol{f}_{ext}$ and the nonlinear terms $\boldsymbol{f}_{nl}$. This distinction helps us better understand their impact when building the CSDs from the data. The forcing terms can be divided into

$$\boldsymbol{B}_f \boldsymbol{f} = \begin{bmatrix} \boldsymbol{B}_{ext} & \boldsymbol{B}_{nl} \end{bmatrix} \begin{bmatrix} \boldsymbol{f}_{ext} \\ \boldsymbol{f}_{nl} \end{bmatrix}. \tag{2.28}$$

where $\boldsymbol{B}_{ext} \in \mathbb{C}^{n \times n_{ext}}$ and $\boldsymbol{B}_{nl} \in \mathbb{C}^{n \times n}$. Typically, the nonlinear region is larger than the region where external forcing is imposed ($n > n_{ext}$). In a linear system, the nonlinear terms $\boldsymbol{f}_{nl}$ are not included, allowing us to analyze the linear dynamics of the flow and to build linear estimators and controllers. However, our ultimate goal is to manipulate the unsteady fluctuations inherent in the actual flow, which necessitates considering nonlinearity. For the nonlinear system, we collect data from the systems without and with external forcing to better capture the behavior of the systems influenced by external forcing. The forcing system (2.1) without and with the external forcing can

be expressed as

$$\frac{d\boldsymbol{q}}{dt}(t) = \boldsymbol{A}\boldsymbol{q}(t) + \boldsymbol{B}_{nl}\boldsymbol{f}_{nl}(t), \tag{2.29}$$

$$\frac{d\boldsymbol{q}_r}{dt}(t) = \boldsymbol{A}\boldsymbol{q}_r(t) + \boldsymbol{B}_{ext}\boldsymbol{f}_{ext} + \boldsymbol{B}_{nl}\boldsymbol{f}_{nl,r}(t), \tag{2.30}$$

where $\boldsymbol{f}_{ext}$ is a space-time color. The subscript r indicates the flow quantity that contains the development of nonlinearity, which was impacted by the external forcing. The $\boldsymbol{f}_{nl,r}$ term is evolved by the external forcing in time and space, so in the nonlinear system, the nonlinear effect can not be negligible. Equation (2.29) is the DNS or LES system without any source term. We assume the correlation between the external forcing and the nonlinearity is zero. Then we obtain

$$\begin{bmatrix} \hat{\boldsymbol{y}}_{f,nl} \\ \hat{\boldsymbol{z}}_{f,nl} \end{bmatrix} = \begin{bmatrix} \boldsymbol{R}_{yf,nl} & 1 \\ \boldsymbol{R}_{zf,nl} & 0 \end{bmatrix} \begin{bmatrix} \hat{\boldsymbol{f}}_{nl} \\ \hat{\boldsymbol{n}} \end{bmatrix}, \tag{2.31}$$

$$\begin{bmatrix} \hat{\boldsymbol{y}}_{f,ext,nl} \\ \hat{\boldsymbol{z}}_{f,ext,nl} \end{bmatrix} = \begin{bmatrix} \boldsymbol{R}_{yf,ext} & \boldsymbol{R}_{yf,nl} \\ \boldsymbol{R}_{zf,ext} & \boldsymbol{R}_{zf,nl} \end{bmatrix} \begin{bmatrix} \hat{\boldsymbol{f}}_{ext} \\ \hat{\boldsymbol{f}}_{nl,r} \end{bmatrix} + \begin{bmatrix} \hat{\boldsymbol{n}} \\ 0 \end{bmatrix}. \tag{2.32}$$

Computing the cross-spectral density of $[\hat{\boldsymbol{y}} \quad \hat{\boldsymbol{z}}]^T$ from (2.31) and (2.32) gives

$$\begin{bmatrix} \boldsymbol{S}_{yy,1} \\ \boldsymbol{S}_{zy,1} \end{bmatrix} = \begin{bmatrix} \boldsymbol{S}_{yy,f,nl} \\ \boldsymbol{S}_{zy,f,nl} \end{bmatrix} = \begin{bmatrix} \boldsymbol{R}_{yf,nl}\hat{\boldsymbol{F}}_{nl}\boldsymbol{R}^{\dagger}_{yf,nl} + \hat{\boldsymbol{N}} \\ \boldsymbol{R}_{zf,nl}\hat{\boldsymbol{F}}_{nl}\boldsymbol{R}^{\dagger}_{yf,nl} \end{bmatrix}, \tag{2.33}$$

$$\begin{bmatrix} \boldsymbol{S}_{yy,2} \\ \boldsymbol{S}_{zy,2} \end{bmatrix} = \begin{bmatrix} \boldsymbol{S}_{yy,f,ext,nl} \\ \boldsymbol{S}_{zy,f,ext,nl} \end{bmatrix} = \begin{bmatrix} \boldsymbol{R}_{yf,nl}\hat{\boldsymbol{F}}_{nl,r}\boldsymbol{R}^{\dagger}_{yf,nl} + \boldsymbol{R}_{yf,ext}\hat{\boldsymbol{F}}_{ext}\boldsymbol{R}^{\dagger}_{yf,ext} + \hat{\boldsymbol{N}} \\ \boldsymbol{R}_{zf,nl}\hat{\boldsymbol{F}}_{nl,r}\boldsymbol{R}^{\dagger}_{yf,nl} + \boldsymbol{R}_{zf,ext}\hat{\boldsymbol{F}}_{ext}\boldsymbol{R}^{\dagger}_{yf,ext} \end{bmatrix}. \tag{2.34}$$

with $\boldsymbol{S}_{yy} = \mathbb{E}\{\hat{\boldsymbol{y}}\hat{\boldsymbol{y}}^*\}$ and $\boldsymbol{S}_{zy} = \mathbb{E}\{\hat{\boldsymbol{z}}\hat{\boldsymbol{y}}^*\}$. The subscripts 1 and 2 indicate the CSDs for the system without (1) and with (2) external forcing. Since the right-hand sides of (2.33) and (2.34) contain the terms needed to build the estimation kernels, this shows that the correlations on the left-hand side can be used in their place. Note that the CSDs inherently contain statistical information about the nonlinearity of the flow within the forcing CSD matrix.

The non-causal and causal estimation kernels in (2.7) and (2.12) are computed by the CSDs of

(2.33) and (2.34) resulting from the data-driven (D) approach, given by

$$\hat{\boldsymbol{T}}_{nc,D}(\omega) = \boldsymbol{S}_{zy,1}(\boldsymbol{S}_{yy,1} + \hat{\boldsymbol{N}})^{-1}, \tag{2.35a}$$

$$\hat{\boldsymbol{T}}_{c,D}(\omega) = (\boldsymbol{S}_{zy,1}(\boldsymbol{S}_{yy,1} + \hat{\boldsymbol{N}})^{-1}_{-})_{+}(\boldsymbol{S}_{yy,1} + \hat{\boldsymbol{N}})^{-1}_{+}. \tag{2.35b}$$

To derive control kernels, it is necessary to use $\boldsymbol{R}_{ya}$ and $\boldsymbol{R}_{za}$, which do not include the forcing covariance matrix. By imposing an impulse forcing at the actuator location in the nonlinear system, we can extract $\boldsymbol{R}_{ya}$ and $\boldsymbol{R}_{za}$,

$$\frac{d\boldsymbol{q}_i}{dt}(t) = \boldsymbol{A}\boldsymbol{q}_i(t) + \boldsymbol{B}_{a,i}\delta(t) + \boldsymbol{B}_{nl}\boldsymbol{f}_{nl,i}(t). \tag{2.36}$$

$$\begin{bmatrix} \hat{\boldsymbol{y}}_a \\ \hat{\boldsymbol{z}}_a \end{bmatrix} = \begin{bmatrix} \boldsymbol{R}_{ya} & \boldsymbol{R}_{yf,nl,i} \\ \boldsymbol{R}_{za} & \boldsymbol{R}_{zf,nl,i} \end{bmatrix} \begin{bmatrix} 1 \\ \hat{\boldsymbol{f}}_{nl,i} \end{bmatrix}. \tag{2.37}$$

The sensor and target reading of the frequency domain in the system forced by the actuator location are subtracted by the $\hat{\boldsymbol{y}}_{f,nl}, \hat{\boldsymbol{z}}_{f,nl}$. Then we obtain

$$\begin{bmatrix} \hat{\boldsymbol{y}}_3 \\ \hat{\boldsymbol{z}}_3 \end{bmatrix} = \begin{bmatrix} \hat{\boldsymbol{y}}_a - \hat{\boldsymbol{y}}_{f,nl} \\ \hat{\boldsymbol{z}}_a - \hat{\boldsymbol{z}}_{f,nl} \end{bmatrix} \approx \begin{bmatrix} \boldsymbol{R}_{ya} \\ \boldsymbol{R}_{za} \end{bmatrix}. \tag{2.38}$$

The CSDs are

$$\begin{bmatrix} \boldsymbol{S}_{yy,3} \\ \boldsymbol{S}_{zz,3} \end{bmatrix} \approx \begin{bmatrix} \boldsymbol{R}_{ya}\boldsymbol{R}_{ya}^{\dagger} \\ \boldsymbol{R}_{za}\boldsymbol{R}_{za}^{\dagger} \end{bmatrix} = \begin{bmatrix} \boldsymbol{Y}_a\boldsymbol{Y}_a^{\dagger} \\ \boldsymbol{Z}_a\boldsymbol{Z}_a^{\dagger} \end{bmatrix}. \tag{2.39}$$

Finally, we can also derive the control kernels using a data-driven approach

$$\hat{\boldsymbol{\Gamma}}_{nc}(\omega) = (\boldsymbol{S}^{\dagger}_{zz,3} + \hat{\boldsymbol{P}})^{-1}\hat{\boldsymbol{z}}_3\boldsymbol{S}_{zy,1}(\boldsymbol{S}_{yy,1} + \hat{\boldsymbol{N}})^{-1}, \tag{2.40a}$$

$$\hat{\boldsymbol{\Gamma}}_{c}(\omega) = \left(\boldsymbol{S}^{\dagger}_{yy,3} + \hat{\boldsymbol{P}}\right)^{-1}_{+}\left((\boldsymbol{S}^{\dagger}_{yy,3} + \hat{\boldsymbol{P}})^{-1}_{-}(-\hat{\boldsymbol{z}}^{\dagger}_3)\boldsymbol{S}_{zy,1}(\boldsymbol{S}_{yy,1} + \hat{\boldsymbol{N}})^{-1}_{-}\right)_{+}(\boldsymbol{S}_{yy,1} + \hat{\boldsymbol{N}})^{-1}_{+}. \tag{2.40b}$$

To apply these kernels to the system that is excited by the external forcing, the $\boldsymbol{S}_{yy,1}$ and $\boldsymbol{S}_{zy,1}$ can be replaced with the $\boldsymbol{S}_{yy,2}$ and $\boldsymbol{S}_{zy,2}$.

CHAPTER 3

Numerical Approach

3.1 Flow Solvers

In this thesis, we utilize two numerical solvers to implement resolvent-based estimation and control tools. Initially, these tools are applied to the flow over a backward-facing step using an incompressible flow solver. Building on this foundation, we extend the development to address large-scale problems within a compressible flow solver, specifically CharLES. This Chapter begins by describing the numerical solvers used for both the incompressible flow (Nek5000) and the compressible flow (CharLES). We then discuss the implementation of the resolvent-based tools within these frameworks.

3.1.1 Nek5000

Nek5000 [Fischer et al., 2008] utilize the Spectral Element Method (SEM) for spatial discretization [Patera, 1984], along with backward difference formulas (BDFk) for temporal discretization. The SEM uses high-order polynomial approximations within each element to represent the solution. As the polynomial degree increases, the error decreases rapidly, leading to a smooth and accurate solution. The computational domain is divided into non-overlapping elements, and high-degree polynomials are used as basis functions

$$u(\mathbf{x}) = \sum_{i=1}^{N} u_i \psi_i(\mathbf{x}), \tag{3.1}$$

where u is the velocity and ψ is a basis function. The incompressible momentum Navier-Stokes equations (1.3) are projected onto the polynomial basis functions using a Galerkin approach, resulting in a system of algebraic equations. That is, by using the mass matrix M_{ij}, the stiffness matrix A_{ij} for the second order term, and the convection operator C_{ij}, the spatial-discretized equation (global form) is expressed as

$$M\frac{du}{dt} = Au - Cu + Mf, \tag{3.2}$$

where

$$M_{ij} = \int_\Omega \psi_i(x)\psi_j(x)\mathrm{d}\Omega = \frac{L}{2}\sum_k \rho_k \psi_i\left(r_k\right)\psi_j\left(r_k\right), \tag{3.3a}$$

$$A_{ij} = \int_\Omega \psi_i'(\mathbf{x})\psi_j'(\mathbf{x})\mathrm{d}\Omega = \frac{L}{2}\sum_k \rho_k \psi_i'\left(r_k\right)\psi_j'\left(r_k\right), \tag{3.3b}$$

$$C_{ij} = \int_\Omega c\psi_i(\mathbf{x})\psi_j'(\mathbf{x})\mathrm{d}\Omega = \frac{L}{2}\sum_k c\left(r_k\right)\rho_k \psi_i\left(r_k\right)\psi_j'\left(r_k\right) \tag{3.3c}$$

for one dimensional case on the new space L for the pressure, defined as

$$L_0^2(\Omega) = \left\{ f \in L^2(\Omega) \mid \int_\Omega f \,\mathrm{d}\Omega = 0, \right\}. \tag{3.4}$$

The linearized Navier-Stokes equations based on perturbations in Nek5000 are given by

$$\rho\left(\frac{\partial \mathbf{u}_i'}{\partial t} + \bar{\mathbf{u}}\cdot\nabla\mathbf{u}_i' + \mathbf{u}_i'\cdot\nabla\bar{\mathbf{u}}\right) = -\nabla p_i' + \mu\nabla^2\mathbf{u}_i' \tag{3.5a}$$

$$\nabla\cdot\mathbf{u}_i' = 0 \tag{3.5b}$$

where $\bar{\boldsymbol{u}}$ is the base flow. We use the linearized Navier-Stokes equations (3.5) within Nek5000 for the application of the backward-facing step flow in Chapter 4.

3.1.2 CharLES

A compressible flow solver CharLES, which has been used in many research studies [Brès et al., 2017, 2018, Yeh and Taira, 2019, Kojima et al., 2020], is used to implement resolvent-based

estimation and control tools for laminar and turbulent airfoils. This solver uses second-order numerical schemes in finite volume method with the time integration of third-order Runge-Kutta scheme [Gottlieb and Shu, 1998]. We perform DNS for a 2D laminar airfoil flow and LES for a spanwise-periodic turbulent flow. The variables are non-dimensionalized as

$$x_i = \frac{x_i^*}{L}, \quad t = \frac{t^* a_\infty}{L}, \quad \rho = \frac{\rho^*}{\rho_\infty}, \quad p = \frac{p^*}{\rho_\infty a_\infty^2}, \quad T = \frac{T^*}{T_\infty}, \quad e = \frac{e^*}{\rho_\infty a_\infty^2}, \quad u_i = \frac{u_i^*}{a_\infty} \tag{3.6}$$

where the $\{\cdot\}^*$ is the dimensional variables and $\rho_{\text{ref}} = 1$, $T_{\text{ref}} = 1$, $p_{\text{ref}} = 0.7143$ and other reference variables are set to 1. CharLES solves the compressible Navier-Stokes equations (1.4) in conservative form, $\boldsymbol{q} = [\rho, \rho u_i, \rho E]^T$ in conservative form. The viscous stress tensor using a subgrid-scale model is

$$\tau_{ij}^{\text{sgs}} = \mu \left(\frac{\partial u_i}{\partial x_j} + \frac{\partial u_j}{\partial x_i} - \frac{2}{3} \delta_{ij} \frac{\partial u_k}{\partial x_k} \right). \tag{3.7}$$

For the subgrid-scale model, we choose Vreman [2004].

3.2 Resolvent-based Estimation and Control Tools

The resolvent-based tools [Martini et al., 2022] were developed using the Nek5000 code and are publicly available on GitHub. A key contribution of this thesis is the implementation of these tools for nonlinear systems and their application to estimation and control within the backward-facing step flow, which will be discussed in Chapter 4. Building on the work by Martini et al. [2022], we further extend the resolvent-based estimation and control tools for the compressible flow solver, CharLES written in C++, enabling their application to large-scale compressible flow problems. In this thesis, the CharLES tools are applied to analyze laminar and turbulent wakes behind airfoils, which will be discussed in Chapter 5 [Jung et al., 2023, 2024] and Chapter 6 [Jung and Towne, 2024a,b].

3.2.1 Resolvent-based estimation and control tools within Nek5000[1]

Nek5000 supports the linearized Navier-Stokes equations with time-stepping for both direct and adjoint runs. The linearization in Nek5000 is performed around a base state, and the linear runs are limited to using homogeneous boundary conditions with different initial conditions. The estimation and control kernels are developed based on the linear system, and this linear estimator and controller are then applied to the nonlinear system, demonstrating the effectiveness of this approach. The actuation signal term $\boldsymbol{B}_a \boldsymbol{a}(t)$ and the external forcing term $\boldsymbol{B}_{f,ext} \boldsymbol{f}_{ext}(t)$ are added into the momentum equation as

$$\frac{d\boldsymbol{u_t}}{dt} + \boldsymbol{u_t} \cdot \boldsymbol{\nabla u_t} = -\boldsymbol{\nabla p_t} + \frac{1}{Re}\nabla^2 \boldsymbol{u_t} + \boldsymbol{B}_a \boldsymbol{a}(t) + \boldsymbol{B}_{f,ext} \boldsymbol{f}_{ext}(t), \tag{3.8}$$

where

$$\hat{\boldsymbol{a}}(\omega) = \hat{\boldsymbol{\Gamma}}_{cl}(\omega)\hat{\boldsymbol{y}}(\omega), \tag{3.9}$$

with $\hat{\boldsymbol{\Gamma}}_{cl}$ based on (2.20), and $\hat{\boldsymbol{y}}$ represents the sensor measurements in the frequency domain of $\boldsymbol{y}_t - \bar{\boldsymbol{y}}$. The subscript t denotes the full variable, e.g., $\boldsymbol{u_t} = \bar{\boldsymbol{u}} + \boldsymbol{u}$. The actuation signal $\hat{\boldsymbol{a}}$ is computed in the time domain using a convolution function, as described in (2.13). Since the flow is convectively evolved downstream, we focus on the streamwise velocity for both the external forcing and the actuation signal, particularly to reduce streamwise velocity fluctuations at the target in the backward-facing step flow.

3.2.2 Resolvent-based estimation and control tools within CharLES [2]

We present the new implementation of the resolvent-based estimation and control tools within a compressible flow solver [Jung et al., 2023, Jung and Towne, 2024b, Towne et al., 2024, Jung et al., 2024, Jung and Towne, 2024a]. In this subsection, we describe the numerical perspective beyond theoretical considerations explained in Chapter 2. The theoretical methodology was developed in the work Towne et al. [2020], Martini et al. [2020, 2022]. We develop software that allows us

[1] *This subsection presents the author's contributions to the work published in: E. Martini, J. Jung, A. Cavalieri, P. Jordan, and A. Towne. Resolvent-based tools for optimal estimation and control via the Wiener–Hopf formalism. J. Fluid Mech., 937:A19, April 2022.*

[2] *This subsection is based on work contained in: J. Jung, R. Bhagwat, and A. Towne. Resolvent-based estimation and control of laminar flow over an airfoil, submitted to: J. Fluid Mech.*

to implement and perform the resolvent-based estimation and control tools within a compressible flow solver for large-scale problems within the high-performance computing environment. The conceptional flow chart for the software is depicted in figure 3.1. The software can be used for any flows simulated within the CharLES solver and can be linked with any external packages written in C/C++. To parallelize linear algebra computation and streaming Fourier transform, we integrated the solver with PETSc [Balay et al., 2019] and FFTW [Frigo and Johnson, 2005].

3.2.2.1 Linearization

The operator-based approach in §2.4 requires having access to the linear operator or the actions of both the linear and adjoint operators. Specifically, extracting the linear operator from large-scale, compressible CFD solvers is a complex and challenging task. Various methods have been proposed in previous studies to tackle this issue [Fosas et al., 2012, Cook et al., 2018, Bhagwat, 2020]. In this thesis, our objective is to accurately obtain linearized Navier-Stokes operators that fully account for all the numerical schemes and boundary conditions employed in the simulation, thereby minimizing runtime errors. To achieve this, we compute and store the linear operator explicitly within the CFD solver, ensuring it is readily available within the main loop of the simulation.

In CharLES solver, the control volume-based finite volume method is used. A straightforward method to achieve linearization is through finite differences, computing the matrix one column at a time. Specifically, the j^{th} column of the matrix can be extracted as

$$\boldsymbol{A}(:, j) = \frac{\mathcal{F}(\bar{\boldsymbol{q}} + \epsilon e_j) - \mathcal{F}(\bar{\boldsymbol{q}})}{\epsilon}, \tag{3.10}$$

where j refers to the j^{th} control volume and $\mathcal{F}$ represents the nonlinear compressible Navier-Stokes operator. However, this approach is computationally expensive, as the number of the global right-hand-side evaluations ($\mathcal{F}$) required to form the operator scales with the size of the problem n.

To address this, we adopt a more efficient technique proposed by Nielsen and Kleb [2006] and further utilized by Cook et al. [2018]. This method involves perturbing multiple degrees of freedom (DOF) simultaneously. The key insight is that perturbing an element of the state vector $\boldsymbol{q}$ affects only a small number of nearby control volumes, known as its computational stencil. This stencil is determined by the numerical schemes used in the solver. Thus, it is feasible to perturb multiple

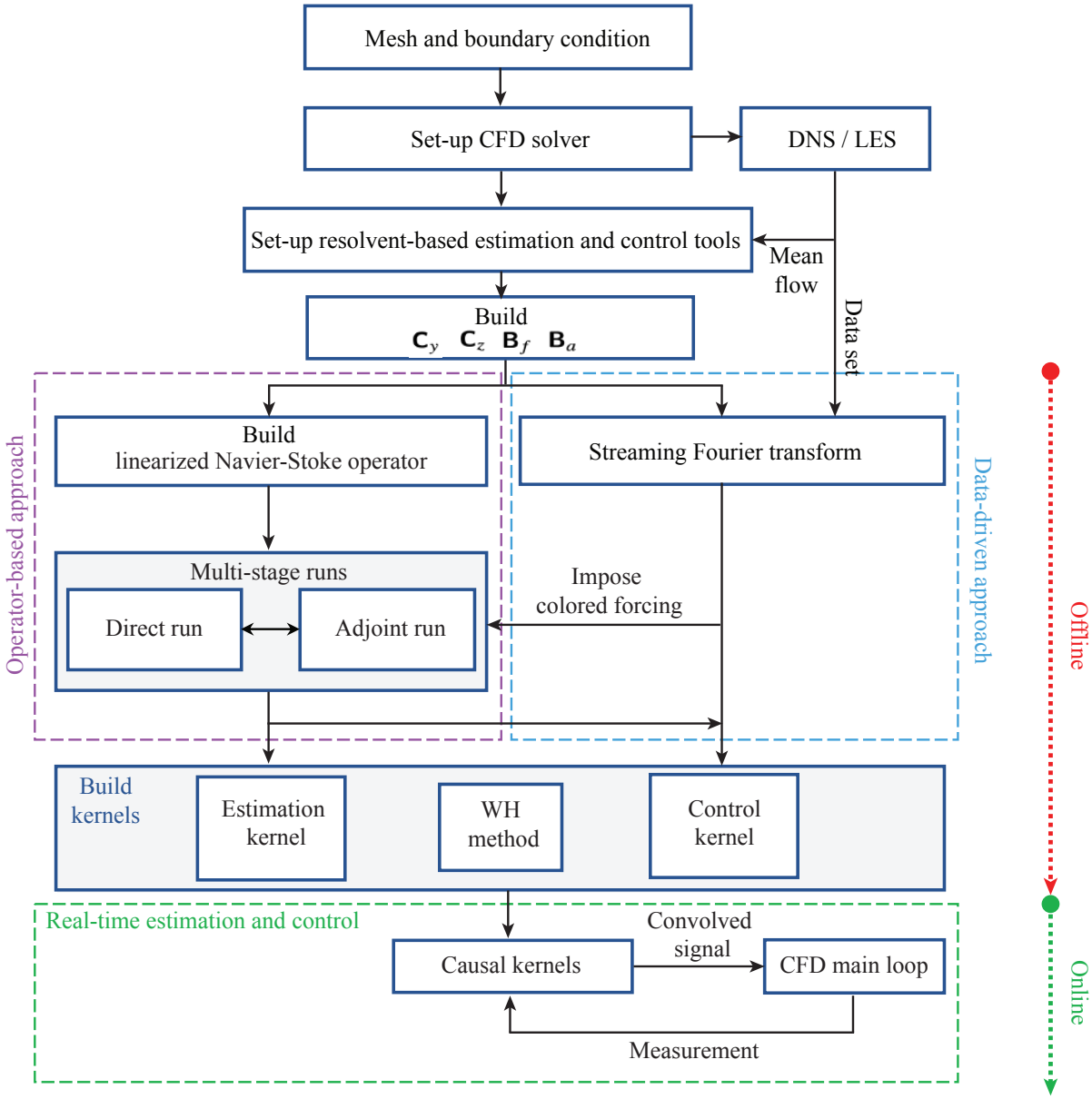

FIGURE 3.1: Flow chart of the suggested resolvent-based control tool within a compressible flow solver.

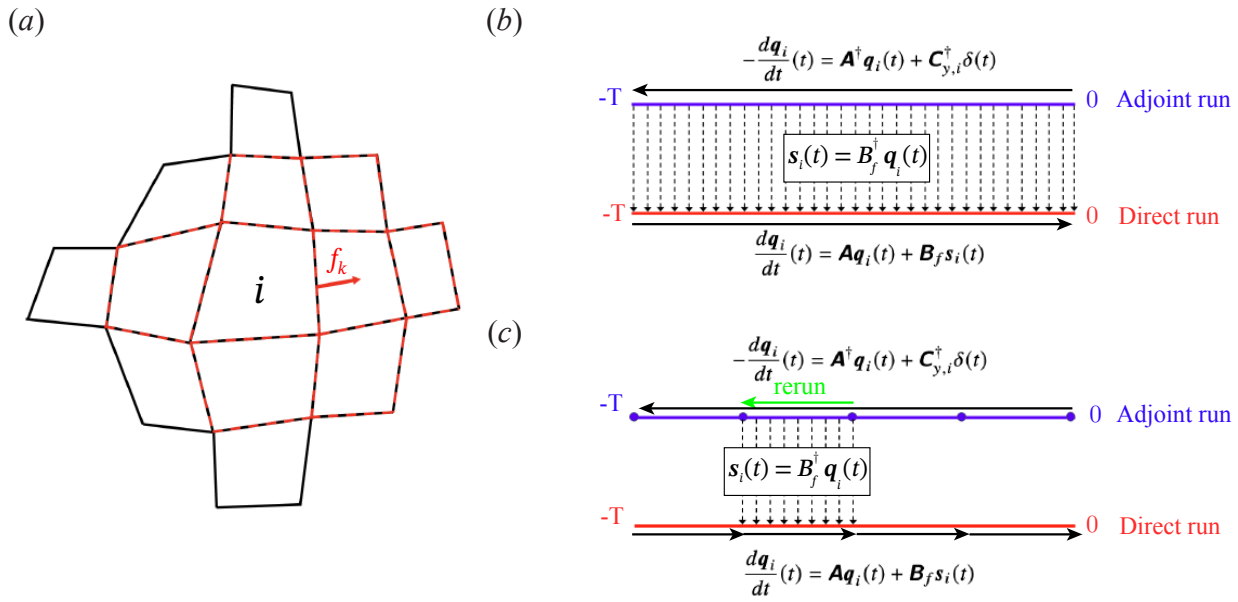

FIGURE 3.2: Resolvent-based tool in the CharLES solver: (a) perturbing the stencil in the CFD solver, (b) two-stage run without checkpointing, and (c) two-stage run with checkpointing.

elements of the state vector at once without the perturbations interfering with each other. This approach allows us to compute multiple columns of $\boldsymbol{A}$ simultaneously, significantly reducing the computational cost. Specifically, the number of right-hand-side evaluations ($\mathcal{F}(\boldsymbol{q})$) scales with the extent of the computational stencil, not with the size of the problem. In the spatial discretization of numerical methods in CharLES, the flux at a face depends on the adjoining control volumes and their immediate face neighbors, as illustrated in figure 3.2(a). In practice, we use second-order finite differences to compute the numerical derivatives as follows

$$\boldsymbol{A}(:,k) = \frac{\mathcal{F}(\bar{\boldsymbol{q}} + \epsilon\tilde{\boldsymbol{e}}_k) - \mathcal{F}(\bar{\boldsymbol{q}} - \epsilon\tilde{\boldsymbol{e}}_k)}{2\epsilon}, \tag{3.11}$$

where $\tilde{\boldsymbol{e}}_k$ represents the multiple degrees of freedom (DOFs) with a reduced number k of perturbing DOFs compared to j in (3.10). The ϵ is empirically chosen to minimize the error in the numerical derivatives. We have found $\epsilon = \epsilon_0||\boldsymbol{q}||$ with $\epsilon_0 = 10^{-6}$ to be an effective and robust choice. The $\|\boldsymbol{q}\|$ is computed separately for each quantity (density, velocities, and energy). To optimize the process, we sort the computational grid into lists of non-overlapping degrees of freedom (DOFs) on a single processor and then broadcast this information to all other processors. This approach tends to minimize the number of total right-hand-side evaluations required to perturb all DOFs

in the system, making the sorted lists more efficient. The linearized compressible Navier-Stokes operator $\boldsymbol{A}$ is extracted and saved at the initial step, and the routine is performed only once before the time-stepping or nonlinear runs (DNS or LES).

3.2.2.2 Time-stepping & checkpointing for direct-adjoint runs

To effectively store and utilize the matrix in large-scale numerical linear algebra computations, especially in parallel setups like matrix-vector products, we employ the open-source linear algebra package PETSc [Balay et al., 2019]. PETSc leverages the underlying domain decomposition used by the CFD solver to partition the computational grid. Once the matrices such as $\boldsymbol{C}_y$, $\boldsymbol{C}_z$, $\boldsymbol{B}_a$, and $\boldsymbol{B}_f$ are constructed, it is used to advance the linear dynamics for single or two-stage runs, as described in §2.4.1. Additionally, linear estimation and control runs are performed within this time-stepping framework. To advance these equations in time, we use the TVD-RK3 scheme [Gottlieb and Shu, 1996], which is consistent with the scheme used by the solver.

In the two-stage run described in §2.4.1.2, we use a checkpointing approach, as shown in figures 3.2(c). The time-series data of $\boldsymbol{s}_i(t)$ from (2.23b) must be stored to serve as the forcing term $\boldsymbol{B}_f\boldsymbol{s}_i(t)$ in (2.24a). However, storing all snapshots from the initial step of the adjoint run through to the point (T) in figure 3.2(b) where the direct run begins becomes prohibitively expensive over long time horizons, particularly depending on the global stability of the system. The checkpointing approach can address this issue by storing only snapshots within particular intervals during the adjoint run in (2.23a). After completing the first full adjoint run, the direct run is advanced in chunks. The adjoint run is then rerun between the last two checkpoints, using only the stored snapshots within that interval, before conducting the direct run through the same interval. This approach reduces memory usage, which is particularly beneficial for large-scale problems. For example, if advancing N_t timesteps in the adjoint run, the storage requirement can be reduced from $O(N_t)$ to $O(W_t+W_t/N_t)$, where W_t is the length of the interval between two checkpoints, and W_t/N_t roughly indicates the number of checkpoints. The minimum memory requirement is achieved when $W_t \approx \sqrt{N_t}$. Thus, checkpointing reduces the memory required from $O(N_t)$ to $O(2\sqrt{N_t})$.

3.2.2.3 Streaming DFTs

The data-driven approach requires the collection of numerous snapshots. However, when each snapshot is large, computing CSDs of the data becomes costly. Computing efficiently the CSDs is also useful when colored forcing is imposed on building the kernels or when Fourier modes are extracted from the high-rank matrix $\boldsymbol{C}_z$. To reduce data size and memory usage, we employ streaming discrete Fourier transforms (DFTs), as proposed by Schmidt and Towne [2019] within the context of a streaming algorithm for spectral proper orthogonal decomposition (SPOD) and further utilized by Farghadan et al. [2023] within a scalable time-stepping algorithm for resolvent analysis.

Typically, the fast Fourier transform (FFT) requires an equal number of snapshots and frequencies (n_{freq}). However, the streaming algorithm processes one instantaneous data point at a time, avoiding the need to store the entire time-series dataset ($n_{req} \times n_f$). This is achieved by using the definition of the discrete Fourier transform (DFT), which yields results equivalent to the FFT. Each snapshot contributes to the summation of the Fourier modes as follows

$$\hat{\boldsymbol{f}}_k^l = \sum_{j=1}^{n_{freq}} \boldsymbol{f}_j^l p_{jk}, \tag{3.12}$$

where $p_{jk} = e^{(k-1)(j-1)(-i2\pi/n_{freq})}$, with k representing the k-th frequency, j the j-th snapshot, and l the l-th block. The full time series data is divided into multiple blocks, each windowed with a 50% overlap. Each snapshot is multiplied by the complex scalar p_{jk} and added to the summation of the Fourier modes.

Our software, integrated with FFTW [Frigo and Johnson, 2005], stores the DFT matrix $\mathbb{C}^{n_{freq} \times n_{freq}}$ during the initialization step of the CFD solver. Subsequently, the high-rank vectors f_{nl} or z are multiplied by the DFT matrix, contributing to the summation of the Fourier modes. It is important to note that we do not save the previous snapshots. By utilizing streaming Fourier transforms, we can construct data-driven estimation and control kernels in (2.35) and (2.40). A brief outline of the algorithm is shown in algorithm 1.

Algorithm 1 Streaming Fourier transform

```
function StreamingFourierTransform
    for each icv ∈ f_nl do
        for each iw ∈ n_freq do
            f̂(iw, icv) += DFTMat(f_nl)
            if tidx = nDFT then
                tblk+=1
            else
                tidx+=1
    return f̂(iw, icv, tblk)
```

Algorithm 2 Extract nonlinear terms $\hat{\boldsymbol{f}}$

```
function ExtractNonlinearTerms(q̄, q_dns, A, B_f, RHS())        ▷ every time step
    for each icv ∈ all control volumes do
        q'(icv) ← q_dns(icv)-q̄(icv)
        dq/dt(icv) ← F(q_dns(icv)))
    dq'/dt ← MatMult(A,q')
    for each icv ∈ all control volumes do
        f(icv) ← dq/dt(icv)- dq'/dt(icv)
    f_nl ← MatMult(B_nl,f)
```

3.2.2.4 Extracting nonlinear terms of Navier-Stokes equations

Extracting the nonlinear terms ($\boldsymbol{f}_{nl}$ in (2.28)) of Navier-Stokes equations is useful to investigate the nonlinear interactions. The terms are extracted within the software developed for the resolvent-based estimation and control tool. The detail of how to extract the nonlinear terms is shown in algorithm 2. The principle is described here.

The nonlinear Navier-Stokes equations $\mathcal{F}$ can be expressed as

$$\mathcal{F}(\boldsymbol{q}) = \mathcal{F}(\bar{\boldsymbol{q}}) + \frac{\partial \mathcal{F}(\bar{\boldsymbol{q}})}{\partial \boldsymbol{q}}\boldsymbol{q'} + nl(\boldsymbol{q'}), \tag{3.13}$$

where $nl(\boldsymbol{q'})$ represents all remaining nonlinear terms after linearization. The forcing vector that accounts for the nonlinear terms can be derived as follows

$$\boldsymbol{f}_{nl}(\boldsymbol{q'}) = \mathcal{F}(\bar{\boldsymbol{q}}) + nl(\boldsymbol{q'}) = \underbrace{\mathcal{F}(\boldsymbol{q})}_{\text{from DNS}} - \underbrace{\boldsymbol{A}\boldsymbol{q'}}_{\text{from linear run}}. \tag{3.14}$$

We run the nonlinear simulation (DNS or LES) in time and, within the same loop, compute the term $\boldsymbol{Aq}'$ to subtract from $\mathcal{F}(\boldsymbol{q})$. The resulting nonlinear term $\boldsymbol{f}_{nl}$ is saved in the solver. Computing the CSDs of the nonlinear term requires significant memory due to the large n_{nl}. Therefore, to efficiently compute $\hat{\boldsymbol{F}}$, we utilize a streaming Fourier transform in algorithm 1, which doesn't require to save all the snapshot $\boldsymbol{f}_{nl}$.

3.2.2.5 Numerical Wiener-Hopf decomposition

We solve Wiener-Hopf problems [Noble, 1958] in the CFD solver. While the addictive factoration is straightforward to solve numerically, the multiplicative factorization is complex. The numerical solutions for the multiplicative factorization, described in §1.5.3, were provided in [Martini et al., 2022]. The solution of the multiplicative factorization can be independently formed as

$$\hat{\boldsymbol{G}}(\omega)\hat{w}_{i,+}(\omega) = \hat{w}_{i,-}(\omega), \tag{3.15}$$

where

$$\hat{\boldsymbol{G}}_{-}(\omega) = [\hat{w}_{1,-}(\omega), \hat{w}_{2,-}(\omega), \cdots, \hat{w}_{n_{freq},-}(\omega)], \tag{3.16a}$$

$$\hat{\boldsymbol{G}}_{+}(\omega) = [\hat{w}_{1,+}(\omega), \hat{w}_{2,+}(\omega), \cdots, \hat{w}_{n_{freq},+}(\omega)]^{-1}, \tag{3.16b}$$

where $\hat{\boldsymbol{G}} \in \mathbb{C}^{n_y \times n_y \times n_{\text{freq}}}$ or $\hat{\boldsymbol{G}} \in \mathbb{C}^{n_a \times n_a \times n_{\text{freq}}}$. To solve (3.15), a Fredholm integral equation of the second kind [Daniele and Lombardi, 2007] is derived as

$$\hat{\boldsymbol{x}}_i(\omega) + \frac{1}{2\pi \mathrm{i}} \int_{-\infty}^{\infty} \frac{\hat{\boldsymbol{G}}^{-1}(\omega)\hat{\boldsymbol{G}}(u) - 1}{u - \omega} \hat{\boldsymbol{x}}_i(u) \mathrm{d}u = \hat{\boldsymbol{G}}^{-1}(\omega) \frac{\hat{\boldsymbol{w}}_{i,-}(\omega_0)}{\omega - \omega_0}. \tag{3.17}$$

Due to the difficulty of the formation of the integration path, Martini et al. [2022] constructed a linear problem with the size $\boldsymbol{G} \in \mathbb{C}^{n_y \times n_y \times n_{\text{freq}}}$, given by

$$\hat{\boldsymbol{x}}_i(\omega) + \frac{1}{2\mathrm{i}} \mathcal{H}\left(\hat{\boldsymbol{x}}_i\right)(\omega) - \frac{1}{2\mathrm{i}} \hat{\boldsymbol{G}}^{-1}(\omega) \mathcal{H}\left(\hat{\boldsymbol{G}}\hat{x}_i\right)(\omega) = \hat{\boldsymbol{G}}^{-1}(\omega) \frac{\hat{\boldsymbol{w}}_{i,-}(\omega_0)}{\omega - \omega_0}, \tag{3.18}$$

where

$$\mathcal{H}(\hat{\boldsymbol{x}}) = P.V. \frac{1}{\pi} \int_{-\infty}^{\infty} \frac{1}{\omega - u} \hat{\boldsymbol{x}}(u) du, \tag{3.19}$$

represents the Hilbert transform of $\boldsymbol{x}(\hat{\omega})$. Equation (3.19) can be solved using the Generalized Minimal Residual (GMRES) iterative method [Saad and Schultz, 1986]. In this thesis, we solve (3.19) directly within the solver to minimize reliance on post-processing tools such as MATLAB and to enhance computational efficiency by enabling faster routines with reduced memory usage.

CHAPTER 4

Resolvent-based Estimation and Control of Flow over a Backward-Facing Step[1]

In this chapter, we apply resolvent-based estimation and control approaches to a two-dimensional flow over a backward-facing step. We first demonstrate the resolvent-based estimation and control approaches for a linear system. The kernels developed from the linear system are then applied to a nonlinear system to assess the effectiveness of these methods. Additionally, we explore the method's performance across various sensor and actuator placements.

4.1 Simulation

The flow is simulated at $Re = 500$, based on the step length, using Nek5000 [Fischer et al., 2008]. At this Reynolds number, the flow is globally stable and a steady state. To induce unsteadiness and create fluctuations that can be controlled, we apply external forcing. For the nonlinear system, the degree of nonlinearity varies with the forcing amplitude, making it important to study how this evolution is captured by the linear estimator and controller.

The computational domain is divided into 600 elements (subdomains), with fifth-order polynomials used for spatial discretization. A Poiseuille profile is applied as the inflow condition at the leftmost boundary, while an outflow boundary condition is imposed at the rightmost boundary. No-slip conditions are enforced on both the upper and bottom walls. For the linear runs, Dirichlet boundary conditions are applied to all boundaries. All sensors and actuators utilize Gaussian spatial

[1] *This chapter presents the author's contributions to the work published in: E. Martini, J. Jung, A. Cavalieri, P. Jordan, and A. Towne. Resolvent-based tools for optimal estimation and control via the Wiener–Hopf formalism. J. Fluid Mech., 937:A19, April 2022.*

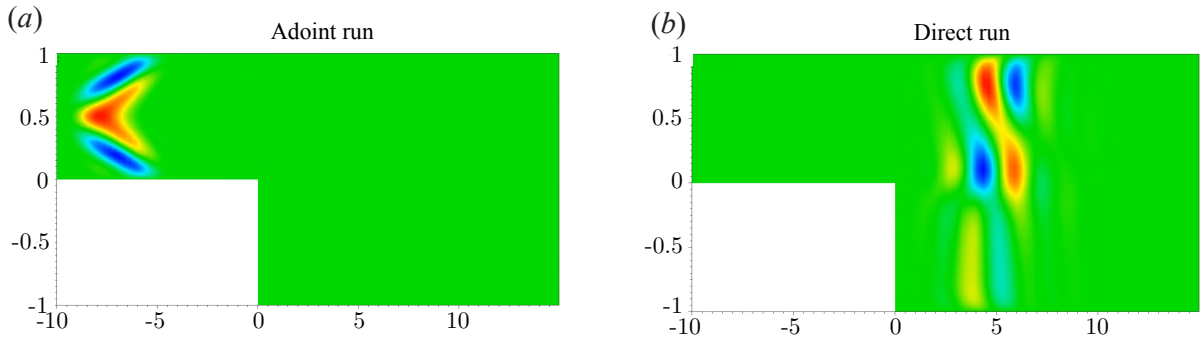

FIGURE 4.1: Two-stage run: (a) adjoint run and (b) direct run with impulse forcing at the sensor location $y = [-0.5, 0.5]$.

support,

$$\exp\left(-\frac{(x-x_c)^2}{2\sigma_x^2} - \frac{(y-y_c)^2}{2\sigma_y^2}\right), \tag{4.1}$$

where $\sigma_x = 0.2$ and $\sigma_y = 0.1$. Figure 4.1 presents the snapshots of the adjoint and direct runs with the sensor positioned at $y = [-0.5, 0.5]$. These linear simulations are used to construct the estimation kernels for the operator-based approach.

4.2 Resolvent-based Estimation

In our study, the reattachment point is located at approximately $x \approx 12$. We focus on target points near the reattachment point for estimation, along with other target points (z_1, z_2, z_3, z_4), as shown in figure 4.2. The point z_1 is particularly interesting because it offers the potential to estimate an upstream target from the sensor. Given the convective nature of this flow, our primary focus is on estimating the streamwise velocity component u_x.

Analyzing the behavior of the estimation kernel in the time domain provides valuable insights. We consider two scenarios to examine the causal impact on the kernels.: the first with the target point located upstream at $z_1 = [-2, 0.5]$, and the second with the target point downstream at $z_5 = [10.5, -0.75]$, using a sensor at $y_2 = [-0.5, 0.5]$. The estimation kernel for the upstream target case is shown in figure 4.2(b), while the kernel for the downstream target case is presented in figure 4.2(c). In the upstream target scenario, the truncated non-causal kernel in figure 4.2(b) lacks the ability to accurately estimate, as it loses essential information from the sensors due to its

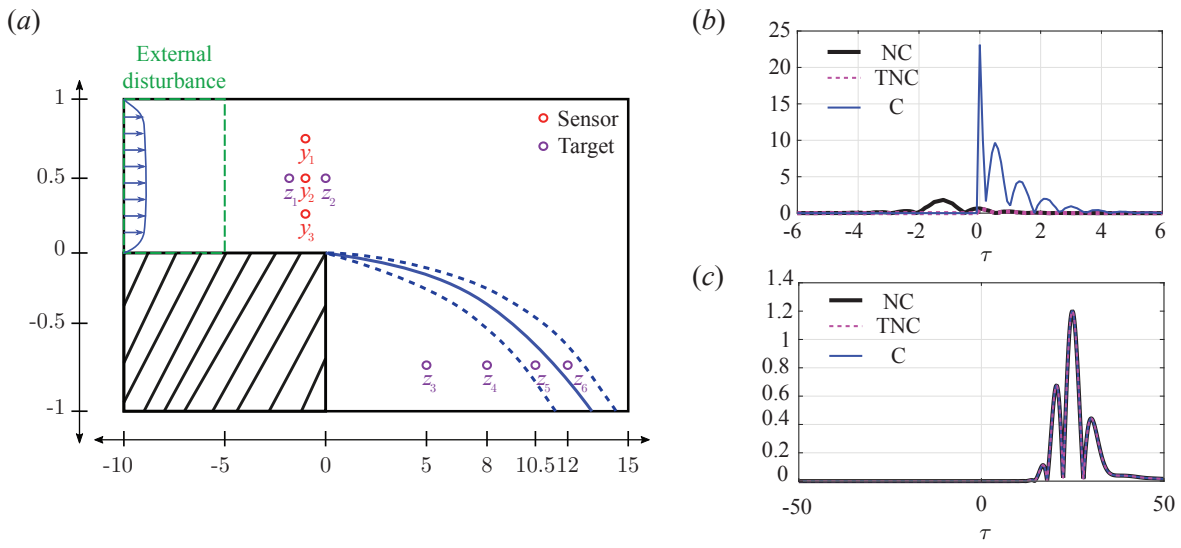

FIGURE 4.2: Estimation setup: Sensor placement for estimation over the backward-facing step flow (a) and the estimation kernels: (b) for y_2 and z_1 and (c) for y_2 and z_5.

significant amplitude in the non-causal part of the kernel ($\tau < 0$). However, the causal kernel retains the ability to evaluate the sensor measurements effectively. In the downstream target scenario, as depicted in figure 4.2(c), from the perspective of the target location, the sensor measures the flow data only from the past, which is that the flow is naturally causal. Consequently, it is expected that the three kernels (non-causal (2.7), truncated non-causal (2.8), and causal (2.12)) are identical. Numerically, when a causal kernel is constructed from the components of the non-causal kernels (2.7) using the Wiener-Hopf method, the future information ($\tau < 0$) is zero. As a result, Computing the causal kernel via the Wiener-Hopf method relies on the available past data ($\tau > 0$), resulting in identical causal kernels.

Figure 4.3 presents the time-series estimated velocity fluctuations at the target locations $[z_1, z_2, z_3, z_4, z_5, z_6]$, using one sensor (SISO) y_2 and three sensors (MIMO) $[y_1, y_2, y_3]$ for the linear system. Figures 4.3(a) and (b) illustrate that the TNC estimation is ineffective, whereas the causal estimation performs well. This is because the causal kernels successfully recover the information lost in the non-causal part. However, when the targets are located far upstream ($x < -2$), the accuracy of the causal estimation diminishes. We observed that when the peak of the causal kernel is closer to $\tau = 0$ for an upstream target, the Wiener-Hopf method improves the estimation by shifting the peak to the causal part of the kernel ($\tau > 0$). Figures 4.3(c) and (d) show that the

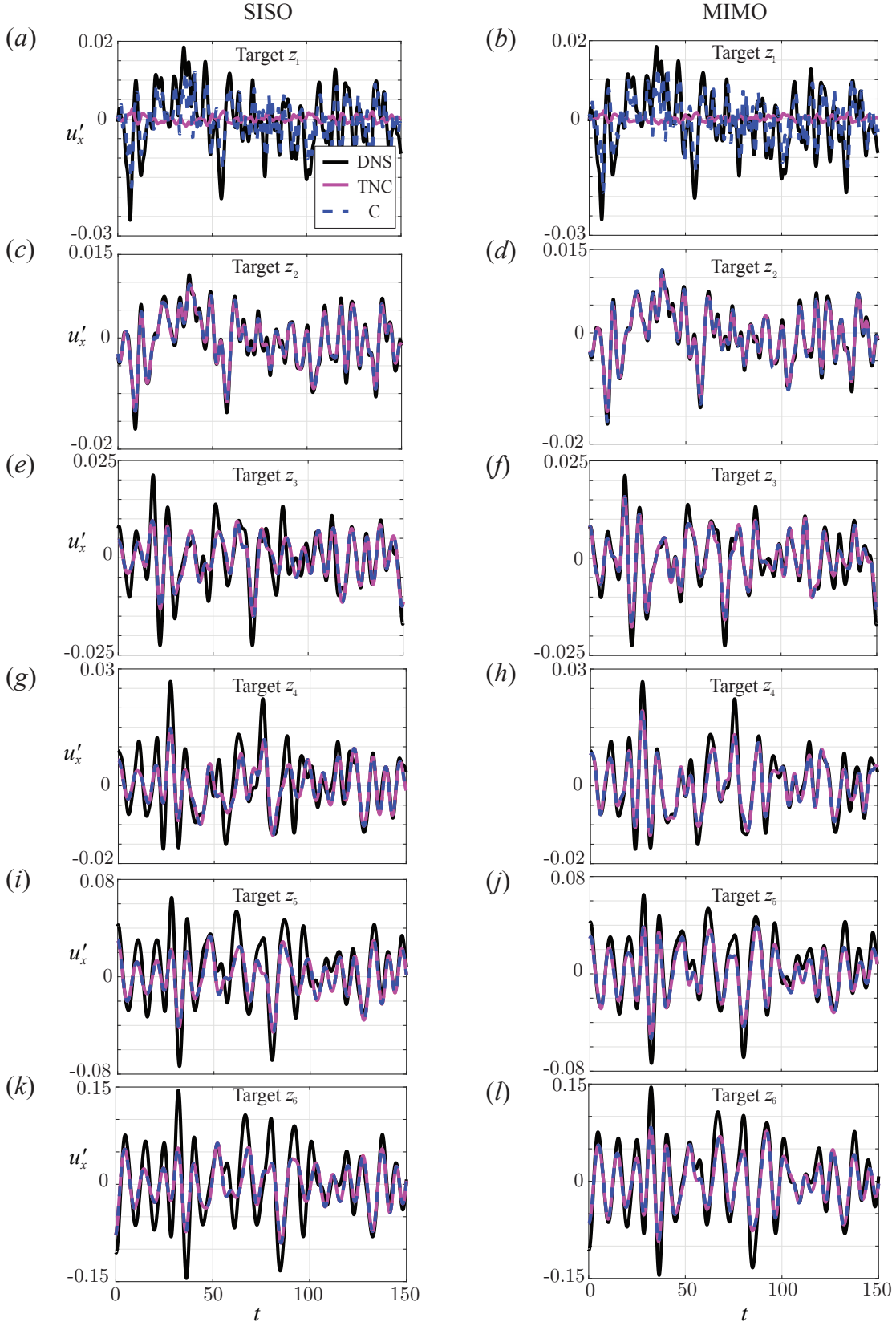

FIGURE 4.3: Time-series of estimated velocity fluctuations for the linear system using a single sensor (left column) and multiple sensors (right column).

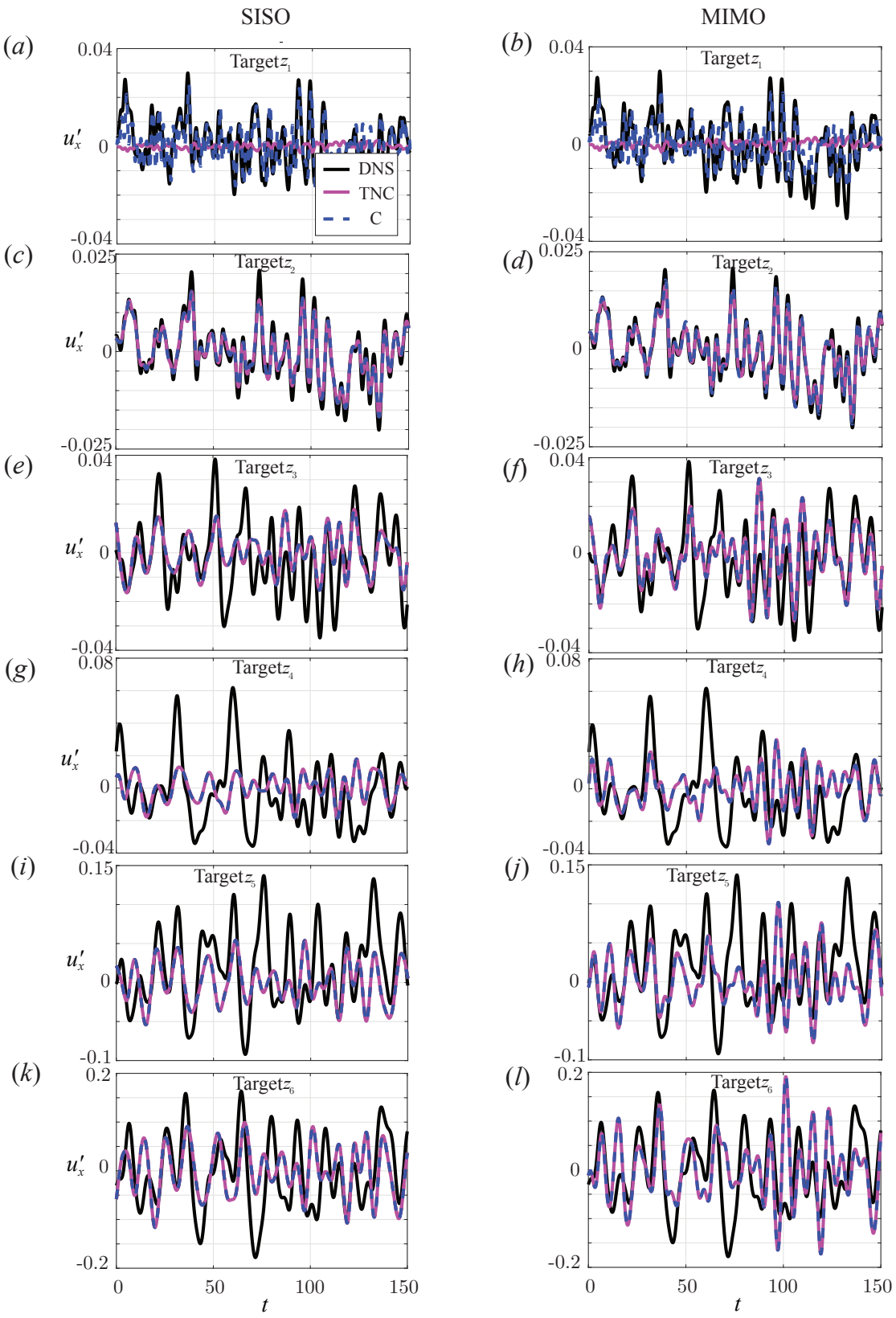

FIGURE 4.4: Time-series of estimated velocity fluctuations for the nonlinear system using a single sensor (left column) and multiple sensors (right column).

estimation closely matches the target readings (DNS), particularly when using three sensors. This result is not surprising, given the proximity of the targets and sensors. In general, the system using three sensors provides better estimates than using a single sensor. However, the estimation accuracy decreases for targets located further downstream, as expected and observed in figures 4.3(k) and (l).

Next, we apply the estimation kernels developed for the linear system to the nonlinear system with an amplitude of $f = 1$, resulting in fluctuated flow at the target that causes a 3-4% variation of the base flow velocity. The sensor and target configurations remain identical to those examined for the linear system, as shown in figure 4.2. Figure 4.4 presents the time series of estimated velocity fluctuations, using the identical estimation kernels for the results of figure 4.3. The estimation for the upstream target shows results comparable to those of the linear system. However, the estimation accuracy for downstream targets deteriorates in the nonlinear system compared to the linear system. This is expected, as nonlinear effects tend to intensify as the flow progresses downstream. In particular, the estimation performs poorly in the recirculation zone (figures 4.4(g) and (h)) after the step. This may be due to the significant evolution of flow perturbations from nonlinear terms in this region compared to more stable regions. In contrast, the flow can be well estimated at targets closer to the sensor (figures 4.4(c) and (d)).

4.3 Resolvent-based Control

We apply resolvent-based control to both the linear and nonlinear systems of backward-facing step flow. Figure 4.5 illustrates the locations of sensors, actuators, and targets. The sensor locations match those used in the estimation system depicted in figure 4.2. We identified the effective actuator placements Martini et al. [2022], concluding that actuator locations positioned behind the sensors yield comparable control performance. Figure 4.5(b) depicts the the control kernels corresponding to the sensor-actuator-target pairs (y_1, a_1, z_1), (y_2, a_2, z_2), and (y_3, a_3, z_3). The control kernels were constructed by integrating the actuation run (single-state run) with the estimation kernels. The causal kernels typically exhibit peak points at $\tau = 0$, indicating that the most recent measurements predominantly influence the actuation signal.

Similar to the approach used in the estimation work, control kernels developed based on the linear system were applied to the nonlinear system (DNS) to compute the actuation signal. The

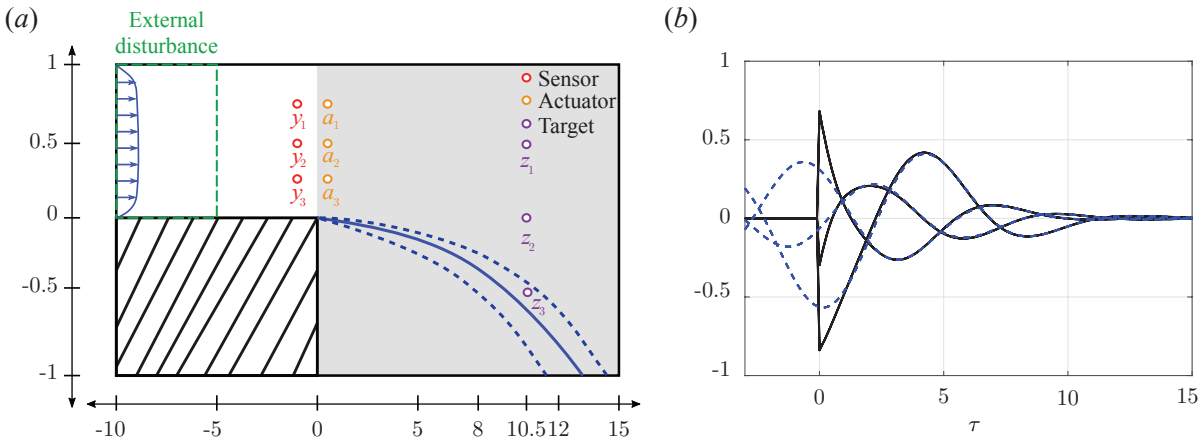

FIGURE 4.5: Control set-up: (a) Sketch of sensors, actuators and targets placement, and (b) three control kernels: non-causal kernels (blue) and causal kernels (black) for (y_1, a_1 and z_1), (y_2, a_2 and z_2), and (y_3, a_3 and z_3).

objective is to attenuate velocity fluctuations around the base flow. The actuation signal is incorporated into the momentum equation for the control system, as discussed in (3.8). The actuation signal $\boldsymbol{a}$ 3.9 is computed by the convolution of the control kernels with sensor measurements, such that $\boldsymbol{a}(t) = \int_0^\infty \boldsymbol{\Gamma}_{cl}(t-\tau)\boldsymbol{y}(\tau)d\tau$. Here, $\boldsymbol{\Gamma}_{cl}$ represents the closed-loop control kernel, and $\boldsymbol{y}$ denotes the sensor measurements of velocity fluctuations. $\boldsymbol{B}_a$ indicates the actuator location and spatial support, using the same Gaussian input parameters as in the estimation system ($\boldsymbol{\sigma}_x = 0.2$, $\boldsymbol{\sigma}_y = 0.1$). It is important to note that the control kernel $\boldsymbol{\Gamma}_{cl}$ is based on fluctuations in the sensor reading ($u_x^{'} = u_x - u_{\text{baseflow}}$) of the nonlinear system. The term $\boldsymbol{B}_{ext}\boldsymbol{f}(t)$ represents white-noise random forcing applied exclusively in the upstream region ($x < -5$) over the step.

This thesis investigates the control performance of both linear and nonlinear systems under conditions of low and high amplitude forcing, utilizing both SISO and MIMO configurations. For SISO, the sensor and actuator are positioned at the center of the three sensors (at $y = 0.5$), while for MIMO, the setup is as shown in figure 4.5. The targets for SISO and MIMO(3) are fixed at $x = 10.5$, $y = 0$ and $x = 10.5$, $y = [-0.5, 0, 0.5]$, respectively.

Figure 4.6 presents the time series of uncontrolled (red) and controlled (blue) fluctuations at the targets z_3 and $z_4 = [10.5, -0.75]$ for both linear and nonlinear systems using MIMO. In figures 4.6(a) and (b), the linear system is independent of the forcing amplitude, as the linearly amplified system is effectively managed by the linear controller. However, in figures 4.6(c) and (d), the linear

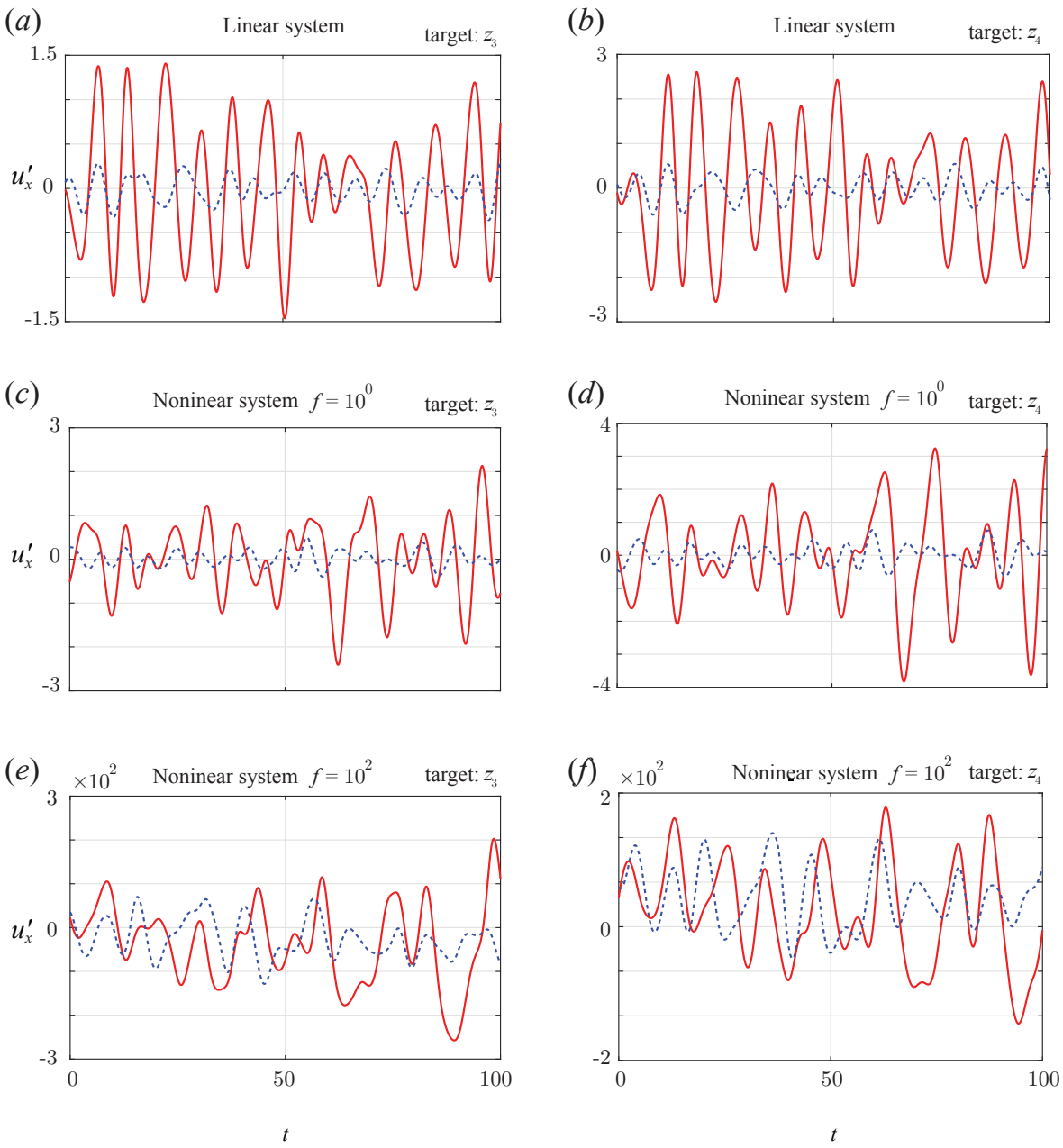

FIGURE 4.6: Time-series of uncontrolled (red) and controlled (blue) fluctuations at the targets z_3 and $z_4 = [10.5, -0.75]$ for the linear and nonlinear systems using MIMO; (*a*) and (*b*) represent the linear system, (*c*) and (*d*) correspond to low amplitude forcing, and (*e*) and (*f*) correspond to high amplitude forcing.

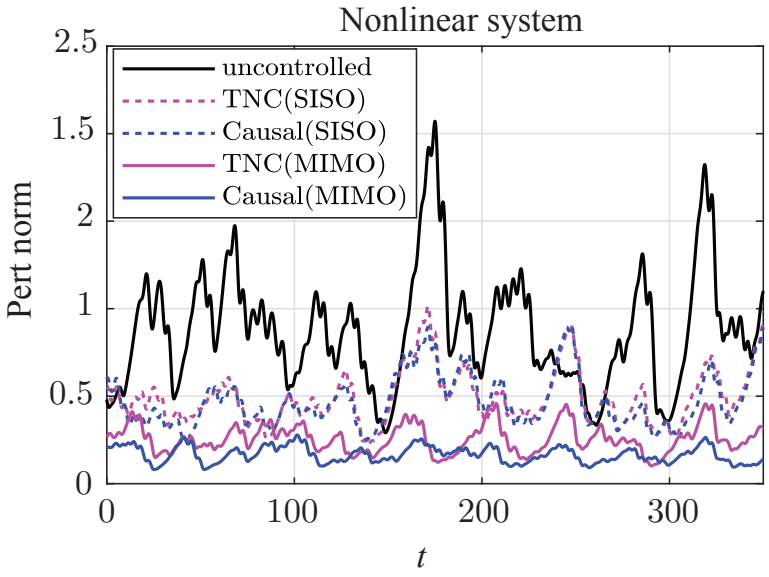

FIGURE 4.7: Comparison of the perturbation norms for the nonlinear system under different control strategies: uncontrolled, causal control (SISO and MIMO), and truncated non-causal control (SISO and MIMO).

controller performs well with low-amplitude forcing, while its control performance diminishes under high-amplitude forcing. As the number of sensors and actuators increases, we can more effectively control the fluctuations at the target. The control performance reaches a point of convergence after a certain number of sensors and actuators. In this study, three sensors and actuators are sufficient, as demonstrated by the similar control performance observed between targets z_3 and z_4. This finding is consistent with the report by Martini et al. [2022], who noted comparable control performance between the entire region target and a three-point target. This is also discussed for laminar airfoil control work in Chapter 5.

Figure 4.7 presents a comparison of perturbation norms for causal and truncated non-causal controls under external forcing ($f = 1$) for both SISO and MIMO configurations. Our findings confirm that causal control achieves superior performance with MIMO(3), and adding more sensors and actuators does not further improve performance, indicating convergence. As expected, the control performance follows the order: Causal(MIMO) > TNC(MIMO) > Causal(SISO) > TNC(SISO). However, for SISO, the difference between truncated non-causal and causal control is minimal. In Chapters 5 and 6, we apply our approaches to more complex flow systems, such as

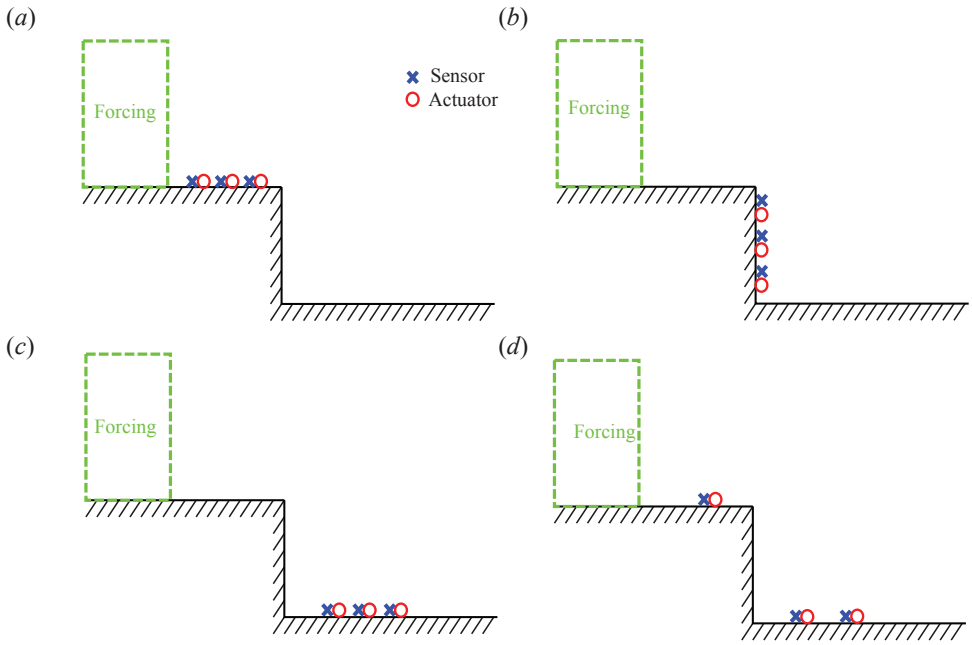

FIGURE 4.8: Sensor and actuator placement scenarios on the surface (*a*) upstep, (*b*) step, (*c*) downstep, (*d*) mixed.

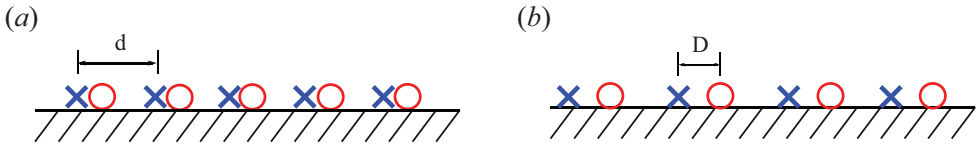

FIGURE 4.9: Relative placement: (*a*) distance between sensors, and (*b*) distance between a sensor and an actuator.

airfoil cases.

4.4 Sensor and Actuator Placement Investigation

In §4.2 and 4.3, the sensors and actuators were placed within the flow [Martini et al., 2022]. However, placing sensors and actuators within the flow is not practical for many applications due to physical constraints. Additionally, the number of sensors and actuators is often limited to reduce installation costs, making it crucial to optimize their placement to ensure sufficient control performance. This section explores different sensor and actuator placement scenarios. Two

strategies are employed in this investigation:

- **Surface Placement:** Sensors and actuators are positioned on the surface in four configurations, as shown in figure 4.8:

  (a) Upstream of the step ($x < 0$),

  (b) At the step ($x = 0$),

  (c) Downstream of the step ($x > 0$), and

  (d) A mixed configuration.

  The perturbation reduction rates for these configurations are shown in figure 4.10(a). As expected, Case (b) exhibits the poorest performance because the actuator at the step struggles to capture coherent flow structures. Case (a), with upstream surface placement, demonstrates better perturbation reduction since the flow is controlled before separation and downstream shearing.

- **Relative Placement:** The relative distance between sensors, and between a sensor and an actuator, as shown in figure 4.9. This strategy involves varying the distance D between pairs of sensors and actuators, where a positive D indicates that the sensor is upstream of the actuator in figure 4.9(b). The distance between sensors in figure 4.9(a) is fixed at $d = 1.5$ in this study. As anticipated, increasing the distance between the sensor and actuator improves the perturbation reduction rate. However, at a specific location around $D = -0.312$, where the actuator is upstream and the sensor downstream, the control becomes detrimental (see the dashed line in figure 4.10(b)).

Figure 4.10(c) compares the control performance between sensor and actuator placements within the flow and on the surface, considering an increasing number of sensors and actuators. Three scenarios are analyzed: within the flow (as in the previous section), Case (a) from figure 4.8, and Case (d) from figure 4.8. Case (b) from figure 4.8 is excluded from this analysis due to its limited control authority, as shown in figure 4.10(a).

The perturbation reduction rate converges after MIMO(4) placement within the flow when the placement is aligned in a line. Case (a) shows decreased performance with an increasing number

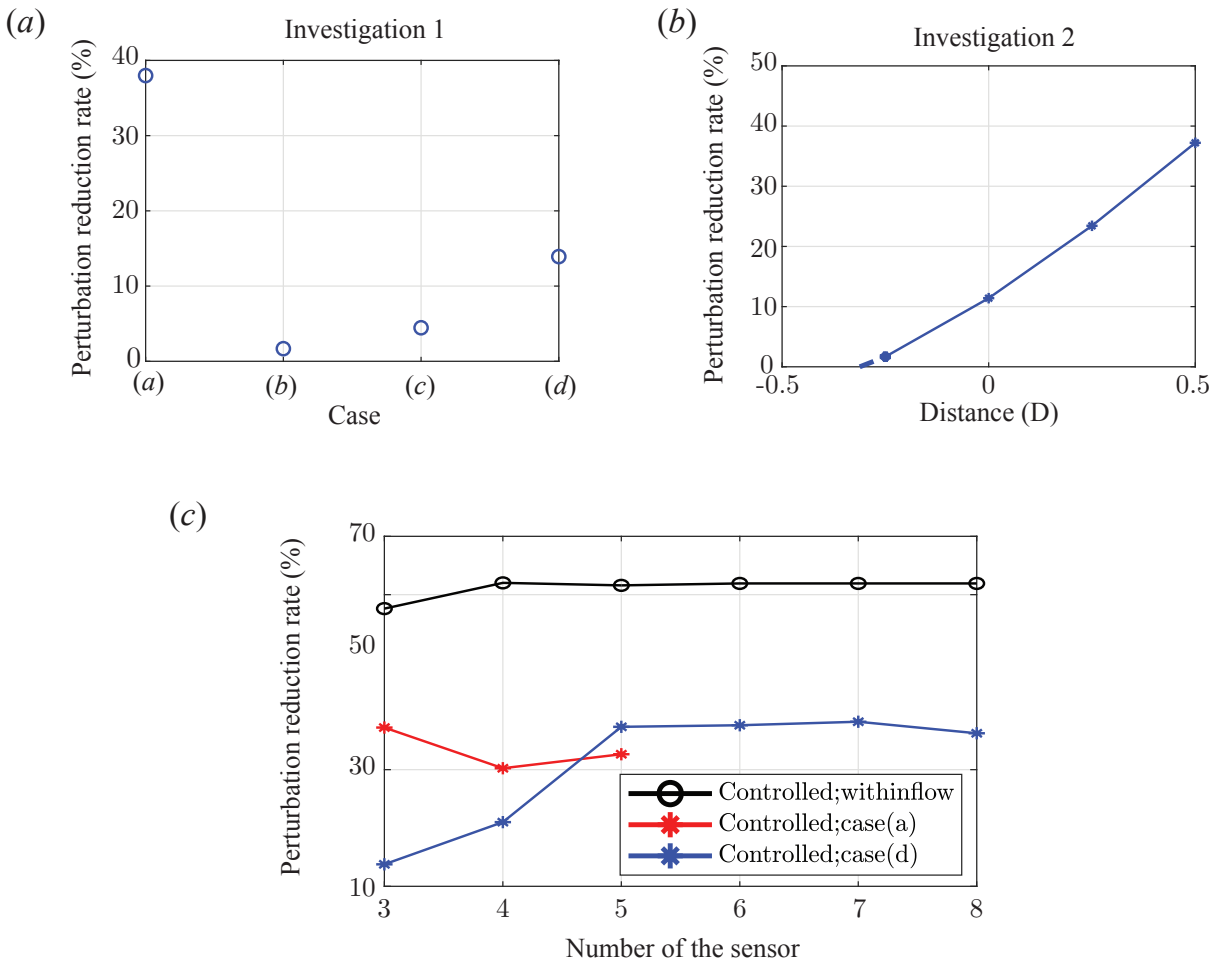

FIGURE 4.10: Sensor and actuator placement analysis: (*a*) Perturbation reduction rates for four cases as shown in figure 4.8; (*b*) the effect of sensor-actuator distance (D) on perturbation reduction rate; and (*c*) a performance comparison between placements within the flow and on the surface.

of sensors and actuators on the upstream surface, likely due to the limited space ($-5 < x < 0$) outside the forcing region. In contrast, Case (d) improves as more sensors and actuators are added, plateauing after five sensors. Overall, the control performance gap between placements within the flow and on the surface is approximately 25% in this study.

CHAPTER 5

Resolvent-based Estimation and Control of a Laminar Airfoil Wake[1]

5.1 Introduction

Laminar airfoil flow is a crucial area of research in fluid mechanics due to its significant influence on the performance and efficiency of aircraft and other aerodynamic systems, such as wind turbines. Wake perturbations, in particular, are of critical importance for several reasons. First, the wake behind an airfoil is closely associated with the separation bubble, which contributes to increased drag [Alam et al., 2010, Chang et al., 2022]. Accurate estimation and control of laminar flow in the wake can help identify and mitigate sources of drag, thereby enhancing overall aerodynamic efficiency. Second, wake perturbations are a key factor in the generation of aerodynamic noise [Wagner et al., 1996, Agrawal et al., 2015]. Effective management of these perturbations not only improves environmental compliance but also reduces noise pollution.

One of the interesting flow dynamics in laminar flows is vortex shedding in the wake. Vortices form on each side of the object and are shed periodically, creating downstream flow patterns such as the Karman vortex street. This vortex shedding is influenced by factors such as the angle of attack, the shape of the object, and the Reynolds number. In NACA0012 airfoils, within the mid-range angle of attack (6-10 degrees), an anticlockwise vortex is generated at the trailing edge, while a clockwise vortex at the front suction side separates and is entrained downstream [Chang et al., 2022]. This indicates that both the front area of the suction side and the trailing edge primarily

[1] *This chapter is based on work contained in: J. Jung, R. Bhagwat, and A. Towne. Resolvent-based estimation and control of laminar flow over an airfoil, submitted to: J. Fluid Mech.*

affect vortex shedding generation. To suppress vortex shedding from such bluff bodies, extensive studies have been conducted on cylinder flow [Jin et al., 2020, Déda et al., 2023, Lin and Tsai, 2024] and airfoil flow [Colonius and Williams, 2011, Broglia et al., 2018].

Obtaining an accurate estimator is essential for successful closed-loop control [Brunton and Noack, 2015] since precise flow state estimates provide the controller with accurate information for better control performance [Stengel, 1994]. Taking account of the intimate relationship between estimation and control, classical estimation and control methods, which are Kalman filter [Kalman, 1960], and Linear-quadratic-Gaussian control (LQG) combined with Kalman filter, respectively, have been noted in fluid mechanics over the last decade, e.g., Kalman filter [Rafiee et al., 2009, Colburn et al., 2011, An et al., 2021], and LQG control [Bagheri et al., 2009, Fabbiane et al., 2014, 2015, 2017, Sasaki et al., 2018a]. However, such a typical method contains two limitations, especially when they are applied to flows that require high-dimensional discretizations, e.g., high Reynolds number flows. First, solving the Riccati equations required to obtain Kalman and LQG gains scales poorly with problem size and becomes computationally expensive or prohibitive for large systems. This issue can be partly mitigated by reducing the system a priori [Pasquale et al., 2017, Gomez et al., 2019], but this potentially degrades the performance of the controller. Second, classical methods can not capture the nonlinear terms of the Navier-Stokes equations, as they typically treat these terms as white noise. As a result, it substantially deteriorates the estimation performance, in particular at high Reynolds numbers [Martini et al., 2020].

Flow estimation and control in high-dimensional systems suffer from determining effective sensor and actuator locations, often resulting in repeated simulations. Even with theoretically sound methods, ineffective placements render estimators and controllers ineffectual. In the field of fluid mechanics, various previous approaches have been explored for optimal sensor and actuator placements [Chen and Rowley, 2011]. Natarajan et al. [2016] addressed placement approaches based on the eigensystem within the compressible flow for flow control. Paris et al. [2021] utilized deep reinforcement learning to investigate optimal sensor placement on a two-dimensional laminar cylinder at low Reynolds numbers. Jin et al. [2022] examined the optimal placement of a single sensor and actuator using H_2-optimal estimators and controllers for laminar cylinders across a low range of Reynolds numbers. Additionally, data-driven approaches leveraging modern control theory techniques have been explored [Manohar et al., 2018, Sashittal and Bodony, 2021]. In this

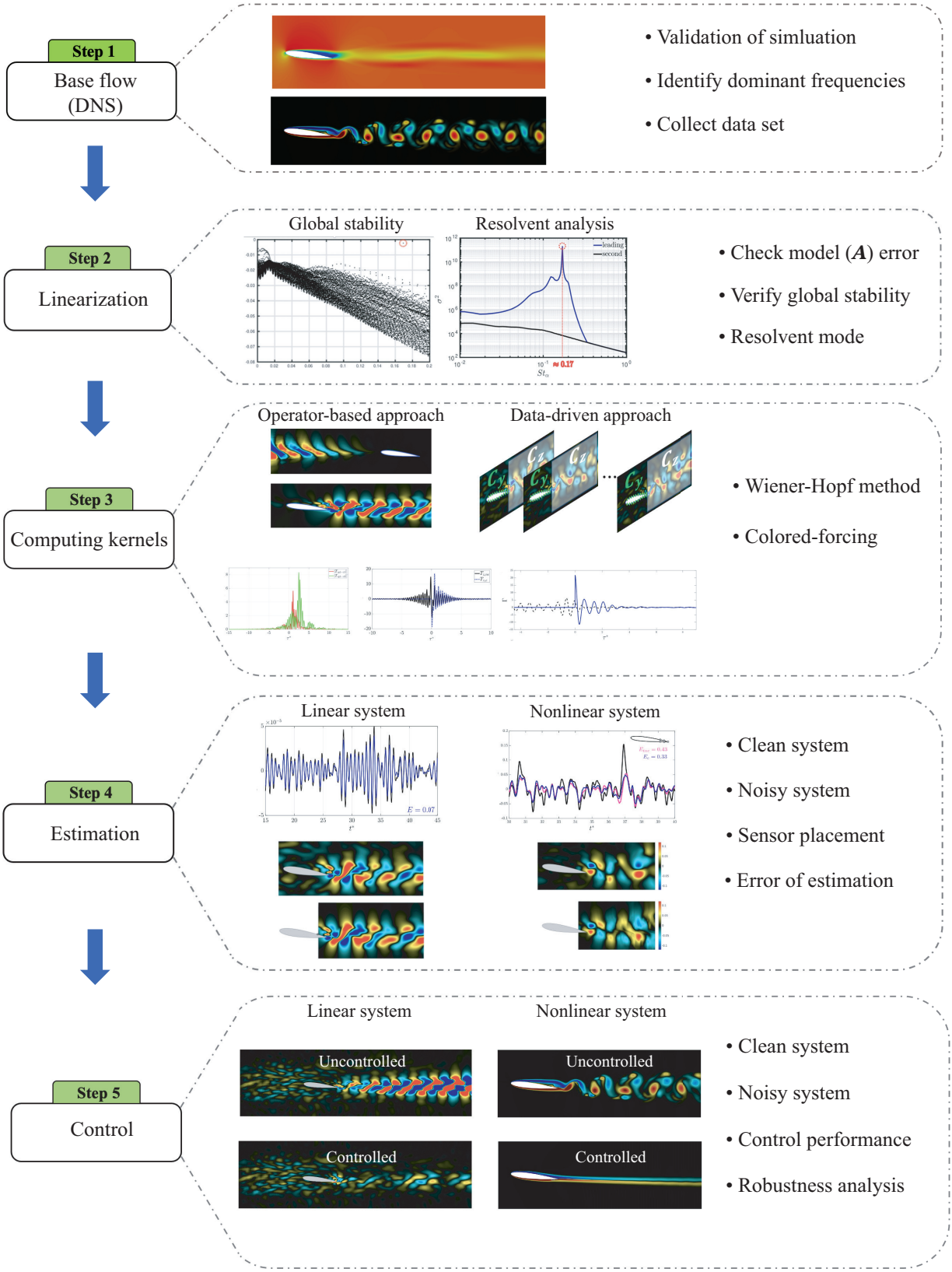

FIGURE 5.1: Roadmap for resolvent-based estimation and control over an airfoil.

work, it is essential to investigate proper sensor and actuator placements that are physically realizable for real-time (causal) estimation and control approaches. Our method determines the most effective placements by leveraging streamline information, which encapsulates the characteristics of laminar flow, and by using estimation errors.

In modern control theory, two main concepts govern control strategies: optimal control and robust control. The notion of robust control has gained significance in controller design since the late 1990s [e.g. Safonov et al., 1992, Zhou and Doyle, 1997]. Robust control entails two key aspects: robustness of stability and robustness of performance. The former concerns the overall stability of the flow system [Schmid and Sipp, 2016], while the latter evaluates how well predesigned controllers can maintain performance amidst changing flow conditions. Consequently, controllers must strike a balance between performance optimization and robustness. Although our optimal controllers aim to optimize target variables, similarly to previous works [Rowley et al., 2006, Bagheri et al., 2009, Fabbiane et al., 2014, Sasaki et al., 2020], we also address the robustness of our controller in how it reacts against the different systems.

This study aims to estimate and control unsteady perturbations in the wake of a two-dimensional NACA 0012 airfoil at $Ma_\infty = 0.3$, $Re_{L_c} = 5000$, and $\alpha = 6.5^\circ$ using resolvent-based approaches. To induce more chaotic fluctuations in the wake, we disrupt the periodic limit cycle by introducing upstream noise. The overall roadmap is outlined in figure 5.1. We begin by computing the flow using direct numerical simulation (DNS) and validate the simulation against existing literature. Subsequently, we analyze global eigenmodes and resolvent modes to validate our linearized compressible Navier-Stokes operator. The next step involves constructing estimation and control kernels through operator-based and data-driven approaches via the Wiener-Hopf method. To address the nonlinear terms, we incorporate colored-forcing statistics into the kernels. We first demonstrate the effectiveness of estimation at a single point and across extended regions of the flow for both linear and nonlinear systems, under conditions of clean and noisy upstream inflows, with the consideration of sensor placement. Following this, we present the effectiveness of resolvent-based control for the same systems and conditions, following the approach used in the estimation.

5.2 Problem Setup and Simulation

5.2.1 Problem description

Following Marquet et al. [2022], we consider laminar flow around a NACA0012 airfoil at a low chord-based $Re_{L_c} = 5000$, $Ma_\infty = 0.3$, and an angle of attack of $\alpha = 6.5°$. Using a resolvent-based approach, we aim to estimate and mitigate unknown time-series (future) and unsteady chaotic flow perturbations in the wake behind the trailing edge. To simulate realistic flow conditions, we impose noisy inflow upstream through random, zero-mean perturbations. This induces chaotic, unsteady fluctuations around the airfoil, disrupting the periodic limit cycle generated by vortex shedding. To evaluate the effectiveness of the estimators and controllers in a nonlinear system, we also consider a clean system without external forcing.

5.2.2 Numerical set-up for the baseflow

A direct numerical simulation using the compressible flow solver CharLES is used to simulate the flow. A C-shape mesh is created by Pointwise, as shown in figure 5.2(a), where the computational grid near the airfoil is also shown in the red box. The leading edge of the airfoil is located at the origin $x/L_c = y/L_c = 0$. The size in the streamwise and normal direction is $x/L_c \in [-49, 50]$, $y/L_c \in [-50, 50]$, respectively. To create a two-dimensional simulation, the spanwise direction is one cell thick ($z/L_c \in [0, 0.1]$) with symmetry boundary conditions. A characteristic boundary condition for the far-field is used $[\rho, u_x, u_y, u_z, P] = [\rho_\infty, U_\infty, 0, 0, P_\infty]$, and the sponge layer is set as an outflow at $x/L_c \in [30, 50]$ with the running-averaged time $tU_\infty/L_c = 20$ to damp the reflected acoustic wave over the length of the sponge layer from the outflow boundary layer. For the time integration, a constant Courant-Friedrichs-Ley number is set to 1. In figure 5.2(c), an instantaneous streamwise velocity field around the airfoil is presented. We can observe the vortex shedding in the wake and separation bubble over the airfoil.

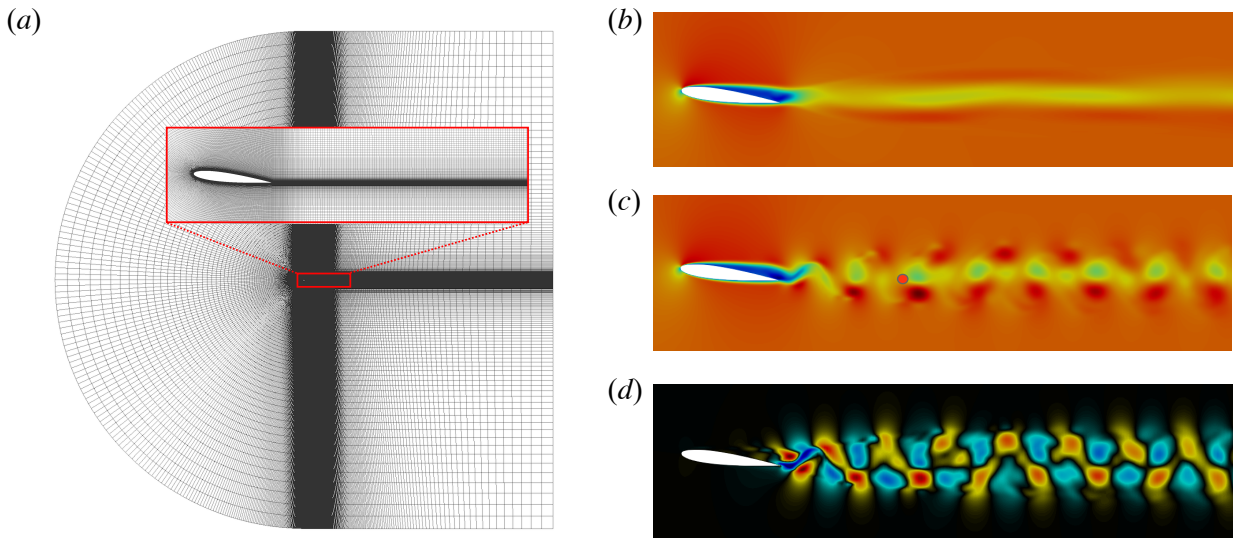

FIGURE 5.2: Direct numerical simulation: (a) the full computational C-shaped grid with a close-up view for the wall and wake regions, (b) the mean streamwise velocity u_x, (c) the instantaneous streamwise velocity u_x field with the red dot indicating the probe location at $(x, y)/L_c = (2.1, -0.11)$ for the power spectral density in figure 5.3, and (d) the streamwise velocity perturbation u'_x field.

5.2.3 Validation of simulation

We study resolution for the convergence of eigenvalue and resolvent gain at the vortex shedding frequency for the base flow. The base flow for this study is at $Ma_\infty = 0.3$, $Re_{L_c} = 5000$ and $\alpha = 6.5°$. The grid points in table 5.1 represent the node numbers along the airfoil, the wake, and the cross-streamwise direction. Due to the need for a fine grid in the wake, including the targets for estimation and control, we use a finer grid in the wake region compared to the typical grids with fewer points used in previous studies [Kojima et al., 2020, Marquet et al., 2022]. The Strouhal number $St_{\alpha,\boldsymbol{A}}$ represents the vortex shedding frequency based on the angle of attack for the linearized Navier-Stokes operator, while $St_{\alpha,DNS}$ corresponds to the same frequency derived from the DNS. Based on our convergence study, we selected Mesh 5 for this work.

We validate the DNS via comparisons of the vortex shedding frequency, aerodynamic forces, and vorticity field against the results of Marquet et al. [2022], who considered incompressible flow over the same airfoil at the same Reynolds number and angle of attack. The probe to measure the wall-normal velocity is located at $x/L_c = 2.1, y/L_c = -0.11$. The vortex-shedding frequency $St_\alpha \equiv \omega_r(L_c sin\alpha)/(2\pi Ma_\infty)$ is found to be approximately 0.169 in the present study, shown as in

Mesh	Grid points	Total cells	$St_{\alpha,A}$	$St_{\alpha,DNS}$
1	$100 \times 90 \times 80$	29,704	0.168319	0.169650
2	$100 \times 180 \times 80$	43,924	0.167249	0.168541
3	$150 \times 135 \times 120$	67,354	0.168933	0.169124
4	$200 \times 180 \times 160$	120,204	0.169140	0.169525
5	$200 \times 268 \times 160$	148,188	0.169241	0.169288
6	$200 \times 300 \times 160$	158,364	0.169222	0.169211
7	$200 \times 360 \times 180$	177,444	0.169207	0.169246

TABLE 5.1: Grid convergence of the vortex shedding frequency for power spectral density and eigenvalue, optimal and suboptimal resolvent gain

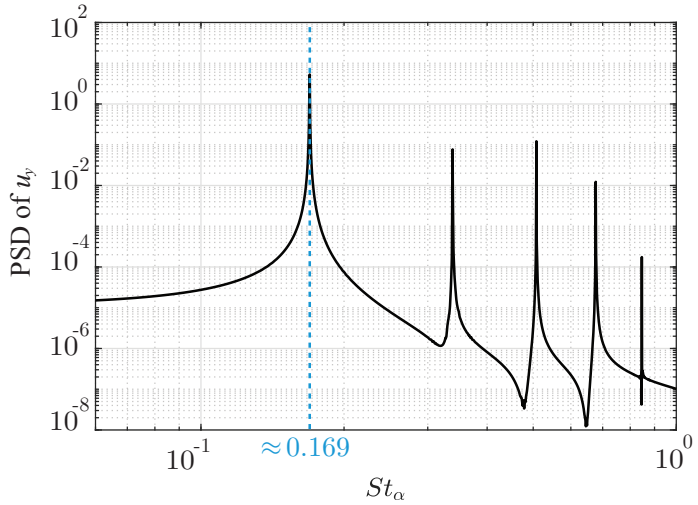

FIGURE 5.3: Power spectral density (PSD) of the wall-normal velocity at $(x, y)/L_c = (2.1, -0.11)$.

figure 5.3, close to the value of 0.18 found by Marquet et al. [2022]. Next, the time-averaged drag and lift coefficients over the surface of the airfoil are considered for validation. The drag and lift coefficients are

$$C_D = \frac{F_D}{\frac{1}{2}\rho_\infty U_\infty^2 A}, C_L = \frac{F_L}{\frac{1}{2}\rho_\infty U_\infty^2 A}. \tag{5.1}$$

Table 5.2 shows that the present study matches the time-averaged drag and lift coefficient results of Marquet et al. [2022] within a 2% tolerance. This slight difference could be the result of minor differences between the incompressible and compressible flow solutions or differences in the grid refinement; the present grid is more finely resolved.

Figure 5.4 presents the vorticity field of both the instantaneous and mean flow, showing a structure similar to the results obtained by Marquet et al. [2022]. The mean flow, time-averaged

	Present study	Marquet et al. [2022]	Error
$\bar{C}_D$	0.0862	0.088	2.05%
$\bar{C}_L$	0.2941	0.289	1.76%

TABLE 5.2: The comparison of the time-averaged drag and lift coefficients at $\alpha = 6.5°$ with the results from incompressible periodic solution for a NACA 0012 airfoil at $Re_{L_c} = 5,000$ and $Ma_\infty = 0.3$.

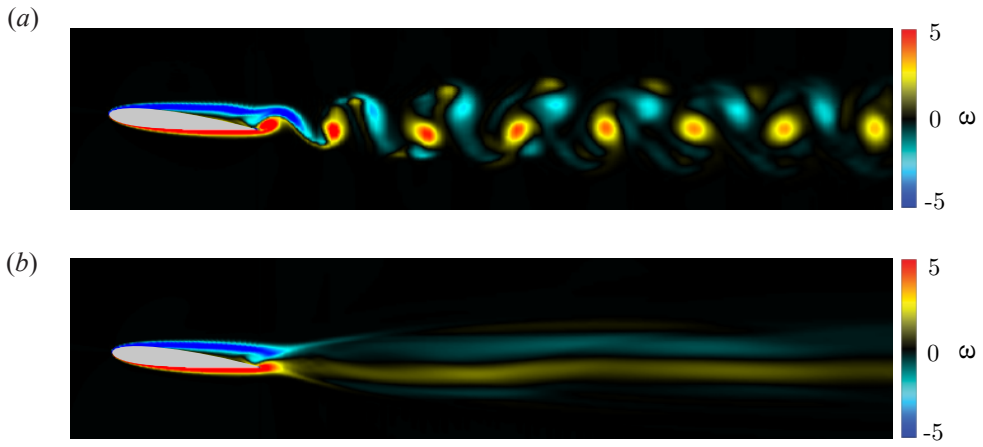

FIGURE 5.4: Vorticity field of (a) the instantaneous flow and (b) the mean flow.

over $tU_\infty/L_c \in [0, 350]$, is used for the linearization work. This extended time window ensures the time convergence of the vortex shedding in the wake flow, providing an accurate representation of the mean flow.

5.3 Global Stability Analysis

Resolvent-based estimation and control are nominally applicable and robust only for globally stable systems [Schmid and Sipp, 2016, Martini et al., 2020, 2022]. Thus, we first conduct a global stability analysis. Figure 5.5 illustrates that all the imaginary parts ω_i of the frequency, defined as $\lambda = -i\omega$, where λ is the eigenvalue of the linearized Navier-Stokes operator $\boldsymbol{A}$, are below zero, indicating that the flow around the airfoil is globally stable. The dominant eigenmode at the vortex-shedding frequency in figure 5.5 is observed at $St_\alpha \approx 0.169$, which corresponds to the power spectral density (PSD) results shown in figure 5.3. As expected, the convective wake mode is well observed from the eigenmodes, as depicted in figure 5.5(b) and (c).

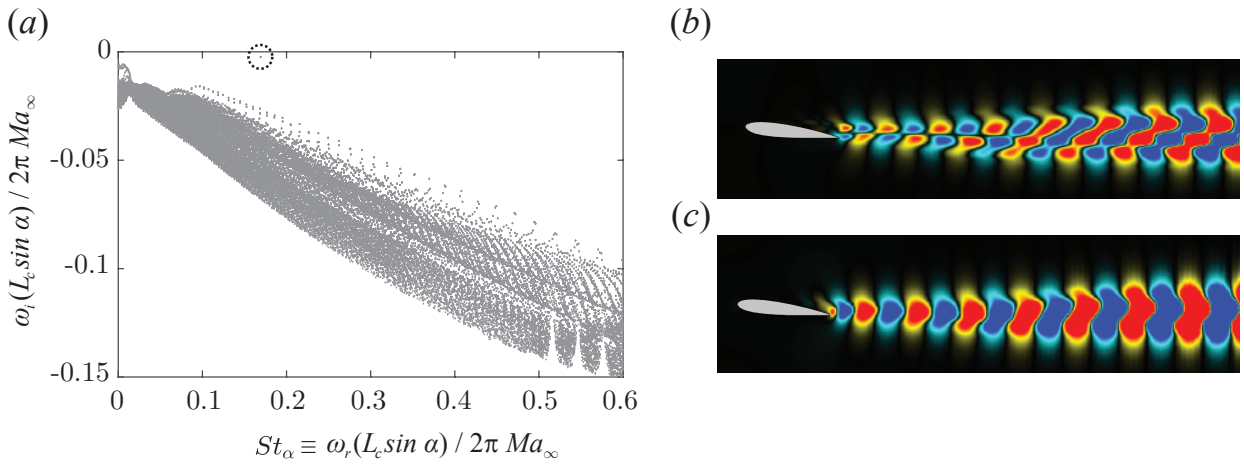

FIGURE 5.5: Eigenspectrum: (*a*) Eigenspectrum. The red circle shows the dominant wake eigenmode at the vortex-shedding frequency $St_\alpha \approx 0.17$, (*b*) the corresponding streamwise velocity eigenmode, and (*c*) cross-streamwise velocity eigenmode.

5.4 Resolvent Analysis

Resolvent analysis is central to our estimation and control methods. Therefore, we conduct it as a preliminary step to validate our implementation and to gain insights into the flow physics and the appropriate sensor and actuator placements. After transforming the linear system into the frequency domain, we obtain

$$\hat{\boldsymbol{q}} = \boldsymbol{R}\hat{\boldsymbol{f}}, \tag{5.2}$$

where the resolvent operator is defined as $\boldsymbol{R} = (-i\omega\boldsymbol{I} - \boldsymbol{A})^{-1}$. Using this operator, we compute the optimal resolvent gains and the corresponding forcing and response modes. To extract primitive variables, we employ a modified resolvent operator [Towne et al., 2018]

$$\tilde{\boldsymbol{R}} = \boldsymbol{W}^{\frac{1}{2}}\boldsymbol{C}\boldsymbol{R}\boldsymbol{B}\boldsymbol{W}^{-\frac{1}{2}}, \tag{5.3}$$

where $\boldsymbol{C}$ and $\boldsymbol{B}$ are identity matrices $\boldsymbol{I}$, while these matrices represent the sensor locations and forcing regions for estimation and control work. The weight matrix $\boldsymbol{W}$ used for the norm [Chu,

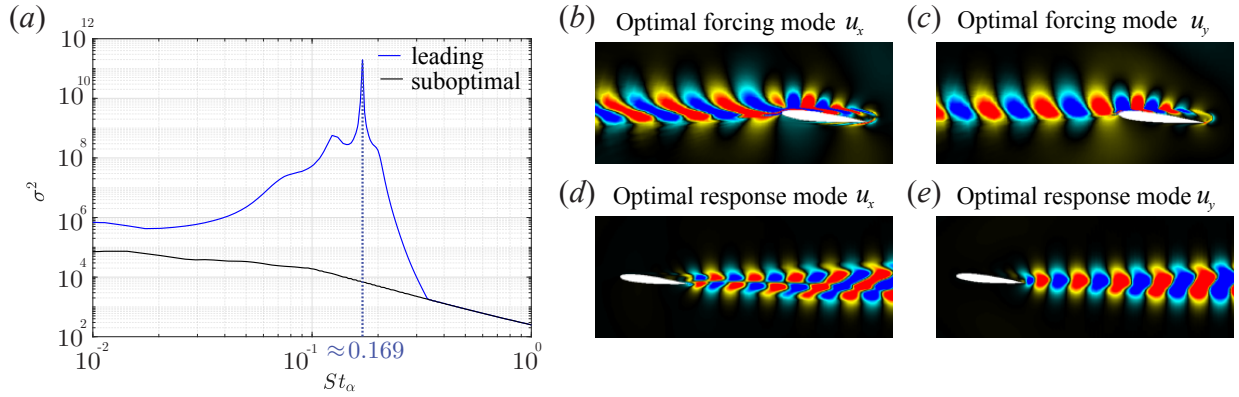

FIGURE 5.6: Resolvent gains, optimal forcing and response modes: (a) leading and second optimal gains (red circle is expressed for the optimal resolvent modes (*b*),(*c*),(*d*),(*e*)), (*b*) optimal forcing mode of u_x, (*c*) optimal forcing mode of u_y, (*d*) optimal response mode of u_x, and (*e*) optimal response mode of u_y.

1965] is defined as

$$\langle \boldsymbol{q}_1, \boldsymbol{q}_2 \rangle = \boldsymbol{q}_1^* diag\left(\frac{\bar{a}_0^2}{\bar{\rho}\gamma}, \bar{\rho}, \bar{\rho}, \bar{\rho}, \frac{\bar{\rho} c_v}{\bar{T}}\right)^T \boldsymbol{q}_2 = \boldsymbol{q}_1^* \boldsymbol{W} \boldsymbol{q}_2, \tag{5.4}$$

where $\{\cdot\}^*$ indicates the conjugate transpose. The resolvent gains are computed via the eigen-decomposition

$$\tilde{\boldsymbol{R}}^\dagger \tilde{\boldsymbol{R}} = \tilde{V} \Sigma^2 \tilde{V}^\dagger, \tag{5.5}$$

where $\Sigma = diag[\sigma_1, \sigma_2, ..., \sigma_{n_{freq}}]^T$, σ_1 indicates the optimal resolvent gain, and $\{\cdot\}^\dagger$ indicates the adjoint operator. The action of $\boldsymbol{R}$ in (5.5) is obtained by computing its LU decomposition, and the eigenvalue problem is solved using Arnoldi iteration [Jeun et al., 2016, Schmidt et al., 2018]. The forcing and response modes can be recovered by $\boldsymbol{V} = \boldsymbol{W}^{-\frac{1}{2}} \tilde{\boldsymbol{V}}$ and $\boldsymbol{U} = \boldsymbol{W}^{-\frac{1}{2}} \tilde{\boldsymbol{U}}$.

In figure 5.6, the peak point of the leading resolvent gain is observed at the vortex shedding frequency $St_\alpha \approx 0.169$, which is dominant in this flow. The optimal forcing and response modes are shown in figure 5.6(*b*)-(e). The optimal forcing mode is shaped upstream and over the airfoil, while the optimal response mode is well observed downstream in the wake. As the flow is convective from upstream, the input (forcing) and output (response) are located along the flow direction. The optimal response modes are similar to the dominant eigenmodes.

5.5 Resolvent-based Estimation of the Airfoil Flow

As demonstrated in figures 5.5 and 5.6, the flow is globally stable, and the resolvent analysis effectively explains the flow physics of the airfoil. This suggests that resolvent-based estimation and control approaches have significant potential for this flow. We consider two systems for estimation: linear and nonlinear. The linear system, for which we construct the estimation kernels, is expected to perform optimally in theory. The nonlinear system represents the actual physical system, which could be modeled through nonlinear simulations e.g., DNS or LES, or an experimental setup. First, we begin by analyzing the resolvent-based estimation for the linear system, introducing a random, zero-mean external disturbance in a small region upstream of the airfoil. We then estimate flow perturbations for the nonlinear system, both with and without the external disturbance, which are referred to as noisy and clean systems in this thesis. These external disturbances are designed to mimic free-stream noise (as shown in figures 5.7 and 5.13(b)) in both the linear and nonlinear systems. This prevents the flow from falling into the periodic limit cycle associated with the vortex shedding process, yielding a chaotic flow instead.

We employ shear stress sensors at one or more points on the surface of the airfoil and is computed from the state $\boldsymbol{q}$ by an appropriately defined measurement matrix $\boldsymbol{C_y}$, such that

$$\boldsymbol{\tau}_w = \boldsymbol{y} = \boldsymbol{C}_y \boldsymbol{q} \tag{5.6}$$

contains the wall shear stress at the sensor locations. The sensor in (5.6) and target $\boldsymbol{z} = \boldsymbol{C}_z \boldsymbol{q}$ correspond to one or more Gaussian spatial supports

$$\alpha e^{-(x-x_c)^2/2\sigma_x^2 - (y-y_c)^2/2\sigma_y^2}, \tag{5.7}$$

where α represents the inverse of the weight summed by the spatial support, and σ_x and σ_y denote the coefficients of the Gaussian function.

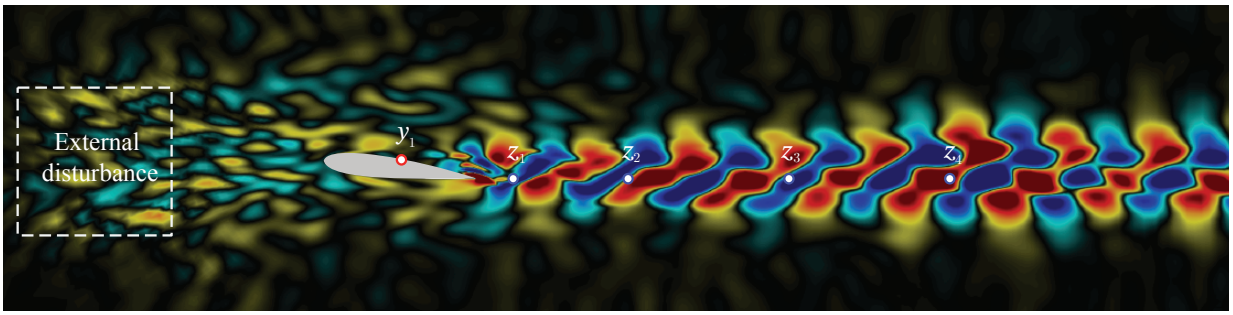

FIGURE 5.7: Estimation set-up for the linear system using the external disturbance. The sensor (red circle) and target (blue circle) locations are shown.

5.5.1 Linear system

Figure 5.7 shows the instantaneous velocity fluctuation field of the linear system, which is driven by an external disturbance in the upstream region. The dominant wake mode, closely resembling the least stable eigenmode and the optimal resolvent response mode, is clearly visible. We begin by demonstrating how to construct the estimation kernel using an operator-based approach. For this, a sensor (y_1) is placed at $x/L_c = 0.5$ on the suction surface of the airfoil, while the targets (z_1, z_2, z_3, z_4) are positioned along the trailing edge at $x/L_c = [1.2, 2.0, 3.0, 4.0]$ and $y/L_c = -0.11$, as illustrated in figure 5.7.

5.5.1.1 Building estimation kernels with white noise forcing

We use the operator-based approach in §2.4.1 to build the estimation kernels that assume the forcing CSD matrix as white noise. In this thesis, we show an example of the two-stage run used to build the operator-based kernel between sensor y_1 and targets z_1 or z_2. Figure 5.8 shows the results of these two-stage runs, including the estimation kernels and the instantaneous velocity fluctuations u'_x field of the adjoint and direct runs. Impulse forcing is applied at the sensor location, as shown in figure 5.8(a) at the initial time step. This impulse forcing is temporally supported by a Gaussian function $e^{-(t-t_0)^2\sigma_t}$ with $\sigma_t = 12.5$ and $t_0 = 0$, and spatially distributed according to (5.7) with $\sigma_x = \sigma_y = 0.02$. The target measurements are also spatially supported by the same Gaussian sensor. The region $\boldsymbol{B}_f$ coincides with the area of external forcing $\boldsymbol{f}_{ext}$, ensuring that $\boldsymbol{F}_{ext}$ is inherently included in the kernel between the modified resolvent operators, such as $\boldsymbol{R}_{yf}$. This inclusion is crucial for constructing the resolvent-based estimation kernel. The forcing CSD matrix is assumed

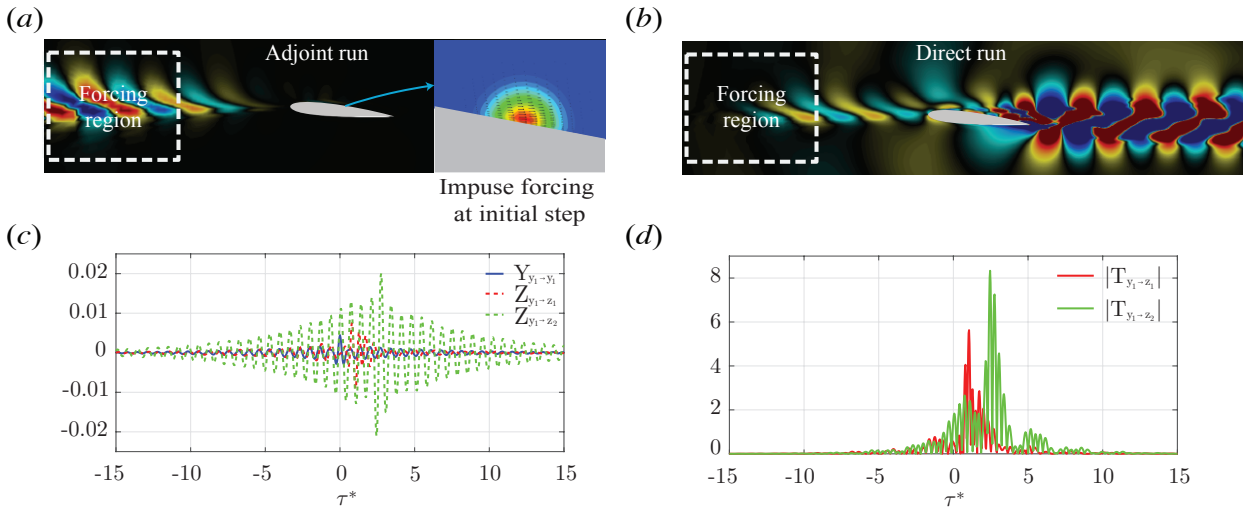

FIGURE 5.8: Operator-based approach: (a) Snapshot of the adjoint run at a specific step, including a zoom-in of the impulse forcing applied at the initial step. (b) Snapshot of the direct run imposed by the forcing using the $\boldsymbol{B}_f$ readings from the adjoint run. (c) Time-series solutions from the direct run corresponding to (b): y_1 [x/L_c = 0.5], z_1 [x/L_c = 1.2], and z_2 [x/L_c = 2.0]. (d) Non-causal estimation kernels are constructed using the solutions from (c).

to be white noise $\boldsymbol{F}_{ext} = \boldsymbol{I}$, implying uncorrelated forcing in space and time.

In figure 5.8(b), the readings from $\boldsymbol{B}_f \boldsymbol{s}_i$ of the adjoint run are used as upstream forcing in the direct run. The forcing modes influence the formation of dominant wake modes downstream. This impact is recorded in the target measurements. To achieve convergence in the adjoint and direct run, we simulate the two-stage run over a time span $tU_\infty/L_c \in [-36, 36]$ with a time step of $2\Delta t_{dns} U_\infty/L_c$, which is twice the DNS time step based on a CFL number of 1. The checkpointing interval $tU_\infty/L_c$is appropriately chosen. All target readings are averaged over small spatial regions weighted by a Gaussian function to account for the finite size and resolution of real sensors and to ensure numerical convergence at a finite grid resolution. The sensor noise $\hat{\boldsymbol{N}} = \epsilon I$, with $\epsilon = 10^{-3}$ of the maximum value of $\hat{\boldsymbol{Y}}$. While sensor noise can affect the smoothness of the estimated data, it does not significantly impact the output amplitude.

Figure 5.8(c) shows the time-domain solutions $\boldsymbol{Y}$ and $\boldsymbol{Z}$ of (2.25) of the above example shown in figure 5.8(a) and (b).Figure 5.8(d) illustrates the estimation kernel $\boldsymbol{T}_{\boldsymbol{nc}}$ of (2.7) computed from the corresponding $\boldsymbol{Y}$ and $\boldsymbol{Z}$. Note that the positive domain $\tau^* > 0$ represents past, while the negative domain $\tau^* > 0$ represents the future time. The Fourier-transformed $\boldsymbol{Y}$ and $\boldsymbol{Z}$, which are $\hat{\boldsymbol{Y}}$ and $\hat{\boldsymbol{Z}}$, are equivalent to $\boldsymbol{R}_{yf}\boldsymbol{R}_{yf}^{\dagger}$ and $\boldsymbol{R}_{zf}\boldsymbol{R}_{yf}^{\dagger}$ which are used to build the resolvent-based kernels. $\boldsymbol{Y}$ is

symmetrical at $\tau^* = 0$, since it is autocorrelation. The perturbation is evolved as it goes downstream from z_1 to z_2, so $Z_{y_1 \to z_2}$ is generally greater than $Z_{y_1 \to z_1}$. The peaks of $Z_{y_1 \to z_1}$ and $Z_{y_1 \to z_2}$ can be explained as the travel time from the sensor location where the impulse forcing is imposed ($\tau^* = 0$) to the target. The impact is well shown in the estimation kernels in figure 5.8(d). The peak points for the $T_{y_1 \to z_1}$ and $T_{y_1 \to z_2}$ are $\tau^*_{z_1} = 1.05$ and $\tau^*_{z_2} = 2.46$, respectively. As the perturbation close to the surface of the airfoil, especially the trailing edge, behaves in some chaotic motions with a rotating effect, it leads to a delay in traveling the perturbation. The second dominant peak is also observed for $T_{y_1 \to z_1}$ and $T_{y_1 \to z_2}$ on the left side of the main peaks. The impact might come from the acoustic waves, which are faster than the hydrodynamic waves. For both kernels shown in figure 5.8(d), the dominant values reside on the causal part $\tau^* > 0$, so the non-causal part is not so great, which is still effective for estimation. However, if the significant values of the kernels reside on the non-causal part, then the estimator loses its effectiveness. To overcome this issue, we consider the optimal causality of the kernel. For the linear system, this impact is trivial, but it significantly affects the nonlinear system, so we will discuss this for the estimation of the nonlinear system.

5.5.1.2 Estimation results of the linear system

We present the causal resolvent-based estimation result only using a single sensor, comparing the true streamwise velocity fluctuation u'_x with the estimated value over time. Additionally, we estimate the fluctuations of both the streamwise u'_x and cross-streamwise u'_y velocity components in an extended region of the targets using a small number of sensors. To quantify the accuracy of these estimations, we calculate the estimation error, defined as

$$E = \frac{\Sigma_i \int (\tilde{\boldsymbol{z}}_{\boldsymbol{i}}(t) - z_i(t))^2 dt}{\Sigma_i \int (z_i(t))^2 dt}, \tag{5.8}$$

where $\tilde{z}_i$ and z_i represent the estimated and true values for the i-th target, respectively. In computing the estimation error, we assume the system is ergodic, allowing the ensemble average to be replaced by the time average. Each run uses a different random seed.

Theoretically, causal estimation for the linear system yields optimal estimation results. In figure 5.9, the result indicates that the target near the trailing edge, positioned in a more complex flow region, has less accurate estimation. In contrast, the other three targets (z_2, z_3, and z_4) show better

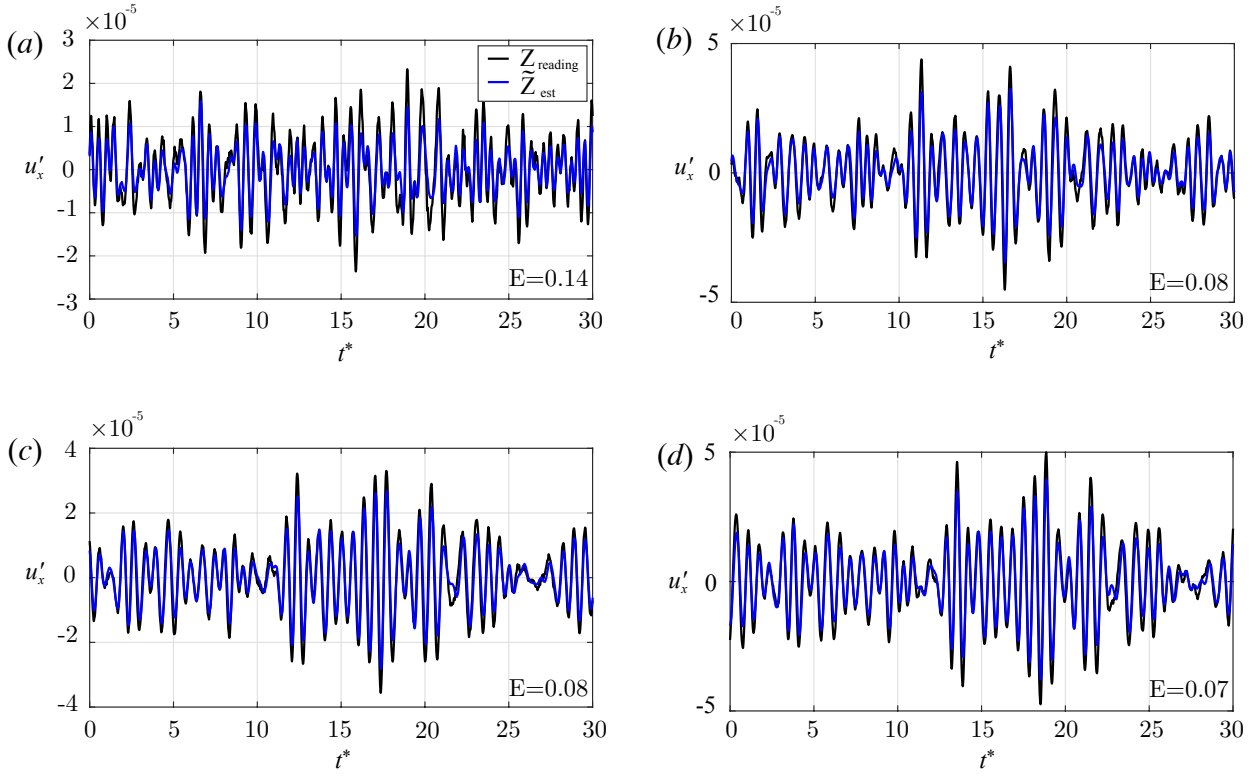

FIGURE 5.9: Causal estimation using an operator-based approach for the linear system at the targets: (*a*) z_1, (*b*) z_2, (*c*) z_3, and (*d*) z_4 at positions $[x/L_c = 1.2, 2.0, 3.0, 4.0]$, as shown in Figure 5.7.

estimation with an error of $0.07 - 0.08$. Overall, the frequency and amplitude of the fluctuations are well estimated. Interestingly, we observe that when the external forcing region overlaps with the optimal forcing resolvent mode, the estimation accuracy improves compared to the case where the external forcing region does not align with the optimal forcing mode. This improvement occurs because the forcing in the direct run maximally amplifies the response wake mode, and this effect is captured in the estimation kernel, leading to better wake estimation.

We focus on the estimation results based on different sensor locations on the airfoil surface. Figure 5.10 shows the estimation error as a function of the target x/L_c location, depending on the six sensor locations y_1, y_2, y_3, y_4, y_5, and y_6. The front sensors on the suction (y_1) and pressure surface (y_6) with the targets near the trailing edge ($x/L_c < 1.5$) produces less accurate estimations. In contrast, the rear sensors (y_3 and y_4), including the middle sensor y_2, which is equivalent to the location for which the kernel was built in the previous section, result in better estimation accuracy. It appears that y_2 and y_3 can capture the flow dynamics near the trailing edge, which is generated

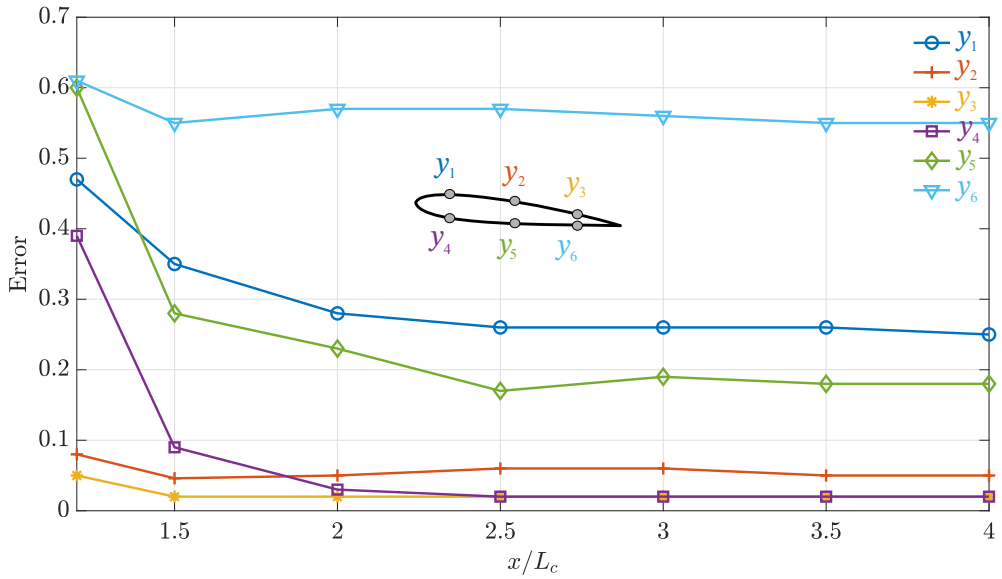

FIGURE 5.10: Estimation error for the linear system as a function of the target x/L_c location.

from the separation bubble over the airfoil. However, while y_4 faces challenges in capturing flow information from the bottom of the airfoil, it can still estimate the downstream targets ($x/L_c > 2$) as effectively as the sensors y_2 and y_3.

Finally, we consider an estimator for the extended regions (high-rank targets) using a limited number of sensors. It allows us to evaluate the impact on estimation accuracy across different regions. The estimation kernel in this context is expressed as

$$\begin{bmatrix} \hat{\boldsymbol{z}}_1 \\ \hat{\boldsymbol{z}}_2 \\ \vdots \\ \hat{\boldsymbol{z}}_{n_z} \end{bmatrix} = \begin{bmatrix} \hat{\boldsymbol{T}}_{z_1 y_1} & \hat{\boldsymbol{T}}_{z_1 y_2} & \dots & \hat{\boldsymbol{T}}_{z_1 n_y} \\ \hat{\boldsymbol{T}}_{z_2 y_1} & \hat{\boldsymbol{T}}_{z_2 y_2} & \dots & \hat{\boldsymbol{T}}_{z_2 n_y} \\ \vdots & \vdots & \ddots & \vdots \\ \hat{\boldsymbol{T}}_{z_{n_z} y_1} & \hat{\boldsymbol{T}}_{z_{n_z} y_2} & \dots & \hat{\boldsymbol{T}}_{z_{n_y} y_{n_y}} \end{bmatrix} \begin{bmatrix} \hat{\boldsymbol{y}}_1 \\ \hat{\boldsymbol{y}}_2 \\ \vdots \\ \hat{\boldsymbol{y}}_{n_y} \end{bmatrix} \tag{5.9}$$

where n_y and n_z represent the number of sensors and targets, respectively. Based on the optimal results from figure 5.10, we utilize the sensor located at y_3 on the suction surface. Figure 5.11 presents snapshots of the estimations in the extended target regions at different time steps. The time steps t_1, t_2, t_3 are selected to represent different phases, taking into account the dominant vortex shedding frequencies. In figure 5.12, the error field indicates that estimation near the trailing edge is less accurate due to complex flow behaviors, with performance deteriorating further as the target

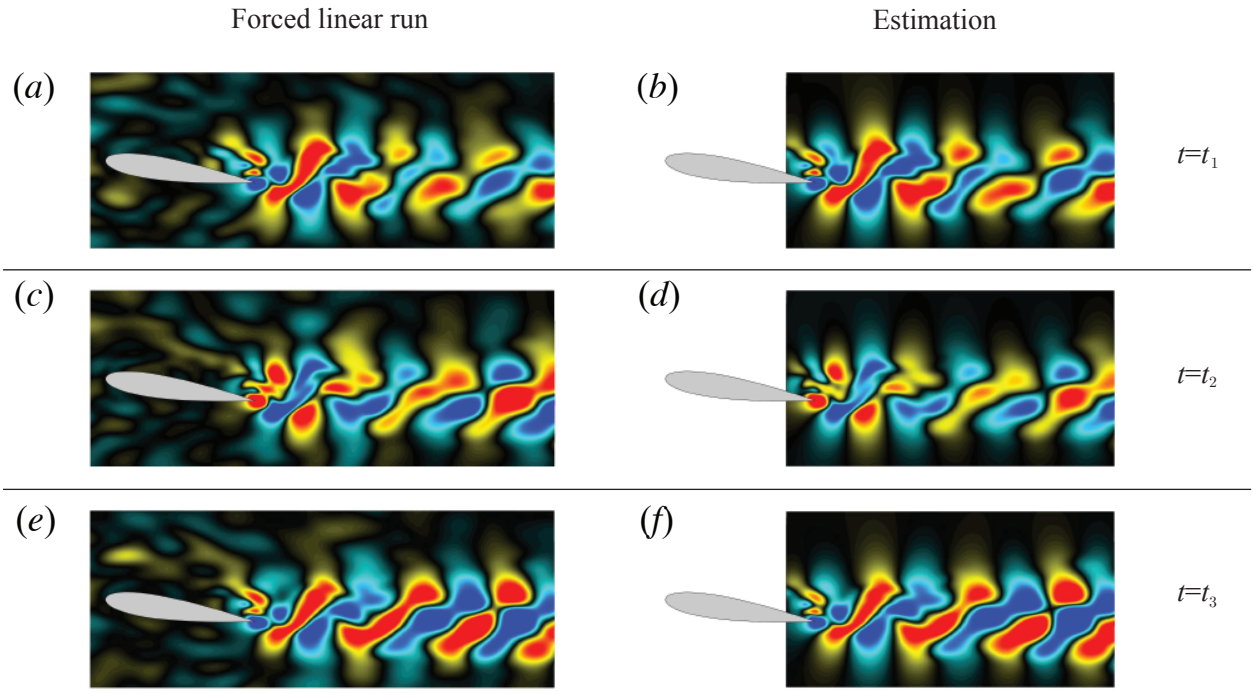

FIGURE 5.11: Estimation of the extended target region at three different time steps for the linear system, using the sensor located at y_3 at $x/L_c = 0.8$, as shown in figure 5.10.

moves downstream.

5.5.2 Nonlinear system

In the previous section, we confirmed that the resolvent-based kernels, derived from the resolvent operator, provide high accuracy for the linear system. These kernels accurately capture the linearized response to perturbations in this flow. We now shift our focus to the actual (nonlinear) system, where it is crucial to evaluate how well our approach accounts for the nonlinear interactions resulting from perturbations. To address this, we employ a data-driven approach, which is assumed to be equivalent to the operator-based method when considering colored forcing statistics. We demonstrate this approach in the estimation of the nonlinear system.

The flow is simulated using DNS with the same numerical setup described earlier in §5.2.2. We begin by performing the estimation on the clean system and then proceed to introduce noisy inflow upstream (external disturbance), as illustrated in figures 5.13(*a*) and (*b*). Since the estimator is defined in terms of perturbations relative to the mean, the mean is removed from the sensor

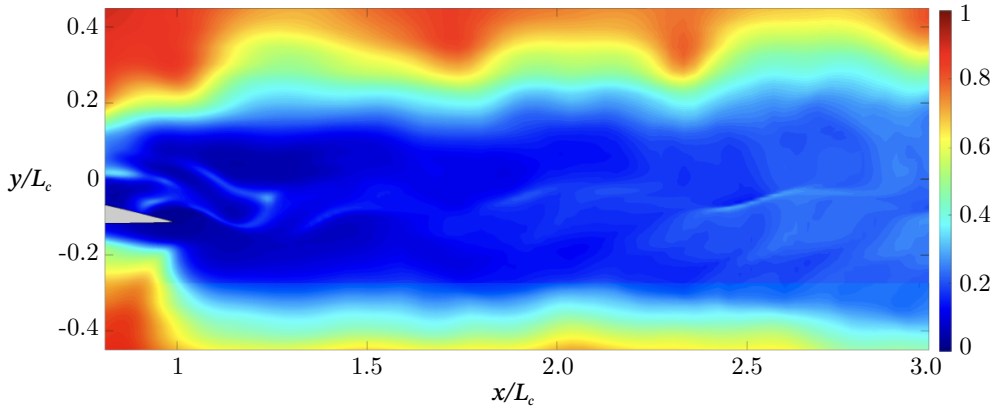

FIGURE 5.12: Estimation error field in the extended target regions for the linear system using a single sensor at y_3.

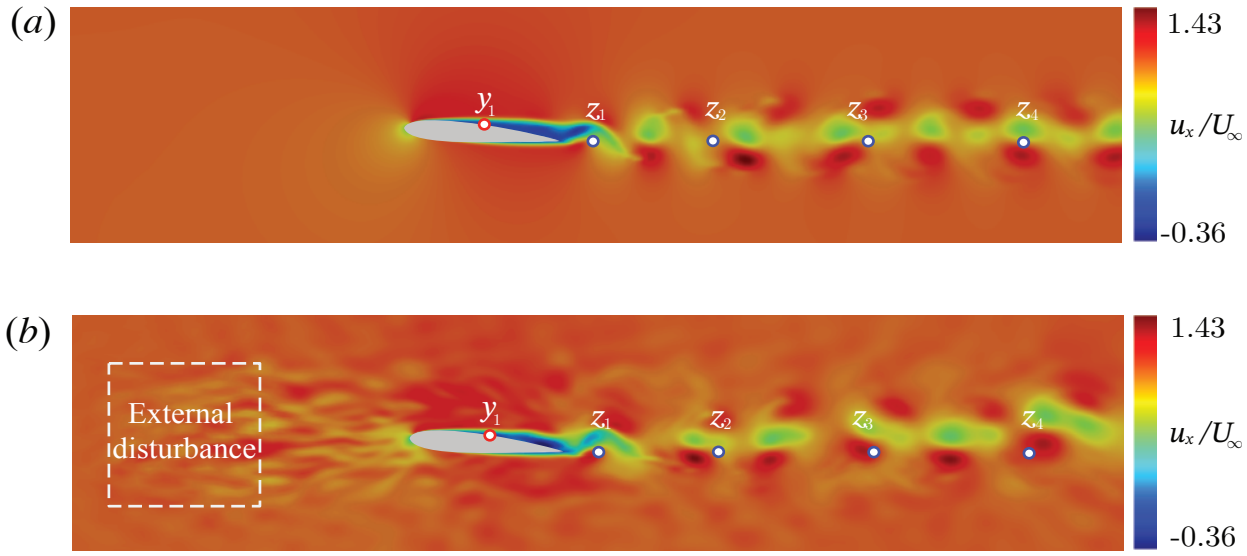

FIGURE 5.13: Instantaneous u_x field for (a) the clean and (b) the noisy inflow upstream systems (DNS), showing the locations of sensors and targets. The external disturbance area is defined as $x/L_c \in [-2,-1]$ and $y/L_c \in [-0.5, 0.5]$.

readings before convolution with the estimation kernels.

5.5.2.1 Nonlinear response to the external forcing

The nonlinear terms of the Navier-Stokes equations are crucial in describing the behavior of laminar airfoil flow. The convective terms capture the changes in velocity as the fluid flows over the airfoil surfaces [Ashley and Landahl, 1985]. These terms contribute to the velocity gradient of the flow and the interaction between the two velocity components, u_x and u_y. External forcing induces nonlinear interactions, which we assume to represent turbulence, consistent with our previous work [Martini et al., 2022]. The linear properties of the system, derived from the mean flow, diminish when the imposed external disturbance is relatively larger than the amplitude of fluctuations around the mean flow. The nonlinear system imposed by external forcing can be expressed as

$$\frac{\partial \boldsymbol{q}}{\partial t} = \mathcal{F}(\boldsymbol{q}) + \boldsymbol{B}_{f,ext}\boldsymbol{f}_{ext}. \tag{5.10}$$

The external forcing $\boldsymbol{f}_{ext}(x,t)$ is a random vector generated in both space and time within the range $[-1,1] \times W$, where W controls the variance of the random vector, adjusting the noise level of the freestream. When $W = 1$, this results in a disruption of the vortex shedding frequency at the point $[x/Lc, y/L_c] = [2.11, -0.11]$. Forcing CSD matrix can be written

$$\hat{\boldsymbol{F}}_{ext} \equiv \boldsymbol{S}_{ff}(\boldsymbol{x}, \boldsymbol{x'}, \omega) = \mathbb{E}\{\hat{f}(x,\omega)\hat{f}(x',\omega)^{\dagger}\}. \tag{5.11}$$

When the forcing is uncorrelated in both space and time, the forcing CSD matrix reduces to white noise in time, expressed as

$$\hat{\boldsymbol{F}}_{ext} = \int_0^{\infty} W^2\delta(x-x')\delta(t-t')e^{-i\omega\tau}d\tau \tag{5.12}$$

$$= W^2\delta(x-x') \tag{5.13}$$

Note that $\hat{\boldsymbol{F}}_{ext}$ for the nonlinear system is not zero-mean due to the nonlinear interactions that evolve in space and time for the nonlinear system. In contrast, the linear system models the nonlinear terms as white noise (an identity matrix) [McKeon and Sharma, 2010].

We analyze the power spectral density across varying noise levels of W, focusing on the impact on

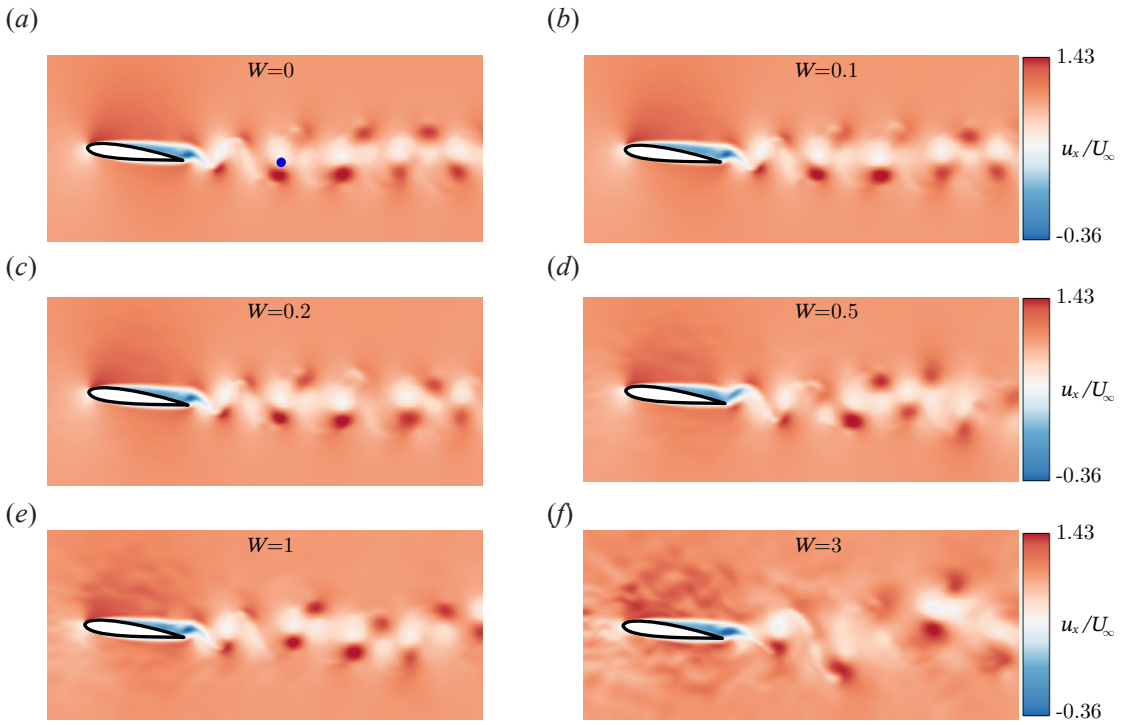

FIGURE 5.14: Instantaneous streamwise velocity fields under varying levels of noisy freestream inflow intensity: (*a*) no noise, (*b*) $W = 0.1$, (*c*) $W = 0.2$, (*d*) $W = 0.5$, (*e*) $W = 1$, and (*f*) $W = 3$. The blue dot in (*a*) indicates the location of the PSD analysis.

vortex shedding frequencies. In this study, the noisy nonlinear systems are defined as DNS systems with upstream freestream inflow at noise levels $W > 0$. The snapshots in figure 5.14 demonstrate that while vortex shedding persists at all noise levels, the temporal periodicity in the streamwise direction is disrupted. Figure 5.15 confirms that vortex shedding frequencies ($St_\alpha \approx 0.17 \times n$ with n=1,2,3) are suppressed at $W > 1$, with $W > 5$ resulting in numerical instability. We select $W = 1$ as the noise level for our estimation and control studies.

We explore how much the nonlinearity interaction is developed from the external forcing $\boldsymbol{F}_{ext}$ for the laminar airfoil flow with the intensity of the external disturbance. If the intensity of the external forcing is sufficiently small, (2.33) is approximately equivalent to (2.34). Figure 5.16 illustrates the instantaneous streamwise velocity fluctuations u'_x field with $W = [0, 1, 3]$ in (*a*), (*c*), and (*e*), and the corresponding the same time step's nonlinear terms in (*b*), (*d*), and (*f*). The nonlinear terms are extracted using our application §3.2.2.4. The clean system ($W = 0$) shown in figure 5.16(*a*) and (*b*) and the noisy systems ($W = [1, 3]$) depicted in figures 5.16(*c*) - (*f*)

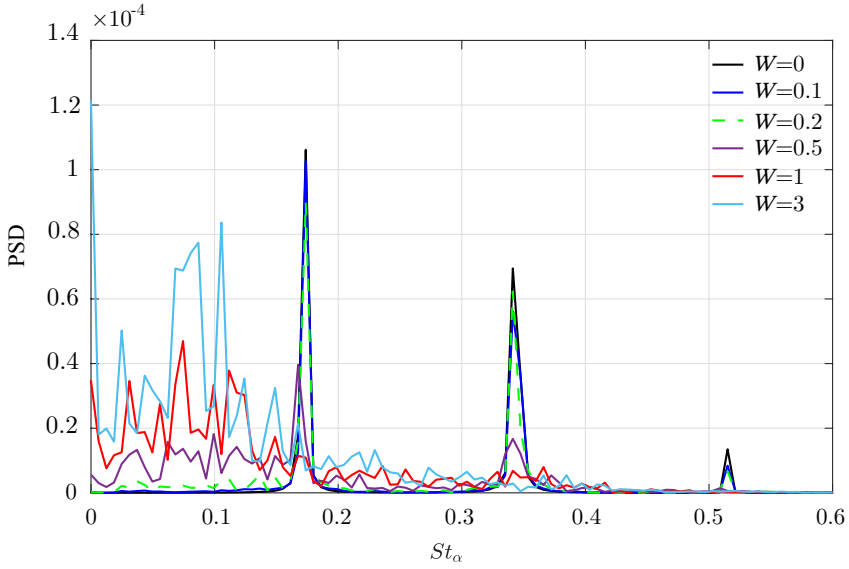

FIGURE 5.15: Power spectral density of the nonlinear system in terms of the noise level W at the point $[x/L_c, y/L_c] = [2.11, -0.11]$ in figure 5.14.

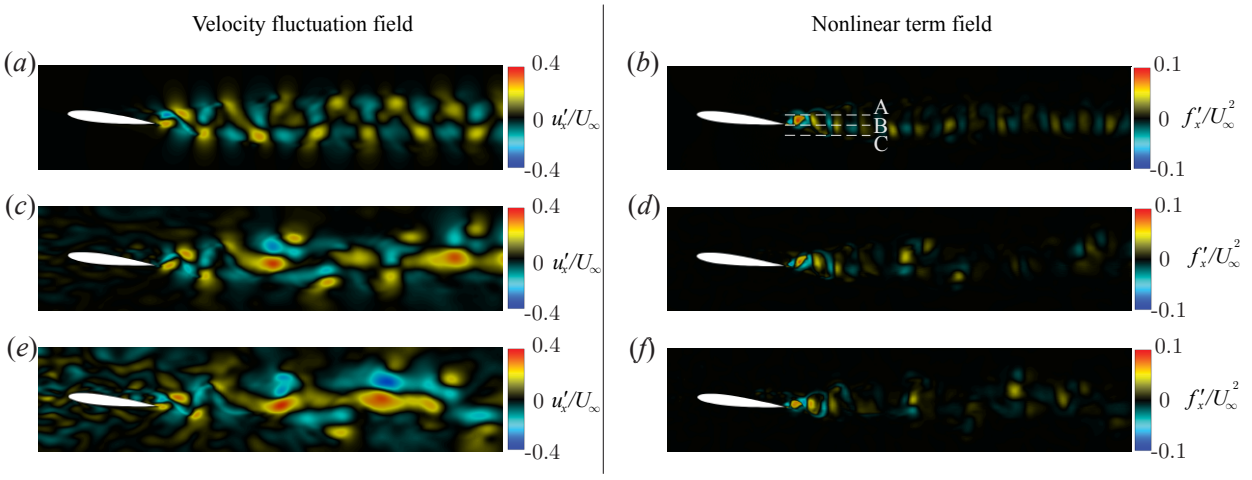

FIGURE 5.16: Instantaneous velocity fluctuation field $u_x^{'}$ ($(a)(c)(e)$) and the corresponding nonlinear terms f_x' ($(b)(d)(f)$) computed from 3.2.2.4. (a), (b): no forcing ($W = 0$); (c), (d): $W = 1$; and (e), (f): $W = 3$.

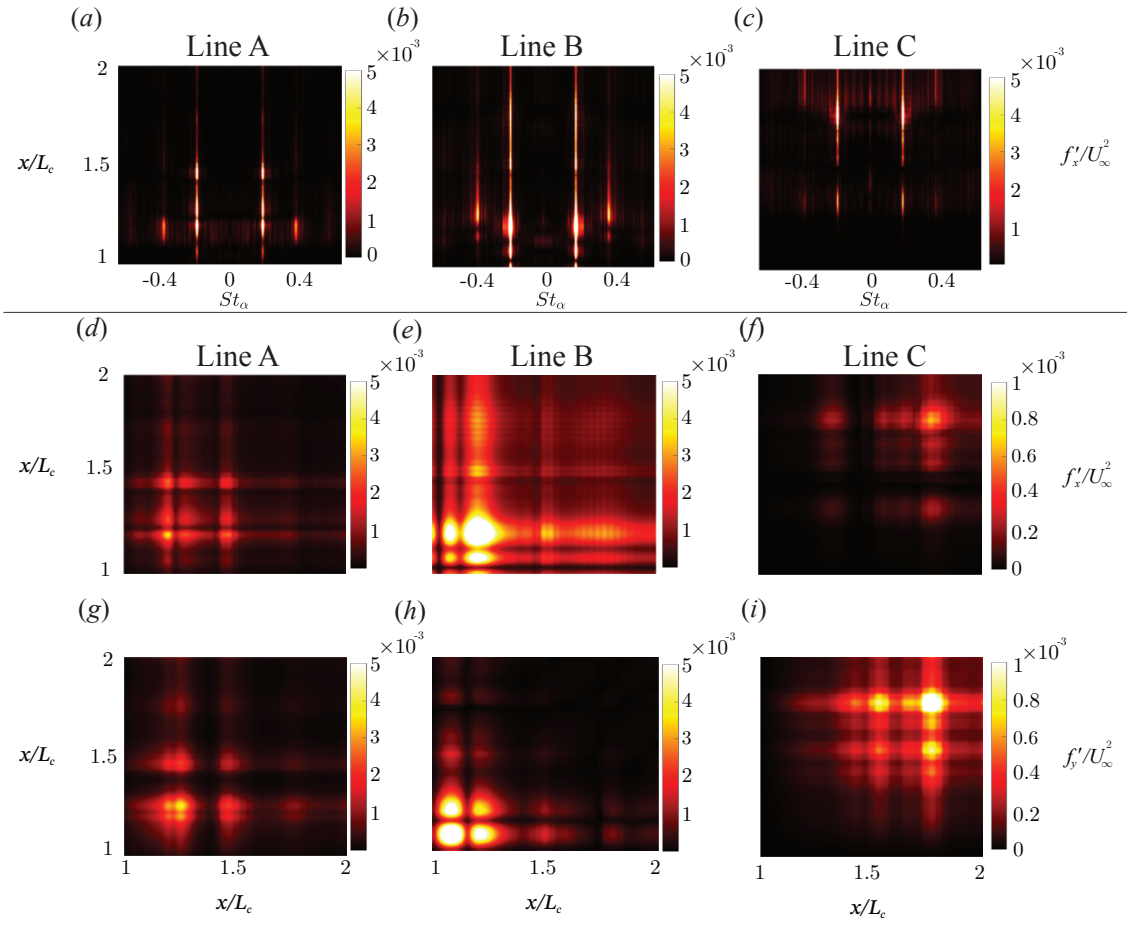

FIGURE 5.17: Power spectral density of the nonlinear terms along: (*a*) Line A, (*b*) Line B, and (*c*) Line C in figure 5.16(*b*). Panels (*d*)–(*f*) present the cross-spectral density (CSD) of f'_x, and panels (*g*)–(*i*) show the CSD of f'_y for Lines A, B, and C, respectively.

demonstrate that nonlinear terms predominantly exist in the wake near the trailing edge and in regions where the gradients of the velocity component are significant.

Figure 5.17 presents the PSDs and the CSDs at vortex shedding frequency ($St_\alpha = 0.17$) of the nonlinear terms along lines A ($y/L_c = 0.01$), B ($y/L_c = -0.11$), and C ($y/L_c = -0.21$) behind the airfoil, shown in figure 5.16(b). In figure 5.17(a)–(c), the nonlinear terms exhibit significant energy at the vortex-shedding frequencies. Strong energy is observed near the trailing edge ($x/L_c < 1.5$) along the top (A) and middle (B) lines, as shown in figures 5.17(a) and (b), while the bottom line (C) shows energetic regions further downstream, as seen in figure 5.17(c). This pattern arises because vortex shedding primarily originates from the separated flow on the suction surface, located slightly above the trailing edge. In figures 5.17(d)–(i), the nonlinear terms for both velocity components exhibit statistically significant strength in the region $1 < x/L_c < 1.2$ along line B, consistent with the observed deterioration in the estimation performance of the linear system. Examining the CSDs tensors $\hat{\boldsymbol{F}}_{nl}$ is meaningful, as they are closely associated with coherent structures [Towne et al., 2018]. By constructing the forcing CSD matrix $\hat{\boldsymbol{F}}_{nl}$, we can account for the nonlinear effects of the flow in the estimation kernels, potentially improving estimation accuracy in turbulent flows.

5.5.2.2 Building estimation kernels with colored-forcing statistics

In §5.5.1.1, we assumed the forcing CSD matrix $\hat{\boldsymbol{F}}_{nl}$ to be white noise (an identity matrix), resulting in kernels equivalent to the Kalman filter. To enhance the accuracy of the estimation kernels, we incorporate colored forcing statistics F_{nl}, which can be obtained in §3.2.2.4. Once the nonlinear terms $\hat{\boldsymbol{f}}_{nl}$, such as those shown in figure 5.17, are available, we compute $\boldsymbol{R}_{yf}\hat{\boldsymbol{F}}_{nl}\hat{\boldsymbol{F}}^{\dagger}_{yf}$ and $\boldsymbol{R}_{zf}\hat{\boldsymbol{F}}_{nl}\hat{\boldsymbol{F}}^{\dagger}_{yf}$ to incorporate $\hat{\boldsymbol{F}}_{nl}$ during the two-stage run outlined in 2.4.1.2. These estimation kernels are equivalent to data-driven kernels when statistical noise is negligible.

Alternately, we implement the data-driven approach [Martini et al., 2022] to obtain the estimation kernels with the colored-forcing statistics [Zare et al., 2017, Towne et al., 2020]. These kernels can statistically account for the flow's nonlinearity [Martini et al., 2022]. The data is directly collected from DNS, with the flow imposed both with and without external forcing. Welch's method [Welch, 1967] is employed to obtain the CSD tensor required for constructing the estimation kernels. The data is divided into 64 time windows of length $tU_\infty/L_c = 5$, with 50% overlap. All other parameters for building kernels and Wiener-Hopf factorization are consistent with those used in

Algorithm 3 Compute $R_{y,f}\hat{F}R_{y,f}^{\dagger}$ and $R_{z,f}\hat{F}R_{y,f}^{\dagger}$

function TwoStageRun
  for each $t \in$ all time steps **do** ▷ Start adjoint run
    $q_i \leftarrow$ adjoint solver with impulse forcing
    $s_i \leftarrow \boldsymbol{B}_f^{\dagger} q_i$
    $\hat{s}_i(t) \leftarrow$ StreamingFourierTransform(s_i)
  for each $iw \in$ all freq. **do** ▷ Insert $\hat{\boldsymbol{F}}$
    for each $i_{blk} \in n_{blk}$ **do**
      $\hat{\boldsymbol{f}}_{nl}^{\dagger}\hat{\boldsymbol{s}}_i(iw, n_{nl})$+=VecMult$(\hat{\boldsymbol{f}}_{nl}(iw, n_{nl}, i_{blk})^{\dagger}, \hat{\boldsymbol{s}}_i(iw, n_{nl}))$
      SUM$[\hat{F}R_{y,f}^{\dagger}(n_{nl}, iw)]$+=VecMult$(\hat{\boldsymbol{f}}_{nl}, \hat{\boldsymbol{f}}_{nl}^{\dagger}\hat{\boldsymbol{s}}_i(iw, n_{nl}))$
    $\hat{F}R_{y,f}^{\dagger}(n_{nl}, iw) \leftarrow$ SUM$[\hat{F}R_{y,f}^{\dagger}(n_{nl}, iw)]/n_{blk}$
  $r(t) \leftarrow$ ifft$(\hat{F}R_{y,f}^{\dagger}(n_{nl}, iw))$
  for each $t \in$ all time steps **do** ▷ Start direct run
    $q_i \leftarrow$ direct solver with $r(t)$
    $y_i(t) \leftarrow \boldsymbol{C}_y q_i$
    $z_i(t) \leftarrow \boldsymbol{C}_z q_i$
  $R_{y,f}\hat{F}R_{y,f}^{\dagger} \leftarrow$ fft(y_i)
  $R_{z,f}\hat{F}R_{y,f}^{\dagger} \leftarrow$ fft(z_i)

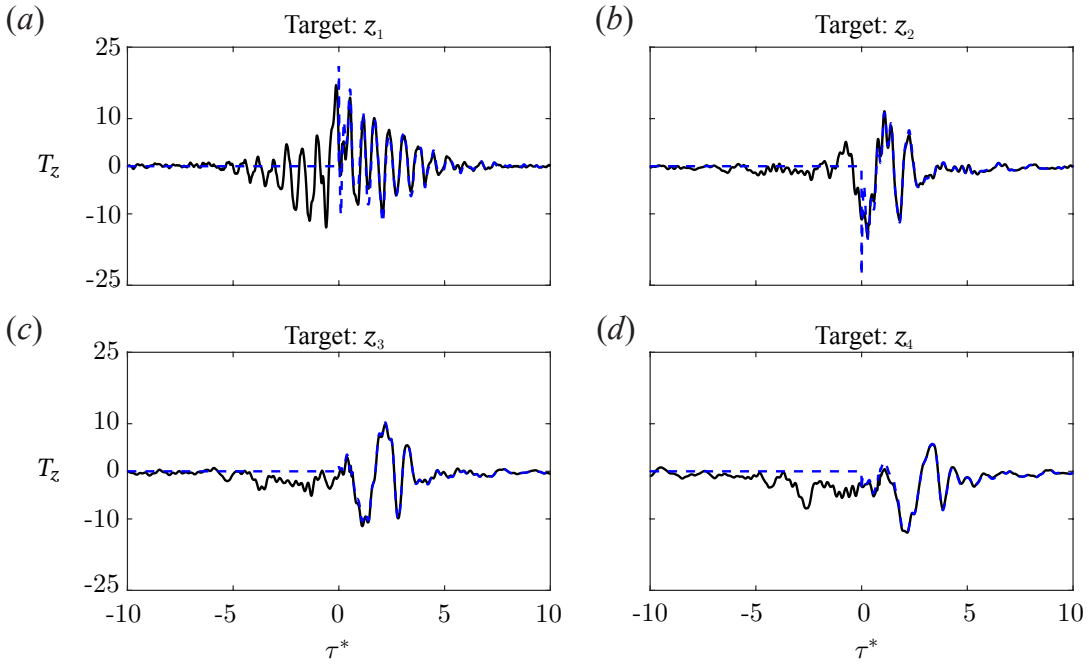

FIGURE 5.18: Data-driven estimation kernels: non-causal (black solid line) and causal (blue dashed line) kernels between (*a*) y_1 $[x/L_c = 0.5]$ and z_1 $[x/L_c = 1.2]$, (*b*) z_2 $[x/L_c = 2.0]$, (*c*) z_3 $[x/L_c = 3.0]$, and (*d*) z_4 $[x/L_c = 4.0]$.

the operator-based approach.

Finally, we show the estimation kernels incorporating colored forcing statistics in figure 5.18. This is the same sensor and target configuration as in the estimation kernel with a white noise, i.e., between the sensor y_1 $[x/L_c = 0.5]$ and the targets z_1, z_2, z_3, and z_4 $[x/L_c = 1.2, 2.0, 3.0, 4.0]$, and the locations are shown in figure 5.13. The kernels for the clean system are not shown here because the travel information is too vague to be analyzed. However, these kernels figure 5.18 shows the distinct peaks and the effects of nonlinear interactions. As discussed in §5.5.2.1, there is a higher degree of nonlinear interaction near the trailing edge, as shown in figures 5.17(d). We learned that the regions near the trailing edge are complex. This behavior is well shown in the kernel of figure 5.18(a). Although it is necessary to study more about the correlation between nonlinearity and causal impact, this is beyond this thesis. If the target is at the region where the nonlinear interactions are significant, the estimation kernel with a colored forcing contains the peak points located in the non-causal region ($\tau^* < 0$), making it challenging to accurately predict target fluctuations for non-causal kernels. However, this negative impact can be somehow mitigated by applying the Wiener-Hopf method, which optimally enforces causality in the kernel. In the further downstream wake regions in figure 5.18(b),(c), and (d), the flow behaves more simply in terms of the nonlinear interaction, resulting in distinct peak points in the estimation kernels, which clarify the noisy travel time. The difference between the causal and non-causal kernels is trivial as the target is set further downstream in the wake, where the natural causality of the flow (convective flow) dominates. This trend is similar to the backward-facing step flow case, reported by Martini et al. [2022].

5.5.2.3 Sensor placement for estimation

We investigate effective sensor placement for causal resolvent-based estimation in laminar flow using two strategies. First, we assess the estimation errors for a single sensor based on its location on the surface relative to the target of interest. Given the two-dimensional and realistic surface of the airfoil, the available locations are limited, making this approach computationally feasible. We consider the estimation errors for both the clean and noisy nonlinear systems. Second, the mean streamline provides valuable insights into predicting the traveling paths of perturbations. This approach is particularly useful because it helps narrow down potential sensor locations, offering

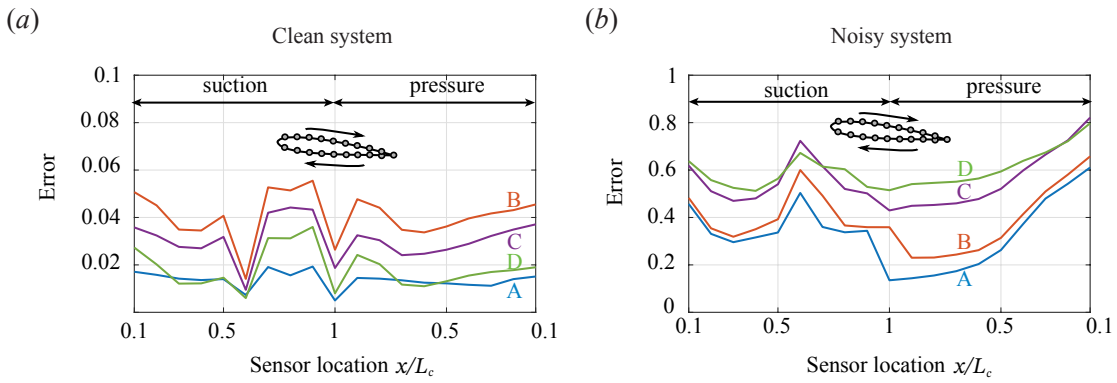

FIGURE 5.19: Averaged estimation errors for the lines A($x/L_c = 1.2$), B($x/L_c = 1.5$), C($x/L_c = 2.0$), and D($x/L_c = 2.5$) based on sensor locations on the airfoil surfaces. The left panel represents the clean system, while the right panel shows the noisy system.

guidance when the effective sensor placement is initially unclear.

Figures 5.19(a) (clean system) and (b) (noisy system) illustrate the averaged estimation errors for the five targets along lines A, B, C, and D when sensors are placed on the airfoil surfaces, which are realistic locations. The errors are significantly lower in figure 5.19(a) compared to figure 5.19(b). Imposing external forcing amplifies the velocity energy, leading to sustained high-energy fluctuations in the wake, as illustrated in figure 5.16(c). This effect generally deteriorates the accuracy of the estimation. The upstream-traveling perturbations from the external forcing (in the noisy system) complicate the estimation as the distance between the sensor and the target increases, due to spatial nonlinearity (estimation error: $D > C > B > A$ in figure 5.19(b)). In contrast, for the clean system, the estimation error is largest at position B.

Interestingly, in figure 5.19(a), sensors positioned within the recirculation region ($0.6 < x/L_c < 1$), which can be detected with the purple solid line in figure 5.20(a), which also verified in work [Marquet et al., 2022], show reduced accuracy. However, this effect is not as evident in figure 5.19(b). This indicates that the traveling perturbations from the noisy freestream have a more significant impact than the effects of the separated flow for the estimation of the noisy nonlinear system. Among the sensors on the suction surface for the noisy nonlinear system in figure 5.19(b), those positioned before the separation bubble ($0.2 < x/L_c < 0.5$) and near the trailing edge ($0.8 < x/L_c < 1.0$) effectively predict the wake dynamics. Notably, rear sensors on the pressure surface show high estimation accuracy.

Next, we exame the five mean streamlines (SL1, SL2, SL3, SL4, and SL5), each passing each five targets (z_1, z_2, z_3, z_4, and z_5), as illustrated in figure 5.20(a). Figure 5.20(b) shows that within a given streamline, the estimation error increases as the distance between the sensor (circle, square, triangle) and the target at $x/L_c = 2.0$ increases. When the flow behavior is straightforward between two points, estimation accuracy is high, as observed with the streamlines for z_4 and z_5. However, z_3 proves to be the most challenging target to estimate. Figure 5.20(c) displays the estimation errors for target z_3 based on sensors located on different streamlines. These results indicate that sensors placed on the same streamline as the estimation at z_3 yield a better result. Based on this finding, we justify that estimation accuracy for targets along the trailing edge, particularly z_3, can be improved by positioning sensors on the pressure side of the airfoil. We empirically evaluate six sensor placement candidates based on estimation error and streamline strategy. Ultimately, we selected candidate 6, as shown in Table 5.3.

	Placement candidates	Errors	
		Clean system	Noisy system
1	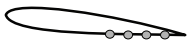	0.04	0.54
2	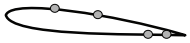	0.03	0.40
3	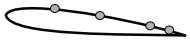	0.02	0.36
4		0.01	0.35
5	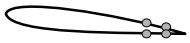	0.001	0.33
6	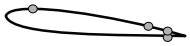	0.001	0.33

TABLE 5.3: Sensor placement candidates for causal resolvent-based estimation

5.5.2.4 Estimation results of the nonlinear system

We present estimation results for nonlinear systems with clean and noisy freestream inflows similar to those imposed on linear systems. These disturbances induce chaotic flow behavior resembling turbulence. Our estimator effectively accounts for the nonlinearity of the flow in

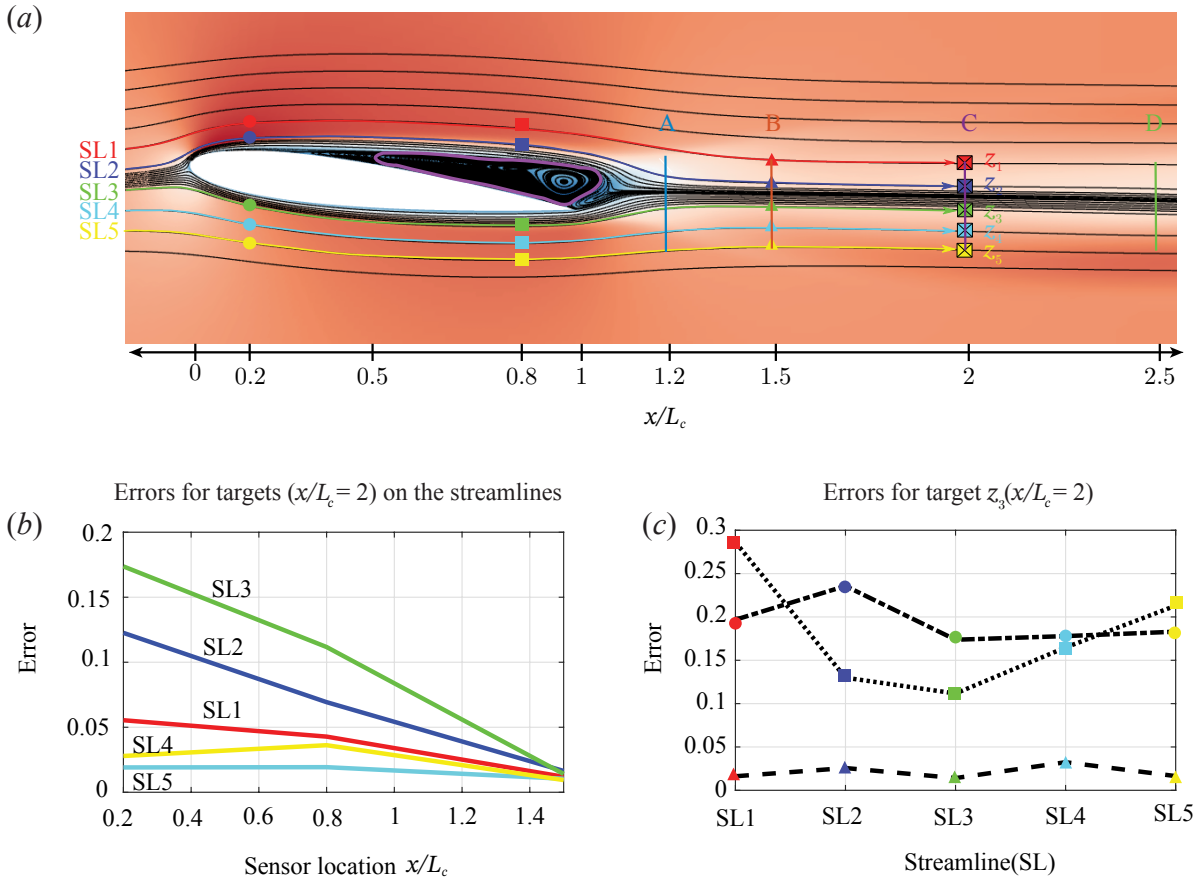

FIGURE 5.20: Sensors and targets placement using the streamlines, shown on the mean streamwise velocity field.

a statistical sense by incorporating the second-order statistics of the nonlinear terms into the estimation kernels [Martini et al., 2020]. These kernels offer two significant advantages. First, they enhance estimation accuracy for nonlinear systems by more accurately accounting for the evolving nonlinearity in space and time. This enhancement is particularly remarkable for systems with noisy freestream inflows. Second, they can potentially improve the prediction of other velocity components, such as cross-streamwise velocity in a 2D system. This improvement is due to including convective nonlinear terms in the estimation kernels, which helps statistically capture interactions between different velocity components. Our focus is on predicting vortex shedding, which involves gradients of both velocity components and is strongly developed in space and time when noisy freestreams pass through the airfoil, as shown in 5.16. Therefore, we present the estimation results for both the streamwise and cross-streamwise velocity components in the nonlinear system with both clean and noisy ($W = 1$) freestreams.

Figures 5.21 and 5.22 present the causal resolvent estimation of u'_x and u'_y, respectively, comparing with other methods and the true reading (DNS) with the clean (left column) and noisy (right column) freestream inflows at the target points ($x/L_c = 1.2, 2.0, 3.0, 4.0$) along the trailing edge. The four sensors (candidate 6) are used based on our investigation in figure 5.3. The clean DNS system is well estimated using the causal resolvent-based approaches. The Kalman filter captures the dominant frequency's high-energy parts effectively but lacks spatial and temporal detail due to the assumption of the nonlinear terms as white noise. This impact is bigger for the noisy system because the linearized Navier-Stokes operator mostly captures within the dominant frequencies. The target near trailing edge, where nonlinearity is strong under the investigation in figure 5.17 has poor estimation using Kalman filter, shown in 5.21(b), while the poor estimation using TNC approach is due to the negative causal impact (peaks of the kernels are primarily located on the non-causal part $\tau^* > 0$). However, the truncated non-causal estimation can account for the nonlinearity, which is acceptable when the causality is not big issue for the target location, e.g., in the case of 5.21(f) and (h). In figure 5.22, we can see the better accuracy of estimation. Within laminar flow over the airfoil with the noisy freestream inflows, the cross-streamwise velocity field is more simple than the streamwise velocity field by preserving the dominant vortex shedding frequency of the cross-streamwise velocity even if the noisy level is strong.

Figure 5.23 summarizes the errors presented in figures 5.21 and 5.22. Notably, the causal

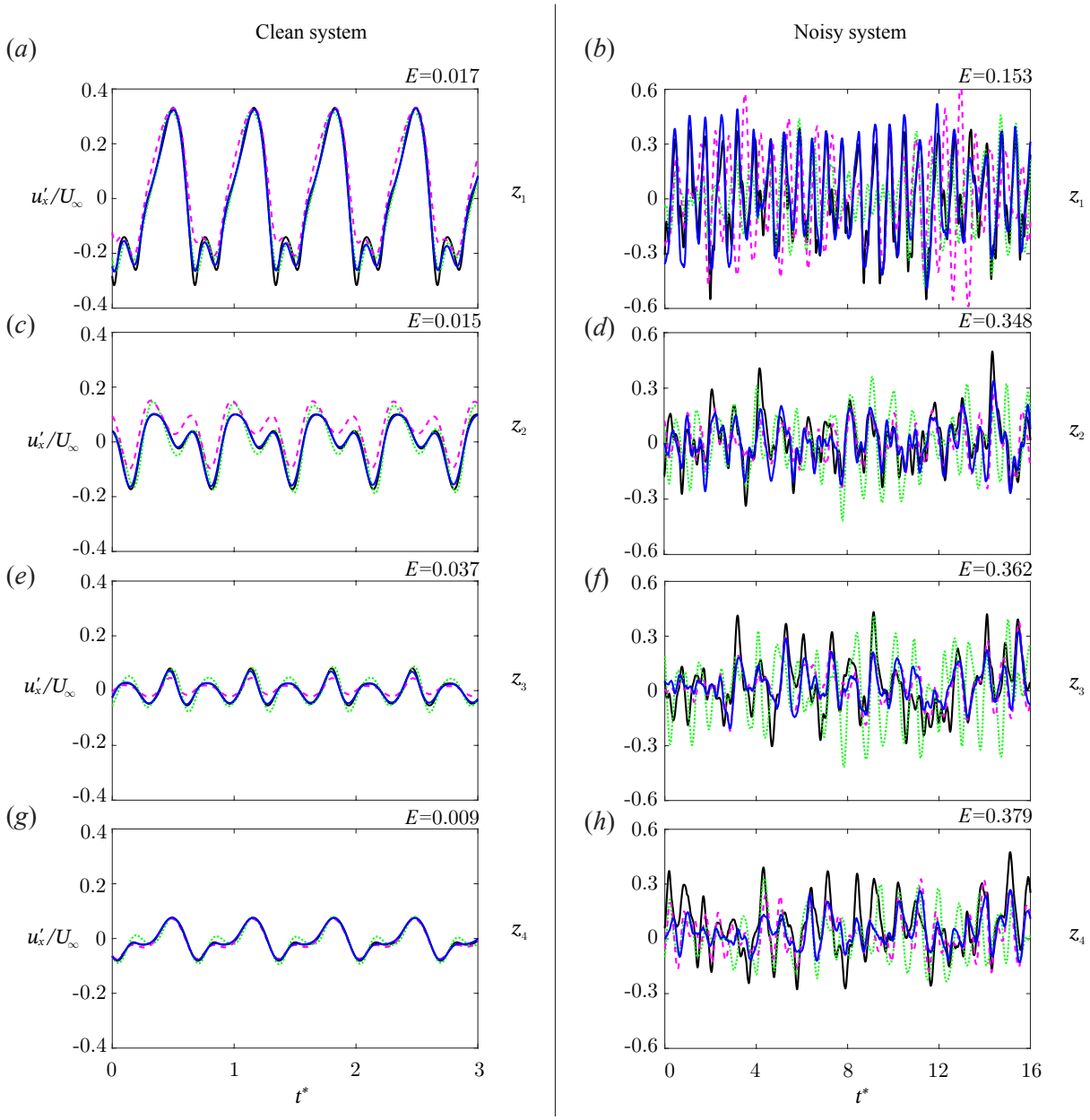

FIGURE 5.21: Estimation of u_x' for the nonlinear system with the clean (left column) and noisy freestream (right column) inflows. The black (solid) line shows the true DNS, while the other lines represent different methods: green (dashed) for Kalman filter, magenta (dashed) for truncated non-causal estimation, and blue (solid) for causal estimation (our method). The target locations are: (*a*), (*b*) at $[z_1 = x/L_c, y/L_c]$ = [1.2, -0.11]; (*c*), (*d*) at [2.0, -0.11]; (*e*), (*f*) at [3.0, -0.11]; and (*g*), (*h*) at [4.0, -0.11], as shown in figure 5.13. The estimation errors for the causal method are noted in the top right corner of each panel.

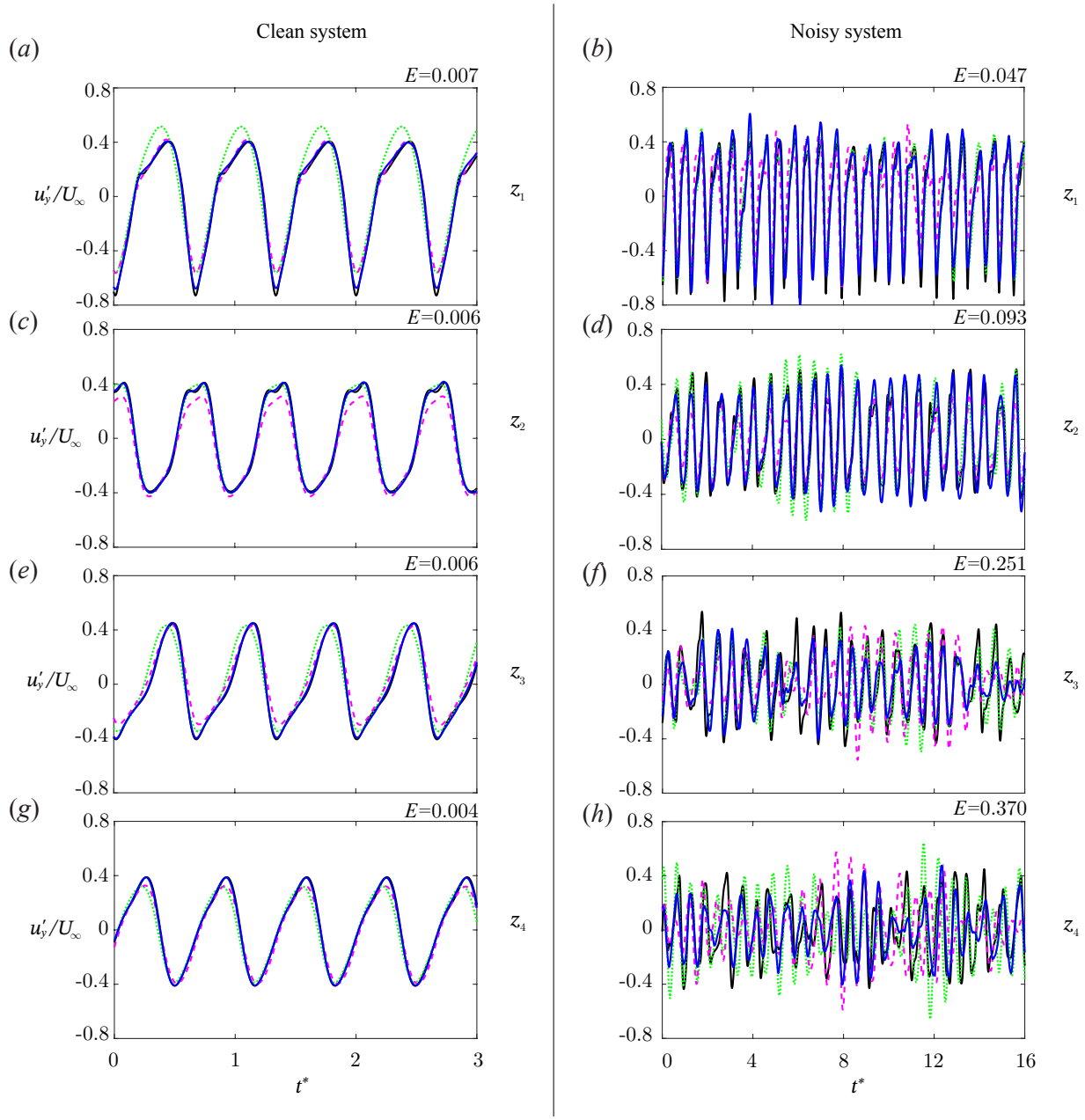

FIGURE 5.22: Estimation of u_y' for the nonlinear system with the clean (left column) and noisy freestream (right column) inflows. The black (solid) line shows the true DNS, while the other lines represent different methods: green (dashed) for Kalman filter, magenta (dashed) for truncated non-causal estimation, and blue (solid) for causal estimation (our method). The target locations are: (*a*), (*b*) at $[z_1 = x/L_c, y/L_c]$ = [1.2, -0.11]; (*c*), (*d*) at [2.0, -0.11]; (*e*), (*f*) at [3.0, -0.11]; and (*g*), (*h*) at [4.0, -0.11], as shown in figure 5.13. The estimation errors for the causal method are noted in the top right corner of each panel.

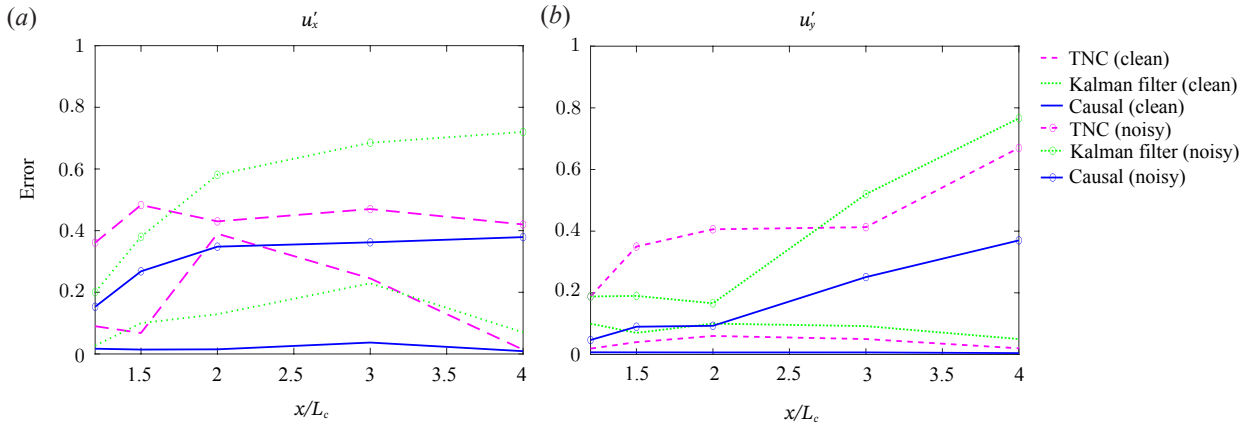

FIGURE 5.23: Estimation errors for the nonlinear systems: (*a*) u_x' and (*b*) u_y'. Circular markers (∘) indicate the system with noisy freestream, while solid lines without markers correspond to the system with clean freestream. Blue lines represent causal resolvent-based estimation, while magenta and green lines denote truncated non-causal estimation using colored forcing and a Kalman filter (white noise), respectively.

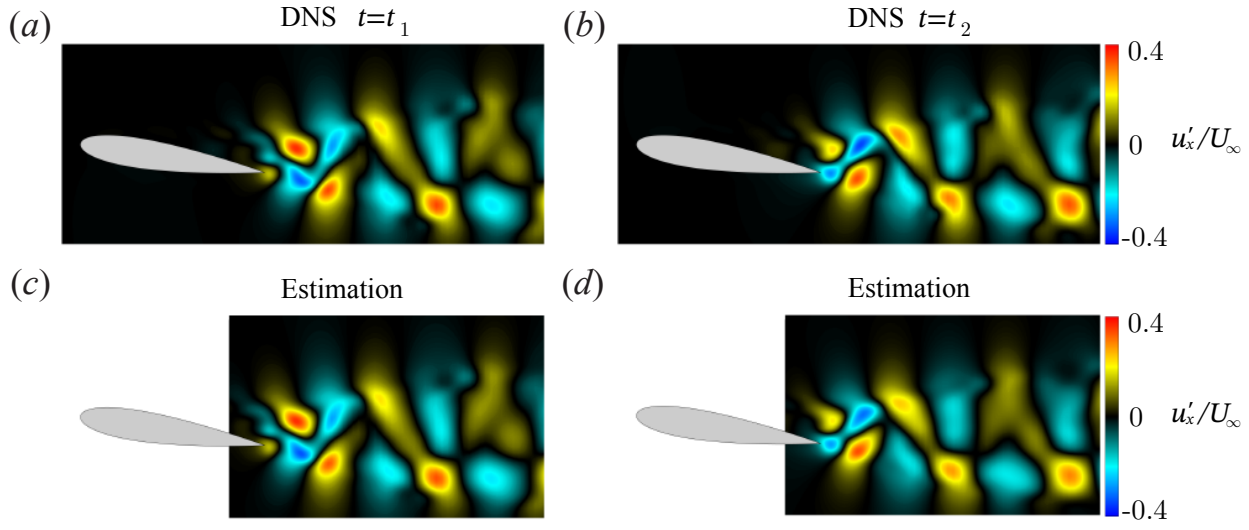

FIGURE 5.24: Estimation of the wake region for u_x' at two different time steps in the nonlinear system without noise: top row shows DNS results, and the bottom row shows results from causal resolvent-based estimation.

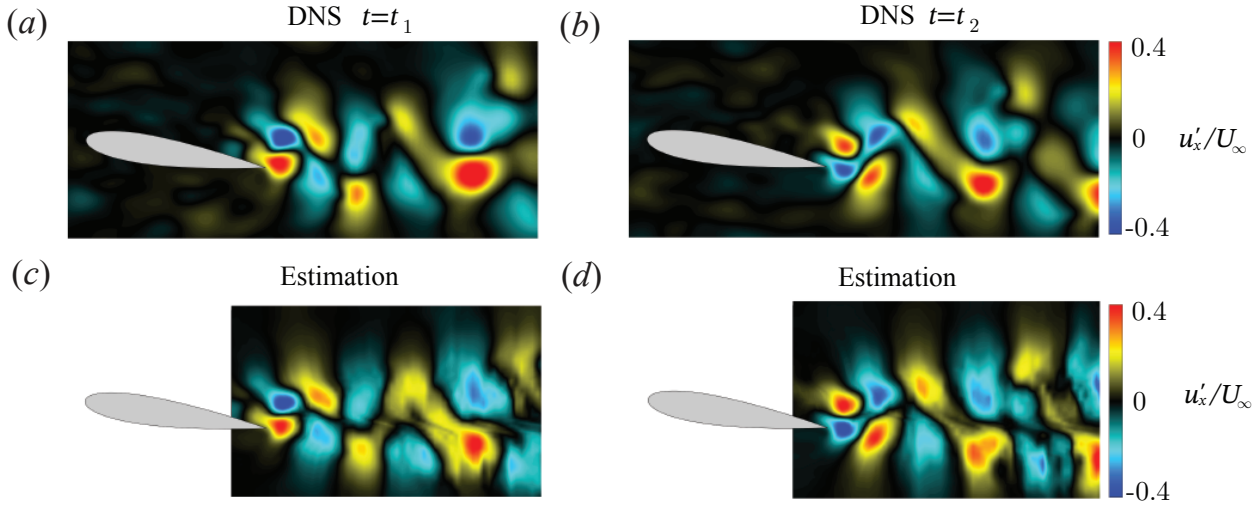

FIGURE 5.25: Estimation of the wake region for u_x' at two different time steps in the nonlinear system with noisy freestream: top row shows DNS results, and the bottom row shows results from causal resolvent-based estimation.

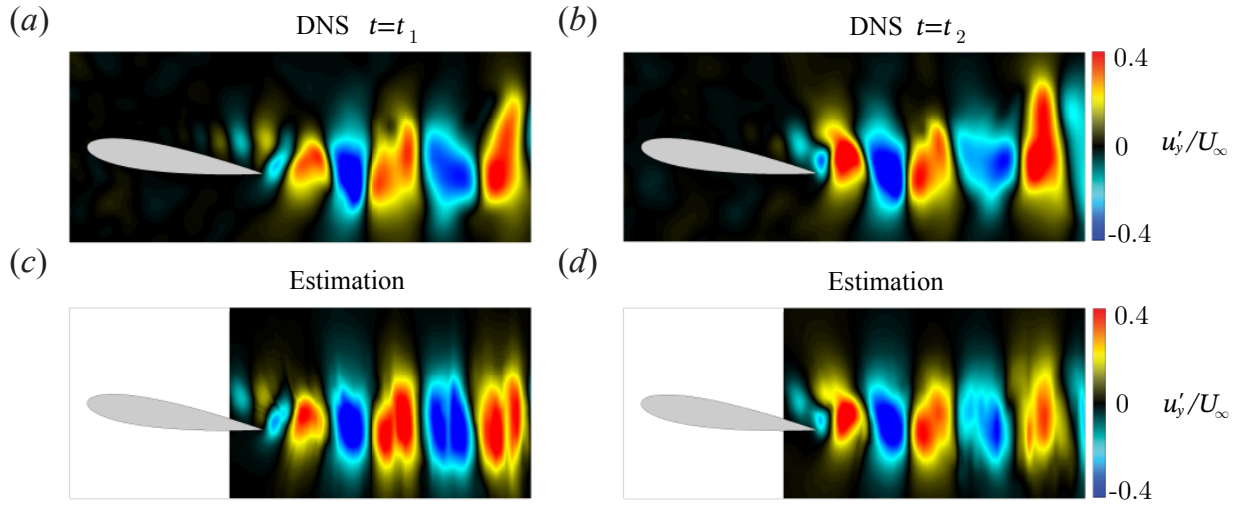

FIGURE 5.26: Estimation of the wake region for u_y' at two different time steps in the nonlinear system with noisy freestream: top row shows DNS results, and the bottom row shows results from causal resolvent-based estimation.

resolvent-based approach estimates the velocity fluctuations u'_x and u'_y in the clean system with near-perfect accuracy. In the noisy system, the estimation accuracy decreases as the distance between the sensor and the target increases downstream. However, for u_y, the accuracy continues to decline as the target moves further downstream. The causal resolvent-based approach enhances estimation accuracy near the trailing edge, even though the negative causal impact and the effects of nonlinearity are most significant.

Using the same four shear stress sensors as suggested in table 5.3, we estimate the velocity fluctuations u'_x and u'_y across the entire wake region in both clean and noisy nonlinear systems. The sensors are positioned near the trailing edge, allowing us to estimate the region behind $x/L_c > 0.8$. We present two snapshots of the estimation, selected to represent different phases based on the vortex shedding frequency. For the clean system, our estimation results for u'_x, as shown in figure 5.24, are highly accurate. In the noisy nonlinear system, however, the estimation accuracy decreases due to perturbations that disrupt the vortex structure. Despite the challenges posed by chaotic fluctuations in space and time within the wake, the causal approach effectively estimates the wake flow, as demonstrated in figures 5.25 and 5.26.

5.6 Resolvent-based control

We employ a closed-loop control strategy to suppress unsteady states around the mean flow in the wake. This control approach, known as the wave-cancelling method, has been demonstrated in previous studies [Sasaki et al., 2018a,b, Morra et al., 2020, Martini et al., 2022, Audiffred et al., 2023]. By leveraging the estimated flow states, implicitly included in the linear controller obtained in the frequency domain, we adjust the actuation force to cancel the target values. In this thesis, we investigate the effectiveness of this approach in suppressing velocity fluctuations and returning the flow to its mean state. We examine both linear and nonlinear systems with noisy freestream inflow at $W = 1$, as defined in §5.5.2.1. We then compare the control performance of the truncated non-causal control with the optimal causal control derived using the Wiener-Hopf method.

5.6.1 Control set-up

Many feedback control methodologies [Flinois and Morgans, 2016, Déda et al., 2023, Lin and Tsai, 2024] rely on sensors located behind the object, e.g., in the wake, but a configuration is impractical in reality. Our approach implicitly facilitates estimating wake flow using an estimator, thus eliminating the need to place sensors in physically unrealistic locations. The target points we estimate and control are the same location of the downstream, where we are interested in reducing the wake.

Various active flow control methods for laminar flows using blowing/suction, synthetic jets, and plasma actuators have been successfully used to suppress vortex shedding behind bluff bodies in both experimental [Ffowcs Williams and Zhao, 1989, Tao et al., 1996, Strykowski and Sreenivasan, 1990, Min and Choi, 1999, Fujisawa et al., 2001] and numerical studies [Roussopoulos and Monkewitz, 1996, Lin and Tsai, 2024]. The suppression of vortex shedding significantly reduces lift and drag fluctuations, attracting considerable scientific interest. In this work, we are interested in the reduction of velocity fluctuations in the wake, which naturally includes the influence of vortex shedding.

The resolvent analysis enables effective actuation by determining the optimal frequency for the forcing input and identifying the most effective actuator locations to maximize forcing amplification within the flow [Yeh and Taira, 2019, Gross et al., 2024] for open-loop control. Our resolvent-based controller can capture all relevant frequencies, as expressed by $\hat{z} = \boldsymbol{R}_{za}\hat{\boldsymbol{f}}\hat{y}$, which appear in the resolvent operators. This allows the controller to influence the flow at the target effectively when the measurement time history is sufficiently long. Consequently, our controller has the potential to be applied to more complex flows characterized by a broad range of frequencies. To verify this, we also see both the time and frequency domains of the control results.

We assume that our flow exhibits both amplifier and oscillator characteristics [Schmid and Sipp, 2016], as it is globally stable and generates vortex shedding from the airfoil. Upstream disturbances are locally amplified as they travel downstream, while vortex shedding induces oscillating flow behaviors. Our proposed sensor and actuator configuration involves pairing an upstream sensor with a downstream actuator. The upstream sensor of the front set, located near the leading edge, receives incoming disturbance information and directs the paired downstream actuator to suppress

vortex shedding [Broglia et al., 2018, Déda et al., 2023]. The rear set sensors capture general flow behaviors, particularly oscillated vortex shedding, enabling the actuators near the trailing edge to mitigate amplified perturbations from external disturbances. We position the front actuators near the leading edge similarly to the prior works[Colonius and Williams, 2011, Broglia et al., 2018, Yeh and Taira, 2019, Asztalos et al., 2021], while the rear set location is determined as suggested in the estimation work §5.5.2.3. Suppressing vortex shedding reduces nonlinear behaviors, resulting in better effectiveness of controllers built based on the linear system.

The actuation signal in this work is designed as unsteady blowing and suction momentum injections, supported by Gaussian functions to resolve the force within the computational domain, as shown in figure 5.27. To implement the actuation force, we compute the convolution function in the time domain. The actuation force is applied to the momentum source term in the CFD solver using $\boldsymbol{B}_a$ and is computed for real-time control. The flow chart for this is referred to in figure 36. We utilize the same metric for control performance from our previous work [Martini et al., 2022], which measures the reduction in perturbation energy compared to uncontrolled perturbation energy at the targets. The control performance ε_{con} is defined as follows.

$$\varepsilon_{\text{con}} = 1 - \frac{\sum_i \int (z_{i,\text{con}}(t))^2 dt}{\sum_i \int (z_{i,\text{uncon}}(t))^2 dt}. \tag{5.14}$$

Another consideration we are taking into account is the different mean flow due to the actuation force and the nonlinear interaction from the noisy freestream. The actuation force disrupts the original mean flow in the controlled system, despite using a linear controller based on the linearized Navier-Stokes operator around the mean flow. Furthermore, the nonlinear interactions evolve over time and space, becoming particularly significant when the noisy freestream is intense, as shown in figure 5.14. These interactions lead to a different mean flow in the nonlinear system, even when the imposed forcing itself has a zero mean. However, our primary objective remains to minimize velocity fluctuations around the mean flow at the target. To address this challenge, we obtain a new mean flow in the actuated system with noisy freestream inflow and apply the linear controller using the updated mean flow [Leclercq et al., 2019]. This results in using the second controller (controller B), as illustrated in figure 5.27.

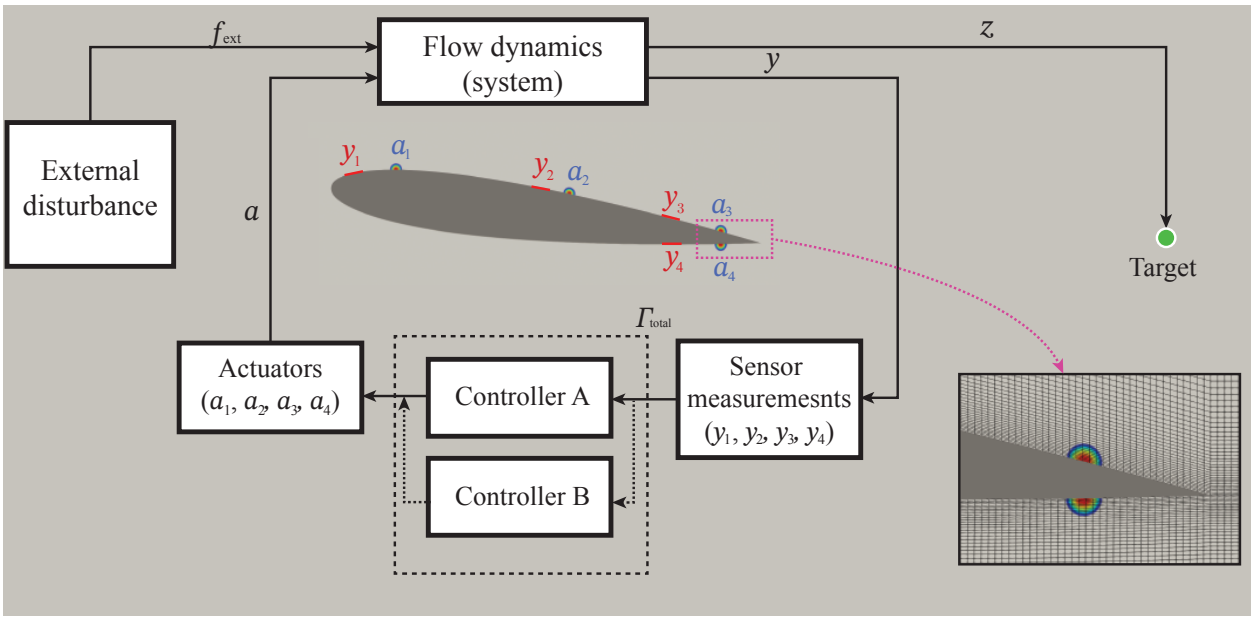

FIGURE 5.27: Control scheme for resolvent-based control of a NACA0012 airfoil. Red markers indicate sensor placements, while contoured circles represent actuator locations with Gaussian spatial support on the airfoil surface. The green circle marks the target location. For the control of the nonlinear system, we use the second controller (controller B) obtained from the updated mean flow. The zoom-in box highlights the grid resolution around the rear actuators.

5.6.2 Linear system

We first consider the linear system that was obtained from the linearized Navier-stokes operator, imposed by the external forcing, and minimize the perturbations at the target. The block diagram for the control system is shown in figure 5.27. For control of the linear system, we only use two actuators (a_3 and a_4), which were obtained only once (Controller A), and the control kernels are shown in both the time and frequency domain in figure 5.28. These kernels are derived using the operator-based approach in 2.4.1. By employing the modified resolvent operators $\boldsymbol{R}_{zf}\boldsymbol{R}_{yf}^{\dagger}$ and $\boldsymbol{R}_{yf}\boldsymbol{R}_{yf}^{\dagger}$ as described in 2.4.1.2, we implement the single-stage run detailed in 2.4.1.1 to obtain $\boldsymbol{R}_{ya}$ and $\boldsymbol{R}_{za}$, and integrate them with the results from the two-stage runs to compute the control kernels.

Figure 5.28(a) illustrates the non-causal and causal control kernels for controller A with the sensor positioned near the trailing edge (y_3) and the target z located at $x/L_c = 1.5$. Note that these control kernels treat the nonlinear terms as white noise, which works ideally in a linear system. In figure 5.28(a), due to the close proximity of the sensor and actuator, a spike occurs near the current time point, as shown in figure 5.28(a). Although the control kernel contains relatively large values

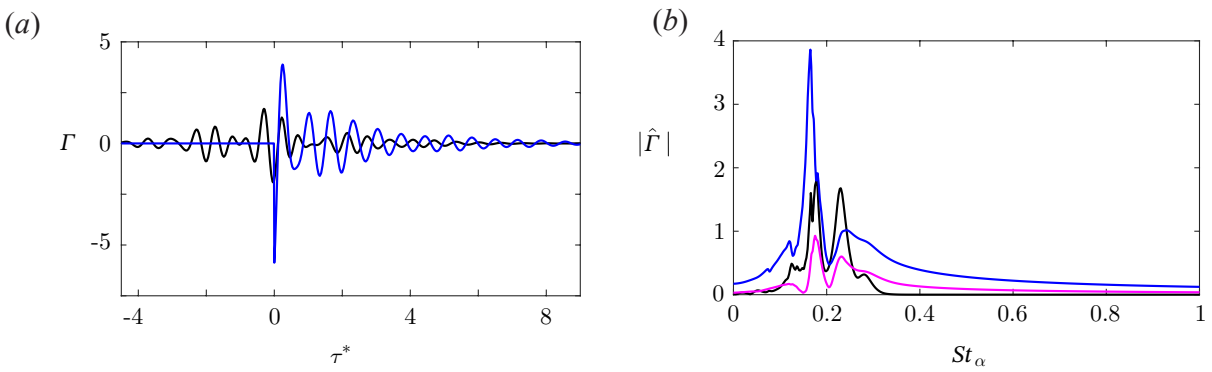

FIGURE 5.28: Control kernels with the sensor positioned near the trailing edge (y_3) and the target z located at $x/L_c = 1.5$ in the time (a) and frequency (b) domains. The black line represents the non-causal control kernel, the magenta line shows the truncated non-causal kernel, and the blue line depicts the causal control kernel computed using the Wiener-Hopf method.

in the non-causal part $\tau^* < 0$, this issue is moderated using the Wiener-Hopf method, similar to the estimation kernels. The current measurement significantly impacts the actuation signal, effectively canceling perturbations at the target, similar to the previous works [Morra et al., 2020, Martini et al., 2022]. Figure 5.28(b) presents the control kernels in the frequency domain, corresponding to those in the time domain shown in Figure 5.28(a). The truncated non-causal control kernel (magenta line) shows a considerable loss in magnitude, while the causal control kernel significantly amplifies the sensor measurement at the vortex shedding frequency ($St_\alpha = 0.17$). We observed that increasing the actuation cost $\boldsymbol{P}$ reduces the relative magnitude of the control kernel, leading to a smaller actuation force. We set $\boldsymbol{P} = \epsilon I$ with ϵ=10^{-1} of the maximum value of $\boldsymbol{R}_{za}$. The direct run of a single stage run is simulated until $tU_\infty/L_c = 48$ to ensure convergence to zero.

Figure 5.29 presents the time-series data for controlled and uncontrolled streamwise and cross-streamwise velocity perturbations at the target. The results show that the fluctuations of both velocity components are reduced using the causal control kernels. The power spectral density (PSD) of the corresponding streamwise velocity is depicted in figure 5.30(a). The causal resolvent-based controller effectively suppresses the dominant vortex shedding frequency, while the truncated non-causal approach fails to accomplish this. Once the vortex shedding frequency is mitigated, the controlled system exhibits different high-frequency components. The second-order norm of the velocity components in the wake region ($x/L_c = [1.1, 5], y/L_c = [-1, 1]$) is illustrated in figure 5.30(b). Using the causal approach, the two actuators at the trailing edge reduce the energy of

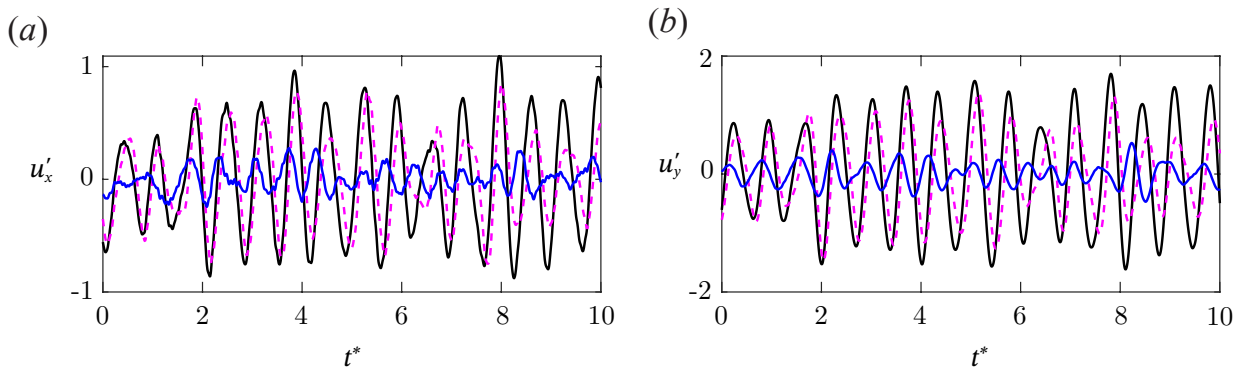

FIGURE 5.29: Time-series of velocity fluctuations for the uncontrolled and controlled linear systems: uncontrolled (black line), truncated control (magenta dashed line), and causal control (blue line). The left panel shows u'_x, and the right panel shows u'_y.

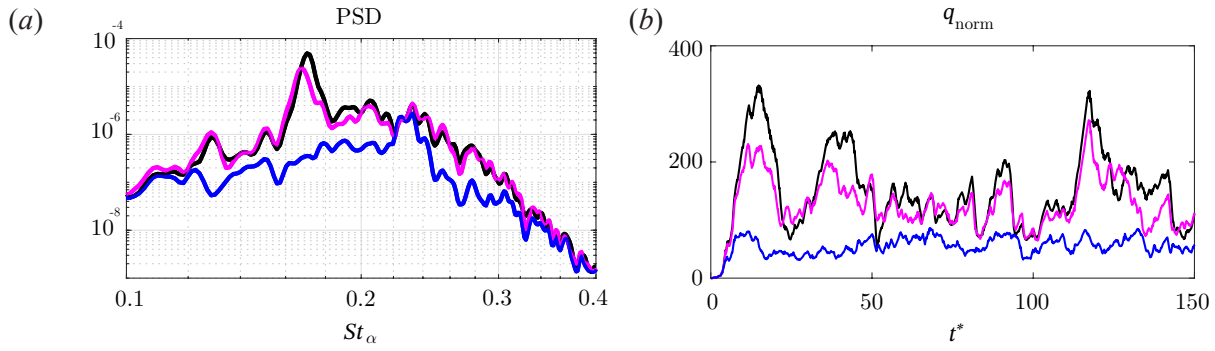

FIGURE 5.30: Control performance of the linear system. (*a*) Power spectral density of the velocity fluctuations u'_x for the controlled (blue) and uncontrolled (black) cases, with the magenta line representing the truncated non-causal control approach. (*b*) Norm of the two velocity components (u'_x and u'_y) corresponding to the cases in (*a*).

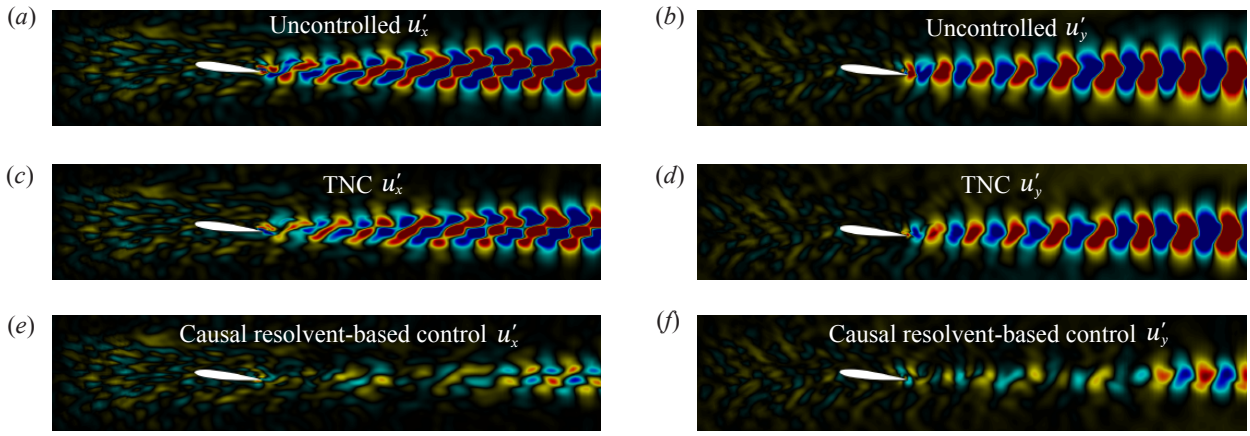

FIGURE 5.31: The streamwise and cross streamwise velocity fluctuations field of the controlled and uncontrolled linear system.

velocity fluctuations, as measured by (5.14), by 85% at the target, while the truncated non-causal approach achieves only a 27% reduction. In terms of RMS velocity fluctuation reduction, the causal approach achieves a 62% decrease, compared to just 14% with the truncated non-causal approach.

Figure 5.31 presents instantaneous snapshots of the controlled and uncontrolled systems for u_x' and u_y'. The wake modes excited by the upstream-generated external disturbance are effectively suppressed by the actuation at the trailing edge, as illustrated in figure 5.31(e) and (f).

5.6.3 Nonlinear system

The ultimate goal for this work is to reduce the wake perturbation in the nonlinear system (DNS) using the optimal linear controller we built using a resolvent-based approach. The data-driven approach is primarily used to build the resolvent operators combined with the colored forcing. The $\boldsymbol{R}_{ya}$ and $\boldsymbol{R}_{za}$ are computed from the operator-based approach. Alternatively, these components can be obtained by using an impulse forcing using the data-driven approach, as we discussed in §2.4.2. Unlike the control of the linear system, we obtain the new mean flow to consider the impact that evolved from the actuation and the noisy freestreams. Due to convective flow, we adjust the front actuators to be unsteady-blowing ones, leaving other rear actuators similar to the one we used for the control of the linear system. The front-blowing actuators primarily destroy the separation bubble behind them. We do not address the clean system for control, as our controller stabilizes the flow, resulting in a steady state. Consequently, the actuator produces a steady-blowing signal.

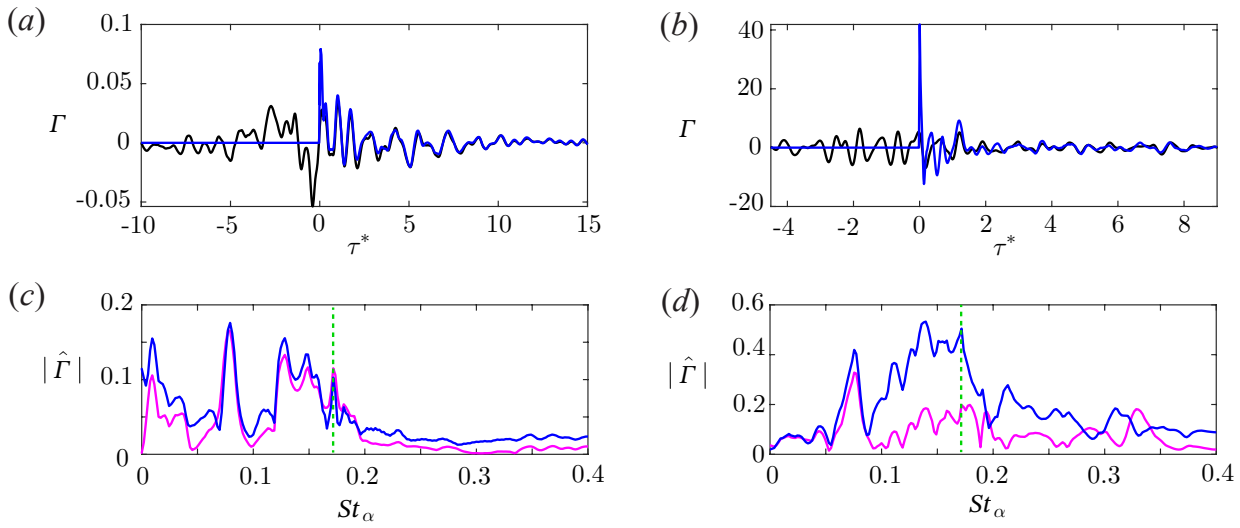

FIGURE 5.32: Control kernels for the nonlinear system: (a) and (b) display the kernels in the time domain, while (c) and (d) present them in the frequency domain. Specifically, (a) and (c) correspond to y_3 and a_3, and (b) and (d) correspond to y_4 and a_4, as shown in figure 5.27. The green dashed line in c and d indicates the vortex shedding frequency.

First, we show the control kernels for the sensor y_3, actuator a_3 and the target z, and the sensor y_4, actuator a_4 and the target z, which are for the paired sensor and actuators located near the trailing edge. The sensor, actuator, and target locations of figure 5.32(a) and (c) are equivalent to the locations for the linear system in figure 5.28. The dominant frequencies, including the vortex shedding frequency, are shown in the uncontrolled flow of the PSD, as shown in figures 5.33 at $x/L_c, y/L_c = [1.5, -0.11)$ and 5.15 ($W = 1$, at $x/L_c, y/L_c = [2.11, -0.11)$. Both control kernels account for the multiple dominant frequencies, which can amplify the actuation signal from the sensor measurements at those frequencies. We observe that the causal control kernels are improved to capture the desired frequencies, such as vortex shedding frequencies, while the truncated non-causal control kernel is lost to capture the dominant frequencies for the kernel, shown in figure 5.32(d). Since our sensor and actuator locations are close, the peaks of the non-causal (black line) in figures 5.32(a) and (b) are close near the zero of τ^*. The oscillatory flow generated from the separation bubble can be captured in the control kernel, which represents the vortex shedding frequency.

Figure 5.33 demonstrates that the energy of velocity fluctuations is reduced for $St_\alpha < 1$, within the range of frequencies of interest. The control performance, measured by the metric in (5.14)

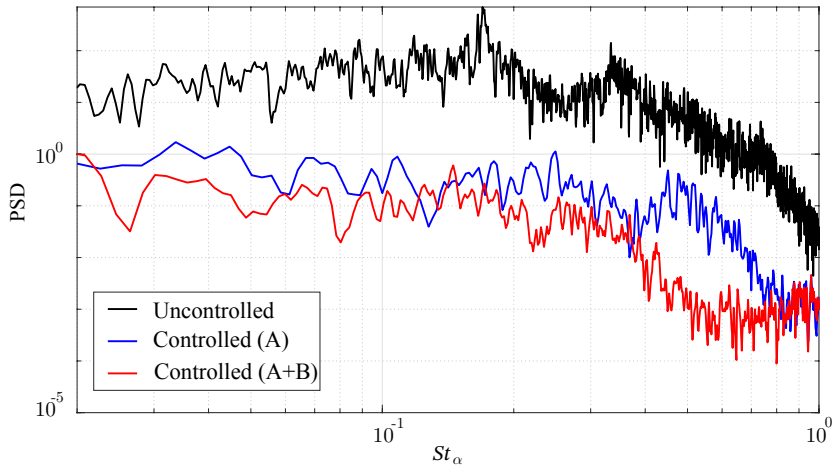

FIGURE 5.33: Power spectral density of the velocity fluctuation (u'_x) at the target location ($z = [1.5, -0.11]$). The black solid line represents the uncontrolled flow, the blue line shows the controlled flow using Controller A, and the red line depicts the controlled flow using the iteratively obtained controller (Controller A + Controller B).

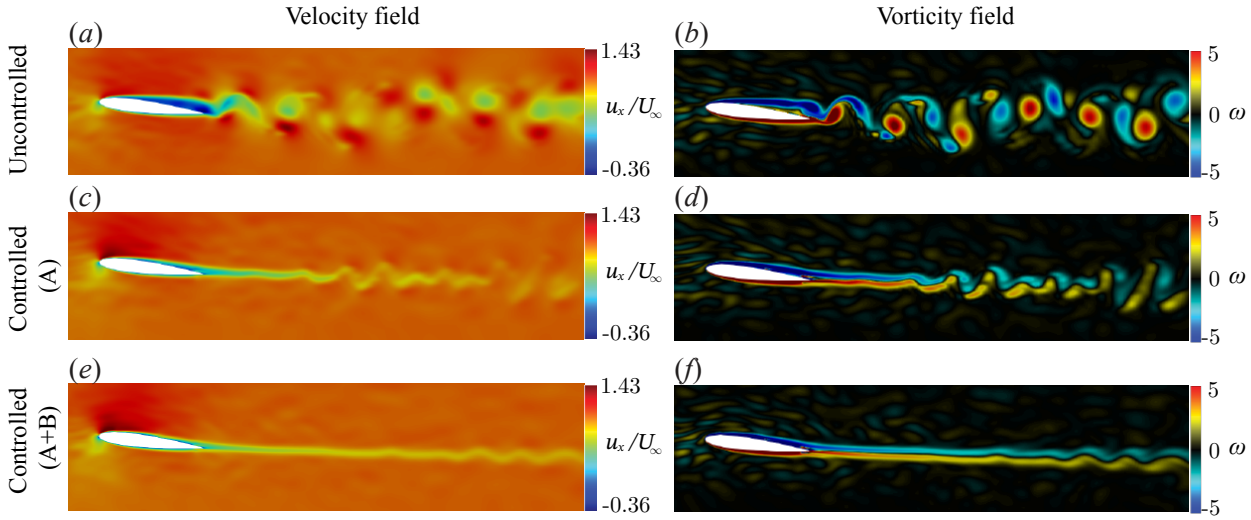

FIGURE 5.34: Velocity (u_x) and vorticity (ω) fields for the system with noisy freestream inflow. (a) and (b) illustrate the uncontrolled flows; (c) and (d) show the controlled flows using Controller A; (e) and (f) present the controlled flows with the iteratively obtained controller (Controller A + Controller B)

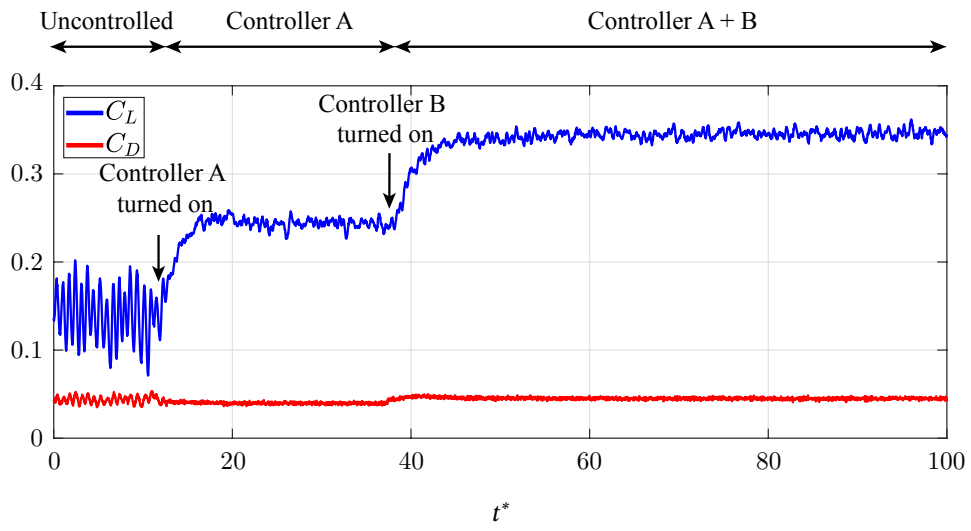

FIGURE 5.35: Lift and drag coefficients for the uncontrolled and controlled flow over time.

and representing the reduction in velocity fluctuation energy, reaches approximately 94% with Controller A. By incorporating a second controller (Controller A + B), the performance improves further, achieving an additional 98% reduction at the target. The reduction in velocity fluctuations (RMS) is 78% with Controller A and 90% when using both Controller A and B. As shown in figure 5.33, this improvement further mitigates target fluctuations at higher frequencies ($0.4 < St_\alpha < 0.7$), which originate from the oscillated flows further downstream, as we can verify in figure 5.34.

Figure 5.34 presents both uncontrolled and controlled snapshots. As shown in figure 5.34(a) and (b), chaotic vortex shedding is prominent in the wake of the uncontrolled flow. However, this can be significantly mitigated by controller A. Introducing controller B further suppresses the oscillated flow downstream ($x/L_c > 2$). In the controlled flow, the mean flow changed, which is essential as the wake fluctuations from vortex shedding originate from the separated flow. Therefore, to effectively reduce the high-energy fluctuations in the wake, it is somehow necessary to address the separation bubble. Figure 5.35 demonstrates the impact of the controllers on the aerodynamic coefficients. The time-averaged lift coefficient ($\bar{C}L$) is improved by 143% with the use of Controllers A and B, while the time-averaged drag coefficient ($\bar{C}D$) remains largely unchanged. Both coefficient fluctuations are effectively suppressed by the controllers. Although handling the aerodynamic coefficients was not the primary objective, we finally reduced their fluctuations and improved the lift coefficient.

5.7 Chapter Summary

This work demonstrates the successful application of resolvent-based estimation and control to a two-dimensional NACA 0012 airfoil at $Ma_\infty = 0.3$, $Re_{L_c} = 5000$, and $\alpha = 6.5°$. Under similar assumptions, our estimator and controller converge to the Kalman filter and LQG controller. However, our approach can incorporate the nonlinear terms of the Navier-Stokes equations using colored-in-time statistics, leading to significantly higher estimator accuracy and improved controller performance.

To construct the estimator and controller, we employed two computational approaches: an operator-based approach and a data-driven approach. The operator-based approach is computationally efficient, does not require a priori model reduction, and accounts for the colored statistics of nonlinear terms from the Navier-Stokes equations that act as a forcing on the linear dynamics. The data-driven approach, which circumvents the need to construct linearized Navier-Stokes operators, naturally incorporates these colored statistics of the nonlinear terms.

We utilized the Wiener-Hopf formalism to enforce causality, enabling the evaluation of only available measurements, which is an optimal strategy for real-time estimation and control. To implement the resolvent-based approach, we developed a new implementation within a compressible flow solver useful for large-scale problems. This implementation allows for the accurate construction of linearized Navier-Stokes operators, accounting for all numerical schemes and boundary conditions used in high-fidelity simulations. Additionally, it facilitates the efficient construction of estimators and controllers across the entire target region and enables real-time computation of estimates and actuation signals for large-scale systems.

Before applying estimation and control to the laminar airfoil, we obtained the mean flow through direct numerical simulation and performed global stability and resolvent analysis around this mean flow. Random upstream perturbations were introduced to disrupt the periodic limit cycle caused by vortex shedding, inducing chaotic fluctuations. We then conducted resolvent-based estimation and control on both linear and nonlinear systems under these conditions.

Our results demonstrate that resolvent-based kernels are effective in estimating and controlling chaotic fluctuations in the wake of an airfoil. The performance of both estimation and control is enhanced when sensors and actuators are strategically placed in effective locations. To determine

these effective placements, we investigated estimation errors and employed a streamline strategy. While we addressed the estimation across the entire wake region, we found that controlling the entire region yields results similar to targeting a single point. In the linear system, the estimation error is approximately 8% with two sensors, and the control performance reaches 85% using two actuators. For the nonlinear system, the estimation error increases to 30% with four sensors, while the control performance improves to 98% using four actuators and two controllers. Future work will focus on optimizing the placement of sensors and actuators and applying resolvent-based methods to turbulent wakes behind an airfoil.

CHAPTER 6

Resovlent-based Estimation of a Turbulent Airfoil Wake[1]

6.1 Introduction

Turbulent flow presents significant challenges across various applications. In aerospace, the turbulent wake resulting from a separation bubble on the surface of an airfoil can degrade aerodynamic coefficients such as drag and lift, compromising overall efficiency and performance [Cebeci et al., 1986]. These unpredictable fluctuations disrupt aerodynamic behavior and flight control, adversely affecting both controllability and performance. Additionally, turbulent wakes have become a focal point in the wind energy field. The turbulent wakes from upstream wind turbines impact downstream turbines, reducing their efficiency, increasing fatigue loads on turbine blades, and elevating noise levels, which can impact surrounding communities [Barthelmie et al., 2010b, Barthelmie and Pryor, 2013b, Stieren and Stevens, 2022]. Thus, controlling and minimizing turbulent wakes behind an airfoil is crucial for improving aerodynamic efficiency, ensuring stability, and mitigating related issues. However, achieving this is challenging due to the chaotic nonlinear dynamics of the flow, the presence of multi-scale turbulent eddies that are difficult to capture with sensors, especially at smaller scales, and the high-dimensional nature of the problem.

Over the past half-century, numerical and experimental investigations have extensively explored turbulent wake dynamics [Gartshore, 1967, Reynolds, 1972, Ghaemi and Scarano, 2011, Shamsoddin and Porté-Agel, 2017, Gupta et al., 2023, Schauerte and Schreyer, 2024]. As the Reynolds

[1] *The contents of this chapter are in preparation for submission as: J. Jung and A.Towne. Resolvent-Based Estimation of a Turbulent Wake, to be submitted to: J. Fluid Mech.*

number increases, turbulent wakes emerge, forming complex, multi-scale structures. At moderate Reynolds number (around 20,000) within mid-rage angle of attack ($6^\circ - 10^\circ$) of airfoils, a laminar separation bubble forms, and von Karman vortex shedding is observed near a Strouhal number based on the airfoil thickness of $St_\alpha \approx 0.2$, with other dominant frequencies below this value [Ducoin et al., 2016, Yeh and Taira, 2019]. Despite the complexity of these structures, a turbulent wake was estimated using a non-physics-based model with experimental data [Hočevar et al., 2005]. Chaotic fluctuations in the wake, caused by upstream random disturbances for a laminar airfoil wake, were estimated in our previous work [Jung et al., 2023].

Resolvent analysis stands as a powerful tool for exploring the physics of turbulent flows, employing a linear mapping of the response (output) and forcing (input) from the most energetically significant gains in the frequency domain. Previous studies [Jovanović and Bamieh, 2005, McKeon and Sharma, 2010, Towne et al., 2018] have applied resolvent analysis using a linearized Navier-Stokes operator to examine the maximally amplified resolvent modes induced by the forcing modes. Using resolvent analysis as a starting point for estimation and control has become popular in recent years. Yeh and Taira [2019] exploited resolvent analysis over a three-dimensional NACA airfoil at $Re_{L_c} = 23,000$, $Ma_\infty = 0.3$ and angle of attack 6° and 9° to design open-loop control input parameters for separation control. Liu et al. [2021] took advantage of resolvent analysis for achieving unsteady open-loop control to reduce pressure fluctuations in a turbulent flow over a cavity. Jin et al. [2022] utilized a resolvent-based iterative algorithm to perform closed-loop estimation and control for the cylinder flow.

A resolvent-based estimation method has gained popularity for its high accuracy and low computational cost for large systems [Towne et al., 2020, Martini et al., 2020, Amaral et al., 2021, Maia et al., 2021, Amaral and Cavalieri, 2023, Ying et al., 2023, Audiffred et al., 2024]. This approach effectively captures the coherent structures of turbulent flows, and the resolvent operators are closely related to the coherent structures identified from data using spectral POD [Towne et al., 2018]. Early versions of resolvent-based estimation used a non-causal approach [Towne et al., 2020, Martini et al., 2020, Amaral et al., 2021], which is not optimal for real-time estimation necessary for practical applications. To address this, the method was extended to create an optimal causal estimator and controller by enforcing causality through the Wiener-Hopf formalism [Martini et al., 2022]. This approach improves control performance, making the kernels suitable for closed-loop

flow control [Jung et al., 2020]. The causal resolvent-based estimator was successfully applied to a laminar flow over an airfoil, as discussed in Chapter 5.

Resolvent analysis is naturally applicable to globally stable flows, and it has been widely applied in such cases [Kojima et al., 2020, Martini et al., 2020, 2022, Marquet et al., 2022, Jung et al., 2023]. However, when the linearized Navier-Stokes operator is globally unstable, the interpretation of resolvent analysis becomes less clear. To address this challenge, some studies have adopted a discounting approach to relocating unstable eigenvalues into the stable domain of the eigenspectrum [Jovanovic and Bamieh, 2001, Yeh et al., 2020]. For the purpose of resolvent-based estimation and control, we proposed in our prior research to use a data-driven implementation [Martini et al., 2022] to circumvent the issues arising from an unstable linearized Navier-Stokes operator [Jung et al., 2023].

Investigating sensor placement is crucial for accurate flow estimation. Practical applications require the realistic positioning of sensors, and the accuracy of estimation can vary significantly depending on their locations. In resolvent-based frameworks, the coherence between the sensor and the target is analyzed to determine the effectiveness of the kernels, as demonstrated in experimental control studies by [Maia et al., 2021, Audiffred et al., 2023, 2024]. Additionally, estimation errors using a single sensor located within a feasible area relative to the target point can provide insights into effective sensor placement for multiple sensor estimations. Streamline analysis can also generally guide the identification of regions where strong coherence exists between two points, providing additional justification for effective sensor placement when external disturbances are traveled [Jung et al., 2024].

The objective of the present study is to estimate unsteady turbulent fluctuations in the wake of a NACA 0012 airfoil at Re=23,000 using a resolvent-based approach. Our methodology involves constructing transfer functions utilizing datasets obtained from a nonlinear Navier-Stokes simulation, which circumvents the use of an unstable linear operator for constructing the estimation and control kernels. This chapter aims to demonstrate the effectiveness of the resolvent-based approach in accurately estimating velocity fluctuations within two-dimensional and spanwise-periodic turbulent wakes.

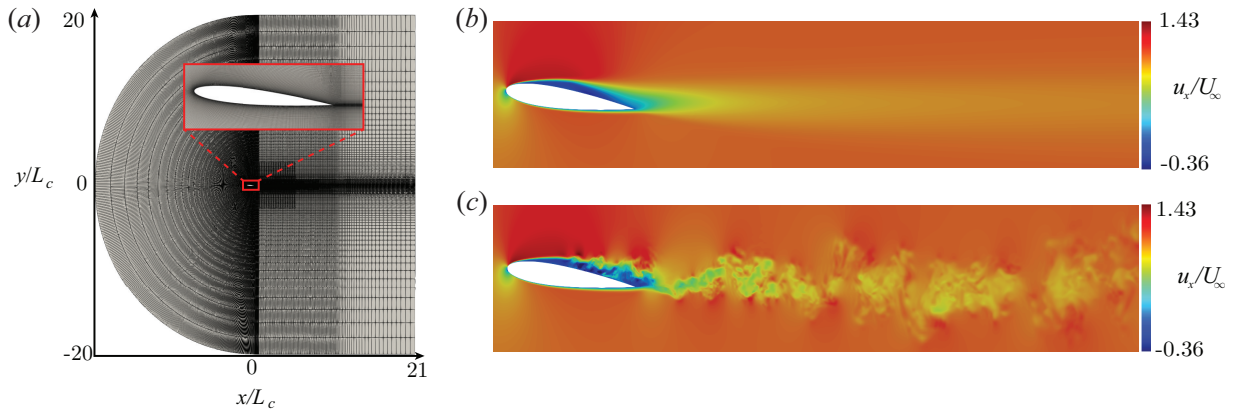

FIGURE 6.1: Computational mesh and simulation: (*a*) the complete C-shaped grid, with a zoomed-in view of the mesh near the wall shown in the inset; (*b*) the mean flow of the streamwise velocity u_x; and (*c*) the instantaneous streamwise velocity u_x obtained from the large-eddy simulation.

6.2 Problem Set-up

6.2.1 Problem description

We consider the turbulent wake of a NACA0012 airfoil at a moderate chord-based Reynolds number of $\mathrm{Re}_{L_c} = 23{,}000$ and an angle of attack of $\alpha = 6°$, as studied in several previous works [Kojima et al., 2013, Munday and Taira, 2018, Yeh and Taira, 2019, Towne et al., 2023]. Shear-stress sensors are placed on the surface of the airfoil, with targets located in the turbulent wake (see §6.3 for details). We present resolvent-based estimation of velocity fluctuations for spanwise-averaged, spanwise-Fourier-transformed, and mid-span-plane flows.

6.2.2 Simulation

An LES utilizing the high-fidelity compressible flow solver CharLES [Brès et al., 2017] is conducted to simulate turbulent airfoil flow. The simulation is performed on the Department of Defense's supercomputer, an HPE SGI 8600 system with a peak performance of 3.05 PFLOPS. For this study, 50 nodes of the supercomputer, each equipped with 48 cores, were utilized. The C-shaped mesh, generated using Pointwise, is depicted in figure 6.1(*a*). Figures 6.1(*b*) and (*c*) illustrate the mean and instantaneous streamwise velocity fields, respectively. The airfoil's leading edge is positioned at the origin, $x/L_c = y/L_c = 0$. The computational domain spans $x/L_c \in [-20, 21]$, $y/L_c \in [-20, 20]$,

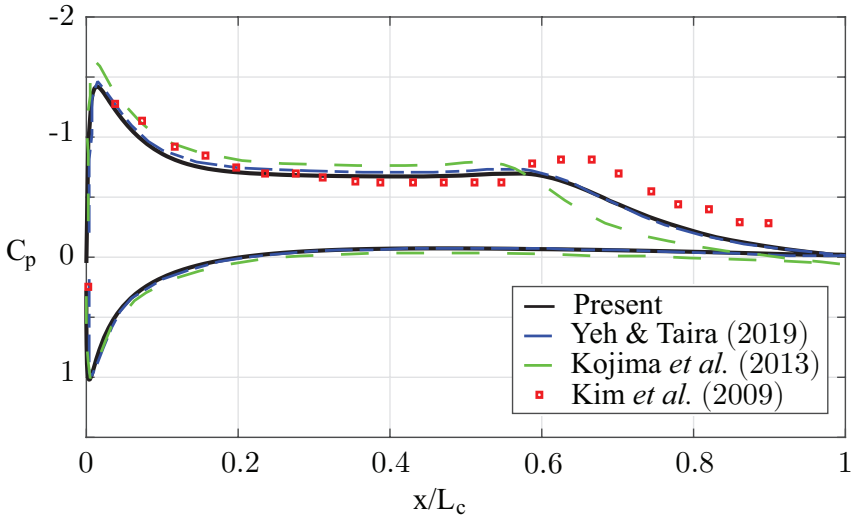

FIGURE 6.2: Comparison of the pressure coefficient C_p with previous works.

and $z/L_c \in [-0.1, 0.1]$. To optimize the mesh resolution, hybrid meshes (unstructured and structured) are employed in the transverse and spanwise directions. A characteristic boundary condition $[\rho, u_x, u_y, u_z, P] = [\rho_\infty, U_\infty, 0, 0, P_\infty]$ is applied at the domain edges, with a sponge layer implemented for $x/L_c \in [11, 21]$ to mitigate spurious reflections at the outflow. The time integration uses a constant Courant-Friedrichs-Lewy (CFL) number set to 0.84. Data for constructing the transfer function were gathered using a constant time step, $\Delta t U_\infty / L_c = 4.32 \times 10^{-5}$.

We validate the LES by comparing the pressure coefficient and aerodynamic forces

$$C_p = \frac{p - p_\infty}{\frac{1}{2}\rho_\infty U_\infty^2 A}, \quad C_D = \frac{F_D}{\frac{1}{2}\rho_\infty U_\infty^2 A}, \quad \text{and} \quad C_L = \frac{F_L}{\frac{1}{2}\rho_\infty U_\infty^2 A} \tag{6.1}$$

with previous works in figure 6.2 and table 6.1. Experimental data is taken from Kim et al. [2009]. The closest analogue to our simulation is that of Yeh and Taira [Yeh and Taira, 2019], which entails the same physical setup and solver but a different grid. The simulations of Kojima et al. [2013] and Munday and Taira [2018] differ due to the use of an incompressible flow solver and a lower Mach number. Our simulation closely aligns with Yeh and Taira [2019], particularly regarding the time-averaged drag and lift coefficients, demonstrating reasonable agreement.

As shown in figure 6.3, the shear layer roll-up on the suction surface occurs at $x/L_c \approx 0.4$, leading to spanwise vorticity. A laminar separation bubble is observed for approximately $0.1 <$

	$\bar{C}_D$	$\bar{C}_L$
Present study	0.0663	0.5836
Yeh and Taira [2019]	0.066	0.609
Munday and Taira [2018]	0.062	0.637
Kojima et al. [2013]	0.054	0.639

TABLE 6.1: The comparison of the time-averaged drag and lift coefficients with the reference data for a NACA 0012 airfoil at $Re_{L_c} = 23,000$ and angle of attack 6°.

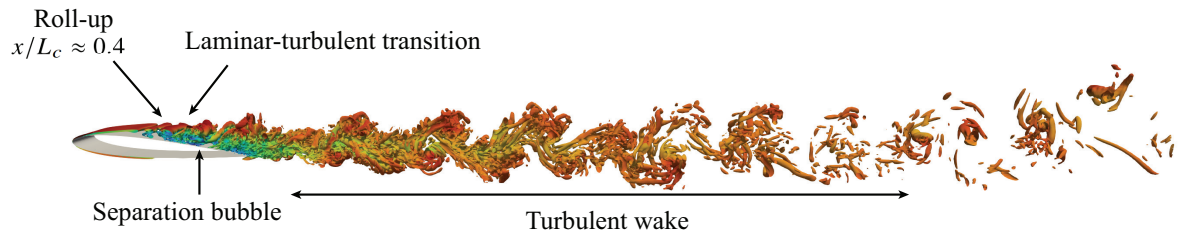

FIGURE 6.3: Flow physics visualized using isosurfaces of the Q-criterion.

$x/L_c < 0.84$, as indicated by the mean streamwise velocity shown in figure 6.1(b). Laminar-turbulent transition is detected at $x/L_c \approx 0.6$, as determined by the termination of the pressure coefficient plateau illustrated in figure 6.2. Finally, a turbulent wake develops behind the airfoil.

6.2.3 Dataset

The dataset consists of $n_t = 75,000$ time-resolved, three-dimensional snapshots of $[\rho, \rho u_x, \rho u_y, \rho u_z, T]$, covering a time window of $tU_\infty/L_c \in [0, 324]$ with a sampling resolution of $\Delta t U_\infty/L_c = 0.00432$. The dominant vortex-shedding frequency is $St \equiv fU_\infty/L_c = 1.44$, spanning approximately 466 shedding cycles within this period. The spatial domain for the data is $x/L_c \in [-0.5, 2.5]$ and $y/L_c \in [-0.5, 0.5]$, with multiple probe data collected along the line at the trailing edge $x/L_c \in [2.5, 6]$ and $y/L_c = -0.11$, allowing for detailed observation of the prevalent turbulent wakes. To efficiently handle the data, we use streaming Fourier transform [Schmidt and Towne, 2019] developed for resolvent-based estimation tools ([Jung et al., 2024]), as shown in figure 6.5. 80% of this data is used for building the estimation kernels, while the remaining 20% is reserved for testing and evaluating the estimation performance.

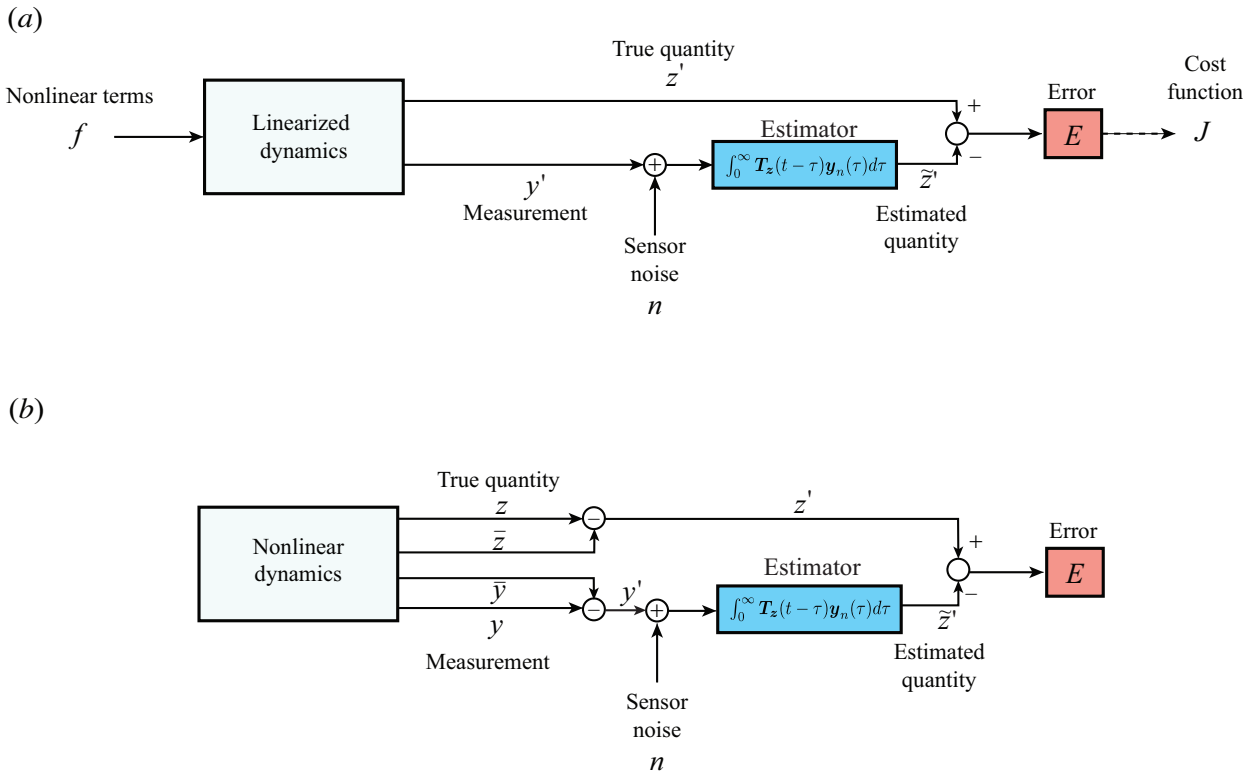

FIGURE 6.4: Block diagram of resolvent-based estimation: (*a*) designing resolvent-based estimator based on the linear system and (*b*) estimation of the nonlinear system

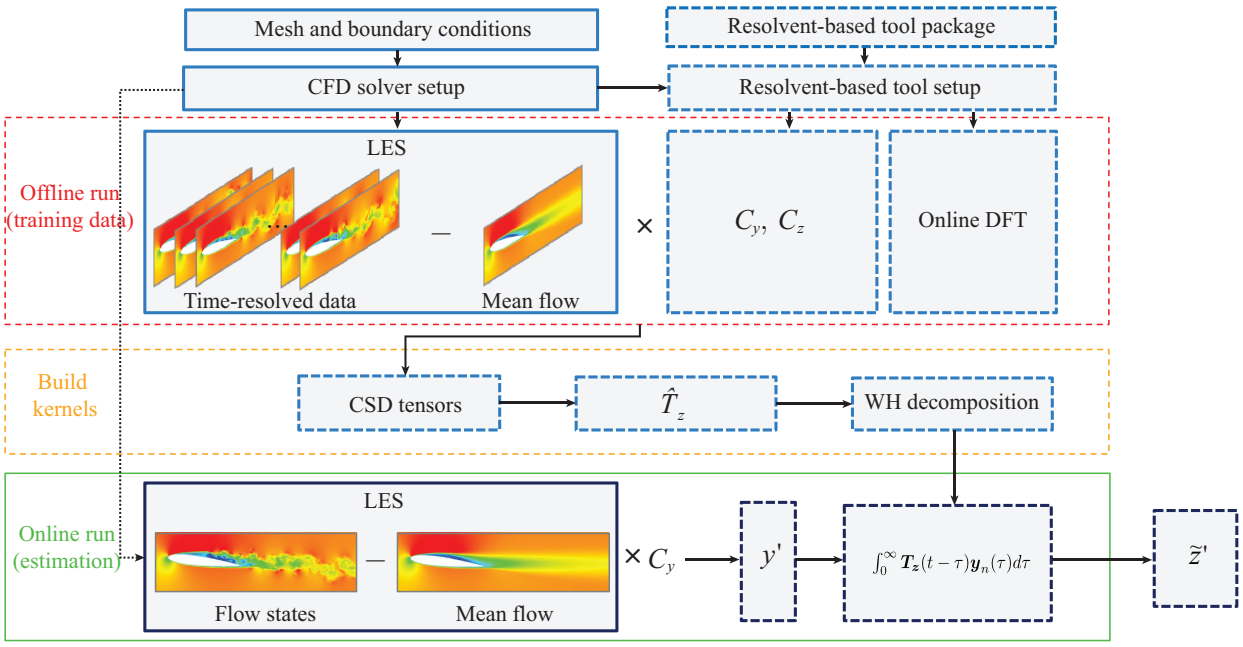

FIGURE 6.5: The flow chart of the proposed resolvent-based estimation tool: dashed line boxes represent the resolvent-based tool integrated with the existing CFD solver (solid line box). Blue boxes indicate the offline process, while black boxes denote the online (estimation) work.

6.3 Resolvent-based Estimation

We demonstrate the effectiveness of optimal resolvent-based estimators on the turbulent fluctuations in the wake of the NACA0012 airfoil at $Ma_\infty = 0.3$, $Re_{L_c} = 23,000$, and $\alpha = 6°$. It is important to note that our estimator relies solely on current and past measurements from upstream sensors via the Wiener-Hopf method, in contrast to the non-causal estimation methods used in previous studies [Towne et al., 2020, Martini et al., 2020, Amaral et al., 2021, Amaral and Cavalieri, 2023], which are limited from optimal estimation in terms of causality.

We focus on the spanwise-averaged and mid-span plane of the spanwise-periodic flow. Spanwise-Fourier modes are commonly used in biglobal instability analysis for three-dimensional flows [Theofilis, 2003]. Previous studies have investigated resolvent gains in terms of spanwise wavenumbers [Yeh and Taira, 2019, Towne et al., 2023]. To further explore spanwise effects, we examine the

spanwise-Fourier modes, defined as

$$\hat{\boldsymbol{q}}(x, y, z_{k_z}, t) = \int_{-\infty}^{\infty} \boldsymbol{q}(x, y, z, t) e^{ik_z} dz, \tag{6.2}$$

where k_z denotes the spanwise wave number. We begin by investigating effective sensor placement on the surface of the airfoil, considering estimation errors and sensor-target coherence. The spanwise-averaged flow captures the overall spatial information along the spanwise direction, allowing us to focus the sensor placement analysis on the streamwise and cross-streamwise directions. By progressively incorporating more complex flow settings, including the mid-span plane, we refine our estimation method to account for spanwise spatial effects. Subsequently, we analyze measurements from shear stress sensors at optimal locations, examining power spectral densities. We also explore estimation kernels in both time and frequency domains, assessing their impact on estimation and the physical insights they provide. Finally, we present estimation results for time-series velocity fluctuations at a single target and across an extended wake region, demonstrating the effectiveness of our method for turbulent wakes.

6.3.1 Sensor placement

We investigate the most effective sensor placement for resolvent-based estimation, leveraging estimation errors and the coherence between the sensor and the target. The three-dimensional surface space offers numerous potential sensor locations. By analyzing estimation errors at two-dimensional locations, we aim to identify the most effective sensor positions in the streamwise and cross-streamwise directions. The estimation error is quantified using the error metric defined as

$$E = \frac{\sum_i \int (\tilde{z}_i(t) - z_i(t))^2 dt}{\sum_i \int (z_i(t))^2 dt}, \tag{6.3}$$

where $\tilde{z}_i$ and z_i represent the estimated and the true values for the i-th target, respectively. Figure 6.6 presents the estimation error map for a single sensor and a single target using both causal (a), (c), (e), (f) and truncated non-causal (b), (d) approaches. The analysis is performed for spanwise-averaged and spanwise-Fourier ($k_z = 10\pi$, $k_z = 20\pi$) mid-span flows. For the spanwise-Fourier flows, we focus on the two lowest frequencies, $k_z = 10\pi$ and $k_z = 20\pi$, which correspond to the

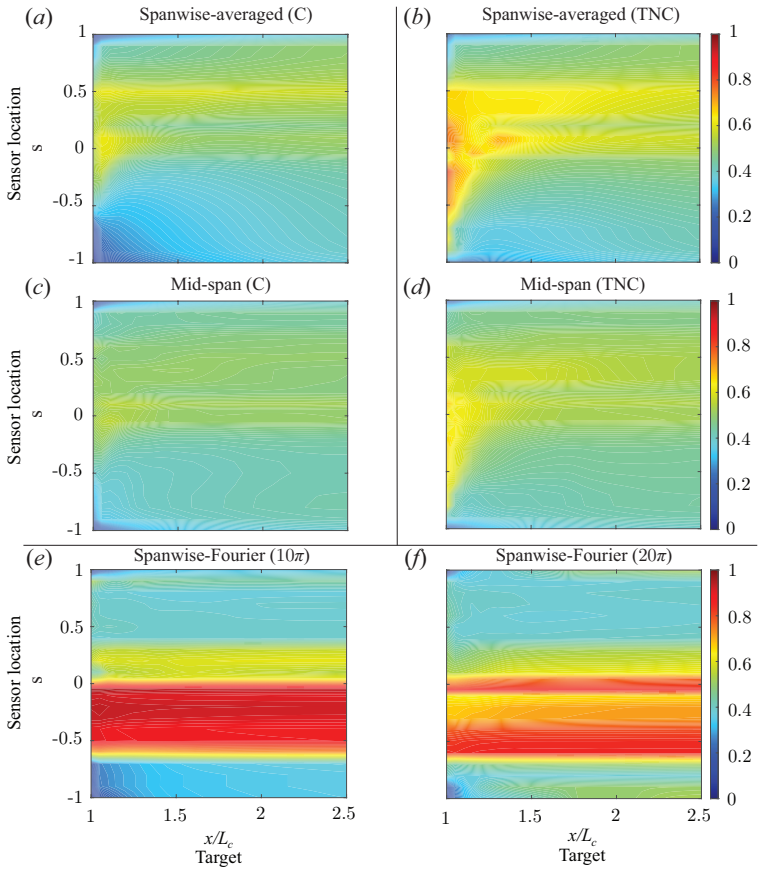

FIGURE 6.6: Estimation error map for a single sensor and a single target using causal (*a*), (*c*), (*e*), (*f*) and truncated non-causal (*b*), (*d*) approaches.

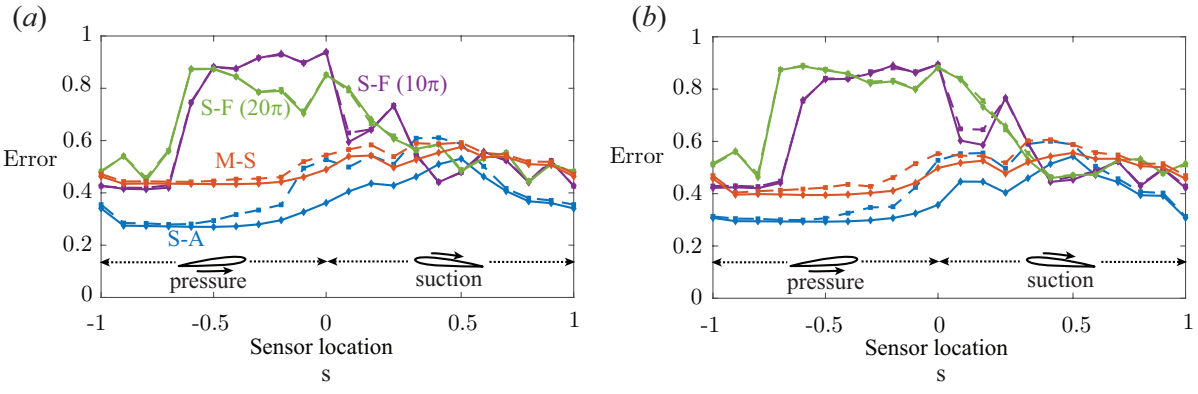

FIGURE 6.7: Estimation errors of streamwise (*a*) and cross-streamwise (*b*) velocities based on sensor locations on the airfoil surface. The blue, orange, purple, and green lines represent spanwise-averaged (S-A), mid-span (M-S), and spanwise-Fourier (S-F) ($K_z = 10\pi, 20\pi$) flows, respectively. The solid diamond ($\diamond$) and dashed square ($\square$) lines denote the causal and truncated non-causal approaches, respectively.

highest energy levels based on the resolvent gain [Yeh and Taira, 2019, Towne et al., 2023]. For convenience, we define the sensor location coordinate (s) such that positive values correspond to the suction surface and negative values to the pressure surface, with the absolute value representing the coordinate (x/L_c).

Overall, the causal estimation method outperforms the truncated non-causal approach. This is particularly evident near the trailing edge region ($1 < x/L_c < 1.5$), especially when the sensors are positioned on the front half surfaces ($-0.5 < s < 0.5$) of the airfoil. The improvement is more pronounced in the spanwise-averaged flow than in the mid-span flow. This is because the front region is predominantly characterized by laminar flow and a larger spanwise spatial structure, leading to low coherence with the turbulent flow at the targets. However, after the transition to turbulence, the coherence increases between the turbulence at the sensor and target locations. This deterioration in estimation accuracy due to the laminar region is clearly observed in the spanwise-Fourier modes. For both spanwise wavenumbers, sensors located in the region ($-0.5 < s < 0.5$) perform poorly in estimation. The laminar region, particularly on the pressure surface ($-0.5 < s < 0$), loses coherence for estimating target fluctuations, with a more significant impact for ($k_z = 10\pi$). This is likely because the spanwise structure is larger in the case of ($k_z = 10\pi$) compared to ($k_z = 20\pi$).

Figure 6.7(a) and (b) presents the average estimation errors in the wake region as a function of sensor location (s) for spanwise-averaged (S-A), spanwise-Fourier (S-F), and mid-span (M-S) flows. The results are shown for (a) the streamwise velocity component u'_x and (b) the cross-streamwise velocity component u'_y. The targets were uniformly distributed within the wake region and averaged to represent the mean error in the wake region as a whole. Overall, the estimation accuracy of the two velocity components is similar, indicating that these components near the wakes are highly interactive and evolve in a comparable manner. The ability of kernels built on the resolvent operator (which inherently includes the linearized Navier-Stokes operator) to estimate both velocity components suggests the potential to estimate other variables of interest, such as the vorticity field. In the simulation, it is observed that laminar flow dominates the region $-0.9 < s < 0.4$ in the sensor location. For spanwise-averaged and mid-span flows, sensors placed on the pressure surface yield better estimation accuracy. In contrast to figure 6.6, the laminar flow region on the suction surface performs well in estimation, although this is not the case for spanwise-Fourier modes. This is because the targets in figure 6.7 are set in the wake region,

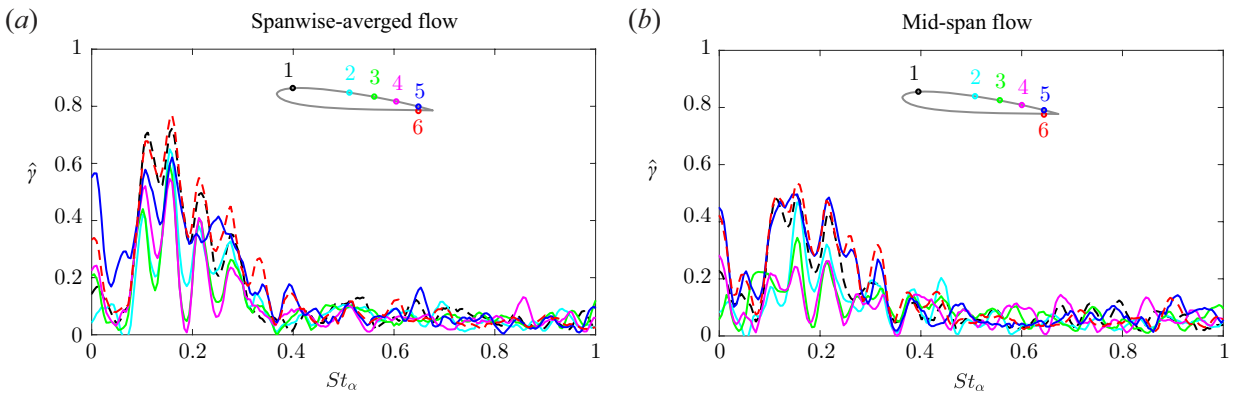

FIGURE 6.8: Coherence of the spanwise-averaged and mid-span flows.

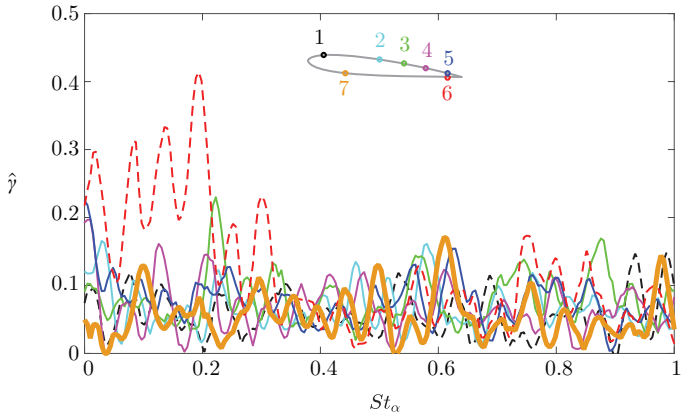

FIGURE 6.9: Coherence of the spanwise-Fourier flow $k_z = 10\pi$.

encompassing the upper and lower regions relative to the trailing edge line. As a result, the overall estimation accuracy for spanwise-averaged flow is higher than for mid-span flow. For spanwise-averaged and mid-span flows, the laminar separation bubble region ($0.4 < s < 0.7$) shows a slight deterioration in estimation accuracy, which improves as the sensor location approaches the trailing edge. In summary, estimation accuracy is generally higher for spanwise-averaged flow compared to mid-span flow. The spanwise-Fourier mode shows intermediate performance when effective sensor placement is considered. The sensor locations ($0.5 < x < 1$) and ($-1 < x < -0.7$) can be considered effective choices for estimation.

Additionally, coherence [Maia et al., 2021] is considered as a valuable metric that provides

information on the frequency-based performance of the estimation, defined as

$$\hat{\gamma}_{yz}(\omega) = \frac{|\boldsymbol{S}_{yz}(\omega)|}{\sqrt{\boldsymbol{S}_{yy}(\omega)}\sqrt{\boldsymbol{S}_{zz}(\omega)}}, \tag{6.4}$$

where $\boldsymbol{S}_{yz}$ is the cross-spectral density between the sensor and the target, and $\boldsymbol{S}_{yy}$ and $\boldsymbol{S}_{zz}$ are the power spectral densities of the respective data. Based on the coherence metric in (6.4), we present the coherence between the sensor locations of interest and the target ($x/L_c = 1.2$) in the near wake in figures 6.8 and 6.9. We placed the sensor on the front suction surface for investigation, which can be interesting. The laminar flow regions exhibit a similar coherence pattern, differing only in magnitude. Consequently, we focus on a single sensor location (y_1) on the front suction side, shown in figures 6.8 and 6.9. We can see that the sensor locations (1 to 6) demonstrate stronger coherence in the range of interest, $St_\alpha < 0.2$ in the spanwise-averaged flow than the mid-span flow. Locations 1 and 6 are identified as the most effective, with location 5 also showing significant potential. Among locations 2, 3, and 4, strong coherence is observed at different frequencies. These sensors are appropriately chosen, confirming the dominant frequencies of the target, which should be considered for amplification or reduction from the kernels in the frequency domain. We are particularly interested in whether coherence is weak for the region $[-0.7 < x/L_c < 0]$ in the spanwise-Fourier flows. To investigate this, we place sensor 7 at $x/L_c = -0.3$ in figure 6.9. The von Karman shedding and other dominant frequencies are present at $St_\alpha < 0.2$, but the coherence does not exhibit significant values below 0.2 for this sensor location, as indicated by the yellow solid line in figure 6.9. However, sensor locations 5 (blue) and 6 (red) exhibit strong peaks in figure 6.9. We ultimately select the most effective sensor locations (1, 5, and 6) for estimation, along with an additional sensor location 4 chosen from locations 2, 3, and 4.

6.3.2 Power-spectral density of the sensor and target readings

Figure 6.10 shows that the streamwise velocity fluctuation fields for spanwise-averaged, spanwise-Fourier-transformedm, mid-span-plane flows along with the sensor and the target locations. The scale of the structure in the flows decreases in the order (a) ¿ (b) ¿ (c) ¿ (d), and the difficulty of estimation follows the same order. Figure 6.11 presents the power spectral density of the sensor and target signals in the spanwise-averaged flow. As discussed, three dominant frequencies are

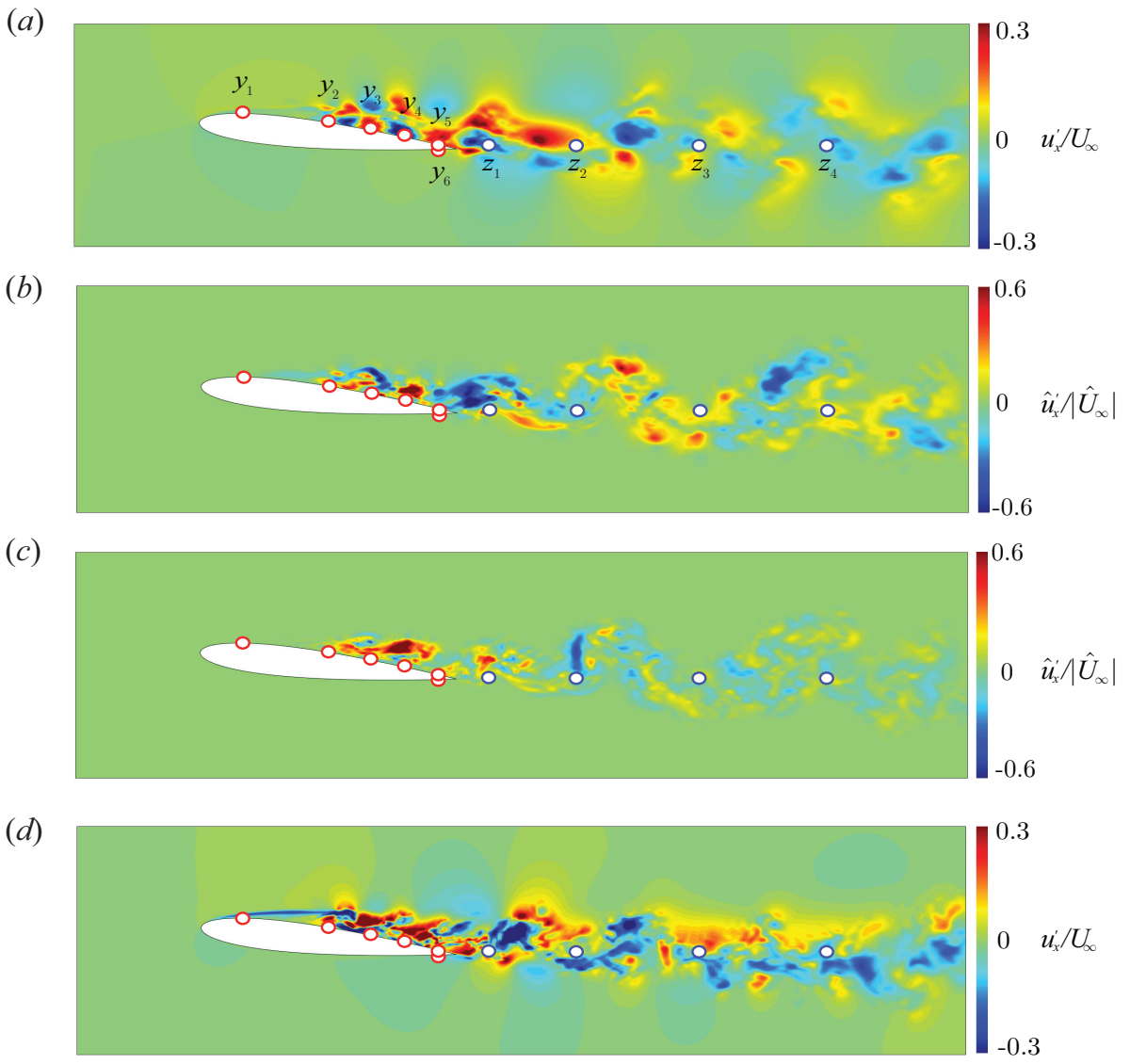

FIGURE 6.10: Streamwise velocity fluctuation u_x'/U_∞ field for spanwise-averaged flow (*a*), spanwise-Fourier mode for $k_z = 10\pi$ (*b*) and $k_z = 20\pi$ (*c*), and mid-span flow (*d*). Sensor locations are indicated by red circles, and target locations are shown by blue circles.

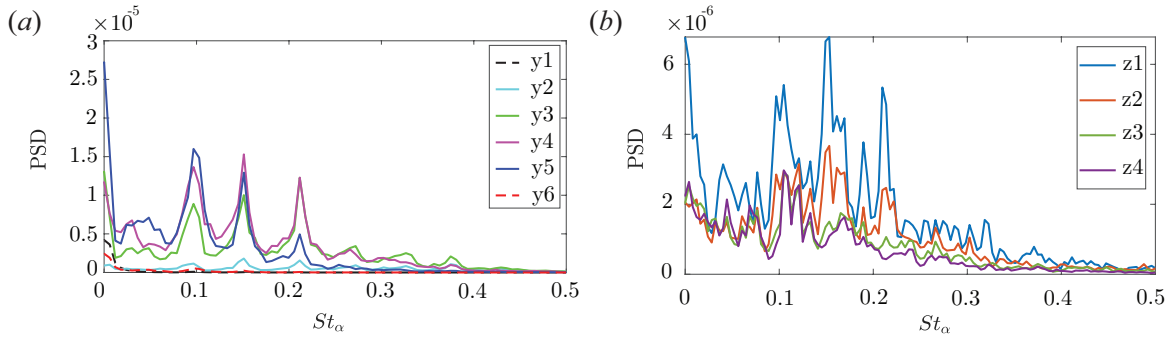

FIGURE 6.11: Power spectral density (PSD) of u'_x for (a) sensor and (b) target readings in the spanwise-averaged flow in figure 6.10. The dashed line ($y1$ and $y6$) represents the laminar flow region.

particularly evident for sensors y_3, y_4, y_5 and target z_1, as shown in figure 6.11(a) and (b). The energy reduces as the target is moved further downstream. The flow separation is caused by mean pressure gradients, and the boundary layer between the separation bubble and the freestream flow is then susceptible to the KH instability, leading to LSB vortex shedding, which oscillates at lower frequencies ($St_\alpha < 0.12$) [Ducoin et al., 2016]. These frequencies are effectively captured in figure 6.11(a) for sensors y_3, y_4, y_5 and target z_1. Dominant von Kármán vortex shedding frequencies are observed at $St_\alpha = [0.152, 0.211]$ [Yeh and Taira, 2019] in the turbulent region on the airfoil and the near wake. In contrast, the laminar regions at sensors y_1 and y_6 show values only near zero frequencies, indicating an almost constant (non-oscillating) signal over time. To achieve higher estimation accuracy, the coherence should exhibit significant values at the dominant frequencies of the target.

Figure 6.12 shows the power spectral density (PSD) of u'_x for sensor and target readings in the spanwise-Fourier modes with $k_z = 10\pi$ (a) and $k_z = 20\pi$ (b). The PSDs are generated using the same parameters as in the spanwise-averaged flow. Lower wavenumbers (k_z) correspond to more energetic and larger spanwise spatial structures, while higher wavenumbers result in smaller structures with reduced energetic impact. The higher energy in the wake is evident when comparing the PSD magnitudes in figure 6.12(a) and (b). The smaller structures are also visible in the instantaneous streamwise velocity field shown in figure 6.10 (b), compared with (c). No distinct peak points are observed in the PSD of the sensor readings for this flow, which limits the physical insights gained from this data; hence, those figures are excluded from this analysis.

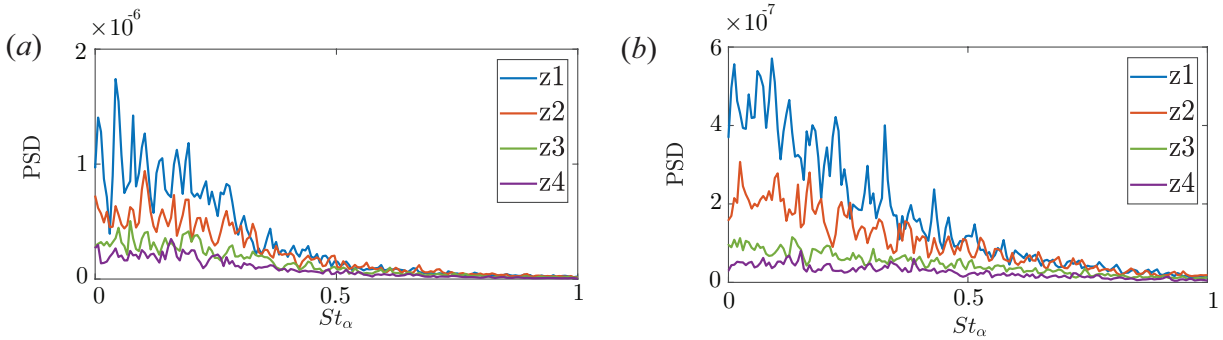

FIGURE 6.12: Power spectral density (PSD) of u'_x for targets readings in the spanwise-Fourier modes in figure 6.10(b) and (c): (a) $k_z = 10\pi$ and (b) $k_z = 20\pi$.

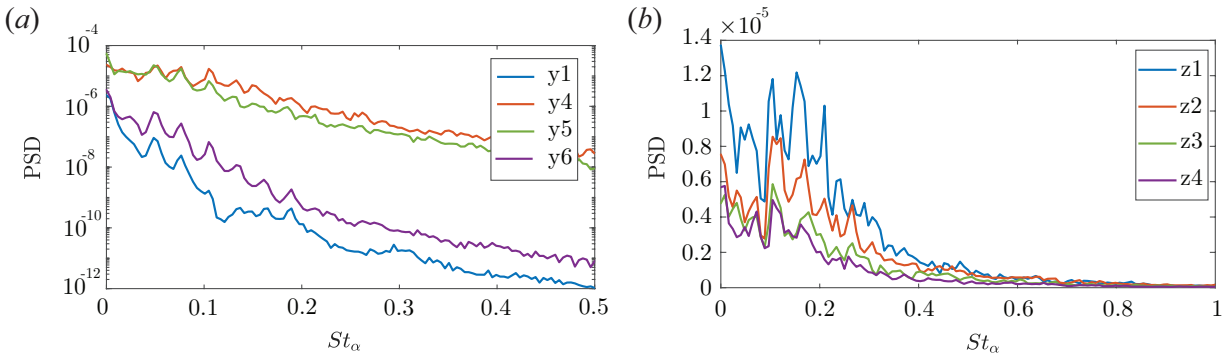

FIGURE 6.13: Power spectral density (PSD) of u'_x for sensor and target readings in the mid-span flow, as shown in Figure 6.10(d). The PSD of the selected sensors ($y1$, $y4$, $y5$, and $y6$) is presented, highlighting the sensors chosen for their effectiveness in achieving the most accurate estimation.

Figure 6.13 presents the PSDs of sensor and target measurements in the mid-span flow, as depicted in figure 6.10. Similar to the spanwise-averaged flow, the laminar flow region (y_1 and y_6) exhibits lower energy fluctuations, with the PSD decreasing as the target moves further downstream due to dissipation. The dominant frequencies around $St_\alpha \approx 0.2$ are clearly visible in figure 6.13(b).

6.3.3 Estimation kernels

Next, we examine the estimation kernels, building on our previous studies [Martini et al., 2020, 2022, Jung et al., 2023], where we initially explored kernels within the resolvent-based framework. A key characteristic of estimation kernels is the presence of peak points, which reveal the time it takes for hydrodynamic waves to travel from the sensor location to the target. Since our estimation kernels are based on the compressible linearized Navier-Stokes operator, they also capture acoustic waves, resulting in additional peaks. Another important characteristic is whether there are significant values in the non-causal part of the kernel ($\tau < 0$), especially the peak point. This information is crucial for estimation, but it may be truncated if it resides in the non-causal part of the kernels. This truncation can lead to a significant difference in the performance between the causal and truncated non-causal approaches. From a numerical perspective, the estimation kernels function by amplifying the frequency signals of the sensor measurements through multiplication with the kernels to approximate the target signals, i.e., $\hat{\tilde{\boldsymbol{z}}}(\omega) = \hat{\boldsymbol{T}}_z(\omega)\hat{\boldsymbol{y}}(\omega)$. Therefore, analyzing the estimation kernels in the frequency domain alongside the PSD of the sensor and target readings provides valuable numerical insights into accurate estimation, e.g., from figure 6.11(a) to figure 6.11(b) via figure 6.14.

We identify four effective kernels, specifically within the single input and multiple outputs configuration (sensor: y_1 and targets: z_1, z_2, z_3, z_4), as illustrated in figure 6.14. This selection is based on the observation that when the sensor is positioned in the laminar region within the effective locations, the kernel's peaks are distinct, with less noise in other frequencies, showing a clear correlation between the sensor and the target signals. In figure 6.14, prominent peak points are observed in the non-causal kernels (a, c, e, g) at $[\tau_{\text{peak},z_1}, \tau_{\text{peak},z_2}, \tau_{\text{peak},z_3}, \tau_{\text{peak},z_4}] = [-0.360, 0.171, 0.676, 1.25]$, respectively. These points represent the primary hydrodynamic wave travel times between the sensor and the targets. The case in figure 6.14(a) serves as a good example of how a causal approach using Wiener-Hopf decomposition can enhance estimation accuracy. However, when applied to

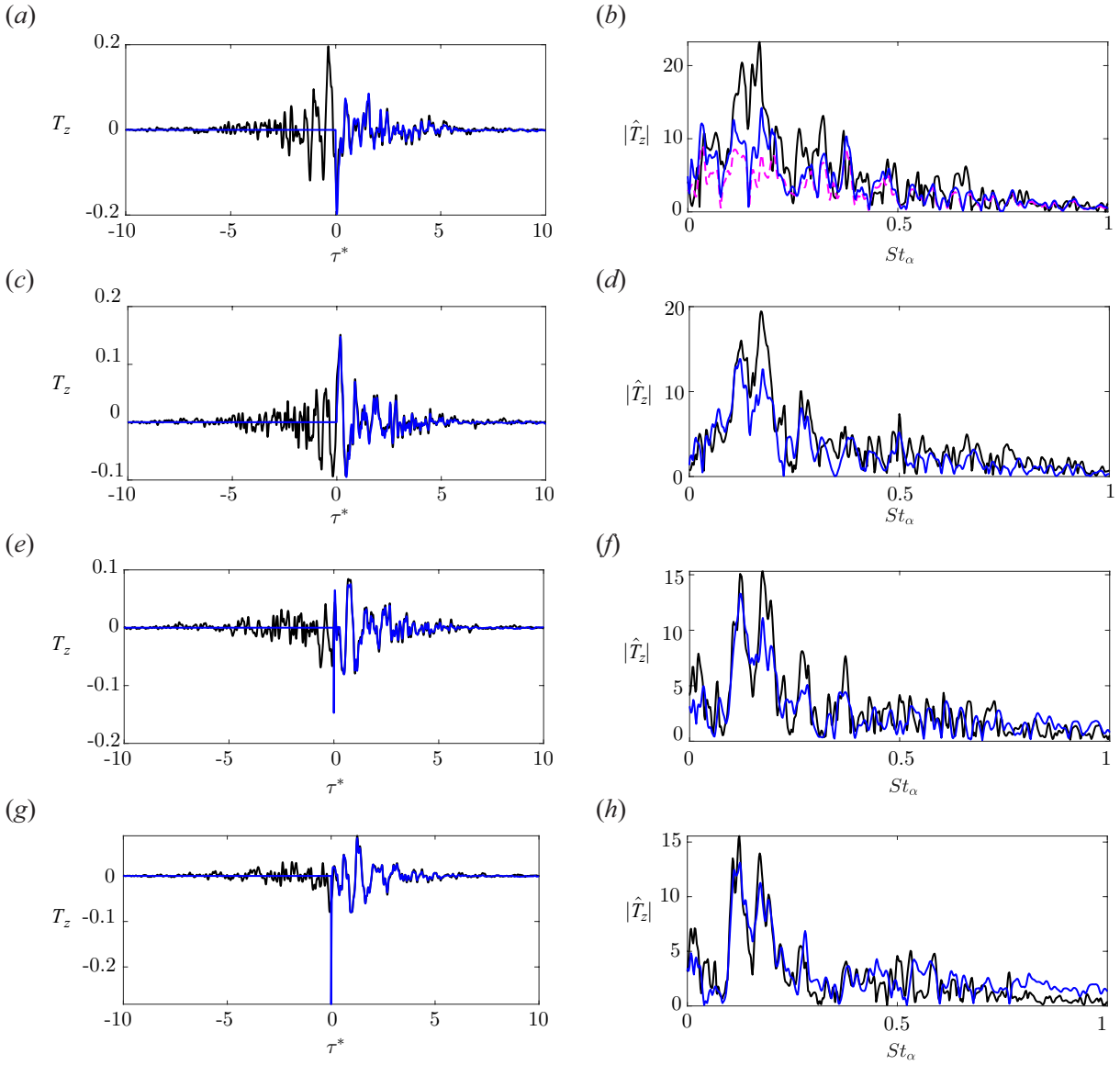

FIGURE 6.14: Estimation kernels between sensor y_1 and targets z_1 (a, b), z_2 (c, d), z_3 (e, f), and z_4 (g, h) for the spanwise-averaged flow, shown in the time domain (left column) and frequency domain (right column). The black line represents the non-causal kernel, the blue line denotes the causal kernel obtained through Wiener-Hopf decomposition, and the magenta dashed line indicates the truncated non-causal kernel.

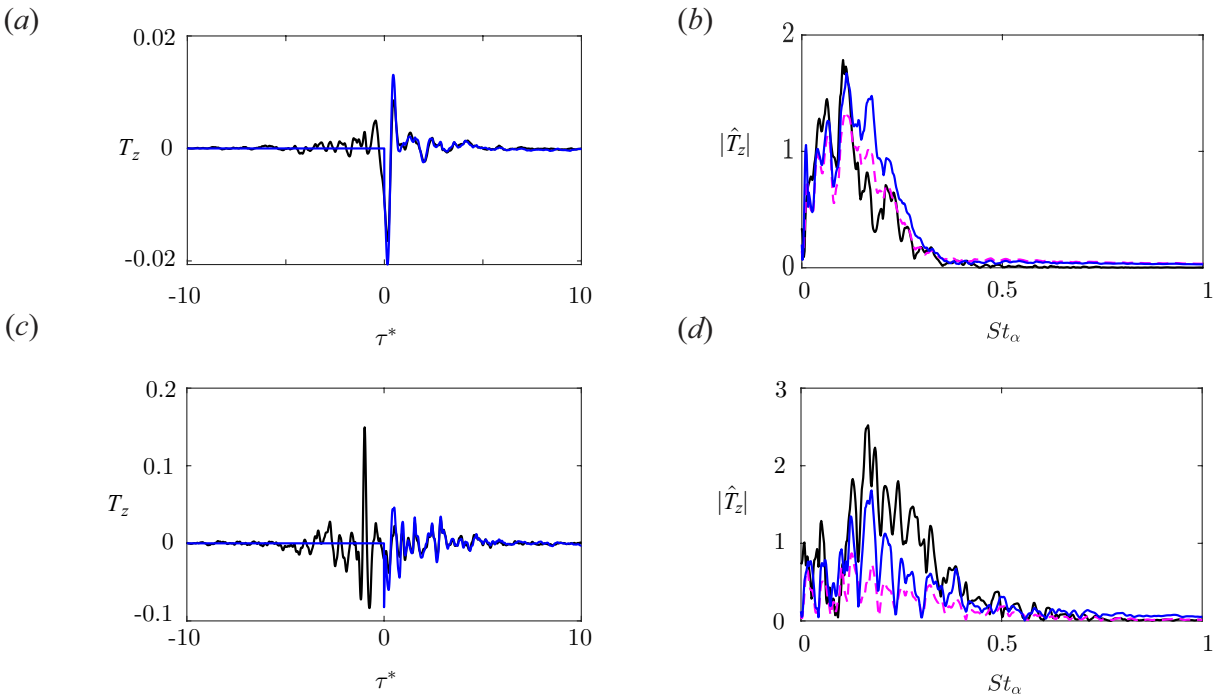

FIGURE 6.15: Estimation kernels between sensors y_1, y_2 and the target (located near the trailing edge $x/L_c = 1.1$: a, b, y_1; c, d, y_2) for the spanwise-averaged flow, presented in the time domain (left column) and frequency domain (right column). The black line represents the non-causal kernel, the blue line indicates the causal kernel obtained through Wiener-Hopf decomposition, and the magenta dashed line shows the truncated non-causal kernel.

real-time estimation, the negative peak, which contains critical travel information of the fluctuations, is truncated. The truncated non-causal kernel in the frequency domain (magenta dashed line) is notably lower in magnitude compared to the causal kernel (blue line). It is important to note that the kernels amplify the sensor measurements at dominant frequencies ($St_\alpha \approx 0.2$).

The dependent DFT parameters were appropriately selected based on an investigation of convergence in terms of estimation errors. Imposing sensor noise is numerically essential for accurately representing realistic sensor behavior and is mathematically necessary to ensure that the inversion of the PSD is well-posed. The noise level is set at 10^{-2} of the maximum PSD value of the sensor measurements. This level of noise also plays a critical role in regularizing the kernel signals.

Figure 6.15(a) and (c) display less effective non-causal kernels for the closer target at $z_0 = 1.1$, with (c) performing worse than (a). When the peak point is located in the negative domain ($\tau < 0$), the truncated non-causal kernel loses effectiveness. This is evident from the lower values of the

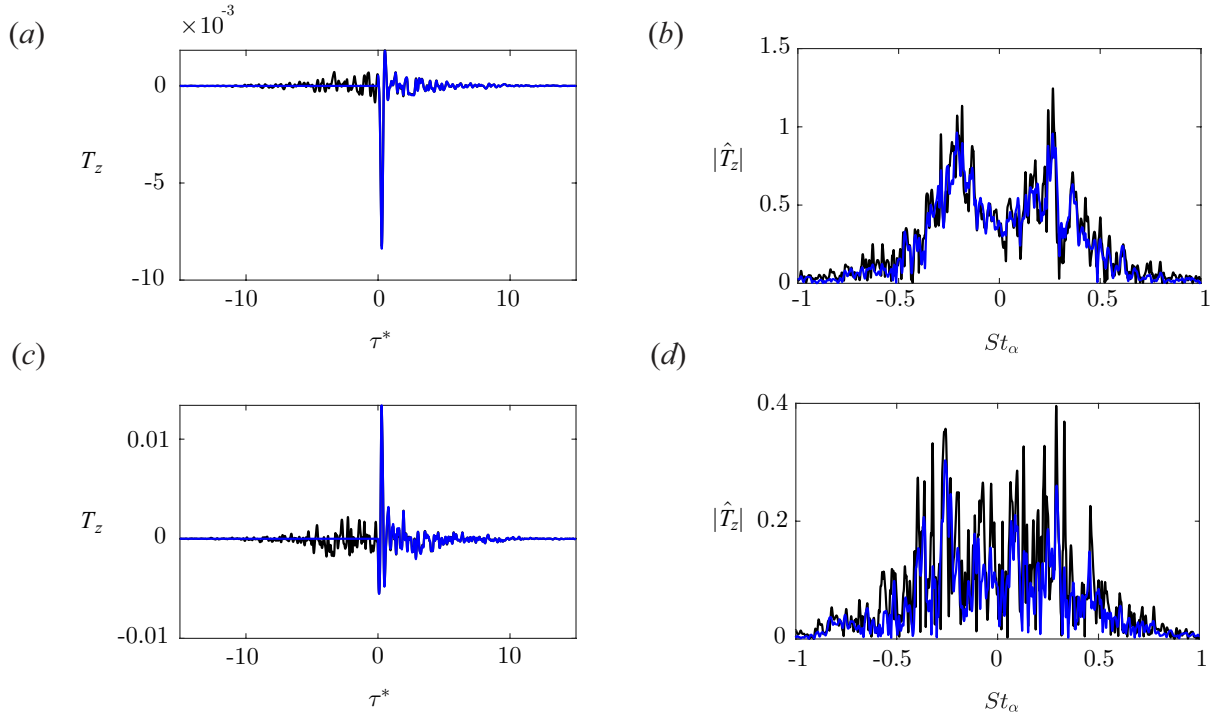

FIGURE 6.16: Estimation kernels in the time and frequency domains: (a) and (b) for $K_z = 10\pi$, and (c) and (d) for $K_z = 20\pi$. The sensor is located at y_5, and the target is at z_1, as shown in figure 6.10. The black line represents the non-causal kernel, while the blue line represents the causal kernel computed using the Wiener-Hopf decomposition.

magenta dashed line compared to the non-causal kernels, indicating a loss of crucial traveling information due to truncation. Again, when the target is close to the trailing edge, the peak point shifts leftward, resulting in poor statistical correlation between the front sensors and the targets near the trailing edge. However, this issue can be mitigated by imposing causality through Wiener-Hopf decomposition, which meaningfully improves estimation accuracy.

Similar to the estimation kernels of the spanwise-averaged flow, we also examine the kernels for the spanwise-Fourier modes. Due to the presence of imaginary components in the state arising from the Fourier transform in the spanwise direction, the computation costs for estimation increased fourfold. Additionally, the kernels are no longer symmetric at $St_\alpha = 0$, as shown in figure 6.16. The peak points are clearly visible (see figures 6.16(a) and (c)), indicating the dominance of hydrodynamic waves in this flow. Consequently, there is minimal difference in performance between the causal and truncated non-causal estimation methods. The kernels are most influential in the range of $|St_\alpha| < 0.2$, allowing them to effectively amplify sensor measurements to obtain the estimated

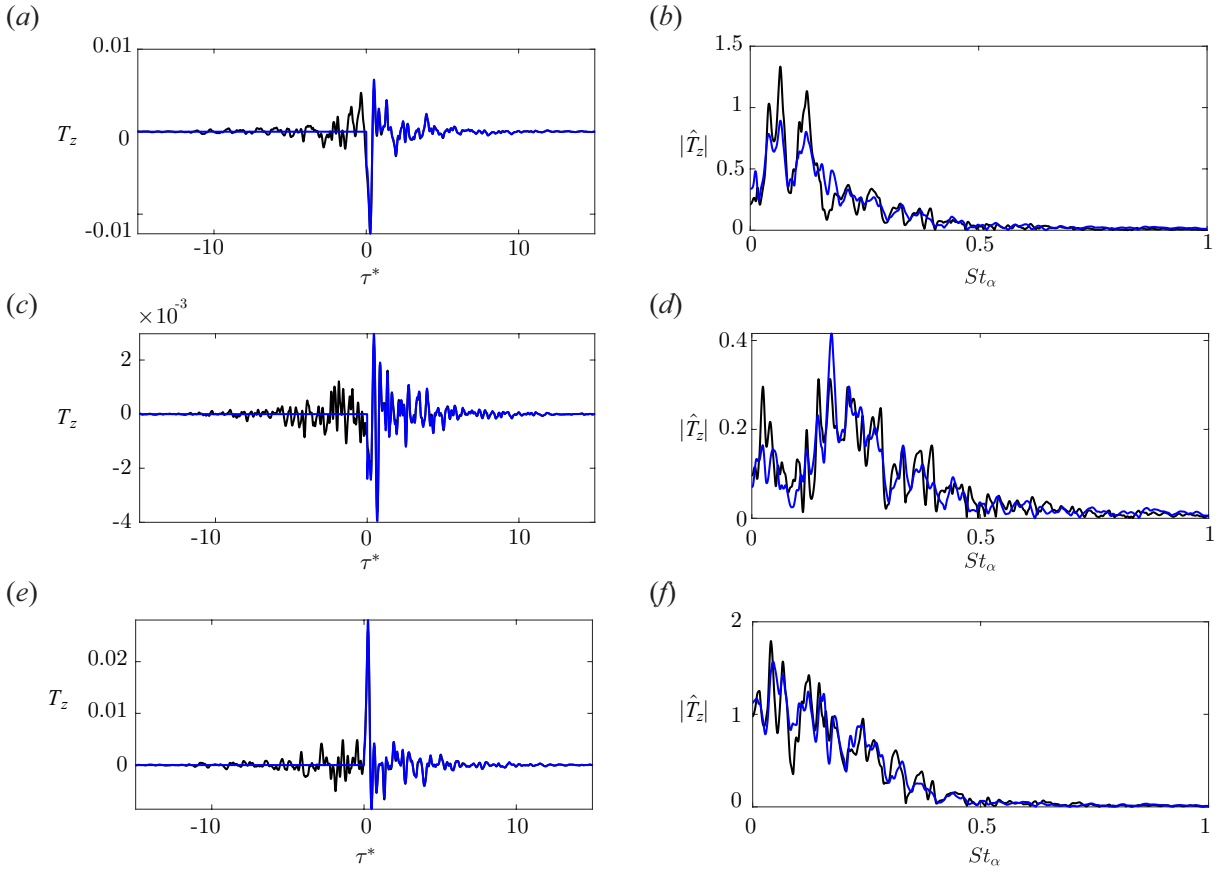

FIGURE 6.17: Estimation kernels between sensors y_1, y_5, y_6 and the target z_1 for the mid-span flow, presented in the time domain (left column) and frequency domain (right column): (a), (b): y_1, (c), (d): y_5, (e), (f): y_6.

data.

The behavior of the kernels for the mid-span flow, as shown in figure 6.17, is similar to that of the spanwise-averaged flow. The prominent peak points in the kernels between sensors (y_1, y_5) and target z_1 closely match those observed in the spanwise-averaged and spanwise-Fourier flows, as depicted in figures 6.14 and 6.16, respectively (the kernel between y_6 and z_1 also aligns well with other flows, though it is not shown here). However, the kernels for the mid-span flow exhibit more noise over a larger τ^*, indicating greater difficulty in achieving temporal convergence. In figure 6.17(a), the kernel reveals a peak point in the positive domain, whereas the same configuration for the spanwise-averaged flow shows the kernel's peak in the negative domain. This discrepancy may stem from smaller spatial structures, particularly acoustic waves that propagate upstream, and reduced laminar effects in the mid-span flow near the front area of the suction surface. These factors

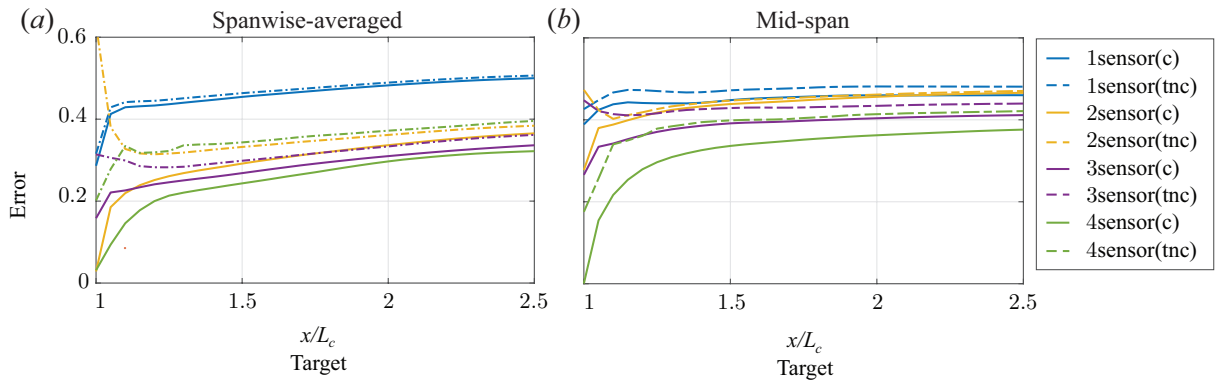

FIGURE 6.18: Estimation error along the trailing edge for spanwise-averaged and mid-span flows using one sensor (y_5), two sensors (y_5, y_6), three sensors (y_5, y_6, y_4), and four sensors (y_5, y_6, y_4, y_1).

contribute to a more convective flow effect, resulting in higher accuracy for truncated non-causal estimation. The kernel between y_4 and z_1 is similar to that between y_5 and z_1 within the mid-span flow, so it is omitted from this figure. Both causal and truncated non-causal kernels for targets further downstream (z_2, z_3, z_4) perform similarly due to their peak points residing in the positive domain.

6.3.4 Estimation results

By selecting sensor locations y_1, y_4, y_5, and y_6 (see figure 6.10(a)) based on the investigation of the most effective locations in §6.3.1, we show the estimation errors for spanwise-averaged and mid-span flows along the trailing edge as additional sensors are introduced, as shown in figure 6.18. The use of sensor y_5 alone does not have big difference between causal estimation and truncated non-causal estimation. However, adding a sensor (y_6) markedly improved estimation accuracy compared to using one sensor. With these two sensors, truncated non-causal estimation performs poorly near the trailing edge, whereas causal estimation remains accurate, which is consistent with the difference we observed in the kernels. The truncated non-causal estimation recovered the accuracy as the target is further, but it is not as accurate as casual estimation. The inclusion of a third sensor (y_4) alongside y_5 and y_6 results in a slight improvement. The best estimation results are achieved using all four sensors (y_1, y_4, y_5, y_6). This sensor configuration has higher accuracy than the use of six sensors uniformly distributed on the pressure side of the airfoil, as reported in

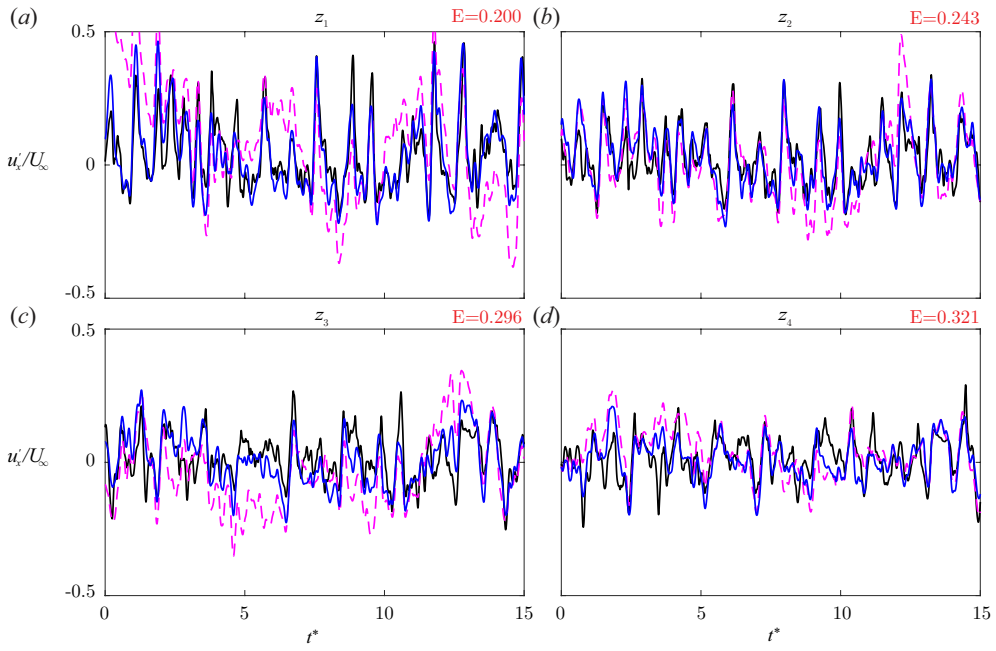

FIGURE 6.19: Estimation of u_x' over time for the spanwise-averaged flow using four sensors for the targets: (a) z_1, (b) z_2, (c) z_3, and (d) z_4. The true data from LES is shown in black, with causal estimation in blue and truncated non-causal estimation in magenta (dashed line). The estimation error is indicated in red in the top right corner.

our previous work [Jung and Towne, 2024b].

Figure 6.19 presents the estimated time-series of u_x' using the four sensors (y_1, y_4, y_5, y_6). The causal estimation error, as defined by (6.3), is displayed in the top right corner. As anticipated, the estimation errors increase as the distance between the sensor and the target grows. The Wiener-Hopf approach significantly improved the estimation accuracy for the close target to the trailing edge in figure 6.19(a). The difference in the estimation accuracy between TNC and C is decreased as the target is further located in the downstream direction. The spanwise-averaged flow is the most structured in scale, leading to the best estimation results among the four cases we investigated.

Figures 6.20 and 6.21 present the time-series estimation of the real part of $\hat{u}x'$ for the spanwise-Fourier modes $[kz = 10\pi, 20\pi]$. As we expected, as the spanwise wavenumber increases, the estimation accuracy decreases. The kernels based on the resolvent operators at the frequencies associated with lower energetic gains result in low estimation accuracy. Smaller scales in the flow, such as $k_z = 20\pi$ compared to $k_z = 10\pi$, reduce the sensor's ability to capture eddies,

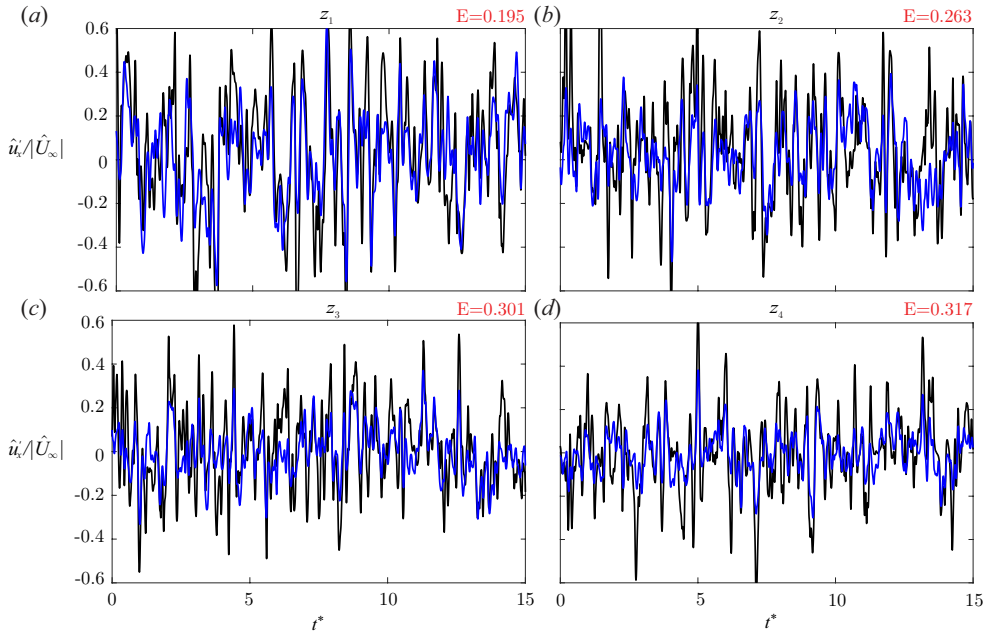

FIGURE 6.20: Estimation of u_x' over time for the spanwise-Fourier mode $k_z = 10\pi$ using four sensors for the targets: (a) z_1, (b) z_2, (c) z_3, and (d) z_4. The true data from LES is shown in black, with causal estimation in blue. The estimation error is indicated in red in the top right corner.

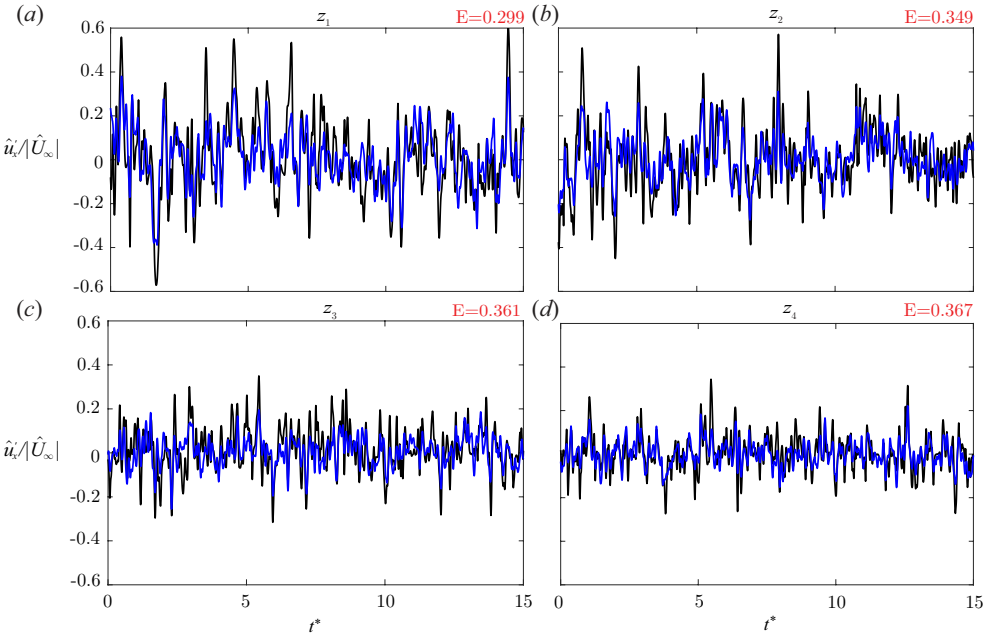

FIGURE 6.21: Estimation of u_x' over time for the spanwise-Fourier mode $k_z = 20\pi$ using four sensors for the targets: (a) z_1, (b) z_2, (c) z_3, and (d) z_4. The true data from LES is shown in black, with causal estimation in blue. The estimation error is indicated in red in the top right corner.

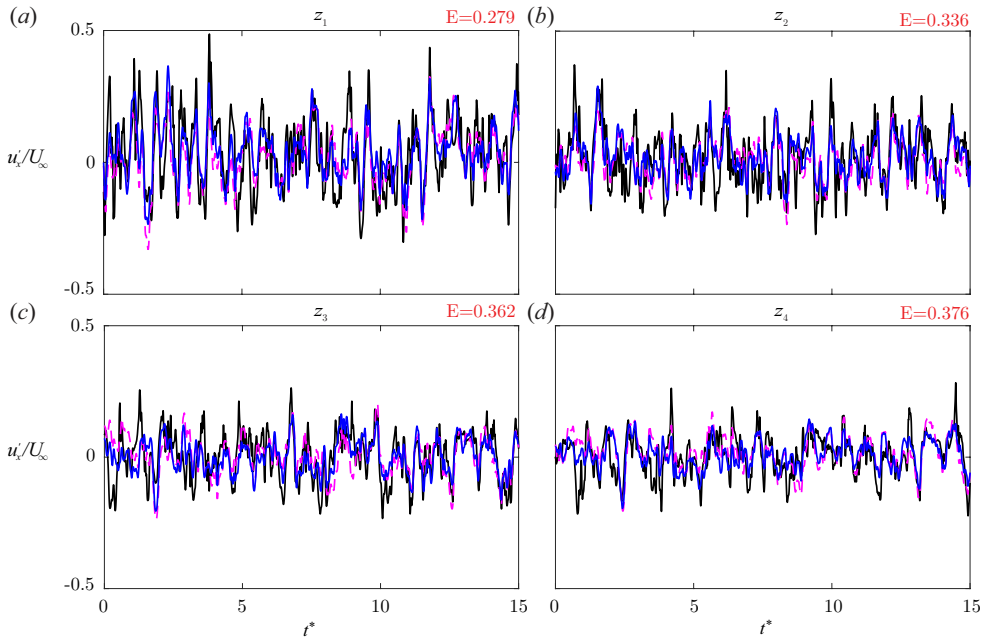

FIGURE 6.22: Estimation of u'_x over time for the mid-span flow using four sensors for the targets: (*a*) z_1, (*b*) z_2, (*c*) z_3, and (*d*) z_4. The true data from LES is shown in black, with causal estimation in blue and truncated non-causal estimation in magenta (dashed line). The estimation error is indicated in red in the top right corner.

further resulting in the lower estimation accuracy for $k_z = 20\pi$. The TNC estimation for the spanwise-Fourier modes is similar to the causal approach, so we have omitted these results from figures 6.20 and 6.21. For the mid-span flow, as shown in figure 6.22, the time-series velocity fluctuations exhibit more random oscillations compared to the other three flows. Nevertheless, the overall trend of velocity fluctuations over time is well predicted, considering the broad trend of flow dynamics. Although the sensor may not fully capture the footprint of turbulence, the estimation remains effective.

Figures 6.23 and 6.24 show three different snapshots of causal estimation in the extended wake region, using the same sensor configuration as in figures 6.19 and 6.22 for the spanwise-averaged and mid-span flows. A 100-period interval based on the dominant frequency was considered, and the three unique phases were selected and uniformly distributed within this period. Although the small-scale structures are not fully captured due to the limitations of the sensors, the causal resolvent-based estimator effectively estimates the wake fluctuations.

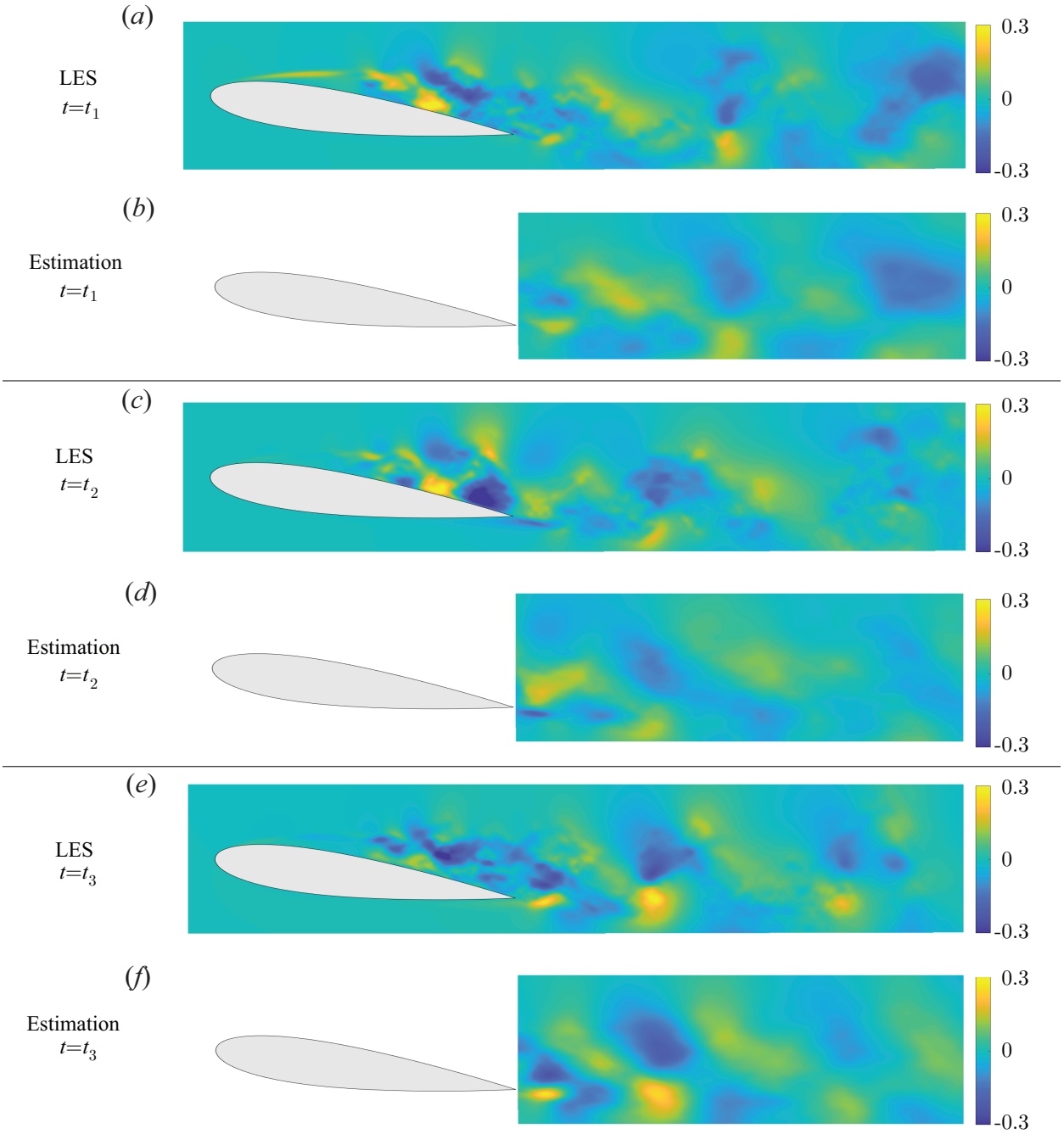

FIGURE 6.23: LES and estimation snapshots of u'_x across the extended wake region for the spanwise-averaged flow, utilizing four sensors. The times t_1, t_2, and t_3 were chosen to represent three distinct phases based on the dominant vortex shedding frequency.

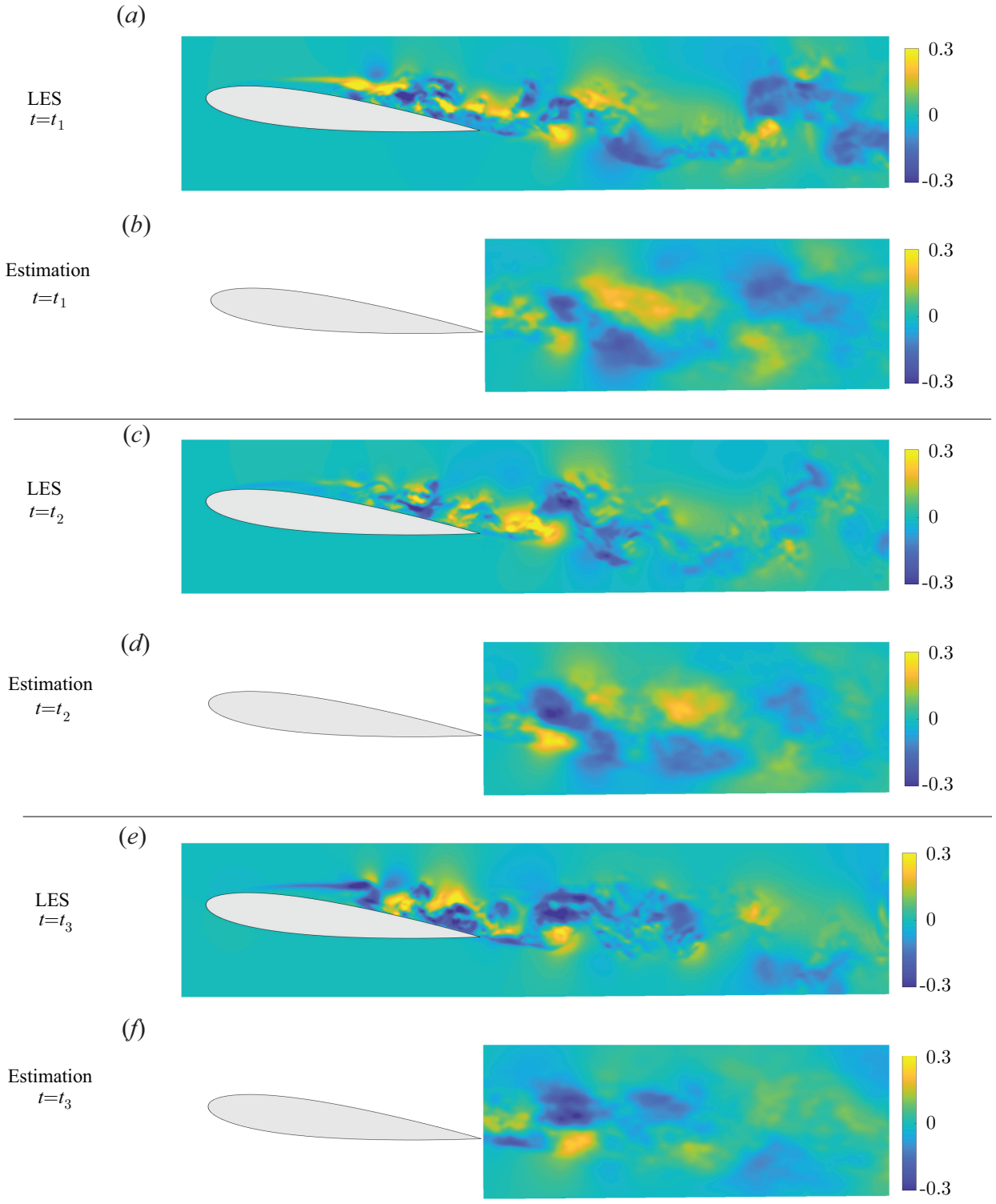

FIGURE 6.24: LES and estimation snapshots of u'_x across the extended wake region for the mid-span flow, utilizing four sensors. The times t_1, t_2, and t_3 were chosen to represent three distinct phases based on the dominant vortex shedding frequency.

6.4 Chapter Summary

Our study employs resolvent-based estimation to predict turbulent fluctuations in the wake of a NACA0012 airfoil at a moderate chord-based Reynolds number of $Re_{Lc} = 23,000$, Mach number of $Ma_\infty \equiv U_\infty/c_\infty = 0.3$, and an angle of attack of $\alpha = 6°$. Using a data-driven approach, we construct resolvent-based kernels capable of statistically accounting for the nonlinearity inherent in turbulent flow dynamics. To impose causality, we employ the Wiener-Hopf formalism, facilitating real-time application using past and present measurements. We demonstrate effectiveness in estimating turbulent velocity fluctuations in time within the spanwise-averaged, spanwise-Fourier, and mid-span flows. Our approach outperforms the truncated non-causal estimator using colored forcing statistics, particularly when sensors are positioned ahead of the airfoil surface with the target in close proximity to the trailing edge for both flow cases. Overall, the causal estimator demonstrates superior accuracy compared to the truncated non-causal estimator. We also achieved estimation of the entire wake region using only the available sensor measurements.

CHAPTER 7

Conclusions

This thesis explores the application of resolvent-based estimation and control approaches to aerodynamic flows, specifically focusing on transitional flow over a backward-facing step and laminar and turbulent flows over an airfoil. The thesis begins with a detailed description of the physical characteristics of these flows, followed by an explanation of the Navier-Stokes equations, including their linearized forms. A brief overview of classical estimation and control methods is then provided, leading into an in-depth discussion of resolvent analysis for flow estimation and control. The theoretical foundations of resolvent-based methods are reviewed, with numerical approaches elaborated upon in the subsequent chapter. Finally, the results of applying these methods to backward-facing step, laminar airfoil, and turbulent airfoil cases are presented.

Under similar assumptions, our estimator and controller converge to the Kalman filter and LQG controller. However, our approach can incorporate the nonlinear terms of the Navier-Stokes equations using colored-in-time statistics, leading to significantly higher estimator accuracy and improved controller performance. To develop the estimator and controller, we employed two computational methods: an operator-based approach and a data-driven approach. The operator-based approach is computationally efficient, does not require a priori model reduction, and accounts for the time-correlated statistics of the nonlinear terms from the Navier-Stokes equations that act as a forcing on the linear dynamics. The data-driven approach, which circumvents the need to construct linearized Navier-Stokes operators, naturally incorporates these colored statistics of the nonlinear terms. We also applied the Wiener-Hopf formalism to enforce causality, allowing the use of only available measurements, which is optimal for real-time estimation and control.

This thesis makes significant contributions to the development and implementation of resolvent-based frameworks. First, it demonstrates the integration and execution of resolvent-based estimation

and control approaches within a high-fidelity CFD simulation. The primary focus is on implementing these methods within the compressible flow solver (CharLES), emphasizing their potential application in high-performance computing for large-scale problems. The incompressible flow solver (Nek5000) is implemented to demonstrate and validate the approach with simpler flow cases, such as backward-facing step flows. Specifically, the linearized Navier-Stokes operator developed in this work is accurate and applicable for parallel computing, making it a powerful tool for large-scale applications. Using a parallel time-stepping approach significantly accelerates computations when handling large-scale linearized Navier-Stokes operators, including using a parallel adjoint solver efficiently. Additionally, the streaming Fourier transform within a solver is valuable for saving memory for constructing cross-spectral densities, which are necessary for building kernels. Another important contribution is the extraction of nonlinear terms of Navier-Stokes equations, which can be applied to other methodologies. Lastly, we solve the Wiener-Hopf problems directly within the solver to minimize reliance on post-processing tools such as MATLAB and to enhance computational efficiency by enabling faster routines with reduced memory usage.

The second major contribution of the thesis is the application of these tools to aerodynamic flows, including backward-facing step (BFS) flow and laminar and turbulent flows over airfoils. In the BFS case, we applied resolvent-based estimation and control to the flow at $Re = 500$ within an incompressible flow solver, which was successfully achieved in both linear and nonlinear regimes. Using three sensors and actuators for estimation and control, the estimation error is within 4%, and the control performance, measured by the energy reduction of fluctuations, is around 96% for the linear system. These results are similar in nonlinear systems, especially when low-amplitude forcing is applied, as the nonlinear system exhibits linear behavior under such conditions. For high-amplitude forcing, which amplifies perturbations by $20 - 30\%$ relative to the base flow in the nonlinear system, the estimation error increases to approximately 24%. Nevertheless, even with this high-amplitude forcing, the control still adheres to the linear assumption and achieves a 96% reduction in perturbation energy. We also investigated the placement of sensors and actuators on the surface, considering various configurations: upstream of the step, at the step, downstream of the step, and mixed arrangements. When at least one sensor and one actuator are placed upstream of the step, the performance is effective. As the number of sensors and actuators increases, the control performance improves, reaching a plateau after five. Overall, the difference in RMS perturbation

reduction rates between placements within the flow and on the surface was approximately 25%.

For the laminar flow over an airfoil, we successfully applied the approaches to a two-dimensional NACA 0012 airfoil at $Ma_\infty = 0.3$, $Re_{L_c} = 5000$, and $\alpha = 6.5°$. We obtained the mean flow through direct numerical simulation and performed global stability and resolvent analysis around this mean flow to identify the dominant frequencies of the flow and verify the accuracy of the linearized Naver-Stokes operator. Random upstream perturbations were introduced to disrupt the periodic limit cycle caused by vortex shedding, inducing chaotic fluctuations. We then conducted resolvent-based estimation and control on both linear and nonlinear systems under these conditions. Our results demonstrated that resolvent-based kernels are effective in estimating and controlling chaotic fluctuations in the wake of an airfoil. The performance of both estimation and control is enhanced when sensors and actuators are strategically placed in effective locations. To determine these effective placements, we investigated estimation errors and employed a streamline strategy. While we addressed the estimation across the entire wake region, we found that controlling the entire region yields results similar to targeting a single point. In the linear system, the estimation error is approximately 8% with two sensors, and the control performance in terms of the energy reduction of the velocity fluctuations reaches 85% using two actuators. For the nonlinear system, the estimation error increases to around 30% with four sensors, while the control performance improves to 98% using four actuators and two controllers.

In the case of the turbulent wake, we predicted turbulent fluctuations behind a NACA0012 airfoil at a moderate chord-based Reynolds number of $ReLc = 23,000$, a Mach number of $Ma\infty \equiv U_\infty/c_\infty = 0.3$, and an angle of attack of $\alpha = 6°$. Using a data-driven approach, we developed resolvent-based kernels that statistically account for the nonlinearities inherent in turbulent flow dynamics. Similar to the laminar case, we applied the Wiener-Hopf formalism to enforce causality on the kernels, enabling real-time application using past and present measurements. We demonstrated the effectiveness of this approach in estimating turbulent velocity fluctuations over time within the spanwise-averaged, spanwise-Fourier, and mid-span flows. Our method outperformed the truncated non-causal estimator using colored forcing statistics, particularly when sensors were positioned ahead of the airfoil surface, with the target located near the trailing edge for both flow cases. Overall, the causal estimator showed greater accuracy, with estimation errors between 20-37%, compared to the truncated non-causal estimator's 32-42% error. Additionally,

we successfully estimated the entire wake region using only the available sensor measurements.

In summary, from a methodological standpoint, beyond achieving effective estimation and control in backward-facing step flow, both approaches were successfully applied to laminar flow over an airfoil, yielding strong results. Furthermore, we achieved effective estimation in the turbulent wake case. These accomplishments are significant, as they demonstrate the feasibility of applying a new closed-loop control method in a numerical setup and achieving reliable estimation, even in the complex dynamics of turbulent flows. This work provides a solid foundation for extending these methods to other turbulent flow scenarios. From a societal perspective, this research has broad applications. Our methods can reduce wake perturbations, which is highly valuable across multiple industries. In the aerospace field, it can enhance flight control, improving safety and performance. In the automotive sector, it can help increase fuel efficiency by minimizing aerodynamic drag and reducing interactions between vehicles. In the wind energy sector, especially in wind farms with multiple turbines, reducing wake interference can significantly improve energy capture, contributing to more sustainable energy solutions. Additionally, wake perturbations are known to generate aerodynamic noise, which is a concern for rotorcraft, including drones and wind turbines, and is also related to the jet noise problem. Estimating and reducing aerodynamic noise is crucial for improving environmental conditions and enhancing the quality of life in human society.

Future work will focus on optimizing sensor and actuator placements, as well as applying control strategies to turbulent wakes behind an airfoil. In this study, we evaluated effective sensor placement based on estimation error and coherence between the sensor and the target, leading to satisfactory estimation and control results. However, the placement and the number of sensors and actuators have not yet been optimized. Addressing this will require formulating and solving a mathematical optimization problem, which will be considered in future research. Additionally, applying closed-loop control strategies to turbulent wakes is another area for future exploration. The positive effects of reducing turbulent wakes in terms of aerodynamic performance should be further investigated.

BIBLIOGRAPHY

B. R. Agrawal, A. Rosenberg, and A. Sharma. Towards identifying contribution of wake turbulence to inflow noise from wind turbines. *E3S Web Conf.*, 5:01002, 2015. ISSN 2267-1242. doi: 10.1051/e3sconf/20150501002.

M. M. Alam, Y. Zhou, H. X. Yang, H. Guo, and J. Mi. The ultra-low reynolds number airfoil wake. *Exp. Fluids*, 48(1):81–103, January 2010. ISSN 0723-4864, 1432-1114. doi: 10.1007/s00348-009-0713-7.

B. Allen. Naca airfoils. https://www.nasa.gov, Jan 2017. Retrieved 27 July 2020.

F. R. Amaral and A. V. G. Cavalieri. Large-eddy-simulation-informed resolvent-based estimation of turbulent pipe flow. *Phys. Rev. Fluids*, 8(7):074606, July 2023. ISSN 2469-990X. doi: 10.1103/PhysRevFluids.8.074606.

F. R. Amaral, A. V. G. Cavalieri, E. Martini, P. Jordan, and A. Towne. Resolvent-based estimation of turbulent channel flow using wall measurements. *J. Fluid Mech.*, 927:A17, November 2021. ISSN 0022-1120, 1469-7645. doi: 10.1017/jfm.2021.764.

X. An, D. R. Wiliams, J. D. Eldredge, and T. Colonius. Lift coefficient estimation for a rapidly pitching airfoil. *Exp. Fluids*, January 2021.

J. D. Anderson. *Fundamentals of Aerodynamics*. McGraw-Hill, 5th edition, 2010.

B. F. Armaly, F. Durst, J. C. F. Pereira, and B. Schönung. Experimental and theoretical investigation of backward-facing step flow. *J. Fluid Mech.*, 127(-1):473, February 1983. ISSN 0022-1120, 1469-7645. doi: 10.1017/S0022112083002839.

H. Ashley and M. Landahl. Aerodynamics of wings and bodies. 1985.

K. J. Asztalos, S. T. M. Dawson, and D. R. Williams. Modeling the flow state sensitivity of actuation response on a stalled airfoil. *AIAA J.*, pages 1–15, April 2021. ISSN 0001-1452, 1533-385X. doi: 10.2514/1.J060304.

D. B. S. Audiffred, A. V. G. Cavalieri, P. P. C. Brito, and E. Martini. Experimental control of tollmien-schlichting waves using the wiener-hopf formalism. *Phys. Rev. Fluids*, 8(7):073902, July 2023. ISSN 2469-990X. doi: 10.1103/PhysRevFluids.8.073902.

D. B. S. Audiffred, A. V. G. Cavalieri, I. A. Maia, E. Martini, and P. Jordan. Reactive experimental control of turbulent jets, February 2024. arXiv:2402.10860 [physics].

S. Bagheri, L. Brandt, and D. S. Henningson. Input–output analysis, model reduction and control of the flat-plate boundary layer. *J. Fluid Mech.*, 620:263–298, February 2009. ISSN 0022-1120, 1469-7645.

S. Balay, S. Abhyankar, M. Adams, J. Brown, P. Brune, K. Buschelman, L. Dalcin, A. Dener, V. Eijkhout, W. Gropp, and Others. Petsc users manual. *Argonne Natl. Lab.*, 2019.

R. J. Barthelmie and S. C. Pryor. An overview of data for wake model evaluation in the virtual wakes laboratory. *Appl. Energy*, 104:834–844, apr 2013a. ISSN 0306-2619. doi: 10.1016/j.apenergy.2012.12.013.

R. J. Barthelmie, S. C. Pryor, S. T. Frandsen, K. S. Hansen, J. G. Schepers, K. Rados, W. Schlez, A. Neubert, L. E. Jensen, and S. Neckelmann. Quantifying the impact of wind turbine wakes on power output at offshore wind farms. *J. Atmos. Oceanic Technol.*, 27(8):1302–1317, aug 2010a. ISSN 1520-0426, 0739-0572. doi: 10.1175/2010JTECHA1398.1.

R. J. Barthelmie, S. C. Pryor, S. T. Frandsen, K. S. Hansen, J. G. Schepers, K. Rados, W. Schlez, A. Neubert, L. E. Jensen, and S. Neckelmann. Quantifying the Impact of Wind Turbine Wakes on Power Output at Offshore Wind Farms. *J. Atmos. Ocean. Technol.*, 27(8):1302–1317, August 2010b. ISSN 1520-0426, 0739-0572. doi: 10.1175/2010JTECHA1398.1.

R.J. Barthelmie and S.C. Pryor. An overview of data for wake model evaluation in the Virtual Wakes Laboratory. *Appl. Energy*, 104:834–844, April 2013b. ISSN 03062619. doi: 10.1016/j.apenergy.2012.12.013.

R. Bhagwat. *Development of Stability Analysis Tools for High Speed Compressible Flows*. PhD thesis, North Carolina State University, 2020.

S. Bordas et al. A mass conservative kalman filter algorithm for computational thermo-fluid dynamics. *Materials*, 11(11):2222, 2018. doi: 10.3390/ma11112222.

R. Broglia, K.-S. Choi, P. Houston, L. Pasquale, and P. Zanchetta. Output feedback control of flow separation over an aerofoil using plasma actuators. *Int. J. Numer. Anal. Model.*, 15, 2018.

S. L. Brunton and B. R. Noack. Closed-loop turbulence control: Progress and challenges. *Appl. Mech. Rev.*, 67(5), September 2015. ISSN 0003-6900, 2379-0407.

G. A. Brès, F. E. Ham, J. W. Nichols, and S. K. Lele. Unstructured large-eddy simulations of supersonic jets. *AIAA J.*, 55:1164–1184, April 2017. ISSN 0001-1452, 1533-385X.

G. A. Brès, P. Jordan, V. Jaunet, M. Le Rallic, A. V. G. Cavalieri, A. Towne, S. K. Lele, T. Colonius, and O. T. Schmidt. Importance of the nozzle-exit boundary-layer state in subsonic turbulent jets. *J. Fluid Mech.*, 851:83–124, September 2018. ISSN 0022-1120, 1469-7645. doi: 10.1017/jfm.2018.476.

T. Cebeci, R. W. Clark, K. C. Chang, N. D. Halsey, and K. Lee. Airfoils with separation and the resulting wakes. *J. Fluid Mech.*, 163:323–347, February 1986. ISSN 0022-1120, 1469-7645. doi: 10.1017/S0022112086002318.

J. Chang, Q. Zhang, L. He, and Y. Zhou. Shedding vortex characteristics analysis of naca 0012 airfoil at low reynolds numbers. *Energy Rep.*, 8:156–174, July 2022. ISSN 2352-4847. doi: 10.1016/j.egyr.2022.01.149.

K. K. Chen and C. W. Rowley. h_2 optimal actuator and sensor placement in the linearised complex ginzburg–landau system. *J. Fluid Mech.*, 681:241–260, August 2011. ISSN 0022-1120, 1469-7645. doi: 10.1017/jfm.2011.195.

Boa-Teh Chu. On the energy transfer to small disturbances in fluid flow (part i). *Acta Mechanica*, 1:215–234, September 1965. ISSN 0001-5970, 1619-6937.

K. B. Chun and H. J. Sung. Control of turbulent separated flow over a backward-facing step by local forcing. *Exp. Fluids*, 21(6):417–426, November 1996. ISSN 0723-4864, 1432-1114. doi: 10.1007/BF00189044.

C. H. Colburn, J. B. Cessna, and T. R. Bewley. State estimation in wall-bounded flow systems. part 3. the ensemble kalman filter. *J. Fluid Mech.*, 682:289–303, September 2011. ISSN 0022-1120, 1469-7645.

T. Colonius and D. R. Williams. Control of vortex shedding on two- and three-dimensional aerofoils. *Philos. Trans. R. Soc. A*, 369(1940):1525–1539, April 2011. ISSN 1364-503X, 1471-2962. doi: 10.1098/rsta.2010.0355.

D. A. Cook, J. Thome, J. M. Brock, J. W. Nichols, and G. V. Candler. *Understanding Effects of Nose-Cone Bluntness on Hypersonic Boundary Layer Transition Using Input-Output Analysis*. 2018. doi: 10.2514/6.2018-0378.

V. Daniele and G. Lombardi. Fredholm factorization of wiener-hopf scalar and matrix kernels. *Radio Sci.*, 42(6):2007RS003673, December 2007. ISSN 0048-6604, 1944-799X. doi: 10.1029/2007RS003673.

A. Ducoin, J.-Ch. Loiseau, and J.-Ch. Robinet. Numerical investigation of the interaction between laminar to turbulent transition and the wake of an airfoil. *European J. Mech. - B/Fluids*, 57: 231–248, May 2016. ISSN 09977546. doi: 10.1016/j.euromechflu.2016.01.005.

T. Duriez, S. L. Brunton, and B. R. Noack. *Machine Learning Control – Taming Nonlinear Dynamics and Turbulence*, volume 116 of *Fluid Mechanics and Its Applications*. Springer, Cham, 2017. ISBN 978-3-319-40623-7 978-3-319-40624-4. doi: 10.1007/978-3-319-40624-4.

T. Déda, W. Wolf, and S. Dawson. Neural networks in feedback for flow analysis, sensor placement and control, August 2023. arXiv:2308.13029 [physics].

A. Einstein. The foundation of the general theory of relativity. *Ann. Phys.*, 354(7):769, 1916. doi: 10.1002/andp.19163540702.

N. Fabbiane, O. Semeraro, S. Bagheri, and D. S. Henningson. Adaptive and model-based control theory applied to convectively unstable flows. *Appl. Mech. Rev.*, 66:060801, November 2014. ISSN 0003-6900, 2379-0407.

N. Fabbiane, B. Simon, F. Fischer, S. Grundmann, S. Bagheri, and D. S. Henningson. On the role of adaptivity for robust laminar flow control. *J. Fluid Mech.*, 767:R1, March 2015. ISSN 0022-1120, 1469-7645.

N. Fabbiane, S. Bagheri, and D. S. Henningson. Energy efficiency and performance limitations of linear adaptive control for transition delay. *J. Fluid Mech.*, 810:60–81, January 2017. ISSN 0022-1120, 1469-7645.

A. Farghadan, E. Martini, and A. Towne. Scalable resolvent analysis for three-dimensional flows, September 2023. arXiv:2309.04617 [physics].

A. Farghadan, J. Jung, R. Bhagwat, and A. Towne. Efficient harmonic resolvent analysis via time stepping. *Theor. Comput. Fluid Dyn.*, May 2024. ISSN 0935-4964, 1432-2250. doi: 10.1007/s00162-024-00694-1.

J. E. Ffowcs Williams and B. C. Zhao. The active control of vortex shedding. *J. Fluids Struct.*, 3 (2):115–122, March 1989. ISSN 0889-9746. doi: 10.1016/S0889-9746(89)90026-1.

P. F. Fischer, J. W. Lottes, and S. G. Kerkemeier. Nek5000: Open source spectral element cfd solver, 2008.

T. L. B. Flinois and A. S. Morgans. Feedback control of unstable flows: A direct modelling approach using the eigensystem realisation algorithm. *J. Fluid Mech.*, 793:41–78, April 2016. ISSN 0022-1120, 1469-7645. doi: 10.1017/jfm.2016.111.

D. P. M. Fosas, D. Sipp, and P. J. Schmid. Efficient evaluation of the direct and adjoint linearized dynamics from compressible flow solvers. *J. Comput. Phys.*, 231(23):7739–7755, October 2012. ISSN 0021-9991. doi: 10.1016/j.jcp.2012.06.038.

M. Frigo and S. G. Johnson. The design and implementation of fftw3. *Proc. IEEE*, 93(2):216–231, February 2005. ISSN 0018-9219. doi: 10.1109/JPROC.2004.840301.

N. Fujisawa, Y. Kawaji, and K. Ikemoto. Feedback control of vortex shedding from a circular cylinder by rotational oscillations. *J. Fluids Struct.*, 15(1):23–37, Jan 2001. ISSN 0889-9746. doi: 10.1006/jfls.2000.0323.

R. Furrer and T. Bengtsson. State estimation in wall-bounded flow systems. part 3. the ensemble kalman filter. *J. Fluid Mech.*, 534:263–294, 2007. doi: 10.1017/S0022112005004575.

M. Gad-el Hak and D. M. Bushnell. Separation control: Review. *J. Fluids Eng.*, 113(1):5–30, March 1991. ISSN 0098-2202, 1528-901X. doi: 10.1115/1.2926497.

I. S. Gartshore. Two-dimensional turbulent wakes. *J. Fluid Mech.*, 30(3):547–560, November 1967. ISSN 0022-1120, 1469-7645. doi: 10.1017/S0022112067001600.

S. Ghaemi and F. Scarano. Counter-hairpin vortices in the turbulent wake of a sharp trailing edge. *J. Fluid Mech.*, 689:317–356, December 2011. ISSN 0022-1120, 1469-7645. doi: 10.1017/jfm.2011.431.

D. F. Gomez, F. Lagor, P. B. Kirk, A. Lind, A. R. Jones, and D. A. Paley. Unsteady dmd-based flow field estimation from embedded pressure sensors in an actuated airfoil. In *AIAA SCITECH Forum*, January 2019. ISBN 978-1-62410-578-4.

S. Gottlieb and C. Shu. Total variation diminishing runge-kutta schemes. *Math. Comput.*, 67, 08 1996. doi: 10.1090/S0025-5718-98-00913-2.

S. Gottlieb and C. Shu. Total variation diminishing runge-kutta schemes. *Math. Comput.*, 67: 73–85, 1998.

A. Gross, C. Marks, and R. Sondergaard. Laminar separation control for eppler 387 airfoil based on resolvent analysis. *AIAA J.*, 62(4):1487–1502, April 2024. ISSN 0001-1452, 1533-385X. doi: 10.2514/1.J063492.

S. Gupta, J. Zhao, A. Sharma, A. Agrawal, K. Hourigan, and M. C. Thompson. Two- and three-dimensional wake transitions of a NACA0012 airfoil. *J. Fluid Mech.*, 954:A26, January 2023. ISSN 0022-1120, 1469-7645. doi: 10.1017/jfm.2022.958.

C. Hah, P. Catalano, and M. Amato. Applying ensemble kalman filter to transonic flows through a two-dimensional turbine cascade. *J. Fluids Eng.*, 140(11):111201, 2019. doi: 10.1115/1.4043072.

A. Hervé, D. Sipp, P. J. Schmid, and M. Samuelides. A physics-based approach to flow control using system identification. *J. Fluid Mech.*, 702:26–58, July 2012. ISSN 0022-1120, 1469-7645. doi: 10.1017/jfm.2012.112.

M. Hočevar, B. Širok, and I. Grabec. A Turbulent-Wake Estimation Using Radial Basis Function Neural Networks. *Flow Turbul. Combust.*, 74(3):291–308, April 2005. ISSN 1386-6184, 1573-1987. doi: 10.1007/s10494-005-5728-4.

P. Huerre and P. A. Monkewitz. Local and global instabilities in spatially developing flows. *Annu. Rev. Fluid Mech.*, 1990.

S. J. Illingworth, J. P. Monty, and I. Marusic. Estimating large-scale structures in wall turbulence using linear models. *J. Fluid Mech.*, 842:146–162, May 2018. ISSN 0022-1120, 1469-7645. doi: 10.1017/jfm.2018.129.

E. N Jacobs, K. E Ward, and R. M Pinkerton. The characteristics of 78 related airfoil sections from tests in the variable-density wind tunnel. Technical Report NACA-TR-460, National Advisory Committee for Aeronautics, 1933.

J. Jeun, J. W. Nichols, and M. R. Jovanović. Input-output analysis of high-speed axisymmetric isothermal jet noise. *Phys. Fluids*, 28(4):047101, April 2016.

Z. Jiang, Z. Hu, Y. Wang, and G. Han. Advances in critical technologies for hypersonic and high-enthalpy wind tunnel. *Chin. J. Aeronaut.*, 33(12):3027–3038, December 2020. ISSN 10009361. doi: 10.1016/j.cja.2020.04.003.

B. Jin, S. J. Illingworth, and R. D. Sandberg. Feedback control of vortex shedding using a resolvent-based modelling approach. *J. Fluid Mech.*, 897:A26, August 2020. ISSN 0022-1120, 1469-7645. doi: 10.1017/jfm.2020.347.

B. Jin, S. J. Illingworth, and R. D. Sandberg. Optimal sensor and actuator placement for feedback control of vortex shedding. *J. Fluid Mech.*, 932:A2, February 2022. ISSN 0022-1120, 1469-7645. doi: 10.1017/jfm.2021.948. arXiv:2103.16802 [physics].

M. Jovanovic and B. Bamieh. Modeling flow statistics using the linearized navier-stokes equations. In *Proceedings of the 40th IEEE Conference on Decision and Control (Cat. No. 01CH37228)*, volume 5, pages 4944–4949. IEEE, 2001.

M. R. Jovanović and B. Bamieh. Componentwise energy amplification in channel flows. *J. Fluid Mech.*, 534:145–183, June 2005. ISSN 0022-1120, 1469-7645. doi: 10.1017/S0022112005004295.

J. Jung and A. Towne. Resolvent-based estimation of a turbulent wake (in preparation). *J. Fluid Mech.*, 2024a.

J. Jung and A. Towne. Toward turbulent wake estimation using a resolvent-based approach. In *AIAA SCITECH 2024 Forum*, Orlando, FL, January 2024b. AIAA. ISBN 978-1-62410-711-5. doi: 10.2514/6.2024-0057.

J. Jung, E. Martini, A. Cavalieri, P. Jordan, L. Lesshafft, and A. Towne. Optimal resolvent-based estimation for flow control. *APS Division of Fluid Dynamics*, G06:004, 2020.

J. Jung, R. Bhagwat, and A. Towne. Resolvent-based estimation of laminar flow around an airfoil. *AIAA SCITECH Forum*, 2023.

J. Jung, R. Bhagwat, and A. Towne. Resolvent-based estimation and control of laminar flow over an airfoil (submitted). *J. Fluid Mech.*, 2024.

R. E. Kalman. A new approach to linear filtering and prediction problems. *J. Basic Engng*, 82: 35–45, 1960.

R. E. Kalman. When Is a Linear Control System Optimal? *J.of Basic Engineering*, 86(1):51–60, March 1964. ISSN 0021-9223. doi: 10.1115/1.3653115.

D.-H. Kim, J.-H. Yang, J.-W. Chang, and J Chung. Boundary layer and near-wake measurements of naca 0012 airfoil at low reynolds numbers. *AIAA Paper*, 2009.

R. Kojima, T. Nonomura, A. Oyama, and K. Fujii. Large-Eddy Simulation of Low-Reynolds-Number Flow Over Thick and Thin NACA Airfoils. *J. Aircraft*, 50(1):187–196, 2013.

Y. Kojima, C. Yeh, K. Taira, and M. Kameda. Resolvent analysis on the origin of two-dimensional transonic buffet. *J. Fluid Mech.*, 885:R1, February 2020. ISSN 0022-1120, 1469-7645.

P. Koumoutsakos and I. Mezic, editors. *Control of Fluid Flow*. Number 330 in Lecture Notes in Control and Information Sciences. Springer, Berlin Heidelberg, 2006. ISBN 978-3-540-25140-8.

D. F. Kurtulus, F. Scarano, and L. David. Reduced-order kalman-filtered hybrid simulation combining particle tracking velocimetry and direct numerical simulation. *J. Fluid Mech.*, 59:308–323, 2007. doi: 10.1017/S0022112007006785.

C. Leclercq, F. Demourant, C. Poussot-Vassal, and D. Sipp. Linear iterative method for closed-loop control of quasiperiodic flows. *J. Fluid Mech.*, 868:26–65, June 2019. ISSN 0022-1120, 1469-7645. doi: 10.1017/jfm.2019.112.

C. Lin and H. Tsai. Feedback flow control on a plunging circular cylinder. *Phys. Fluids*, 36(4): 047126, April 2024. ISSN 1070-6631, 1089-7666. doi: 10.1063/5.0203558.

C. Lin, M. Tsai, and H. Tsai. Flow control of a plunging cylinder based on resolvent analysis. *J. Fluid Mech.*, 967:A41, July 2023. ISSN 0022-1120, 1469-7645. doi: 10.1017/jfm.2023.526.

Q. Liu, Y. Sun, C. Yeh, L. S. Ukeiley, L. N. Cattafesta, and K. Taira. Unsteady control of supersonic turbulent cavity flow based on resolvent analysis. *J. Fluid Mech.*, 925:A5, October 2021. ISSN 0022-1120, 1469-7645.

Z. Ma, S. Ahuja, and C. W. Rowley. Reduced-order models for control of fluids using the eigensystem realization algorithm. *Theor. Comput. Fluid Dyn.*, 25(1-4):233–247, June 2011. ISSN 0935-4964, 1432-2250. doi: 10.1007/s00162-010-0184-8.

I. A. Maia, P. Jordan, A. V. G. Cavalieri, E. Martini, K. Sasaki, and F. J. Silvestre. Real-time reactive control of stochastic disturbances in forced turbulent jets. *Phys. Rev. Fluids*, 6(12): 123901, December 2021. ISSN 2469-990X. doi: 10.1103/PhysRevFluids.6.123901.

K. Manohar, B. W. Brunton, J. N. Kutz, and S. L. Brunton. Data-driven sparse sensor placement for reconstruction: Demonstrating the benefits of exploiting known patterns. *IEEE Control Syst.*, 38(3):63–86, June 2018. ISSN 1066-033X, 1941-000X. doi: 10.1109/MCS.2018.2810460.

J. F. Manwell, J. G. McGowan, and A. L. Rogers. *Wind Energy Explained: Theory, Design and Application*. Wiley, 2002.

O. Marquet, J.S. Leontini, J. Zhao, and M.C. Thompson. Hysteresis of two-dimensional flows around a NACA0012 airfoil at Re = 5000 and linear analyses of their mean flow. *Intl. J. Heat and Fluid Flow*, 94:108920, April 2022. ISSN 0142727X.

F. Martinelli. Feedback control of turbulent wall flows. *PhD thesis*, 2009.

E. Martini, A. V. G. Cavalieri, P. Jordan, A. Towne, and L. Lesshafft. Resolvent-based optimal estimation of transitional and turbulent flows. *J. Fluid Mech.*, 900:A2, October 2020. ISSN 0022-1120, 1469-7645.

E. Martini, J. Jung, A. Cavalieri, P. Jordan, and A. Towne. Resolvent-based tools for optimal estimation and control via the wiener–hopf formalism. *J. Fluid Mech.*, 937:A19, April 2022.

B. J. McKeon and A. S. Sharma. A critical-layer framework for turbulent pipe flow. *J. Fluid Mech.*, 658:336–382, September 2010.

M. Meldi and A. Poux. A reduced order model based on kalman filtering for sequential data assimilation of turbulent flows. *J. Comput. Phys.*, 347:207–234, October 2017. ISSN 0021-9991. doi: 10.1016/j.jcp.2017.06.042.

P. Meliga, D. Sipp, and J.-M. Chomaz. Open-loop control of compressible afterbody flows using adjoint methods. *Phys. Fluids*, 22(5):054109, May 2010. ISSN 1070-6631, 1089-7666. doi: 10.1063/1.3425625.

C. Min and H. Choi. Suboptimal feedback control of vortex shedding at low reynolds numbers. *J. Fluid Mech.*, 401:123–156, December 1999. ISSN 0022-1120, 1469-7645. doi: 10.1017/S002211209900659X.

P. Morra, K. Sasaki, A. Hanifi, A. V. G. Cavalieri, and D. S. Henningson. A realizable data-driven approach to delay bypass transition with control theory. *J. Fluid Mech.*, 883:A33, January 2020. ISSN 0022-1120, 1469-7645. doi: 10.1017/jfm.2019.793.

P. M. Munday and K. Taira. Effects of Wall-Normal and Angular Momentum Injections in Airfoil Separation Control. *AIAA J.*, 56(5):1830–1842, May 2018.

M. Natarajan, J. B. Freund, and D. J. Bodony. Actuator selection and placement for localized feedback flow control. *J. Fluid Mech.*, 809:775–792, December 2016. ISSN 0022-1120, 1469-7645. doi: 10.1017/jfm.2016.700.

N. Navaneeth and S. R. Chakravarthy. A kalman filter-based approach for flow field estimation using reduced-order models. *J. Fluid Mech.*, 872:1125–1150, 2019.

E. J. Nielsen and W. L. Kleb. Efficient construction of discrete adjoint operators on unstructured grids using complex variables. *AIAA J.*, 44(4):827–836, 2006. doi: 10.2514/1.15830.

B. Noble. *Methods Based on the Wiener-Hopf Technique for the Solution of Partial Differential Equations*, volume 7 of *Int. Ser. Monogr. Pure Appl. Math.* Pergamon Press, New York, 1958.

A. C. Or and J. L. Speyer. Robust control for convection suppression in a fluid layer: The effects of boundary properties, actuator lag, and major parameter uncertainties. *Phys. Rev. E*, 73(4): 046307, April 2006. ISSN 1539-3755, 1550-2376. doi: 10.1103/PhysRevE.73.046307.

V. Oruç. Passive control of flow structures around a circular cylinder by using screen. *J. Fluids Struct.*, 33:229–242, August 2012. ISSN 0889-9746. doi: 10.1016/j.jfluidstructs.2012.05.002.

R. Paris, S. Beneddine, and J. Dandois. Robust flow control and optimal sensor placement using deep reinforcement learning. *J. Fluid Mech.*, 913:A25, April 2021. ISSN 0022-1120, 1469-7645. doi: 10.1017/jfm.2020.1170.

L. Pasquale, R. Broglia, K.-S. Choi, D. Durante, and P. Zanchetta. Robust control of flow separation over a pitching aerofoil using plasma actuators. *IFAC-PapersOnLine*, 50(1):11120–11125, July 2017. ISSN 2405-8963.

A. T. Patera. A spectral element method for fluid dynamics: Laminar flow in a channel expansion. *J. Comput. Phys.*, 54(3):468–488, June 1984. ISSN 0021-9991. doi: 10.1016/0021-9991(84)90128-1.

J. Rabault, M. Kuchta, A. Jensen, U. Réglade, and N. Cerardi. Artificial neural networks trained through deep reinforcement learning discover control strategies for active flow control. *J. Fluid Mech.*, 865:281–302, April 2019. ISSN 0022-1120, 1469-7645. doi: 10.1017/jfm.2019.62.

M. Rafiee, Q. Wu, and A. M. Bayen. Kalman filter based estimation of flow states in open channels using lagrangian sensing. In *Proceedings of the 48h IEEE Conference on Decision and Control (CDC)*, pages 8266–8271. IEEE, December 2009. ISBN 978-1-4244-3871-6.

W. C. Reynolds. Large-scale instabilities of turbulent wakes. *J. Fluid Mech.*, 54(3):481–488, August 1972. ISSN 0022-1120, 1469-7645. doi: 10.1017/S0022112072000813.

J. H. M. Ribeiro, C. Yeh, and K. Taira. Randomized resolvent analysis. *Phys. Rev. Fluids*, 5(3): 033902, March 2020. ISSN 2469-990X. doi: 10.1103/PhysRevFluids.5.033902.

K. Roussopoulos and P. A. Monkewitz. Nonlinear modelling of vortex shedding control in cylinder wakes. *Phys. D Nonlinear Phenom.*, 97(1-3):264–273, October 1996. ISSN 0167-2789. doi: 10.1016/0167-2789(96)00151-0.

C. W. Rowley. Model reduction for fluids, using balanced proper orthogonal decomposition. *Int. J. Bifurc. Chaos*, 15(03):997–1013, 2005. doi: 10.1142/S0218127405012429.

C. W. Rowley, D. R. Williams, T. Colonius, R. M. Murray, and D. G. Macmynowski. Linear models for control of cavity flow oscillations. *J. Fluid Mech.*, 547:317, January 2006. ISSN 0022-1120, 1469-7645.

Y. Saad and M. H. Schultz. GMRES: A generalized minimal residual algorithm for solving nonsymmetric linear systems. *SIAM J. Sci. Stat. Comput.*, 7(3):856–869, July 1986. ISSN 0196-5204, 2168-3417. doi: 10.1137/0907058.

M. G. Safonov, D. J. N. Limebeer, and R. Y. Chiang. Robust control toolbox user's guide. The MathWork, 1992.

K. Sasaki, P. Morra, N. Fabbiane, A. V. G. Cavalieri, A. Hanifi, and D. S. Henningson. On the wave-cancelling nature of boundary layer flow control. *Theor. Comput. Fluid Dyn.*, 32(5): 593–616, October 2018a. ISSN 0935-4964, 1432-2250. doi: 10.1007/s00162-018-0469-x.

K. Sasaki, G. Tissot, A. V. G. Cavalieri, F. J. Silvestre, P. Jordan, and D. Biau. Closed-loop control of a free shear flow: A framework using the parabolized stability equations. *Theor. Comput. Fluid Dyn.*, 32(6):765–788, December 2018b. ISSN 0935-4964, 1432-2250. doi: 10.1007/s00162-018-0477-x.

K. Sasaki, P. Morra, A. V. G. Cavalieri, A. Hanifi, and D. S. Henningson. On the role of actuation for the control of streaky structures in boundary layers. *J. Fluid Mech.*, 883:A34, January 2020. ISSN 0022-1120, 1469-7645.

P. Sashittal and D. J. Bodony. Data-driven sensor placement for fluid flows. *Theor. Comput. Fluid Dyn.*, 35(5):709–729, October 2021. ISSN 0935-4964, 1432-2250. doi: 10.1007/s00162-021-00584-w.

C. J. Schauerte and A. Schreyer. Experimental investigation on the turbulent wake flow in fully established transonic buffet conditions. *CEAS Aeronautical J.*, 15(1):125–147, January 2024. ISSN 1869-5582, 1869-5590. doi: 10.1007/s13272-023-00690-x.

P. J. Schmid and D. Sipp. Linear control of oscillator and amplifier flows. *Phys. Fluids*, 1:040501, August 2016. ISSN 2469-990X.

O. T. Schmidt and A. Towne. An efficient streaming algorithm for spectral proper orthogonal decomposition. *Comput. Phys. Commun.*, 237:98–109, April 2019. ISSN 0010-4655. doi: 10.1016/j.cpc.2018.11.009.

O. T. Schmidt, A. Towne, G. Rigas, T. Colonius, and G. A. Brès. Spectral analysis of jet turbulence. *J. Fluid Mech.*, 855:953–982, November 2018. ISSN 0022-1120, 1469-7645.

S. Shamsoddin and F. Porté-Agel. Turbulent planar wakes under pressure gradient conditions. *J. Fluid Mech.*, 830:R4, November 2017. ISSN 0022-1120, 1469-7645. doi: 10.1017/jfm.2017.649.

A. Sharma, D. Limebeer, B. McKeon, and J. Morrison. Stabilising control laws for the incompressible navier-stokes equations using sector stability theory. In *3rd AIAA Flow Control Conf.*, San Francisco, California, June 2006. AIAA. ISBN 978-1-62410-036-9. doi: 10.2514/6.2006-3695.

D. Simon. *Optimal State Estimation: Kalman, H Infinity, and Nonlinear Approaches*. John Wiley & Sons, 2006.

D. Sipp, O. Marquet, P. Meliga, and A. Barbagallo. Dynamics and control of global instabilities in open-flows: A linearized approach. *Appl. Mech. Rev.*, 63(3):030801, May 2010. ISSN 0003-6900, 2379-0407. doi: 10.1115/1.4001478.

V. I. Smirnov. *A Course of Higher Mathematics - Vol. IV*. Pergamon Press, Oxford, 1964.

Robert F. Stengel. *Optimal Control and Estimation*. Dover Publ., 1994.

A. Stieren and R. J.A.M. Stevens. Impact of wind farm wakes on flow structures in and around downstream wind farms. *Flow*, 2:E21, 2022. ISSN 2633-4259. doi: 10.1017/flo.2022.15.

P. J. Strykowski and K. R. Sreenivasan. On the formation and suppression of vortex 'shedding' at low reynolds numbers. *J. Fluid Mech.*, 218:71, September 1990. ISSN 0022-1120, 1469-7645. doi: 10.1017/S0022112090000933.

S. Symon, D. Sipp, and B. J. McKeon. A tale of two airfoils: resolvent-based modelling of an oscillator versus an amplifier from an experimental mean. *J. Fluid Mech.*, 881:51–83, December 2019. ISSN 0022-1120, 1469-7645. doi: 10.1017/jfm.2019.747.

J. S. Tao, X. Y. Huang, and W. K. Chan. A flow visualization study on feedback control of vortex shedding from a circular cylinder. *J. Fluids Struct.*, 10(8):965–970, November 1996. ISSN 0889-9746. doi: 10.1006/jfls.1996.0061.

V. Theofilis. Advances in global linear instability analysis of nonparallel and three-dimensional flows. *Prog. in Aerosp. Sci.*, 39(4):249–315, May 2003. ISSN 03760421. doi: 10.1016/S0376-0421(02)00030-1.

N. Thomareis and G. Papadakis. Resolvent analysis of separated and attached flows around an airfoil at transitional reynolds number. *Phys. Rev. Fluids*, 3:073901, July 2018. ISSN 2469-990X.

A. Towne, O. T. Schmidt, and T. Colonius. Spectral proper orthogonal decomposition and its relationship to dynamic mode decomposition and resolvent analysis. *J. Fluid Mech.*, 847:821–867, July 2018.

A. Towne, A. Lozano-Durán, and X. Yang. Resolvent-based estimation of space–time flow statistics. *J. Fluid Mech.*, 883:A17, January 2020. ISSN 0022-1120, 1469-7645.

A. Towne, S. T. M. Dawson, G. A. Brès, A. Lozano-Durán, T. Saxton-Fox, A. Parthasarathy, A. R. Jones, H. Biler, C. Yeh, H. D. Patel, and K. Taira. A Database for Reduced-Complexity Modeling of Fluid Flows. *AIAA J.*, 61(7):2867–2892, July 2023.

A. Towne, R. Bhagwat, Y. Zhou, J. Jung, E. Martini, P. Jordan, D. Audiffred, I. Maia, and A. Cavalieri. Resolvent-based estimation of wavepackets in turbulent jets. In *30th AIAA/CEAS Aeroacoustics Conf. (2024)*, Rome, Italy, June 2024. AIAA. ISBN 978-1-62410-720-7. doi: 10.2514/6.2024-3413.

A. W. Vreman. An eddy-viscosity subgrid-scale model for turbulent shear flow: Algebraic theory and applications. *Phys. Fluids*, 16(10):3670–3681, October 2004. ISSN 1070-6631, 1089-7666. doi: 10.1063/1.1785131.

S. Wagner, R. Bareiß, and G. Guidati. *Wind Turbine Noise*. Springer-Verlag, 1996.

Y. X. Wang, K.-S. Choi, M. Gaster, C. Atkin, V. Borodulin, and Y. Kachanov. Opposition control of turbulent spots. *J. Fluid Mech.*, 943:A3, July 2022. ISSN 0022-1120, 1469-7645. doi: 10.1017/jfm.2022.396.

P. Welch. The use of fast fourier transform for the estimation of power spectra: A method based on time averaging over short, modified periodograms. *IEEE Trans. Audio Electroacoust.*, 15(2): 70–73, June 1967. ISSN 0018-9278.

C. Yeh and K. Taira. Resolvent-analysis-based design of airfoil separation control. *J. Fluid Mech.*, 867:572–610, May 2019. ISSN 0022-1120, 1469-7645.

C. Yeh, S. I. Benton, K. Taira, and D. J. Garmann. Resolvent analysis of an airfoil laminar separation bubble at Re = 500 000. *Phys. Rev. Fluids*, 5(8):083906, August 2020. ISSN 2469-990X.

A. Ying, T. Liang, Z. Li, and L. Fu. A resolvent-based prediction framework for incompressible turbulent channel flow with limited measurements. *J. Fluid Mech.*, 976:A31, December 2023. ISSN 0022-1120, 1469-7645. doi: 10.1017/jfm.2023.867.

K. Yousefi and A. Razeghi. Determination of the critical reynolds number for flow over symmetric naca airfoils. In *2018 AIAA Aerosp. Sci. Meet.*, Kissimmee, Florida, January 2018. AIAA. ISBN 978-1-62410-524-1. doi: 10.2514/6.2018-0818.

A. Zare, M. R. Jovanović, and T. T. Georgiou. Colour of turbulence. *J. Fluid Mech.*, 812:636–680, February 2017. ISSN 0022-1120, 1469-7645. doi: 10.1017/jfm.2016.682.

K. Zhou and J. C. Doyle. *Essentials of Robust Control*. Prentice Hall, 1997.